AD 621 447

INSTITUTE FOR AEROSPACE STUDIES

UNIVERSITY OF TORONTO

DESIGN, INSTRUMENTATION AND PERFORMANCE OF
THE UTIAS 4-in.x 7-in. HYPERSONIC SHOCK TUBE

by

A. G. Boyer

CLEARINGHOUSE
FOR FEDERAL SCIENTIFIC AND
TECHNICAL INFORMATION

Hardcopy	Microfiche	
$5.00	$1.00	171 pp as

ARCHIVE COPY

DDC
RECEIVED
OCT 4 1965
DDC-IRA E

MAY 1965

UTIAS REPORT NO. 99
AFOSR 65-1400

DESIGN, INSTRUMENTATION AND PERFORMANCE OF THE UTIAS 4-in.x 7-in. HYPERSONIC SHOCK TUBE

by

A. G. Boyer

MAY 1965

UTIAS REPORT NO. 99
AFOSR 65-1400

ACKNOWLEDGEMENT

The author wishes to express his appreciation to Dr. G.N. Patterson, Director of the Institute for Aerospace Studies, for his continued encouragement during the present work.

The project was carried out under the direction of Dr. I.I. Glass, whose advice and support throughout the course of the work are gratefully acknowledged.

Sincere appreciation is extended to G.F. Bremner for his invaluable contribution to the shock tube design, and for his capable handling of the stress analysis. The assistance received from J.H.W. Lau and A.K. Roberts during the early stages of the project is acknowledged, and special thanks are accorded B.G. Dawson and J.E. Drewry for their assistance in the calibration of the facility.

The financial assistance received from the U.S. Air Force Office of Scientific Research under Grant No. AF-AFOSR-365-65 and the Defence Research Board of Canada is gratefully acknowledged.

SUMMARY

A detailed account is presented of the research and development, design, calibration, and performance of the UTIAS 4-in.x 7-in. Hypersonic Shock Tube, which is used as a modern aerophysical research facility for dissociated and ionized gas flows. The component design and construction features, operating and control systems, safety features, and the diaphragm techniques employed, are described. The instrumentation for monitoring tube performance and operation is also discussed. The operating characteristics, including theoretical and observed performance, are presented. An account of various problems which arose during the development and operation of this very large facility, and the corrective measures taken, is included.

TABLE OF CONTENTS

		Page
	NOTATION	vi
1.	INTRODUCTION	1
2.	SHOCK TUBE DESIGN AND CONSTRUCTION	1
	2.1 General Description of Shock Tube	1
	2.2 Design Criteria	2
	2.2.1 General Considerations	2
	2.2.2 Tube Length and Cross-section	2
	2.2.3 Method of Driving the Shock Tube	3
	2.2.4 Operating Pressures and Vacuum Requirements	5
	2.2.5 Dynamic Loading of Shock Tube	6
	2.2.6 Protection of Personnel	6
	2.3 Specific Design and Construction	7
	2.3.1 Driver and Diaphragm Station	7
	2.3.2 Transition Section	8
	2.3.3 Driven Section	8
	2.3.4 Test Section	10
	2.3.5 Dump Tank	11
	2.3.6 Recoil System	12
3.	CONTROL SYSTEMS	13
	3.1 Driver Gas Mixing	13
	3.2 Driver Ignition System	14
	3.3 Control, Pressure, and Vacuum Systems	16
4.	SHOCK TUBE HAZARDS AND SAFETY PRECAUTIONS	18
	4.1 Driver Blockhouse and Test Section Blast Mat	18
	4.2 Alarm Systems	19
	4.3 General Safety Features	20
5.	DIAPHRAGMS	22
	5.1 General Requirements	22
	5.2 Diaphragm Materials, Preparation, and Calibration	22
6.	INSTRUMENTATION	25
	6.1 Pressure Transducers	25
	6.2 Ionization Gauges	27
	6.3 Heat Flux Gauges	27
	6.4 Wave Speed Measurements	28
	6.5 Optical Systems	28

7. SHOCK TUBE OPERATION 29

7.1 General Operating Procedure 29
7.2 Operational Problems 30

7.2.1 Loss of Diaphragm Material 30
7.2.2 Fluid Leakage from Recoil Shock Absorbers 30
7.2.3 Tube Contamination 31

8. SHOCK TUBE PERFORMANCE AND CALIBRATION 31

8.1 Maximum Operating Conditions 31
8.2 Predicted Performance 32
8.3 Shock Tube Calibration 40

8.3.1 Range of Calibration 40
8.3.2 Comparison with Predicted Performance 41

9. CONCLUDING REMARKS 43

REFERENCES 44

TABLES 1-10

FIGURES 1-108

NOTATION

a	sound speed
C_p	specific heat at constant pressure
C_v	specific heat at constant volume
D	hydraulic diameter: (4 x area/perimeter)
e	specific internal energy
E	modulus of elasticity
h	specific enthalpy
k	strain gauge factor
K	specific refractivity: $(n-1)/\rho$
l,L	length
m	molecular weight
n	index of refraction
p	pressure
$\mathcal{R}$	universal gas constant
R	gas constant per unit mass, resistance
Re	Reynolds number
S	entropy, fringe shift
t	time
t_c	flow time terminated by arrival of interface
T	absolute temperature
u	particle velocity
v	relative velocity
w	shock wave velocity
x	distance, degree of ionization
x_c	flow length between shock and interface
Z	compressibility factor: $p/\rho RT$
α	degree of dissociation

γ	specific heat ratio: C_p/C_v
γ^*	isentropic index: $\rho a^2/p$
λ	wavelength
μ	viscosity
ρ	density
σ	stress

Subscripts 1, 2, 3, etc. to physical quantities refer to the value of the quantity in the shock tube flow regions shown in Fig. 1 or 2.

Non-dimensional variables:

$A_{ij} = a_i/a_j$	sound speed ratio
$M_i = u_i/a_i$	flow Mach number
$M_s = w/a_1$	shock Mach number
$P_{ij} = p_i/p_j$	pressure ratio
$T_{ij} = T_i/T_j$	temperature ratio
$U_{ij} = u_i/a_j$	particle velocity to reference sound speed ratio
$\Gamma_{ij} = \rho_i/\rho_j$	density ratio

Symbols:

D_1	represents the primary or driver diaphragm
D_2	represents the second or buffer diaphragm
$\vec{C}$	represents an interface moving in direction of arrow
$\vec{R}$	represents an expansion wave facing in direction of arrow
$\vec{S}$	represents a shock wave facing in direction of arrow
H_2/Air	represents a diaphragm or interface separating hydrogen and air

1. INTRODUCTION

The development of hypersonic vehicles such as ballistic missiles and satellites has given rise to many enviromental problems, particularly in the realms of fluid dynamics and high-temperature gas physics. For example, the relative kinetic energy of the air intercepted by a vehicle travelling at the satellite velocity is large enough to dissociate all of the oxygen and a considerable portion of the nitrogen molecules, and to thermally ionize a significant fraction of the air. In addition, chemical reactions between some of the constituents will occur. To obtain aerodynamic and thermodynamic data at these extreme physical conditions requires experimental facilities capable of generating the high stagnation temperatures encountered by these hypersonic vehicles.

The ability of the shock tube to simulate the high temperatures and velocities of hypersonic flight has led to its widespread use as a primary tool for high-temperature gasdynamic research.

The conventional shock tube consists of a duct of constant cross-section separated by a diaphragm into a high pressure or driver section and a low pressure or driven section. When the diaphragm is ruptured, a shock wave is generated which propagates into the low pressure region, accelerating the gas and raising its temperature. Simultaneously an expansion wave propagates into the high pressure region, accelerating the driver gas into the driven section. The flow regions induced behind these waves are separated by an interface or contact surface across which the pressure and velocity are equal, but the density and temperature are in general different. Between the incident shock wave and the interface there exists a short duration quasi-steady flow of compressed and heated gas which is available for test purposes. (A wave diaphragm of the basic shock tube flow is shown in Fig. 1.) The theory and operation of shock tubes have been well reported in the literature (see Refs. 1 and 2 and their bibliography). Therefore details of shock tube theory and operation will not be discussed here.

This report presents a detailed account of the development and performance of the UTIAS 4-in.x 7-in. combustion driven hypersonic shock tube, which was established to study problems in gas physics and real gas dynamics associated with hypersonic flight. The design criteria and component design and construction features are described in detail. The operating and control systems, safety features, and the diaphragm techniques employed, are also described. The instrumentation for monitoring tube performance and operation is discussed. The operating characteristics, including theoretical and observed performance, are presented. The envelopes of maximum performance for air and argon as test gases are presented in the form of tables and charts. An account of several problems which arose during the development and operation of this facility, and the corrective measures taken, is included.

2. SHOCK TUBE DESIGN AND CONSTRUCTION

2.1 General Description of Shock Tube

The UTIAS 4-in.x 7-in. hypersonic shock tube is a constant-area, combustion-driven tube designed to simulate the high stagnation enthalpies and pressures typical of hypersonic flight. The shock tube consists of a driver, transition section, driven section, test section, dump tank, and recoil sections. Table 1 presents a description of these principal components. A schematic assembly of the complete facility is shown in Fig.3 and

overall views in Figs.4-9. The structural design of the principal components is shown in Figs.10-16. The considerations leading to these designs are described in the following sections.

2.2 Design Criteria

2.2.1 General Considerations

With the diversified applications of the shock tube in current research, shock tube designs have become somewhat specialized. Specific design features are determined by the particular application and funds available Programs proposed for this facility include measurements of dissociation, ionization, and recombination rates; study of non-equilibrium flows of dissociated and ionized gases; study of effects of dissociation, ionization, and recombination on boundary layer parameters such as heat transfer and transition; and studies of plasmadynamics of flows about space-vehicle models including the effects of heat transfer, pressure drag, and skin friction.

Since these studies require temperatures high enough to realize significant, if not complete, dissociation or ionization of the test gas, the first requirement was to produce shock waves strong enough to achieve such temperatures. Shock Mach numbers in the range from 7 to 20 were therefore required.

2.2.2 Tube Length and Cross-section

The driver and driven section lengths of a shock tube are determined by required testing times and the driving method. In this case, however, available laboratory space limited the length of the driven section (diaphragm to dump tank) to 48 feet. The minimum driver length to avoid reduction of hot-flow testing time by the expansion wave reflected from the end of the driver, is that for which the reflected head of the expansion wave overtakes the interface at the test section (see Fig.1).

For a constant area tube, the ratio L_1/L_4 of driven length to minimum driver length, as a function of shock Mach number M_s, is given by (Ref.1)

$$\frac{L_1}{L_4} = \frac{2M_s}{A_{41}}\left[1-\frac{\gamma_4-1}{2}\cdot\frac{U_{21}}{A_{41}}\right]^{-\frac{\gamma_4+1}{2(\gamma_4-1)}}\left[\frac{U_{21}+M_{sr}}{M_s+M_{sr}}\right] \qquad (2.1)$$

where M_{sr} = reflected shock Mach number from the end of the driven section.

Under normal operating conditions, the lowest shock Mach number in air was taken to be 7. For a constant volume combustion driver, and equilibrium air behind the shock wave, Eq. (2.1) gives $L_1/L_4 = 3.6$ for $M_s = 7$. The maximum driver length required is therefore 13.5 feet.

For a shock Mach number of 20 the required driver length is less than 1-ft. Thus the use of different driver lengths for various operating conditions was proposed in order to conserve gas consumption and economize on the operation of the facility.

The intended use of an existing 9-inch plate Mach-Zehnder interferometer[3] as a prime instrument in conjunction with the facility dictated the rectangular 4-in.x 7-in. internal dimensions of the driven section . The 7-in. height allows full use to be made of the 7-in.x 9-in. elliptic field of view of the interferometer. The 4-in. width is essentially a compromise between size and cost considerations and requirements for good optical sensitivity. The relation between fringe shift S (sensitivity of interferometer) and density change between two states 1 and 2 is (Ref. 1)

$$\rho_2 = \rho_1 + \frac{\lambda S}{KL} \tag{2.2}$$

or

$$S = \rho_1 (\Gamma_{21} - 1) \frac{KL}{\lambda} \tag{2.3}$$

where S is expressed in fringe numbers.

The fringe shift S increases with the optical path length L (test section width). Hence a wide test section is desirable for good optical sensitivity, particularly at low testing densities (ρ_1 small). As an example, from Eq. (2.3) with λ= 5180 Å and L = 4-ins., the fringe shift across a normal shock wave of M_s = 7 propagating into air at an initial pressure of 1 mm Hg, is S = .42 fringes. Fringe shifts of this order are rather small for accurate quantitative measurements of density, and in practice would usually be about an order greater.

2.2.3 Method of Driving the Shock Tube

The important parameters governing the shock strength are the diaphragm pressure and sound speed ratios. The basic shock tube equation relating shock Mach number M_s with the diaphragm pressure ratio P_{41}, for a constant-area tube, is (Ref. 1)

$$P_{41} = \left[1 + \frac{2\gamma_1}{\gamma_1 + 1} (M_s^2 - 1) \right] \left[1 - \frac{\gamma_4 - 1}{\gamma_1 + 1} \cdot \frac{M_s^2 - 1}{A_{41} M_s} \right]^{-\frac{2\gamma_4}{\gamma_4 - 1}} \tag{2.4}$$

where $A_{41} = a_4/a_1$ is the ratio of driver to driven gas sound speeds. Although the assumptions of perfect gases and ideal shock tube flow entering Eq. (2.4) are violated in practice, this relation does serve as a general guide to shock tube performance.

Shock Mach number increases with diaphragm pressure ratio and the limiting value of M_s attained asymptotically as $P_{41} \to \infty$ is, from Eq. (2.4)

$$\lim_{P_{41} \to \infty} M_s = \frac{\gamma_1 + 1}{\gamma_4 - 1} \cdot \frac{A_{41}}{2} + \left[\left(\frac{\gamma_1 + 1}{\gamma_4 - 1} \cdot \frac{A_{41}}{2} \right)^2 + 1 \right]^{\frac{1}{2}} \tag{2.5}$$

For $A_{41} > 1$, this may be written approximately as

$$\lim_{P_{41} \to \infty} M_s \approx \frac{\gamma_1 + 1}{\gamma_4 - 1} \cdot A_{41} \tag{2.6}$$

which indicates A_{41} must be as large as possible to obtain strong shocks. For perfect gases, A_{41} is given by

$$A_{41} = \frac{a_4}{a_1} = \left[\frac{\gamma_4 \, m_1 \, T_4}{\gamma_1 \, m_4 \, T_1} \right]^{\frac{1}{2}} \tag{2.7}$$

where m_4, m_1 and T_4, T_1 are the molecular weights and absolute temperatures of the driver and driven gases respectively. In general the type of driven gas is dictated by the particular requirements of a research project, and attention is therefore directed to the driver conditions to increase A_{41}. It is evident from Eq. (2.7) the driver sound speed can be increased by using a light gas at a high temperature.

Consequently, the generation of strong shock waves requires large diaphragm pressure ratios and a low molecular weight, high temperature, driver gas. Combustion of a light gaseous mixture in the driver is a proven and practical means of achieving these conditions.[1,4,5] Constant volume combustion of a stoichiometric hydrogen-oxygen mixture diluted with 75% helium, with spontaneous diaphragm rupture from the resulting increase in pressure, is the particular driver technique adopted for this facility.

Combustion heating, however, is not without inherent difficulties. The primary shock strength and attenuation, and the degree of flow non-uniformity behind the shock with combustion drive depend very much on the method of ignition and on the stage of the combustion process at which the diaphragm ruptures. Further, the possibility of severe detonations occurring increases the structural design problems of the driver.

To improve performance and avoid the use of combustion drivers, various modifications of the basic shock tube have been made. These modifications include the use of a double diaphragm driver with monatomic buffer gases, and an area contraction at the diaphragm station.[6-12] The double diaphragm driver with an area contraction permits the generation of strong shock waves, using cold hydrogen or helium as a driver gas, with overall pressure ratios comparable to those required by combustion drivers.

The advantages of these techniques cannot be overlooked. However, the use of an area contraction with the fixed 4-in.x 7-in. driven dimensions would lead to an extremely large and expensive driver. For example, an area contraction ratio of 5, which offers approximately 70% of the maximum possible gain available with an infinite area ratio,[11] would require a 13.4-in. internal diameter driver. Further, expensive compressor equipment would be required to charge the driver. The use of an area contraction was therefore not considered practical, and a constant-area configuration was adopted, resulting in a 6-in. internal diameter driver.

The double-diaphragm modification with a monatomic buffer gas, although producing only marginal gain in driver efficiency for a constant-area tube, offers a method of isolating the combustion-test gas interface, thereby avoiding flow disturbances associated with combustion at the interface. Provision for an argon buffer region was therefore incorporated in the design. A wave diagram of the initial flow in a double diaphragm constant-area tube is shown in Fig.2. The second diaphragm is assumed to be very weak so that ideally it is instantly ruptured and no reflected shock wave occurs.

2.2.4 Operating Pressures and Vacuum Requirements

The required shock strengths, desirable density levels for interferometric studies, and size and cost considerations, were the factors determining the driver and driven section operating pressures.

A preliminary performance analysis based on data presented in Ref. 1 showed that it would be possible to generate the required shock strengths, at convenient initial pressure levels, with driver combustion pressures of the order of 10,000 psi.

Interferometric studies of flow fields require a reasonable density level behind the primary shock wave. For a driver combustion pressure of 10,000 psi and an initial driven pressure of 1 mm Hg, it is theoretically possible to generate a shock Mach number of 20.8 in air. In this case the density behind the shock is approximately $.02\rho_o$, where ρ_o is standard atmospheric density. Although the fringe shift across the primary shock is small under these conditions ($S = 1$ from Eq. (2.3)), the fringe shift is approximately 6 across the bow wave of a model in the flow. Effects such as attenuation will, of course, modify these values in a real shock tube flow. However, as fringe shifts of this order are more than adequate for quantitative interferometric studies, and since combustion pressures of this order can be realized by using commercially available gas cylinders to charge the driver initially, the driver operating pressure was set at 10,000 psi.

Although a natural choice for quantitative interferometry, the large rectangular cross-section of the driven section does present problems with respect to structural strength and ease of construction and sealing. This is particularly true for the test section, which must incorporate interferometer quality windows of relatively large area. Consideration of size and cost indicated an operating pressure of 500 psi would be practical for the driven and test sections.

If the primary shock wave was allowed to reflect from the end of the driven section, it would be possible to achieve pressures in the driven section approaching the order of the driver pressures. Reflection of the primary shock wave can be prevented by terminating the driven section with a large volume dump tank. The dump tank would also serve to reduce the overall pressure after a run to a reasonable value, and thus avoid subjecting the large test section windows to high loads any longer than necessary. A 3-ft. diameter cylinder, 6-ft. high (35-cu.ft. volume), would satisfy space limitations and limit the maximum equilibrium pressure in the facility after a run to an acceptable level of 75 psi.

The main problem in the design of the dump tank is the selection of its operating pressure. This is very difficult to predict accurately. The operating pressure will be determined by the reflections of the primary shock wave from the walls of the dump tank. Due to the geometry of the dump tank and the attenuation of the primary and reflected shock waves, this reflection process is highly complex. In order to estimate the pressure behind the reflected shock wave, certain assumptions must be made: the primary shock wave becomes a spherical wave front as it emerges into the dump tank; the attenuation of the wave is inversely proportional to the square of the radius of the wave front (for waves of intermediate strength);

and the reflection process is given approximately by the planar case. With these assumptions, and considering the dump tank to be a 3-ft. diameter vertical cylinder, the maximum pressure behind the reflected wave is 300 psi at a shock Mach number of 10.5 and initial pressure of 3.54 psi. These conditions give the maximum operating pressure (500 psi behind the shock wave) in the driven section. The dump tank was therefore designed for an operating pressure of 300 psi. A theoretical analysis of the dump tank pressure-time history is given in Ref. 13.

For dissociation and ionization studies it is necessary to know the precise nature of the test gas. To minimize contamination of the test gas, the driven section should be capable of being evacuated to a pressure of at least 1 micron Hg, and of maintaining this pressure with a very small leak rate (say, 1 micron Hg/minute pressure rise).

2.2.5 Dynamic Loading of Shock Tube

In combustion driven shock tubes very high axial loads can occur. At the driver end the load results from the pressure exerted by the combustion gas until it is relieved by the incoming expansion wave. The load on the dump tank end of the tube results from the deceleration of the gas flow by the walls of the dump tank.

Whether or not the dynamic loading on a shock tube will be a design problem depends on the size of the facility. If the driver cross-sectional area is of the order of 5 sq.ins., the entire facility may be coupled together and designed for the peak end load with an adequate safety factor. However, for larger drivers, the solution is not so simple. For the present shock tube, peak driver pressures of 10,000 psi will be encountered, resulting in an axial load of 280,000 lbs. In addition, pressures up to 15,000 psi (425,000 lbs load) could be experienced if detonation of the combustion gases occurs. (Since a rupture disc at the end of the driver will blow out at 15,000 psi, this represents the highest possible axial load.)

A shock tube constructed as a solid assembly, with flanges capable of withstanding axial loads of this magnitude, would be a massive and expensive piece of equipment. However, if the driver and dump tank are allowed to recoil instead of being rigidly attached to the driven section, then the driven section is effectively isolated from any axial loads. This would then permit the driven section to be designed for a minimum of loading, and also eliminate relative motion of the test section with respect to the optical system. A recoil system comprising telescopic recoil sections and energy absorbing damping jacks, which would allow the driver and dump tank to recoil some prescribed distance while applying a reaction to oppose the load, was therefore proposed for the facility (see Sec. 2.3.6).

2.2.6 Protection of Personnel

High-pressure shock-tube operation presents some obvious potential hazards, particularly with the use of explosive gas mixtures. A structural failure during operation of the facility, for example, would be disastrous to unprotected personnel. As it is not possible to design the driver to withstand such a combustion phenomenon as over-detonation[14] (a phase in the formation of normal detonation in which pressures can attain values three

or four times those of normal detonation), which would require a safety factor of at least 20, it was decided to house the driver and several feet of the driven section in a reinforced concrete blockhouse. A driver failure during high pressure operation would require reinforced concrete walls at least 12-in. thick for adequate protection.[15] As a further precaution, laboratory exposed sections of the shock tube would be designed where possible with a safety factor of 5. Adequate protection around the test section must also be provided in case of window failure.

A description of the general safety features of this facility is given in Sec. 4.

2.3 Specific Design and Construction

2.3.1 Driver and Diaphragm Station

The driver has an internal diameter of 6-ins., a wall thickness of 4-ins., and a total length of 13.5-ft. Constructed of chrome-molybdenum steel, the design operating pressure after combustion is 10,000 psi with a safety factor of 6. Overall views of the driver are shown in Figs. 4 and 5.

Several methods exist for designing thick wall cylinders for service under high internal pressure.[16,17] In Fig. 17, the single and compound methods of construction are shown. The yield pressure indicated for each configuration is for a material with an ultimate tensile strength of 168,000 psi and a yield point strength of 150,000 psi (Atlas Ultimo-4). The configuration of Fig. 17(a) was adopted for the driver as this represents the most economical manner in which to fulfill the design criteria.

The driver is made in two 3-ft. sections, one 6-ft. section, and a 1.5-ft. end section. The structural design of the 6-ft. section is shown in Fig. 10. The joints between sections are spigot and counterbore joints with hard (90 durometer) O-ring seals. The spigot has a 2-in. spherical radius (see Fig. 18). This type of coupling facilitates alignment and eliminates binding of the mating sections. The removable flanges are designed to transmit the end load occurring at the yield pressure. To prevent corrosion, the bore and end faces of each section are plated with a .002-in. layer of hard chromium.

The 1.5-ft. end section is terminated with a rupture disc designed to fail between 14,000 and 15,500 psi (Figs. 19 and 20). Inclusion of the rupture disc limits the axial load at the end of the driver to 425,000 lbs. The rupture disc is held by a 2.5-in. thick clamping ring bolted to the end of the section (see Fig. 44). The 4.5-in. diameter burst area of the rupture disc is offset from the driver axis to accomodate an instrumentation port for mounting a pressure pickup at the end of the driver. A gas port and an electrical lead entry port for charging the driver and igniting the gas mixture are provided in the wall of the section. Any particular driver configuration always includes this section. The basic design is shown in Fig. 21.

For ease of handling in the assembly of the various driver lengths, the driver sections are supported by individual stands which are mounted on tracks running the length of the blockhouse enclosing the driver (Fig. 4).

The driver-stand attachment bolts allow horizontal and vertical adjustment of ± 1-in. for alignment of the sections. An overhead hoist of 2 tons capacity spanning the 20-ft. width of the blockhouse is used to lift the driver sections into place.

Located between the driver and the driver recoil section is a short section which holds the diaphragm as shown in Fig. 22. This section employs a 'floating piston' arrangement[18] to prevent the diaphragm drawing in during the combustion process. The annulus of the piston exposed to the internal pressure is equal in area to the driver bore. Any elongation of the clamping bolts due to the pressure load allows the piston to move and maintain the clamping load on the diaphragm. A pneumatic jack between the driver and driver recoil section opens and closes the diaphragm station (Fig. 36).

2.3.2 Transition Section

The transition section is an 1.5-ft. section located between the driver recoil section and the driven section. The design is shown in Fig. 11. The internal cross-section is a straight transition from the driver 6-in. internal diameter to the driven 4-in.x 7-in. rectangular dimensions. In the horizontal plane there is a contraction from the 6-in. diameter to the 4-in. width, and in the vertical plane an expansion to the 7-in height, without any area change. This gradual transition reduces flow disturbances arising from the change in cross-section between the driver and driven sections.

Manufactured from a steel casting (material equivalent to driver material) and heat treated to obtain an ultimate tensile strength of 148,000 psi and a yield point strength of 130,000 psi, this section can withstand a transient pressure loading of 3500 psi. The design details (external dimensions, flange and dowelled construction) are similar to the driven sections (see Sec. 2.3.3). A heavy chrome plate .005-in. thick provides erosion and corrosion protection to the bore and end faces.

2.3.3 Driven Section

The design specifications require the driven section to be 40 feet in length with a 4-in.x 7-in. cross-section capable of withstanding a transient pressure loading of 500 psi. To maintain the dimensions of the driven section at a reasonable size, a high strength alloy steel commensurate with good machinability was chosen for the design. The material used was SPS-245 normalized with an ultimate tensile strength of 135,000 psi and a yield point of 112,000 psi.

A number of cross-sectional configurations were examined to determine the most suitable method of construction (see Fig. 23). Of the configurations shown, that of Fig. 23(a) was selected on the basis of relative ease of manufacture and assembly with a minimum of sealing surfaces. In order to eliminate any possible leak path and provide a positive vacuum seal with such a design, the longitudinal sealing grooves must terminate in the O-ring groove at the end of the section (see Fig. 26). A butt seal between the end O-ring and the longitudinal seal was therefore required. Further, in such a design, there exist regions where the stresses will be influenced by stress concentrations, viz. at the bottom corners of the 4-in.x 7-in. slot and around bolt holes and ports in the top plate. Due to these

stress concentrations, it is not possible to obtain a reliable stress analysis. To ensure the structural integrity and good sealing features of the design, a 2-ft. section was built to undergo strain gauge and vacuum tests. The design of this pressure test section is shown in Fig. 24.

Standard techniques[19] were employed in conducting the strain gauge tests. SR-4 type A-7 strain gauges were located around a bolt hole and the port opening in the top plate, and on an end face of the section at the bottom corners of the 4-in.x 7-in. slot. These locations are the critical regions where high stress concentrations would be expected to occur. Temperature compensation of the strain gauges was achieved by mounting a strain gauge on a piece of material the same as that of the section (SPS-245), and using this dummy gauge as one of the ratio arms of a Wheatstone bridge circuit used to measure the resistance of each strain gauge. The resistances of the various gauges were measured for internal air pressures of 0, 250, 500, 750, 1000, and 1250 psig. The change in resistance (ΔR), from the reference value at the 0 psig (1 atmosphere) level, was then transformed into the stress σ by the standard relation[19]

$$\sigma = E \Delta R / Rk \tag{2.8}$$

where E = modulus of elasticity (28.6×10^6 psi for SPS-245)

R = strain gauge resistance ($119.5 \pm .2\Omega$)

k = strain gauge factor ($1.97 \pm 2\%$)

The maximum stress measured, around the bolt hole in the top plate, was 24,800 psi for an internal pressure of 1250 psig. This represents just 22% of the yield strength (112,000 psi) of the material.

Initially it was anticipated that these tests would be conducted up to the 2000 psi pressures available from commercial gas cylinders. However, as it was necessary to place shims between the end plate and the section to avoid crushing the strain gauges mounted on the end face, this end of the section could not be adequately sealed for internal pressures in excess of 1250 psig. The strain gauge tests were therefore limited in scope. However, extrapolating the test results indicates the section top plate would yield around an internal pressure of 5000 psi, and that the driven section could therefore operate at transient pressures of 1000 psi with an adequate safety factor.

From the vacuum tests, it was found that a suitable butt seal could be obtained between the longitudinal and end O-rings by significantly reducing the groove dimensions. With the groove area reduced to 92% of the cross-sectional area of the O-ring, the longitudinal seal would extrude upon assembly. Carefully trimming and sanding the ends flush with the surface provided an extremely good seal. An ultimate vacuum of less than 0.2 microns Hg with a leak rate (pressure rise) of 1 micron in 30 minutes was eventually achieved with this section. Incorporating this type of sealing arrangement into the desgin of the driven sections, a leak rate of 0.4 microns Hg/minute was obtained after final assembly of the driven sections and dump tank (approximately 45-cu.ft. volume).

The final design of an 8-ft. section is shown in Fig. 12. The 40 feet of driven section is composed of four 8-ft. and two 4-ft. sections, bolted together through split flanges designed to transmit axial loads of 30,000 lbs. with a safety factor of 5. Due to the heat treament of each section, the maximum length was fixed at 8 feet. The two 4-ft. sections were included to provide a greater degree of flexibility in tube configuration. The method of construction involves machining of a 4-in. x 7-in. slot into 11-in. diameter solid stock and capping the slot with a 1.5-in. thick steel plate (see Figs. 25 and 26). The dimensions of the rectangular slot were called up with a ± .002-in. tolerance, and a maximum curvature of .020-ins. over 8 feet. However, manufacturing difficulties have resulted in tolerances of approximately ±.005-ins. on the 4-in.x 7-in. dimensions.

In order to minimize wall viscous effects, the internal surfaces were ground to a 32 micro-inch finish. To provide protection against corrosion and erosion, these surfaces and the end faces of each section are plated with a .002-in. thick layer of chromium. Inner surface discontinuities at the joints were eliminated by individual honing and blending of the surfaces. Alignment of adjacent sections is maintained by two $\frac{1}{2}$-inch diameter dowels.

Instrumentation ports are provided every 4 feet in the driven sections. Located in the top plates of the sections, these ports are identical in order to allow pressure, ionization, or other instrumentation gauges to be installed anywhere in the tube. In addition, one 4-ft. and one 8-ft. section each have two large ports for evacuation and gas loading purposes. The diameters and depths of all ports have been accurately measured and stamped directly on the tube. Matching of instrumentation plugs to these dimensions eliminates steps on the inside surfaces.

The double diaphragm or buffered operation of the tube requires dual pumping and gas loading systems. The driver recoil section, transition section, and a driven section comprise the buffer region. The second diaphragm station is provided by a filler block placed between two driven sections. The filler block absorbs the aligning dowels and provides O-ring seals on both sides of the diaphragm.

In common with the driver, the driven sections are track-mounted on individual stands. Overall views are shown in Figs. 6 to 9.

2.3.4 Test Section

The test section is a special 4-ft. section incorporating two interferometer quality glass windows for optical studies of flow phenomena. The design is shown in Fig. 13 and general views in Figs. 27 and 28.

The internal dimensions, surface finish, mounting and alignment techniques, material and heat treatment specifications, are identical to the driven sections. The method of construction, however, is different. The test section is formed by capping the 7-in. slot dimension with a 2-in. thick steel side plate. Figure 29 shows construction details. The two components, tube proper and side plate, were machined from single billets with ends upset forged for the flanges. Dowelled construction provides accurate alignment of the two components. Large rectangular tapered openings are provided to accomodate the windows.

Six instrumentation ports are located in this section. These also serve as model support openings, or models may be sting-mounted on horizontal or vertical struts which can be inserted through the test section downstream of the windows.

The 4.5-in. thick windows, of 10-in.x 12-in. overall dimensions, provide a 7-in.x 9-in. field of view (Fig. 30). Material is borosilicate crown optical glass type 517-645. Striae, seed grade, homogeneity, and annealing are in accordance with U.S. Joint Army-Navy Specification JAN-G-174. The viewing surfaces of each window are ground and polished to a smoothness of 1/2 wavelength (sodium D-line), and are parallel to within 2 seconds of arc. With the test section in use, these windows limit the maximum operating pressure of the driven section to 500 psi.

Each window is mounted in a frame assembly consisting of an inner flanged frame and an outer frame. The frame bolts are tightened to a torque of 30 ft-lbs to provide an initial compressive load on the windows. Asbestos gaskets prevent glass-to-metal contact and an O-ring in the inner frame bears on the bevelled edge of the raised window face to provide a pressure and vacuum seal. The complete assembly is bolted to the body of the test section through the flange on the inner frame. An exploded view of the side plate window frame assembly (minus the gaskets) is shown in Fig. 31.

The window frame assemblies are ball-bushing mounted on two parallel shafts so they may be pulled out easily and quickly to provide access to the interior of the test section for model adjustments or installation, cleaning of windows, etc. Figures 32 and 33 show the window frame bolted in place and extended to provide access to a double-wedge type expansion model mounted in the test section.

Chromium plating again provides protection to all surfaces exposed to the gas flow. In this case, however, to preserve the close tolerances of the test section, a flash chromium deposit .0005-ins. thick was used.

The test section is mounted on a special cantilever type stand (Figs.3 and 9). This stand allows the interferometer to straddle the test section with adequate clearance for vertical adjustment of the instrument. The centre of the field of view of the interferometer may be located anywhere between the top and bottom surfaces of the test section. A pneumatic jack enables the test section to be withdrawn from the driven section, providing clear access to the test section windows, without disturbing the interferometer.

2.3.5 Dump Tank

The dump tank has been designed according to the Unfired Pressure Vessel Code.[20] Constructed of SA-285B steel, it has an internal diameter of 3-ft., an overall height of 6.5-ft., and a volume of 35.4-cu.ft. The operating pressure is 320 psi with a safety factor of 3.

The dump tank is shown in Fig. 34, and the design in Fig. 14. Of all-welded construction, the dump tank consists of two hemispherical heads separated by a cylinder. A 300-lb service, 16-in. manway provides access to the interior, and a 600-lb service welding neck connects the dump tank to the driven section. Four adjustable wheel assemblies, welded to the

bottom hemispherical head, support the dump tank on the driven section tracks.

The internal surfaces have not been plated. Instead, the wall thickness of the hemispherical heads and cylindrical portion was increased by 1/16-in., the corrosion allowance recommended by the Code. As an added precaution, steel deflection plates are located inside the dump tank to protect the downstream surface from damage in case of the loss of diaphragm material. An instrumentation port is provided in the downstream surface behind these plates.

2.3.6 Recoil System

A schematic of the recoil system is shown in Fig. 35. The recoil system comprises (1) two telescopic recoil sections of 6-in. stroke which allow the driver and dump tank to move independently of the driven section, (2) liquid spring shock absorbers to absorb the recoil energy and to limit the recoil distance, and (3) floor foundation and connecting struts to anchor the driven section to the floor. Figures 36 and 37 show the driver and dump tank recoil sections with the liquid spring shock absorbers installed in their cradles.

The design of the driver recoil section is shown in Fig. 15. The internal diameter is 6-ins. and length 3-ft. The upstream end of this section is connected directly to the driver section and forms part of the diaphragm station (see Fig. 22). The overall dimensions, flange attachment, material and heat treatment specifications, etc., are identical to the driver sections. A replaceable liner is incorporated to protect the internal surface from damage when the diaphragm ruptures. The downstream end is connected to the transition section; design details (flange and dowelled construction) are therefore identical to the transition and driven sections. Two teflon O-rings and one standard (buna-N base) O-ring provide a self-lubricating pressure and vacuum seal at the telescopic joint. The telescopic joint is open 1.5-ins. in its neutral position, allowing the driver to recoil either forwards or backwards; if the rupture disc in the driver end-plate blows out, and the primary diaphragm remains intact (a possible situation at high driving pressures with a fatigue weakened rupture disc), then recoil motion is t wards the driven section. All surfaces exposed to the gas flow are hard chromium plated, and the section is track-mounted on an individual stand.

The dump tank recoil section is a 1-ft. section located between the driven section and the dump tank. The design is shown in Fig. 16. The upstream end has a 4-in.x 7-in. opening and is flanged and dowelled to mate with the driven section; the 8-in. internal diameter matches that of the dump tank welding neck. Material and heat treatment specifications, chromium plating of internal surfaces, etc., are identical to the driven sections. The telescopic joint is sealed with teflon and standard O-rings, and is open 0.53-ins. in the neutral position (no recoil in the reverse direction can be experienced at the dump tank).

The liquid spring shock absorbers are reliable, compact, and simple to maintain. They are mounted in specially designed cradles (Fig. 38) which transfer normal (diaphragm burst) and recoil (rupture disc burst) dynamic force, whichever is generated during operation of the shock tube, directly into the shock absorbers in such a manner that the shock absorber is always compressed (see Fig. 39). Two cradles, each with a shock absorber,

are located at each recoil section. The cradles are firmly attached by bolting and welding, and are diametrically opposed to equalize the load distribution.

The liquid spring shock absorber comprises a heavy steel cylinder, a chromium plated piston rod and piston with a recoil damping device and a special high pressure gland and bearing nut (Fig. 40). Each liquid spring is completely filled with fluid (MIL-H-5606) and pressurized to 7500 psi to obtain a degree of preload. The application of an external load forces the piston rod into the cylinder thereby compressing the fluid which exerts an opposing load on the piston rod and brings the shock tube to rest. Removal of the external load permits the internal fluid pressure to re-extend the rod and replace the shock tube in readiness for the next load application. A recoil damping device is fitted to the piston head to dissipate the stored energy and limit the speed at which the rod extends. The speed of recoil is controlled to ensure that a minimum of the stored energy is imparted to the driven section. A functional diagram of the shock absorber is shown in Fig.41.

The shock absorbers and their cradles were designed by Dowty Equipment of Canada Ltd. The shock absorbers were also manufactured by Dowty. The design criteria (pressure-time histories at the driver end-plate) are presented in Ref. 21, along with a description of the performance characteristics of liquid springs. The various driver lengths and recoiling masses reported in Ref.21 in determining the design criteria and required performance of the shock absorbers, have since been increased, principally as a result of the addition of a rupture duct (see Sec. 4.1) to the end of the driver. The lengths and masses of the various driver configurations used during actual operation are tabulated in Table 2 for the shock Mach number range of the shock tube. The masses represent the total recoiling mass of each driver configuration, which includes the stands and also the driver valving and pumping system, ignition system comprising power supply and capacitor bank, and the rupture duct. These appendages are described in following sections.

The floor foundation consists of two 4-ft.x 3-ft.x 4-ft. deep reinforced concrete footings, 23-ft. apart, connected by a 10WF45 steel beam (see Fig. 3). Sunk into the concrete footings flush with the floor are heavy steel pads. Steel beam (8WF48) struts are bolted to these floor pads and to driven section flanges, rigidly connecting the driven section to the floor foundation, as shown in Fig. 42. The floor foundation is capable of withstanding the maximum spring reaction (20,000 lbs.) and the corresponding moment that occurs at the floor.

3. CONTROL SYSTEMS

3.1 Driver Gas Mixing

The constant volume combustion of a stoichiometric hydrogen-oxygen mixture diluted with 75% helium is the driver technique employed. To produce uniform combustion and to minimize the possibility of detonation in the driver, thorough mixing of the constituent gases is necessary. To accomplish this, an internal mixing tube with small orifices spaced every six inches, runs the complete length of the driver bore, and the gases are injected under high pressure through this tube into the driver. The turbulent motion thus induced aids in the mixing of the constituent gases, which promotes even burning of the oxygen and hydrogen and thus uniform heating of the helium.

An investigation was conducted to ascertain the best location of the mixing tube in the driver bore, and the best orifice size and distribution, to produce a uniform gas mixture before ignition. The investigation consisted of loading the 6-ft. driver section to pressures of approximately 300 and 1000 psi with a nominal 8% oxygen-92% helium mixture, and sampling the mixture from the end of the driver every few minutes with a Beckman Model D Oxygen Analyzer, which gave a direct reading of the percentage of oxygen in the sample. Three different locations (top, centre, and bottom) of the mixing tube in the driver bore, were tested for various orifice diameters and distribution (in line, facing up and down, and helical).

Some typical results are presented in Fig. 43. These indicate that a period of approximately ten minutes is necessary for the oxygen content to stabilize. All of the configurations tested gave virtually the same result, though the oxygen content of the samples was consistently 1/2% lower than that indicated by partial pressures. This is not considered significant, however, in view of the rated 1/2% oxygen accuracy of the analyzer. A test conducted without the mixing tube (single point injection of gases at end of driver) also required approximately ten minutes to stabilize, although in this case the results were not quite as uniform. This can be seen in Fig. 43, which includes this particular result. Also, for this test without the mixing tube, the oxygen content was approximately $1\frac{1}{4}$% lower than the partial pressure value, which is a more significant discrepancy. As the driver was evacuated to less than 5 mm Hg before each test, the initial pressure before loading could not affect the results within the accuracy of the experiment. Also, the volume of the loading line was approximately 1.1% of the driver volume, too low for the gas remaining in the line (after the driver is isolated) to account for the difference. Even if such were the case, the order of loading the gases (helium last) would result in a higher oxygen content as helium would remain in the loading line. In any event, the objectives of the investigation, to supply answers to the questions of mixing time and mixing tube configuration, were achieved.

As the tests indicate the configuration is not critical for good gas mixing, the final configuration adopted is one of convenience and ease of installation. That is, with the mixing tube running along the bottom of the driver, with all orifices in line and facing up. The orifice diameter is such that the total orifice area is equal to the minimum cross-sectional area of the loading line.

The mixing tube itself is a 5/16-in. I.D.x 9/16-in. O.D. type 302 stainless steel tube. The upstream end is rigidly connected to the gas inlet port in the driver end section by a special elbow and tube connector (see Fig. 44). The downstream end is capped and is supported by a cross-strut at the diaphragm station (Fig. 45).

3.2 Driver Ignition System

The technique by which the driver gas is ignited is as important to the success of detonation-free combustion as the mixing of the constituent gases. The initiation of combustion must be uniform throughout the driver, and should be as gentle as possible.

Two ignition methods have been used during the development of this facility. The first method, a fused wire technique, was used successfully during early operation, but proved to be somewhat unreliable for initial driver pressures in excess of 600 psi. Also, this method tended to introduce debris into the flow (see Sec. 7.2.1). The second method, a heated wire technique,[22] was subsequently adopted, and is the method currently in use. Apart from the actual ignition element and the energy level of operation, the ignition systems for each method are identical. The two methods will now be discussed in turn.

In the fused wire method, a single .0126-in. diameter annealed aluminum wire (type 2-S) is stretched along the centreline the full length of the driver bore. The wire is crimped every 6-ins. to produce local high resistance points. A sudden capacitor discharge through the wire of sufficient energy to fuse the wire at these points, generates a series of sparks which ignites the combustible gas mixture in the driver.

The aluminium wire is mechanically attached and electrically grounded to the mixing tube strut at the downstream end of the driver (Fig. 45). The shock tube itself is connected by a ground strap to a copper-sheathed steel ground rod sunk 10 feet into the ground beneath the driver. The upstream end of the wire is attached to an insulated high voltage electrical connector inserted through the wall of the driver end section close to the rupture disc (Fig. 44). This connector consists of a teflon-sheathed conductor terminating in a standard HN receptacle, and pressure and vacuum sealed with a special gland nut (see Fig. 46).

A 4.5 microfarad, 25,000 volt capacitor bank and power supply provide a continuously variable 1400 joule source of electrical energy. The capacitor bank, charged to a voltage depending on the wire (driver) length, is discharged through a triggered gas-type spark gap to the wire. An induction coil, relay operated by the firing switch on the console (see Sec.3.3), applies an 8000-volt pulse to the trigger electrode of the spark gap, which induces sufficient ionization to break down the main gap and initiate the capacitor bank discharge. (The capacitor charging and firing circuit can be seen in Fig.52.)

The energy required for the various driver lengths, typically 40-44 joules per foot of wire, will vary somewhat with the amount of crimping or deformation of the wire. Crimping is accomplished with the rig shown in Fig. 47. The wire is cranked between two rollers, on one of which is an adjustable knife edge which deforms the wire every 6-ins. to produce the local high resistance points. The knife edge is carefully adjusted with the aid of feeler gauges and locked in position by two set screws. If the knife edge is set up too much, the wire will either be cut through or so weakened that it breaks when pulled taut during attachment in the driver bore. On the other hand, too little a deformation of the wire results in very little margin between the energy required to fuse the wire at the crimps and that which will blow the wire into pieces smaller than the 6-in. lengths. For this particular wire diameter, a .006-.008 inch gap between the knife edge and the bearing roller proved quite successful.

The required energy is determined by trial and error. The capacitor bank is discharged through the appropriate length of crimped wire stretched alongside the driver and connected to the ignition connector and

driver ground strap. Open-air firings of this nature, using different energies, are repeated until the desired performance is obtained. The energy is varied by varying the capacitor charging voltage. Two threshold values are determined: the energy for which the wire just fails to fuse at every crimp, and the energy for which the wire tends to fuse at points other than the crimps. The mean of these values is then checked for successful performance, and is the energy subsequently used during actual operation. The complete process must be repeated if the knife edge is readjusted or disturbed in any way.

To ensure satisfactory performance under driver operating conditions, the system was checked in a high-pressure helium atmosphere. Duplicating normal operation, but with the driver charged with helium to pressures of 500 and 1000 psi, the ignition system performed as desired in that only 6-in. lengths of wire, equivalent to the original total length, remained after the discharge. (During the combustion process, however, the aluminium wire is completely vaporized.)

Although these tests were quite successful, this ignition method was not entirely satisfactory during actual combustion operation. Detonations were occasionally experienced, particularly at high initial pressures. Although less violent than a high energy discharge sufficient to disintegrate the wire completely, it is not as gentle a process as the heated wire method now used. In this method, the ignition element is a .010-in. diameter tungsten wire (General Electric type 218-CS). The energy discharged through the wire is 45-50 joules per foot of wire. This energy, as determined from open-air tests, causes the wire to glow a bright orange colour along its entire length. With energies of 55-60 joules per foot, the wire became incandescent and copious fumes were generated during the discharge. At lower energies, approximately 35-40 joules per foot, the wire glowed a bright red to orange colour, but the colour did not always appear uniform along the entire length of the wire.

This heated wire method has given reliable detonation-free combustion up to the pressures of 6500 psi so far used with this technique. The tungsten wire actually remains intact and ready for the next firing. Repetitive operation (3 or 4 times) with the one ignition wire has been successful for moderate driver pressures (<4000 psi), and is a definite convenience in the operation of the shock tube. (A resistance check is made after each firing to ensure good electrical contact is maintained.) For higher pressures, the wire generally becomes quite kinked and is automatically replaced after each firing.

3.3 Control, Pressure, and Vacuum Systems

All controls for the complete operation of the shock tube are located on the central console shown in Figs.48 and 49. All valves not located on the console have solenoid controlled pneumatic operators for remote operation. Console switches operate these valves, and panel lights indicate the valve position (fully open or fully closed) when small microswitches mounted directly on the valve bodies are activated by the valve stem or piston of the pneumatic operator. A schematic of the plumbing system is shown in Fig.50, and a parts list in Fig.51. The wiring diagram of the electrical system is shown in Fig.52.

All gases are stored in standard high-pressure cylinders in the blockhouse and are fed to the console by lines designed for an operating pressure of 3400 psi. Nine helium cylinders manifolded together, six hydrogen, and three oxygen, provide a suitable storage reservoir and avoid frequent changing of cylinders for the driver gas charging system. Single cylinders of argon and air (or other test gas) constitute the buffer and driven gas supply. In addition, nitrogen and air cylinders are incorporated to purge the driver and driven systems. Regulators are installed at the gas cylinders to obtain the desired pressures at the console, and check valves are used at the console to prevent accidental mixing of the gases in the lines.

At the console, the various driver gases are connected by 20,000 psi-service valves to a common loading line which conducts the gas into the driver mixing tube through a high pressure valving system located at the driver end section. This system consists of a 60,000 psi vent valve to release the driver gases any time this should be necessary, a 60,000 psi manifold valve backed by a 20,000 psi positive check valve to isolate the driver from the console and gas charging system, and a 10,000 psi valve connecting the loading line to a Cenco Hyvac 14 vacuum pump which serves to evacuate the driver and loading line prior to loading. The pump is mounted on the driver end section stand and operated from the console. Three Heise bourdon type pressure gauges (0-500, 0-1000, and 0-2000 psi ranges) are used to measure the gas pressure during the loading process and are individually connected to the loading line by 20,000 psi valves. A similar valve also connects the loading line at the console to a high pressure line vented into the blockhouse, which enables the pressure gauges and loading line to be vented to atmosphere after the driver is charged.

The buffer and driven section gas loading and vacuum systems are similar to that of the driver. They are, however, completely independent of the driver system. Console valves connect the gas lines to loading lines running to dual manifold systems. High pressure and vacuum service valves connect these manifolds to the buffer and driven sections, and to a vacuum system consisting of a Heraeus Roots Type VP-RG-350A pump backed with a Kinney Type KS-47 pump. This pumping system is capable of evacuating the driven section and dump tank to a pressure of approximately 1/2 micron Hg. The Kinney pump is operated from the console area, and a pressure switch incorporated in the Roots pump automatically activates this pump when the pressure is less than approximately 35 mm Hg. Both pumps are water cooled, and a water pressure switch in the coolant line renders the Roots pump inoperative if the cooling water supply fails. A 1-in. diameter valve in the driven section manifold allows the pumps or the driven section and dump tank to be rapidly vented to atmosphere.

Pressures in the buffer and driven sections greater than 1 mm Hg are measured with separate banks of vacuum gauges (Wallace and Tiernan Type FA 160) connected by 1-in. diameter lines and isolating valves to each manifold. A precision mercurial calibrating standard (Wallance and Tiernan Type FA-187) is used to periodically calibrate these gauges. Pressures less than 1 mm Hg are monitored with a four station Pirani gauge (Consolidated Vacuum Corp. Type GP-140), with the gauge heads located in the buffer and driven section vacuum gauge lines, and in a line connecting the interferometer compensating chamber to the test section. The fourth gauge head is located between the vacuum pumps for leak detection purposes.

The driver ignition system and interferometer spark source unit are also operated from the console. The control switches, panel lights, and voltmeters, of the power supplies servicing these units are duplicated on the console. The driver ignition circuit incorporates an adjustable time delay relay which inactivates the firing switch for a period of 10 minutes after the driver is charged and the ignition DC voltage turned on. This waiting period, determined from the gas-mixing tests, allows the driver gases to mix thoroughly before ignition. At the end of this period, a pilot light indicates the firing switch is armed and the tube ready to be fired.

The firing switch not only initiates the driver ignition process, but also operates the interferometer camera shutter with a 6-volt DC power supply. A switching circuit permits the firing switch to either initiate the driver ignition directly, or to allow the flash contacts of the interferometer camera shutter to complete the firing circuit and initiate the driver ignition when the camera lens is fully open. With a shutter exposure time of 1/50 second, this system ensures the camera lens is open for the duration of the shock tube flow, but not long enough to permit objectionable fogging of the film by ambient light. For normal operation of the tube, however, the rise-time to peak pressure during the combustion process (10-15 millisecs.) is more than sufficient for the camera lens to open fully, and the driver ignition is usually initiated directly from the firing switch. Both the switching circuit and the time delay relay are located on a rear panel of the console.

Hydrogen detectors, warning lights, and alarm switches (see Sec.4) complete the console controls.

4. SHOCK TUBE HAZARDS AND SAFETY PRECAUTIONS

There are many hazards involved in shock tube operation. Failure of shock tube components from high pressure, the use of hydrogen and oxygen, and high-voltage electrical equipment, are a few of the sources of hazard encountered in this facility. The following sections describe the protective devices incorporated into the facility as a safeguard against potentially lethal accidents. The driver blockhouse and test section blast mat, the hydrogen detection and warning systems, the interlocking of electrical controls, fail-safe valve operation, and provision of protective devices such as check valves and rupture discs, all help to provide adequate protection to personnel from accidents as a result of structural failure, ignorance of safe pressure limits, or carelessness.

A thorough understanding of the equipment and the adoption of a standard operating procedure are, of course, essential for the successful and safe operation of the facility. Equally important is developing and maintaining proper respect for the dangers involved.

4.1 Driver Blockhouse and Test Section Blast Mat

A schematic of the driver blockhouse can be seen in Fig.3. The blockhouse is a 20-ft. wide by 30-ft. long enclosure housing the entire driver and 8 feet of the driven section, their associated pumping and gas handling systems, and the gas storage cylinders. The diaphragm test rig (see Sec.5.2) is also located in the blockhouse. All four walls of the blockhouse are 12 in. thick reinforced concrete, and four 5-ft.x 5-ft. blister domes designed to

blow out with a small pressure differential, are incorporated in the ceiling as pressure relief diaphragms. It should be noted that this layout is not exactly as shown in Fig. 3. The rear wall of the blockhouse was originally of a light steel frame and panel construction (see Fig.5), and served as the relief diaphragm. However a recent extension to the laboratory building has made it necessary to completely enclose the blockhouse as described above.

During operation of the shock tube the blockhouse is ventilated by a 24-in. diameter, 8250-cu.ft./min. explosion-proof exhaust fan located in the ceiling near the rear wall. An air intake is located in the opposite corner of the blockhouse. An appreciable cross-draft is generated and minimizes the possibility of hydrogen accumulating in the blockhouse. Exhaust gases from the vacuum pumps and the tube and console vents, which all discharge directly into the blockhouse, are also quickly removed.

A $3\frac{1}{2}$-in. thick steel door provides access from the laboratory proper. The shock tube passes through a 19-in. diameter opening in the front wall, and, with the tube in position, this opening is effectively shielded by close fitting steel plates 2-ins. thick. A series of 3-in. diameter pipes at the floor level allow entry of electrical and gas leads servicing the driver and driven sections.

Incorporation of the rupture disc in the end of the driver prevents excess pressure from developing in the driver sections. Failure of the rupture disc can occur either through a high-pressure detonation or by eventual fatigure without exceeding the original bursting pressure of the disc. The latter can be avoided by replacement with a new disc whenever the disc in use shows excessive bulging. To avoid unnecessary damage by fragments from a bursting rupture disc, a duct is attached to the end of the driver during high-pressure operation to confine and direct such fragments into a 2-in. thick wood lining on the rear wall of the blockhouse. The driver duct can be seen in Fig. 5. As mentioned previously, the blockhouse layout as shown in this figure has been changed. Prior to the blockhouse alteration, an external wood barricade was used to absorb rupture material, and this original barricade, and the driver duct protruding through the open double doors, is shown in Fig.5. The duct is manufactured of 12-in. nominal diameter extra strong steel pipe and is track-mounted on an individual stand.

A 20-ft. wide by 10-ft. high blast mat woven of 3/8-in. diameter steel cable is erected around the test section and dump tank. In the event of a test section failure, this mat will confine any fragments to the test section area. The blast mat is supported by a steel pipe framework socketed in 3-ft. deep concrete and steel footings. One end is hinged so that it may be swung clear to allow installation or removal of equipment. The plot plan of the bast mat is included in Fig.3, and a partial view in the top corner of Fig.6.

4.2 Alarm Systems

When high-pressure gases are handled in vessels or through piping and valving systems, there is always a possibility that a leak may occur. Hydrogen detectors, with visual and audible 'high gas' signals are used to monitor the air and detect the concentration of hydrogen gas present.

The detection equipment employed is the Series #11-3000 Diffusion Type Continuous Combustible Gas Analyzer System manufactured by Davis Emergency Equipment Co., Newark, N.J. This comprises four remote detector heads with one series type control unit and two selective type control units, each incorporating dual relays for actuation of high-gas concentration and circuit trouble alarms. Two of the heads are connected in series and located in the ceiling of the blockhouse above the diaphragm station and the end of the driver. The other two heads are located in the ceiling of the laboratory above the operating console and above the test section. The control units are mounted in a single cabinet located near, and powered from, the operating console.

The control units are normally set to give a warning when the hydrogen gas reaches a concentration in air of 20% of the lower explosive limit, i.e. 20% of the lowest concentration of hydrogen in air that will propagate flame. The explosive limits of hydrogen are 4.1% to 74% by volume in air,[23] which means the warning is given when the hydrogen concentration in the air reaches approximately 0.8% by volume. When such a situation occurs, the analyzer operates a relay which sounds an alarm siren and starts the blockhouse exhaust fan. Front panel lights on the cabinet housing the control units give an immediate visual indication of which of the three units is registering the high gas signal. Any failures in the detection circuit, such as burnt out filaments in the remote heads, will cause the second relay to operate an alarm bell and a second set of panel lights.

Thus four fail-safe hydrogen detectors blanket the shock tube area and provide a warning when a hazard is being formed by the accumulation of hydrogen gas. With detection at 20% of the lower explosive limit, ample time is afforded to close off all gas storage cylinders and completely vent the shock tube and gas loading lines.

Suitable warning lights and signs are used to discourage the entrance of unauthorized personnel to the shock tube area during operation of the facility. All warning lights are on a common circuit operated by a control switch on the console (see Fig.52).

4.3 General Safety Features

This facility has a number of safety features in addition to the blockhouse and alarm systems. These features are briefly described below.

(1) Interlocking control system:

All control switches on the console are interlocked to prevent the tube from being fired in an unsafe condition. With this interlocking system the capacitor bank of the driver ignition system cannot be charged unless all remote valves are fully closed, the hydrogen detectors and warning lights are on, and the blockhouse door is closed. In addition, the hydrogen detectors must be on in order to operate the pneumatic jack which opens and closes the diaphragm station.

(2) Fail-safe valve operation:

All remote control valves (solenoid controlled, pneumatically operated) are of fail-safe operation . In the event of a power or air supply failure, all valves except one will automatically close and isolate

the shock tube. The exception is the driver vent valve, which automatically opens and vents the driver to atmosphere.

(3) Timing and fire control system:

As described in Sec. 3.3, a time delay relay disarms the firing circuit for a period of 10 minutes after the ignition DC supply is turned on. It is impossible to fire the shock tube during this 'gas-mixing' period.

(4) Ignition power supply cutout:

The console firing switch, besides initiating ignition of the driver gas mixture, also operates a relay which cuts the AC supply to the ignition system, so that the capacitor bank is not automatically recharged.

The capacitor bank itself is enclosed in a steel mesh cabinet which is grounded directly to the shock tube. A plunger type insulated switch is provided to completely discharge the capacitor bank. The ignition power supply and trigger unit are rack mounted in a cabinet fitted with interlocks which cut the power when the cabinet is opened. These precautions minimize the possibility of lethal contact with a high voltage source.

(5) Vacuum line rupture discs:

Rupture discs incorporated in the buffer and driven section vacuum gauge lines and in the driver pumping line, provide a safeguard against accidental admission of high pressure gas into these lines. The rupture discs are 3/4-in. in diameter, and consist of .002-in. thick aluminium foil sealed in vacuum couplings. These devices blow out with a pressure differential slightly greater than one atmosphere. (The maximum case pressure of the Wallace and Tiernan vacuum gauges is 45 psi.) No rupture disc is provided in the driver gas loading line. A 3/4-in. thick plexiglass shield is strut mounted $2\frac{1}{2}$-ins. in front of the driver pressure gauges as a protection against bourdon tube failure.

(6) Check valves:

Check valves are used in all lines from the gas storage cylinders to the console to prevent accidental mixing of the gases in these lines. A check valve in the driver gas loading line provides an additional measure of safety in case the driver isolating valves hammer open under high pressure detonation loads.

(7) Console power switch:

The main console power switch provides power to all operating controls of the shock tube with the exception of the driven section vacuum pumps and the blockhouse exhaust fan. In the event of any malfunction, throwing this single switch shuts off all power supplies and closes all valves except the driver vent valve, which opens and vents the driver.

5. DIAPHRAGMS

5.1 General Requirements

The successful operation of the shock tube hinges on satisfactory diaphragm performance. The ability to repeat test conditions from run to run is primarily dependent upon the attainment of diaphragms having consistent bursting strengths and opening characteristics. Consistent diaphragm opening at the peak driver pressure precludes the possibility of detonation of partially burned driver gases as a result of any disturbances associated with premature opening of the diaphragm, and realizes the highest possible values of driver pressure and temperature and the accompanying performance advantages of constant volume combustion operation.

With premature opening of the diaphragm, the combustion proceeds within the driver gases as they expand at a relatively constant pressure into the driven section. Although more efficient in producing strong shock waves, constant pressure combustion suffers from severe attenuation of the shock wave and a rapidly decaying pressure behind the shock, i.e. the flow does not have constant properties.[5]

5.2 Diaphragm Materials, Preparation, and Calibration

Stainless steel, cold-rolled steel, and copper, have been used as diaphragm materials. Diaphragms are 14-ins. in diameter, and material specifications and thicknesses used are listed below:

Material		Thickness (ins.)
Stainless Steel Type 302	No.2B Finish	.063, .109, .172
Stainless Steel Type 302	No.1 Finish	.250
SAE 1010 Cold Rolled Steel	White Finish	.105, .135
$\frac{1}{4}$ Hard Temper Cold Rolled Copper		.125, .250, .375

To permit petalling, the diaphragms are machine scribed in the form of a 90° cross in the centre of the diaphragm, and at 45° to the mill roll marks (a weaker diaphragm results from scribing along the mill roll marks). A milling machine with a 4-in. diameter, 90° included angle, high-speed steel cutter is used for this operation. A cutter crest radius of .020-ins. is maintained in order to keep the stress concentration consistent. To obtain reproducible results extreme care must be taken to ensure that diaphragms are identical. Dimensions such as .020-in. crest radius do not appear to be too important as long as there is no variation from diaphragm to diaphragm.

The pressure at which the diaphragm bursts is controlled by varying the material thickness and the depth of the scribe. The diaphragms are generally scribed from 25% to 45% of their thickness. For scribe depths less than 25% (relatively high bursting pressure) the petal root thickness may be insufficient to hold the petals of thin diaphragms. Petals torn loose from the diaphragm could cause considerable damage to tube walls and test section windows, as well as completely destroying any model mounted in the tube. During the early stages of operation, petals were lost from .063-in. thick stainless steel diaphragms scribed to 15% of their thickness, and in one case very nearly lost from a .109-in. thick diaphragm also with a 15%

scribe depth. Petals were also sheared from a .172-in. thick diaphragm with a 15% scribe depth during a run when detonation of the driver gas mixture occurred. No abnormal tearing of petal roots has been observed with the .172-in. thick diaphragms with a 20% scribe depth, or with the .250-in. thickness with a 15% scribe depth. As a result of these experiences with stainless steel diaphragms, minimum scribe depth limits of 25%, 20%, 20%, and 15%, are imposed on diaphragm thicknesses of .063, .109, .172, and .250 inches respectively. On the other hand, for scribe depths over 45%, the petal root thickness can prevent the diaphragm from opening fully with the relatively low bursting pressure, i.e. a poor rupture results, with consequent loss in tube performance. Figure 53 illustrates the range of diaphragm materials, thicknesses, and scribe depths, used.

Diaphragm bursting pressures are determined in a hydraulic test rig shown in Fig.54. An air driven, 24,000 psi oil pump hydraulically loads the diaphragm which is located and sealed in a thick wall cavity by a double-threaded press. An insert in the cavity duplicates the geometry of the driver diaphragm station in order to simulate the loading area and deforming radius encountered during operation. A second insert is available to allow testing and preforming of the driver rupture discs. Pressure is measured and recorded with Helicoid pressure gauges equipped with maximum reading hands. A schematic of the hydraulic loading system is shown in Fig.55.

Both preformed and flat-scored diaphragms have been used in this facility. Preforming of diaphragms was carried out in the hydraulic test rig. The procedure for a batch of identical scribed diaphragms was to load two to destruction to obtain a value of the bursting pressure, and then preload the remainder to within 10% of this value. This procedure automatically eliminates any weak diaphragms. It was also anticipated that the preloading process would provide more consistent diaphragm opening characteristics, since most of the work of deforming and rupturing the diaphragm had already been carried out. However, no detectable difference was experienced in performance of the shock tube with preformed and flat stainless steel diaphragms.

With the cold-rolled steel diaphragms, the bursting strength was increased by 15-25% due to the cold working of the material in the preforming process. This resulted in a series of hangfires, or firings in which the diaphragm fails to burst. As variations of this order cannot be tolerated, and since no improvement arising from preforming was noticeable with the stainless steel, the use of preformed diaphragms was abandoned in favour of flat diaphragms. Figures 56 and 57 show preformed, flat-scored, and ruptured diaphragms.

In the early stages of diaphragm development the objective of obtaining a reliable calibration curve of bursting pressure versus scribe depth for each thickness of diaphragm was not fully realized. Although the bursting pressure of diaphragms from the same batch varied by no more than 2%, differences of as much as 30% were experienced between essentially identical batches scribed at different times or by different machinists. Figures 58 to 60 show the early burst-pressure calibration curves obtained for the stainless steel, cold-rolled steel, and copper diaphragms. In these graphs the ratio of effective thickness, or thickness of material left after scribing, to the original material thickness, is plotted against the bursting pressure.

Variations in material thickness (and scribe depths) undoubtedly contributed to the 30% variations in bursting pressure which were experienced. For the .250-in. thick stainless steel diaphragms, which are cut from plate stock, the thickness varied by as much as .008-ins. in a single diaphragm. Sheet stock is manufactured with much closer tolerances than the plate, and individual sheets are generally quite uniform. In fact diaphragms cut from the same stainless steel sheet have been found to vary in thickness by no more than .0005-ins. Consequently the use of plate stock for diaphragms has been discontinued and only sheet stock used. The type 302 stainless steel (2B finish) is used exclusively at present for all operating pressure levels.

In addition to closer thickness tolerances, the better surface finish obtainable in stainless steel, and the higher tensile strength of stainless steel compared to mild steel and copper (90,000 psi, 55,000 psi, and 35,000 psi average values respectively) further influenced this choice of diaphragm material. The higher tensile strength allows use of a thinner diaphragm for a particular burst pressure, which can become a practical necessity at high driving pressures.

The maximum thickness obtainable in stainless steel sheet stock without special mill orders is .172-ins (USS Gauge 8). For bursting pressures greater than that attainable with this thickness, two diaphragms may be stacked together to provide twice the bursting pressure of a single diaphragm. This technique has worked quite well in tests with two .109-in. thick diaphragms at driver pressures of 5500 psi. However, excessive tearing of petal roots of stacked diaphragms indicates that care must be exercised to avoid loss of petals. For stacked diaphragms the minimum scribe depth is at least 25% of the material thickness to provide a relatively larger root thickness of the petals. The scribes on each diaphragm are carefully aligned when inserted in the shock tube.

In view of the early difficulties mentioned above, the procedure adopted to achieve a particular diaphragm bursting pressure was to (1) select a diaphragm thickness and scribe depth for the desired bursting pressure from the calibration curves of Fig.58, (2) scribe and test to destruction such a diaphragm, (3) on the basis of this result vary scribe depth up or down until the desired bursting pressure is obtained, (4) produce the number of diaphragms required, and (5) test the last diaphragm to destruction as a check of the bursting pressure, which could be affected by cutter wear (if a large number of diaphragms were required, one or more were tested in the middle of the production). Although such a procedure could become quite expensive and time consuming, the desired bursting pressure was generally obtained after the second or third attempt. Each diaphragm tested also provided calibration data which aided in the original selection of scribe depth.

A continuing effort is made to improve the diaphragm quality, and a very satisfactory method of diaphragm preparation and calibration has been developed A vacuum check to hold the diaphragms on the milling machine and the use of accurate dial indicators to monitor scribe depth during and after the machining operation, has improved the accuracy and speeded up the preparation of the diaphragms. (This technique originated at the General Electric Research Laboratory to prepare diaphragms for use in their hypersonic shock tunnel.)[24] With precise measurement of diaphragm thickness and scribe depth (±.0001-in. accuracy), reliable correlation with burst pressure has been obtained. Diaphragms with burst pressures within 1% of a desired value can be

readily and reliably produced. In general, the test rig is now used only to check the first and last of a quantity production of identical diaphragms, and to check several diaphragms of a new shipment from the supplier.

6. INSTRUMENTATION

As shock tube testing times are very short (order of several hundred microsecs.), instrumentation is a most important problem. In fact the success of any shock tube experiment depends largely on the solution of the instrumentation problems. In recent years, however, remarkable progress in the development of fast response instrumentation has been made, and today there are available a number of instruments suitable for shock tube investigations.

6.1 Pressure Transducers

Standard Kistler* SLM quartz pressure transducers are used to measure pressures in the shock tube. The model 605, with a pressure range of 15,000 psi, is used to measure driver pressures, and the model 601, with a pressure range of 5000 psi, the driven section and dump tank pressures. The transducers are mounted and sealed in the shock tube wall or a probe plug with the use of model 624 thread adaptors. Figure 61 shows an exploded view of the 601 transducer and thread adaptor, together with an assembled unit mounted in a probe plug ready for insertion in the shock tube.

The complete pressure transducer system consists of the transducer and its mounting adaptor, a special low-noise, low-capacitance cable connecting the transducer to a Kistler model 652 piezo calibrator unit, and an oscilloscope and camera to display and record the output of the transducer. The calibrator unit matches the high impedance of the transducer to the input impedance of the oscilloscope. A range switch controls a capacitor attenuator at the input to the calibrator, so that full output voltage is obtained for various ranges of pressure applied to the transducer. For the 601-652 combination, the pressure ranges are 0-10, 100, 1000, and 5000 psi.

The short term static response of this system allows accurate static calibration on a dead weight tester. The calibration equipment includes a Mansfield and Green Type T 130 pressure test unit, with a range of 15,000 psi, and a Keithley Model 603 electrometer amplifier for direct measurement of output voltage. The pressure transducer is mounted on the dead weight tester and connected to its calibrator unit. Test pressures applied with the dead weight tester produce output voltage signals from the calibrator unit which are measured and correlated with the applied pressures. The slope of the output voltage versus applied pressure curve is the calibration factor for the particular transducer and range setting. Very linear and consistent static calibrations are obtained. Calibrations conducted several months apart give practically identical results. Typical calibration curves for a 605 and a 601 transducer are shown in Figs.62 and 63.

Since the circuit capacitance is different for each setting of the range switch, a separate calibration must be conducted for each range. This also applies to the low-noise cable connecting the transducer to the

---

* Kistler Instrument Corporation, Clarence, New York.

calibrator unit. The use of a cable of different length will alter the capacitance of the system and necessitate a new calibration.

Figure 63 also shows the results of a dynamic calibration of the particular transducer. This was accomplished by installing the transducer in the test section of the shock tube and subjecting it to the pressure increase behind weak shock waves (shock Mach numbers from 1.31 to 2.05 into air at atmospheric pressure). The applied pressure was calculated from normal shock relations using the measured shock wave velocity (see Sec.8.2). The output voltage of the transducer was measured from the oscilloscope camera trace with a travelling microscope. As can be seen in the figure, the dynamic and static calibrations were in complete agreement. (This is contrary to the results reported in Ref. 13, where an unexplained difference of approximately 4-8% was obtained between the dynamic and static calibrations.)

Pressure-time traces obtained with these transducers located in the driver, test section, and dump tank, are shown in Fig. 64. From such oscilloscope records the peak pressure during the combustion process and the pressure rise across the shock can be measured.

Although quite suitable for most applications, the relatively large size and small output of the Kistler pressure transducers make their use difficult for model instrumentation. Consequently, for some of these investigations small lead-zirconium-titanate (abbreviated PZT) pressure transducers*, with a linear range to 60 psi, are used. Figure 65 shows a Kistler 601 and a PZT pressure transducer. These transducers have considerably greater output than the Kistler type. They are, however, much more sensitive to vibration and must be shock mounted in rubber. This characteristic can be seen in Fig. 66, which shows oscilloscope traces of the outputs of four of these transducers mounted in the double-wedge type expansion model shown in Fig. 32. The transducers measure the pressure ahead of the expansion corner and at three locations behind the expansion corner. The second transducer behind the corner (third trace from the top) was poorly shock-mounted and consequently vibrated rather badly.

The PZT pressure transducer is connected by a low-noise cable to a cathode follower. The output of the cathode follower is controlled by a precision attenuator and fed to an oscilloscope. Calibration is achieved by recording and measuring the response to a sudden application of a known pressure. A reservoir tank equipped with a precision differential pressure gauge (Wallace and Tiernan type FA 145) is connected by a solenoid valve to an adaptor plug housing the PZT transducer. The reservoir tank is filled with air through a needle valve to the desired calibration pressure. Opening the solenoid valve applies this pressure to the face of the transducer, and at the same time triggers the oscilloscope used to record the transducer response. The calibrating rig and associated equipment is shown in Fig. 67. The volume of the line and adaptor housing the transducer is extremely small in comparison with the reservoir volume, so that no measurable error is introduced in assuming the full reservoir pressure is applied to the transducer. A coil of very fine bore hypodermic tubing serves as a bleed to atmosphere to ensure that the transducer is initially at atmospheric pressure. Figure 68 shows a typical calibration curve obtained in such a manner. As in the case of the Kistler transducers, very linear and

* Manufactured by J. Bialy, 14 Markus Drive, Buffalo 25, N.Y.

consistent calibrations are obtained.

The Kistler and PZT transducers are both temperature sensitive. Kistler state that at temperatures above 500°F the internal resistance of their transducers decreases rapidly, causing the oscilloscope trace to drift. In fact, 'negative' pressure levels behind the reflected expansion wave in the driven section were indicated by these transducers during some early calibration firings of the shock tube. This was caused by a radiative and convective heating effect on the transducer and was rectified quite simply by applying a film of silicone grease (Dow Corning #44 medium) to the face of the transducer. The silicone grease provides an excellent thermal barrier. The Kistler transducers are recessed approximately 1/16-in. from the shock tube wall; the cavity helps to retain the silicone grease and obviates the necessity of reapplication after every run. The existing cavity in the PZT transducer case (see Fig.65) serves the same purpose.

6.2 Ionization Gauges

Ionization gauges detect the large change in conductivity caused by ionization in the hot shock front. They consist of a simple air gap (approx. .03-in. wide) with 300 volts DC between the centre electrode and the outer wall (Fig.69). The ionization of the gas due to a strong shock wave breaks down the resistance across the gap, effectively shorting the centre electrode to the wall of the tube. Connected to a suitable circuit, the resultant voltage change provides a fast rise output pulse.

Ionization gauges are used in the driven section of the shock tube as shock detectors for time of arrival measurements, and as triggers for starting oscilloscope sweeps and other recording instrumentation.

However, a word of caution is given here regarding the use of these gauges as shock detectors in argon. With argon as a test gas, at initial pressures less than 55 mm Hg and with an electrode potential of 200-300 volts DC, a glow discharge occurs between the centre electrode and the outer wall of the gauge. Under these conditions the gauges behave erratically, and the output signals are usually very poorly defined and reduced in magnitude by as much as a factor of 8. (Relatively inexpensive pressure pickups (Atlantic Research type LD-25) and heat flux gauges (see Sec.6.3) are used as shock detectors in argon.)

6.3 Heat Flux Gauges

A thin platinum film painted and baked on a glass base acts as a resistance thermometer and serves as a shock detector and trigger source for moderate strength shock waves where the temperature increase is insufficient to produce ionization. This type of gauge has been developed to a fine degree[25-28] and extensively used in gasdynamic research to measure transient surface temperatures and heat transfer rates.

Figures 69 shows a thin-film heat gauge. For these particular gauges the resistance of the platinum film is about 100-150 ohms, and a current of 50 milliamps is used to detect a voltage variation produced by a change in the film resistance brought about by the temperature increase across the shock wave. The film forms part of a suitable network wherein the voltage change is amplified and used to fire a thyratron which provides positive and negative timing and trigger pulses.

To enable the gauges to be used at higher temperatures for which the gas becomes ionized, the platinum film is coated with a thin (600-800 Å) layer of silicon dioxide (or magnesium fluoride). This insulating coating prevents the ionized gas from short-circuiting the platinum film. Coated gauges have been used successfully as shock detectors in argon up to shock Mach numbers of 15.

6.4 Wave Speed Measurements

The instrumentation used to determine the shock wave velocity as a function of driven tube length consists of the ionization or heat flux gauges which serve as time of arrival pickups, a modified Tektronix Type 545 oscilloscope incorporating a raster generator, a ten channel control unit to control and feed the gauge outputs to the oscilloscope, and a Tektronix Type 180A Time Mark Generator for accurate calibration of the displayed raster pattern.

A typical raster record is shown in Fig.70(a). Signals at 10 microsec. intervals, produced by the Time Mark Generator, are displayed as vertical markers on the horizontal sawtooth pattern, while the signals from ten ionization gauges are used to intensity modulate the display. The ten modulations are indicated on the figure. (As the first signal is also used to trigger the oscilloscope, the very beginning of the raster trace is intensity modulated.) A curve of shock Mach number versus distance along the driven section, obtained from such raster data, is shown in Fig. 70(b).

In normal operation of the shock tube, the shock-wave velocity is independently measured across or just ahead of the test section. A switching circuit in the ten channel control unit permits independent operation of three of the channels. Pulses from these channels are used to start and stop chronographs, and to trigger, through a time delay unit, the interferometer spark source.

6.5 Optical Systems

The 9-inch plate Mach-Zehnder interferometer used to obtain density records of flow fields is described fully in Ref.3. The optics of this instrument can also be used for schlieren and shadowgraph studies.

To enable the instrument to be used with this shock tube facility, a new compensating chamber was designed and installed. This chamber has a 4-in. internal width and incorporates windows of quality and thickness equal to those of the test section. The design is shown in Fig.71 and a general view in Fig.72.

An interferogram of the flow over the double-wedge type expansion model, taken with this optical system, is shown in Fig.73. The primary shock wave, and the expansion wave generated by the corner, may be readily seen, as well as the interface and oppositely facing shock wave induced by the flow.

7. SHOCK TUBE OPERATION

7.1 General Operating Procedure

The first step in the operation of the shock tube is the preparation of the ignition system for firing. The ends of the tungsten ignition wire are clamped to the ignition connector and mixing tube strut. To prevent sagging, considerable tension is maintained on the wire during attachment. A resistance check of the installed wire serves as an indication of good electrical contact.

The diaphragm, with a bursting strength suitable for the particular operating conditions (see Sec.5) is mounted in the driver diaphragm station and the station securely bolted. A final check is made of the ignition wire before the end clamping ring and rupture disc are bolted into place.

With all model and instrumentation adjustments complete, the entire facility is evacuated to a low pressure prior to loading. The driver is evacuated to less than 5 mm Hg pressure, and the driven section generally to 10-20 microns Hg. The latter pressure depends on the type of investigation being conducted. For chemical kinetic studies a flushing procedure is adopted to reduce the percentage of foreign contaminants. The driven section is evacuated to the order of 1 micron Hg, pressurized with the test gas to 5 mm Hg, and re-evacuated to the micron level. The test gas is then re-admitted slowly until the driven section is pressurized to the desired operating level. The control valves are then closed to completely isolate this section.

At this stage the driver blockhouse and test section areas are vacated by personnel, warning lights switched on, and the driver loading commenced. The oxygen is injected first, then half of the total helium charge. Next, the hydrogen is added in stoichiometric proportions with the oxygen. Finally, the remainder of the helium is injected at high pressures to produce turbulent mixing in the driver and to clear the loading line of combustible gases. The driver is then isolated and the console vented to atmosphere.

As described in Sec. 3.3, the shock tube enters a 10 minute holding period to allow the driver gases to mix thoroughly. During this interval final adjustments to recording instrumentation can be made. At the end of the holding period the ignition circuit is automatically armed, and the shock tube is then fired.

After the run, the tube is vented to atmosphere through the driver vent valve. The ruptured diaphragm is removed, the end of the driver and the dump tank manway opened, and clean dry air blown through the facility for 15 minutes to remove water vapour and residual gases.

Prior to the next operation, a 'cleaning run' is taken to remove any dust particles, etc. from the driven section. For this purpose a thin (.005-.010 in.) mylar diaphragm is used. The driven section is evacuated to a few microns Hg, and the driver slowly pressurized with helium until the diaphragm ruptures. The resulting flow is quite effective in cleaning out the driven section. The cleaning run can be recommended as a worthwhile procedure.

7.2 Operational Problems

7.2.1 Loss of Diaphragm Material

The loss of diaphragm and other material presented a serious problem in the early operation of the shock tube. The presence of any debris or particles in the flow can severely damage models mounted in the tube, and also scratch the test section windows. Figure 74 shows the extensive damage inflicted by particles on a 1.05-in. diameter steel cylinder which was strut-mounted horizontally across the tube at the test section. The state of the steel cylinder before and after a single run is shown. By using such cylinders to monitor the extent of the damage, it was found that particles originated from the primary diaphragm, the buffer diaphragm (cellophane), the protective liner at the primary diaphragm station (see Sec.2.3.6), and from the aluminium ignition wire (see Sec.3.2).

For buffered operation of the shock tube, a single sheet of 600-MSTL red laminated cellophane was used as a buffer diaphragm. This material shatters on impact of the shock wave, and for this reason provides a highly satisfactory diaphragm. However, this introduces considerable debris into the flow. During unbuffered operation of the tube, the particle damage was found to be vastly reduced, indicating the cellophane diaphragm to be the main contributor to the damage. Therefore this material is no longer used. The use of thin metal diaphragms which petal and are retained completely at the buffer station, is one solution to this aspect of the problem.

Copper impact craters observed on test cylinders during operation with copper diaphragms and a stainless steel liner, and during operation with stainless steel diaphragms and a copper liner, provided evidence of the loss of material from both the primary diaphragm and the protective liner at the diaphragm station. Also, occasional impact craters were quite silvery in colour, and it was concluded that these were caused by debris from the aluminium ignition wire which was vaporized under the combustion temperature. However, the heated wire ignition method, with tungsten wire as the ignition element, eliminated this last source of debris.

Although there is no experimental evidence, the close control of diaphragm bursting pressures is considered essential to minimize the loss of material. Clearly the use of any consumable material which will introduce debris into the flow is undesirable. By avoiding such materials, and by using 'cleaning runs' as described in the preceding section, this particle damage has been reduced to a level where it is no longer a problem in our range of operations.

7.2.2 Fluid Leakage From Recoil Shock Absorbers

Persistent fluid leakage from the high pressure gland assemblies of the liquid spring shock absorbers, indicating loss of pressure, has occurred since their installation. As there is no provision for monitoring the pressure in the shock absorber, leakage can only be detected by the external accumulation of the pressurizing fluid. This evidence of leakage generally appears some two to three weeks after pressurization, even when the shock absorbers remain static in their cradles.

A complete overhaul of the shock absorbers and installation of a modified version of the gland assemblies met with little success in preventing any leakage. A maintenance routine of daily checks for external evidence of fluid leakage and frequent repressurization has prevented this leakage problem from hindering the satisfactory operation of the shock tube.

7.2.3 Tube Contamination

An excessive powder deposit on the walls of the driven section occurred during preliminary operation of the shock tube, particularly after high pressure runs. An analysis of this powder revealed a high percentage of titanium and aluminium. The source of titanium was a protective coat of white glyptal paint on the internal walls of the dump tank, and the aluminium source was the driver ignition wire. The titanium was eliminated by stripping and cleaning the dump tank walls, and the use of the tungsten ignition wire eliminated the aluminium contamination.

Maintaining clean dump tanks walls aids significantly in keeping the tube clean. Most of the contaminating matter tends to accumulate on the dump tank walls, and some of this is swept back up the tube when outflow from the dump tank occurs. Evidence of this is given by the grey-black deposit on the downstream face of the test cylinders used to monitor the particle damage. Occasional swabbing of the driven section is nevertheless necessary to keep the walls clean.

8. SHOCK TUBE PERFORMANCE AND CALIBRATION

8.1 Maximum Operating Conditions

Limitations on operating pressure levels in this shock tube are imposed by the recoil system, the test section, and the driver.

The design and performance analysis of the liquid spring shock absorbers reported in Ref.21 shows that, to limit spring deflections to a maximum of 1.25-ins., the maximum spring reaction must always be greater than the applied load at times later than 20 millisecs. after diaphragm rupture, i.e. all late loads on the driver end plate must not exceed 18,000 lbs.

A late load is the result of a shock wave that propagates upstream from the dump tank towards the driver. The primary shock itself is not reflected back up the tube because of the dissipation in the dump tank. However, as mass flows into the dump tank, the pressure there builds up until it is such that supersonic flow into the dump tank can no longer exist, and the flow becomes subsonic. Compression waves then start to move upstream from the dump tank, coalescing into a shock wave which eventually reaches and reflects from the driver end plate. This double compression of the gas yields a step increase in the pressure that causes the driver to recoil. The pressure after the double compression depends on the pressure before the shock arrives and the strength of the shock, which in turn depend on the initial shock tube conditions.

For a given shock Mach number, the value of the initial driven pressure which just allows a late load increase to reach 18,000 lbs., is the maximum allowable initial driven pressure for that particular shock

Mach number. For the case combustion driver/driven air, this limitation imposed by the recoil system applies for shock Mach numbers $M_s < 10.5$. For $M_s > 10.5$, the test section and driver maximum operating pressures dictate a lower initial driven pressure than that required by the recoil system.

The test section maximum operating pressure of 500 psi limits the initial driven pressure to such values that the shocked gas pressure does not exceed 500 psi. The driver maximum operating pressure of 10,000 psi (for normal constant-volume combustion) also limits the initial driven pressure to such values that realize required diaphragm pressure ratios without exceeding a 10,000 psi driver pressure.

Again for the case of driven air, the test section operating pressure dictates the maximum initial conditions in the range $10.5 \leq M_s \leq 12.0$, and the driver operating pressure for all values of $M_s > 12$. The maximum initial driven pressure (p_1 max) as a function of shock Mach number for equilibrium air is tabulated in Table 3 and presented graphically in Fig. 75. Table 3 also includes the corresponding shocked gas pressure (p_2) and driver pressure (p_4). Similar maximum operating conditions for equilibrium argon are given in Table 4 and Fig. 76.

8.2 Predicted Performance

Shock Waves in Perfect Gases

The usual conservation equations applied to the unsteady motion of a shock wave moving into a perfect gas at rest, become (Ref. 1)

Continuity, $$\rho_1 w_1 = \rho_2 (w_1 - u_2) \tag{8.1}$$

Momentum, $$p_1 + \rho_1 w_1^2 = p_2 + \rho_2 (w_1 - u_2)^2 \tag{8.2}$$

Energy, $$\tfrac{1}{2} w_1^2 + h_1 = \tfrac{1}{2}(w_1 - u_2)^2 + h_2 \tag{8.3}$$

or $$\tfrac{1}{2} w_1^2 + \frac{a_1^2}{\gamma - 1} = \tfrac{1}{2}(w_1 - u_2)^2 + \frac{a_2^2}{\gamma - 1}$$

The thermally perfect equation of state is given by

$$p = \rho \frac{\mathcal{R}}{m} T = \rho R T \tag{8.4}$$

From these equations we may derive the following non-dimensional relations for the changes of state parameters across the shock wave:

Pressure ratio $$P_{21} = 1 + \frac{2\gamma}{\gamma + 1} (M_s^2 - 1) \tag{8.5}$$

Density ratio $$\Gamma_{21} = \frac{(\gamma + 1) M_s^2}{(\gamma - 1) M_s^2 + 2} \tag{8.6}$$

Temperature and sound speed ratios

$$T_{21} = A_{21}^2 = \frac{[2\gamma M_s^2 - (\gamma - 1)] \; [(\gamma - 1) M_s^2 + 2]}{(\gamma + 1)^2 M_s^2} \tag{8.7}$$

Particle velocity ratio $$U_{21} = \frac{2}{\gamma+1}\left(\frac{M_s^2 - 1}{M_s}\right) \tag{8.8}$$

Flow Mach number $$M_2 = \frac{M_s^2 - 1}{\left[\left(\gamma M_s^2 - \frac{\gamma-1}{2}\right)\left(\frac{\gamma-1}{2} M_s^2 + 1\right)\right]^{\frac{1}{2}}} \tag{8.9}$$

From Eqs. (8.5), (8.6), (8.7), (8.8), and (8.9) the pressure, density, temperature, sound speed, flow velocity, and flow Mach number behind the shock wave can be determined if the initial conditions and the shock Mach number (M_s) are known. It is important to note that these relations are only true for perfect gases (constant specific heat ratio γ). However they do predict accurately the behaviour of an inert monatomic gas such as argon up to fairly high temperatures ($\sim$6000 ^{o}K, $M_s \sim 8$), but above this electronic excitation and ionization will begin to modify the predicted ideal values. For air (or oxygen and nitrogen) these relations may be used with reasonable confidence up to temperatures $\sim$1000 ^{o}K ($M_s \sim 4$) before conditions deviate significantly due to the onset of gas imperfections with increasing temperature.

It is worthwhile nevertheless to examine the limits of the above relations for strong shock waves, and compare the results with the real or imperfect gas values considered below. For strong shock waves ($M_s \rightarrow \infty$), Eqs. (8.5) to (8.9) reduce to the following:

$$\begin{aligned}
P_{21} &\rightarrow \frac{2\gamma}{\gamma+1} M_s^2 \\
\Gamma_{21} &\rightarrow \frac{\gamma+1}{\gamma-1} \\
T_{21} &\rightarrow \frac{2\gamma(\gamma-1)}{(\gamma+1)^2} M_s^2 \\
A_{21} &\rightarrow \frac{\sqrt{2\gamma(\gamma-1)}}{\gamma+1} \cdot M_s \\
U_{21} &\rightarrow \frac{2}{\gamma+1} \cdot M_s \\
M_2 &\rightarrow \sqrt{2/\gamma(\gamma-1)}
\end{aligned} \tag{8.10}$$

Note that the density ratio and flow Mach number approach finite limiting values. For the case of air, with $\gamma = 1.4$, $\Gamma_{21} \rightarrow 6$ and $M_2 \rightarrow 1.89$ as $M_s \rightarrow \infty$.

Shock Waves in Imperfect Gases

The limitations of the ideal shock wave relations have been indicated above. For strong shock waves in imperfect gases it is no longer possible to employ these relations. At high temperatures (high Mach numbers) and low pressures (high altitudes), the effects of thermal and caloric imperfections must be considered. For example, the enthalpy h_2 and molecular weight m_2 behind

the shock will be functions of the pressure p_2 and temperature T_2 behind the shock, i.e. $h_2 = h_2(p_2,T_2)$ and $m_2 = m_2(p_2,T_2)$. Also, relaxation processes will take place immediately behind the shock front as equipartition of energy proceeds between the active and inert degrees of freedom. However, we are only interested here in the final equilibrium flow quantities, where the hot gas flow is considered to be an equilibrium mixture of reacting gases. Since the flow quantities in this equilibrium region behind the shock (region 2^*) are independent of the intervening processes which establish equilibrium between the active and inert degrees of freedom[29], it is not necessary to consider the relaxation zone in computing the final equilibrium values.

Using shock fixed coordinates ($v_2 = w_1 - u_2$; $v_1 = w_1$), the system of gasdynamic equations for an imperfect gas is,

Continuity, $$\rho_1 v_1 = \rho_2^* v_2^* \tag{8.11}$$

Momentum, $$p_1 + \rho_1 v_1^2 = p_2^* + \rho_2^* v_2^{*2} \tag{8.12}$$

Energy, $$\tfrac{1}{2}v_1^2 + h_1 = \tfrac{1}{2}v_2^{*2} + h_2^* \tag{8.13}$$

For a dissociated or ionized gas, the thermally imperfect equation of state is given by

$$p = \rho \frac{\mathcal{R}T}{m(p,T)} = Z\,(p,T)\;\rho RT \tag{8.14}$$

and the calorically imperfect equation of state by

$$h = h(p,T) = \int_0^T C_p(p,T)dT \tag{8.15}$$

where $Z(p,T) = m_1/m_2(p,T) > 1$

m_1 = molecular weight of cold gas

m_2 = molecular weight of shocked gas

For a single dissociating and ionizing diatomic gas

$$Z = [1 + \alpha(p,T)]\;\;[1 + x(p,T)] \tag{8.16}$$

where α = degree of dissociation

x = degree of ionization

Equations(8.11), (8.12), (8.13), (8.14), (8.15), and (8.16), may be solved for the unknown flow quantities p_2^*, ρ_2^*, T_2^*, v_2^* (= $w_1 - u_2^*$), h_2^*, and Z_2, in the equilibrium region behind the shock wave. It should be noted that this cannot be done explicitly, and an iteration procedure must be used (see Ref.1, for example).

The remaining quantities to be determined are the sound speed (a_2^*) and the flow Mach number(M_2^*). The sound speed is given by (Ref.1),

$$a_2^{*2} = \gamma^* \left(\frac{p_2}{\rho_2}\right)^* \tag{8.17}$$

where

$$\gamma^* = \left(\frac{\partial \ln p}{\partial \ln \rho}\right)_S \tag{8.18}$$

The isentropic index $\gamma^* = \gamma^*(p,T)$ may be found graphically from Mollier diagrams by plotting ln p against ln ρ along isentropes. The local slope then gives the value of γ^*, and the sound speed determined from Eq. (8.17). Once the sound speed is known, the flow Mach number can be calculated from the expression,

$$M_2^* = u_2^*/a_2^* = U_{21}^*/A_{21}^* \tag{8.19}$$

The peak diaphragm pressure ratio (P_{41}) as a function of shock Mach number (M_s) will now be considered. As previously noted (Sec.2.2.3), the basic shock tube equation (Eq.2.4) relating diaphragm pressure ratio to resulting shock Mach number assumes perfect gases and ideal shock tube flow, and consequently leads to large inaccuracies in the values of P_{41} for the production of strong shock waves. However, a good approximation may be obtained by using the perfect expansion wave relation (Ref.1),

$$P_{34} = \left(1 + \frac{\gamma_4 - 1}{2} U_{34}\right)^{\frac{2\gamma_4}{\gamma_4 - 1}} \tag{8.20}$$

and matching the pressure and velocity across the interface with the appropriate imperfect shock wave values for a given M_s and p_1.

Applying the conditions

$$p_3 = p_2^* \quad \text{or} \quad P_{34} = P_{21}^*/P_{41}$$

$$u_3 = u_2^* \quad \text{or} \quad U_{34} = U_{21}^*/A_{41}$$

across the interface, Eq. (8.20) becomes

$$P_{41} = P_{21}^* \left(1 - \frac{\gamma_4 - 1}{2} \cdot \frac{U_{21}^*}{A_{41}}\right)^{-\frac{2\gamma_4}{\gamma_4 - 1}} \tag{8.21}$$

(Eq. (8.21) is in fact Eq. (2.4) expressed in terms of the pressure and velocity ratios (imperfect) instead of shock Mach number.)

The values of a_4 and γ_4 must also be those appropriate to the high temperature, high pressure, driver gas. Reference 5 shows equilibrium values of a_4 = 7550 fps and γ_4 = 1.46 following an adiabatic constant-volume combustion of a stoichiometric oxygen-hydrogen plus 75% helium mixture. Although the calculations neglected dissociation of the driver gases, these values were assumed in computing P_{41} from Eq. (8.21).

These calculations were carried out for maximum operating conditions (Sec.8.1) and the solution of Eq. (8.21) therefore involved an iteration procedure for those combinations of M_s and p_1 (giving p_2^* max = 500 psi) which required a driver pressure in excess of 10,000 psi. With

p_4 max = 10,000 psi, the calculated P_{41} values for these combinations ($M_s > 12$ in air, $M_s > 14.5$ in argon) necessitated a new (lower) value of p_1, which in turn revised the values of P^*_{21} and U^*_{21} for the particular M_s. Solution of Eq. (8.21) using these revised values gave the final P_{41} ratios (and p_1 max for the particular M_s). Only a single iteration proved necessary since both P^*_{21} and U^*_{21} are relatively insensitive to changes in p_1. Figures 77 and 94 show the peak diaphragm pressure ratios obtained in this manner for driven air and argon r ctively.

The shock induced flow quantities have been determined for the entire shock Mach number range of the shock tube. Dimensionless ratios of thermodynamic and dynamic variables across the moving shock wave, and the thermodynamic and dynamic variables of the equilibrium region behind the moving shock wave, have been evaluated as a function of shock Mach number for air and argon as test gases ($T_1 = 300^oK$ is assumed throughout). The following three cases are considered:

(a) Combustion driver/driven air, for max. operating conditions

(b) Combustion driver/driven air, for an initial pressure $p_1 = 1$ cm Hg.

(c) Combustion driver/driven argon, for max. operating conditions

Cases (a) and (c) provide the maximum performance envelope for driven air and argon respectively. Case (b) is included to compared the experimental calibration data with theoretical predictions (see Sec. 8.3.2).

In the evaluation of all these flow quantities liberal use has been made of charts, tables, and Mollier diagrams presented in Refs. 1, 10, 30-33. The results are tabulated in Tables 5 to 10 for the three cases, and are limited to three figure accuracy because of the graphical interpolation required in determining most of the flow quantities. The results are also presented graphically, and an index to the corresponding figures is included in the various tables. (Note that the notation of Fig. 1 applies in these tables and graphs, and all shock ratios and quantities in region 2 the imperfect values denoted by an asterisk in the text.)

Before discussing these results it is perhaps necessary to briefly review the behaviour of imperfect gas flow properties with increasing shock Mach number, and in particular their variation with decreasing initial pressure at a given shock Mach number.

The density and temperature display the most significant departure from perfect gas values. The density ratio (Γ^*_{21}) increases markedly with increasing shock Mach number (M_s) and decreasing initial pressure (p_1). The temperature ratio (T^*_{21}) increases with M_s for a given p_1, but is greatly reduced from the perfect gas value, and decreases markedly with p_1 at a given M_s. The pressure ratio (P^*_{21}) is relatively insensitive to changes in p_1, increasing only slightly with decreasing p_1. The same applies to the particle velocity ratio (U^*_{21}). The sound speed ratio (A^*_{21}) is less than the perfect gas value and decreases with p_1 at a given M_s. The flow Mach number ($M^*_2 = U^*_{21}/A^*_{21}$) as a consequence, is greater than the perfect gas value and increases with decreasing p_1 at a given M_s. The compressibility factor (Z_2), equal to unity for a perfect gas, increases with decreasing p_1 at a given M_s. These effects are summarized in the following table:

Imperfect		Perfect	Variation of imperfect value with decreasing p_1
P^*_{21}	>	P_{21}	increases slightly -essentially constant
Γ^*_{21}	>>	Γ_{21}	increases markedly
T^*_{21}	<<	T_{21}	decreases markedly
U^*_{21}	>	U_{21}	increases slightly
A^*_{21}	<	A_{21}	decreases
M^*_2	>	M_2	increases
Z_2	>	1	increases

Case (a): Driven air, $p_1 = p_1$ max

Case (a) performance curves are shown in Figs. 78 to 86. The thermodynamic ratios P^*_{21}, Γ^*_{21}, and T^*_{21} are plotted in Fig.78 and the quantities U^*_{21} and A^*_{21} in Fig.79. When examining these curves it is important to realize the initial pressure p_1 is different for each value of M_s. As a result the density ratio Γ^*_{21} increases more rapidly at the higher shock Mach numbers, instead of levelling off as would be the case for constant p_1. The opposite behaviour occurs with the temperature ratio T^*_{21}, which is seen to actually decrease for $M_s > 18$, where the normal increase in T^*_{21} with M_s (for fixed p_1) is overcome by the marked decrease in T^*_{21} with decreasing p_1. Similarly, Fig.79 shows the sound speed ratio A^*_{21} to increase less rapidly as M_s increases. (These effects are more obvious when compared to the corresponding curves for Case (b), where p_1 = 1 cm Hg, constant throughout. Figures 87 and 88 show T^*_{21} increasing, Γ^*_{21} beginning to level off, and A^*_{21} increasing more rapidly, at the higher shock Mach numbers. A comparison of these figures for Cases (a) and (b) also demonstrates the relative insensitivity of P^*_{21} and U^*_{21} to changes in p_1; in both cases these curves are practically identical.)

The equilibrium flow quantities, obtained directly from the dimensionless shock ratios and the initial conditions p_1 max (Fig.75) and T_1 = 300°K, are plotted in Figs.80 to 83. The pressure p^*_2 is shown in Fig.80. The initial pressure p_1 and driver pressure p_4 are included in this figure to demonstrate the maximum pressure levels for this shock tube for each value of M_s in driven air. In the region limited by the recoil system, p^*_2 increases rapidly with M_s and p_1 max until, at M_s = 10.5, the maximum test section pressure of 500 psi is reached. p^*_2 then remains constant until the driver pressure p_4 reaches its maximum value of 10,000 psi at M_s = 12.0. Thereafter, with p_4 now held constant, p^*_2 decreases as M_s increases.

The density ρ^*_2 is shown in Fig.81, along with the initial density ρ_1 corresponding to p_1 max and T_1 = 300°K. The form of these curves is the same as p_1 max, where the abrupt changes in slope as M_s increases mark the regions of tube performance limited by the recoil system, test section pressure, and driver pressure, respectively.

Figure 82 shows the equilibrium temperature T_2^* behind the shock wave. It is worth noting that, due to the driver pressure limitation, the maximum static temperature (6850°K) is obtained at $M_s = 18.4$, less than the maximum M_s which can be generated in this facility. The remaining flow quantities, particle velocity u_2^*, sound speed a_2^*, and flow Mach number M_2^*, are plotted in Fig.83, and the compressibility factor Z_2 in Fig.84.

Unit Reynolds number has also been evaluated for Case (a). Reynolds number is defined by

$$Re = \rho u \, l/\mu$$

where μ = coefficient of viscosity

l = an arbitrary linear dimension

The Reynolds number per foot in region 2^* may be expressed as

$$(Re/l)_2 = \frac{\rho_2^* \mu_2^*}{\mu_2} = \frac{\gamma_1 p_1}{a_1} \frac{\Gamma_{21}^* U_{21}^*}{\mu_2} \tag{8.22}$$

Using viscosity data for air given in Ref. 31, the Reynolds number was calculated from Eq. (8.22) and is plotted in Fig. 85. Since Reynolds number is directly proportional to density, this curve also exhibits the abrupt changes in slope characteristic of the pressure and density curves for maximum operating conditions.

Finally, the degree of dissociation of oxygen (α_O) and nitrogen (α_N) have been determined for the equilibrium pressures and temperatures of Case (a). These values were interpolated from the equilibrium composition data for air given in Ref. 32. Plotted in Fig.86, they are intended to serve only as a general guide for air, since only oxygen and nitrogen atom concentrations have been considered (all other species, including ionization, were ignored).

<u>Case (b)</u>: Driven air, p_1 = 1 cm Hg.

Case (b) performance curves are shown in Figs.87 to 92. The dimensionless shock ratios P_{21}^*, Γ_{21}^*, T_{21}^*, and U_{21}^*, A_{21}^*, are plotted in Figs. 87 and 88 respectively, and the equilibrium flow quantities p_2^*, ρ_2^*, T_2^*, u_2^*, a_2^*, M_2^*, and Z_2, in Figs. 89 to 92. The driver pressure p_4 is also included with p_2^* in Fig.89. It should be noted that, although these curves are plotted up to $M_s = 20$, the limiting M_s is 17 for p_1 = 1 cm Hg (see Fig.75).

Figure 93 is a plot of the theoretical hot gas flow duration (t_c) at the test section, and of the length (x_c) of the hot gas region between the shock and interface when the shock is located in the test section. Assuming constant wave speeds, and the shocked gas flow to be terminated by the arrival of the interface, then

$$t_c = \frac{x}{a_1}\left(\frac{1}{U_{21}^*} - \frac{1}{M_s}\right) \tag{8.23}$$

and

$$x_c = u_2^* t_c = x\left(1 - \frac{U_{21}^*}{M_s}\right) \tag{8.24}$$

where x = distance from diaphragm to test section (45.75-ft.)

It is stressed that this figure represents theoretical values. In a real shock tube flow, where shock attenuation and viscous effects occur, measured testing times are roughly 50% or less of those predicted by real gas theory.[34]

The noticeable fluctuations in the plots of M_s with T_{21}^*, Γ_{21}^*, and Z_2, are brought about by the addition of energies of dissociation, and, if carried to higher shock speeds, of single and multiple ionization. As previously mentioned, for low shock Mach numbers the temperature closely follows the perfect gas value since the active translational and rotational degrees of freedom only are excited. As M_s increases, the heat capacity of the gas is increased due to vibrational excitation, and the temperature rise falls below the ideal value. This behaviour becomes more pronounced as dissociation begins to absorb heat. As M_s increases, the degree of dissociation at first increases rapidly, then proceeds at a steady rate, and finally slows considerably as dissociation nears completion (see behaviour of α_0 in Fig.86). The heat capacity of the gas increases in a similar manner. The temperature thus rises less rapidly as dissociation begins, increases slowly during the main dissociation process, and then rises rapidly as the dissociation rate falls off. This behaviour may be repeated many times in a polyatomic gas like air, as the various species dissociate and as single and multiple ionization occurs.

The density behaves in a similar fashion, though in the opposite sense to the temperature. As M_s increases, the density increases above the ideal gas value due to the corresponding decrease in temperature rise as the vibrational mode becomes excited. When dissociation occurs, the density increases more rapidly, the gas becomes more monatomic, and the molecular weight decreases. When dissociation nears completion, and the temperature begins to rise more rapidly, the density falls off. This behaviour continues until further dissociation or ionization becomes effective in reducing the temperature rise, thus causing the density to increase again.

Case (c): Driven argon, $p_1 = p_1$ max

Case (c) performance curves for driven argon are shown in Figs. 95 to 102. The dimensionless shock ratios are plotted in Figs. 95 and 96, and the equilibrium flow quantities (determined from the above ratios and the initial conditions p_1 max (Fig.76), $T_1 = 300°K$) in Figs. 97 to 100. The initial pressure p_1 and driver pressure p_4 are included with p_2^* in Fig. 97, and the initial density ρ_1 with the density ρ_2^* in Fig.98. Figure 101 shows the Reynolds number per foot $(Re/l)_2$ evaluated from Eq. (8.22) with viscosity data for argon from Ref.33. Finally, the degree of ionization (x_2) is plotted in Fig.102 from data given in Ref.10.

The discussion of the performance curves for Case (a) applies equally to these results for Case (c), and they are therefore presented without further comment.

8.3 Shock Tube Calibration

The calibration reported in this section was conducted with the argon buffer, so that the notation of Fig.2, for double-diaphragm operation, applies here. Actually this changes only the driver notation, which is now referred to as region (8), and introduces the buffer region (6).

8.3.1 Calibration Range and Procedure

The calibration of this facility involved the measurement of pressure-time histories in the driver, test section, and dump tank, and the measurement of shock Mach numbers as a function of initial conditions and driven length. Essentially limited in scope, the calibration was designed primarily to determine the peak overall diaphragm pressure ratio required to produce a given shock Mach number in the test section. The test section pressure and wave-speed measurements enable a comparison with theory of the pressure ratio across the moving shock, while the dump tank pressure-time history would provide some basis for comparison with the theoretical predictions of Ref.13.

The calibration procedure was conducted throughout with air as the test gas at an initial pressure p_1 = 1 cm Hg (.193 psi) and argon buffer pressure p_6 = 1 cm Hg. With the initial driven conditions thus fixed, the peak driver pressure was varied (by varying the initial mixture pressure) to produce shock Mach numbers in the range from 8 to 17, the latter being the maximum for p_1 = 1 cm Hg.

No attempt was made to achieve a particular shock Mach number in the test section. The actual driver pressures, and therefore shock Mach numbers, were dictated by the bursting strengths of the diaphragms. The diaphragm thickness and scribe depth were varied to produce diaphragms with bursting strengths sufficient to provide a reasonable coverage of the shock Mach number range. For each thickness and scribe depth chosen, a minimum of four diaphragms were manufactured. Of these, two were tested to destruction in the test rig (Sec.5.2) to determine the burst pressure (and therefore the required peak driver pressure), and the remaining two used in the shock tube for actual calibration runs. At least two runs were therefore made at each set of initial conditions.

The instrumentation used for this calibration procedure has been described in Sec.6. From the recorded outputs of Kistler pressure transducers mounted in the driver end plate, test section, and dump tank (see Fig.64), the peak pressure during the driver combustion process, the pressure rise across the moving shock wave, and the pressure-time history in the dump tank, were measured. The raster oscilloscope and ionization gauges were used to determine the shock wave velocity as a function of driven tube length (see Fig.70). A schematic of the shock tube configuration and location of instrumentation for the calibration procedure is shown in Fig.103.

8.3.2 Comparison with Predicted Performance

The results of the pressure calibration measurements are presented in Figs.104 and 105 together with the theoretically predicted curves (Case (b), Sec.8.2). Figure 104 shows the shock Mach number as a function of peak overall diaphragm pressure ratio. Two sets of data are presented in this figure, corresponding to wave speeds measured at distances of 12.75-ft. and 44.75-ft. (test section) from the primary diaphragm. Shock wave attenuation and the non-ideal diaphragm opening characteristics account for the displacement of the experimental points from the theoretically predicted curve.

Based on assumptions of perfect inviscid gases and instantaneous diaphragm opening, the ideal shock tube flow is characterized by a shock wave of constant velocity and regions of equal and constant pressure and velocity separated by an interface (Fig.1). The performance of a real shock tube differs significantly from this ideal flow. In reality the shock attenuates as it moves down the tube, the pressure and velocity behind the shock do not remain constant, and the interface becomes an extended mixing region, whose front accelerates, resulting in a significantly reduced testing time, as noted previously.

Figure 105 is a plot of the pressure ratio across the moving shock wave versus shock Mach number for test section shock pressure and wave speeds. The experimental data is in close agreement with the theoretically predicted curve.

The measurements of the test section pressure-time history show the pressure to be essentially constant in a small region immediately behind the shock, and to then increase steadily with time. This effect can be seen in Fig.64, which is quite typical of all the shock pressure-time results. The pressure rise behind an attenuating shock decreases as the shock moves down the tube, so that the pressure would be expected to be lower immediately behind the shock and to increase as the flow progresses past a station in the tube.

Although there is no experimental evidence, it is believed this pressure rise occurs before the arrival of the interface. This is shown to be the case in Ref. 35. Evidently, such nonuniform flow effects can considerably limit the available uniform testing time for aerodynamic studies. For the particular test section pressure trace of Fig.64, the pressure increase begins approximately 225 microsecs. after passage of the shock (M_s = 11). For a test section shock Mach number M_s = 15, this time is reduced to approximately 110-120 microsecs.

The theoretical analysis presented in Ref.13 of the pressure-time history in the dump tank was made for maximum operating conditions at shock Mach numbers of 10, 15, and 20 (p_1 = 3.50, .584, and .0314 psi respectively). As the calibration procedure was conducted with p_1 = 1 cm Hg = .193 psi, no direct comparison of the experimental pressure-time history with the theoretical prediction is possible. However, in spite of the inadequacy of the comparison, a theoretical case is included with an experimental result in Fig.106. The initial conditions are indicated in the figure. Although the absolute pressure levels differ by a factor of four, it is seen that the experimental variation with time is quite similar to that predicted analytically.

Some representative curves of shock Mach number versus distance along the driven section, obtained from the raster data, are shown in Fig. 107. The shock trajectories observed in this facility are quite typical of high performance shock tubes.[1,5,36]

The shock velocity history involves two phases, an initial acceleration or formation-distance phase, followed by a decleration or distance-attenuation phase. The initial acceleration involves the formation of the sharp shock front by the coalescing compression waves generated by the opening of the diaphragm.[37] The attenuation phase is due mainly to the growth of the boundary layer on the tube walls behind the moving shock wave (Fig.108). The thickness of the boundary layer at any point on the wall increases with time, and the displacement effect of the boundary layer on the flow is equivalent to the wall moving normal to the flow with a velocity equal to the vertical velocity at the edge of the boundary layer. This equivalent motion produces pressure waves in the flow which overtake and decay the shock wave.[38]

Effects such as combustion at the driver-test gas interface, initial nonuniformity of the driver, and chemical kinetic effects, can also constitute mechanisms for producing attenuation,[39] particularly when combustion drivers are used.

The formation and attenuation phases can be seen in the shock histories shown in Fig.107. For these results the formation distance is approximately 40 hydraulic diameters, and is relatively independent of shock strength. The experimental data also indicate the attenuation to be relatively independent of shock strength. The percentage rate of decay of shock speed is typically 0.4-0.5% per foot for the present shock Mach number range. Shock attenuation is, however, highly dependent on driver gas sound speed, increasing strongly with increasing sound speed.[5,35] Shock attenuation is also affected by the size and geometry of the shock tube. For example, data presented in Ref.5 for a 1.92-in. diameter combustion driven tube shows an attenuation rate of 1.5% per foot for a shock Mach number of 9.

Many analytical and experimental studies of shock wave attenuation have been made (Refs. 35, 38, 40, for example). Most of the theories are concerned with the growth of the boundary layer on the walls of the tube. The boundary layer is assumed to be thin relative to the diameter of the tube, and the effect of the boundary layer formation is studied by introducing small perturbations representing the displacement effect of the boundary layer on the flow. However, these theories do not accurately predict the attenuation for strong shock waves such as are encountered in this facility.[5,36]

9. CONCLUDING REMARKS

The high performance shock tube reported herein has been successfully developed as a hypersonic test facility. The unusually large 4-in. x 7-in. cross-section (for a facility of this type), permitting the use of fairly large instrumented models, and the association with the facility of a 9-inch plate Mach-Zehnder interferometer, provides a powerful research tool for the study of dissociated and ionized gas flows.

The constant volume combustion of hydrogen-oxygen-helium mixtures is an economical and practical method of driving such a facility. The inherent difficulties of combustion heating can be largely overcome by careful attention to uniformity of gas mixture, the ignition of the mixture, and diaphragm control. For the operating conditions of this facility, the driver mixing process takes about 10 minutes to yield a uniform gas mixture.

Shock tube performance is highly dependent on the diaphragm opening characteristics. Close control of diaphragm bursting pressures is essential. Depending on the diaphragm thickness, scribe depths between 15-25% and 45% of the diaphragm thickness are necessary to avoid loss of petals and to ensure a satisfactory rupture for the particular geometry of this facility.

Telescopic recoil sections and liquid spring shock absorbers are an effective solution to the problem of dynamic loading in a facility of this size. Despite the leakage problem, liquid spring shock absorbers have proven to be a reliable means of dissipating the recoil energies.

A high-pressure shock tube is a potentially lethal weapon, particularly with the use of explosive gas mixtures. Adequate protection in the form of safety barricades, fail-safe devices, remote operation, and strict adherence to proven safe operating procedures, is an absolute necessity.

The overall shock tube performance agrees satisfactorily with the theoretical performance presented. Fast response instrumentation (quartz pressure pickups, ionization and heat flux gauges, raster oscilloscope) have been successfully used to monitor tube performance. Thermal protection in the form of a thin layer of silicone grease is necessary to avoid erroneous long duration (> 1 millisec.) measurements with the Kistler pressure transducers.

Shock wave attenuation (expressed as a percentage decrement in Mach number per foot) is shown to be substantially independent of shock strength for shock waves generated in the present facility. The results of direct measurements of the static pressure history behind normal shock waves in air substantiate that shock wave attenuation may appreciably limit the available shock tube testing time for gasdynamical studies requiring a reasonably constant pressure field.

Excellent stagnation point heat transfer data on a right circular cylinder have already been obtained in this facility.[28]

REFERENCES

1. Glass, I.I. Hall, J.G. — Handbook of Supersonic Aerodynamics, Section 18, Shock Tubes. NAVORD Report 1488 (Vol.6), Bureau of Naval Weapons, 1959.

2. Ferri, A. (ed.) — Fundamental Data Obtained From Shock Tube Experiments. AGARDograph No. 41 Pergamon Press, 1961.

3. Hall, J.G. — The Design and Performance of a 9-Inch Plate Mach-Zehnder Interferometer. UTIAS Report 27, Institute for Aerospace Studies , University of Toronto, 1954.

4. Nagamatsu, H.T. Martin, E.D. — Combustion Investigation in the Hypersonic Shock Tunnel Driver Section. J. App. Physics Vol. 30, No. 7, 1959.

5. Wittliff, C.E. Wilson, M.R. — Shock Tube Driver Techniques and Attenuation Measurements. Cornell Aero.Lab. Report No.AD-1052-A-4, 1957.

6. Henshall, B.D. — The Use of Multiple Diaphragms in Shock Tubes. ARC Tech.Report 19062, CP No. 291, 1956.

7. Bird, G.A. — A Note on Multiple Diaphragm Shock Tubes. RAE Tech. Note No. Aero 2469, 1956.

8. Alpher, R.A. White, D.R. — Ideal Theory of Shock Tubes with Area Change Near Diaphragm. General Electric Res.Lab. Report No.57-RL-1664,1957.

9. Schexnayder, C.J. — On the Performance of a Double-Diaphragm Shock Tube Using the Reflected Shock Method and a Light Gas Buffer. J.Aero/Space Sciences Vol. 25, No.8, 1958.

10. Resler, E.L. Lin, S.C. Kantrowitz, A. — The Production of High Temperature Gases in Shock Tubes. J. App.Physics Vol.23, No.12, 1952.

11. Russo, A.L. Hertzberg, A. — Modifications of the Basic Shock Tube to Improve its Performance. Cornell Aero.Lab.Report No.AD-1052-A-7, 1958.

12. Chapin, S.G. Heyman, R.J. — Performance Characteristics of a Chambered Buffered Shock Tube. Proceedings of the Hypervelocity Techniques Symposium, Institute of Aero/Space Sciences,1960.

13. Lau,J.H.W. — Combustion Chamber and Dump Tank Pressures in the 4-in.x 7-in. Hypersonic Shock Tube. M.A.Sc. Thesis, Institute for Aerospace Studies, University of Toronto, 1961.

14. White, D.R. — On the Existance of Higher Than Normal Detonation Pressures. J. Fluid Mech. Vol. 2, Part 5, 1957.

15. Streiff, M.L. — Results of Shock Tube Hazard Studies. Convair Astronautics Report AZR-001, 1957.

16. Hill, R. — The Mathematical Theory of Plasticity. Oxford University Press, London, 1956.

17. Harvey, J.F. — Pressure Vessel Design: Nuclear and Chemical Applications. D. Van Nostrand Co. Inc., Princeton, 1963.

18. Cox, S.G. — Development of the R.A.E. 6-Inch Diameter Shock Tube, Part 1. RAE Tech. Note Aero 2510, 1957.

19. Perry, C.C. Lissner, H.R. — The Strain Gauge Primer. McGraw-Hill Book Co., New York, 1955.

20. A.S.M.E. — ASME Boiler and Pressure Vessel Code Section VIII, Rules for Construction of Unfired Pressure Vessels. ASME Publication, 1956.

21. Roberts, A.K. — Design of the Recoil System for the 4-in.x 7-in. Hypersonic Shock Tube. UTIAS Tech. Note No. 42, Institute for Aerospace Studies, University of Toronto, 1960.

22. Hendershot, K.C. — Development of a Combustion Driven Shock Tunnel. Proceedings of the Hypervelocity Techniques Symposium, Institute of Aero/Space Sciences, 1960.

23. Sax, N.I. — Handbook of Dangerous Materials. Reinhold Publishing Corp., New York, 1951.

24. Nagamatsu, H.T. — Private communication. General Electric Res. Lab., Schenectady, N.Y.

25. Rabinowicz, J. Jessey, M.E. Bartsch, C.A. — Resistance Thermometer for Transient High-Temperature Studies. J. App. Physics, 27, 97, 1956.

26. Hall, J.G. Hertzberg, A. — Recent Advances in Transient Surface Temperature Thermometry. Jet Propulsion Vol. 28, 1958.

27. Taylor, B.W. — Development of Thin Film Heat Transfer Gauges for Shock Tube Flows. UTIAS Tech. Note No. 27, Institute for Aerospace Studies, University of Toronto, 1959.

28. Walenta, Z.A. — Analogue Networks for High Heat-Transfer Rate Measurements. UTIAS Tech. Note No. 84, Institute for Aerospace Studies, University of Toronto, 1964.

29. Bethe, H.A. Teller, E. — Deviations from Thermal Equilibrium in Shock Waves. BRL Report X-117, Ballistic Research Laboratory, Aberdeen Proving Ground, Md. 1945.

30. Feldman, S. — Hypersonic Gas Dynamic Charts for Equilibrium Air. AVCO Research Report 40, 1957.

31. Hansen, C.F. — Approximations for the Thermodynamic and Transport Properties of High-Temperature Air. NACA TN 4150, 1958.

32. Gilmore, F.R. — Equilibrium Composition and Thermodynamic Properties of Air to 24,000°K. Rand Corporation RM-1543, 1955.

33. Hilsenrath, J. Touloukian, Y.S. — The Viscosity, Thermal Conductivity, and Prandtl Number for Air, O_2, N_2, NO, H_2, CO, CO_2, H_2O, He, and A. Transactions of the ASME, Vol. 76, No. 6, 1954.

34. Rose, P.H. Stark, W.I. — Stagnation Point Heat-Transfer Measurements in Dissociated Air. J. Aeronaut. Sciences, Vol. 25, No. 2, 1958.

35. Jones, J.J. — Experimental Investigation of Attenuation of Strong Shock Waves in a Shock Tube with Hydrogen and Helium as Driver Gases. NACA TN 4072, 1957.

36. Rose, P.H. Nelson, W. — On the Effect of Attenuation on Gas Dynamic Measurements Made in Shock Tubes. AVCO Research Report 24, 1958.

37. White, D.R. — Influence of Diaphragm Opening Time on Shock-Tube Flows. General Electric Res.Lab.Report No.58-RL-1999,1958.

38. Mirels, H. — Attenuation in a Shock Tube due to Unsteady-Boundary-Layer Action. NACA Rep. 1333, 1957.

39. Spence, D.A. Woods, B.A. — A Review of Theoretical Treatments of Shock Tube Attenuation. RAE Tech. Note No. Aero. 2899, 1963.

40. Trimpi, R.L. Cohen, N.B. — A Theory for Predicting the Flow of Real Gases in Shock Tubes with Experimental Verification. NACA TN 3375, 1955.

TABLE 1

DESCRIPTION OF SHOCK TUBE COMPONENTS

SHOCK TUBE	Overall Length Driven Length / Diameter Driver Length / Driven Length	77 ft. 115 .282 max.
DRIVER	Total Length Internal Diameter Wall Thickness Section Lengths Maximum Pressure Material Weight	13.75 ft. 6 ins. 4 ins. 6-ft, 3-ft, 3-ft, 1.5-ft. 60,000 psi Atlas Ultimo-4 510 lbs/ft.
DRIVER RECOIL SECTION	Length Internal Diameter Wall Thickness Maximum Pressure Material Weight	3 ft. 6 ins. 4 ins. max. 37,000 psi Atlas Ultimo-4 1830 lbs.
TRANSITION SECTION	Length Cross-section Outside Diameter Maximum Pressure Material Weight	1.5 ft. 6-in. dia. to 4-in. x 7-in. 11 ins. 7000 psi Atlas Ultimo-4 (equiv.) 450 lbs.
DRIVEN SECTION	Total Length Cross-section Outside Diameter Section Lengths Maximum Operating Pressure Material Weight	40 ft. 4-in. x 7-in. 11 ins. 4 x 8-ft, 2 x 4-ft. 1000 psi SPS-245 normalized 310 lbs/ft.
TEST SECTION	Length Cross-section Outside Diameter Windows (Interferometer) Maximum Operating Pressure Material Weight	4 ft. 4-in. x 7-in. 11 ins. 7-in. x 9-in. field of view 500 psi SPS-245 normalized 2040 lbs.
DUMP TANK RECOIL SECTION	Length Internal Diameter Wall Thickness Maximum Operating Pressure Material Weight	1 ft. 8 ins. 1.5 ins. 3000 psi SPS-245 normalized 360 lbs.
DUMP TANK	Height Internal Diameter Wall Thickness Volume Maximum Operating Pressure Material Weight	6.5 ft. 3 ft. .5 ins. min. 35.4 cu. ft. 300 psi SA-285 B 2270 lbs.

TABLE 2

DRIVER CONFIGURATIONS

M_s	Length feet	Recoil Mass slugs
7 - 8	13.75	358
8 - 9	10.75	298
9 - 12	7.75 (2x3-ft sections)	255
9 - 12	7.75 (1x6-ft section)	238
12 - 20	4.75	195

TABLE 3

MAXIMUM OPERATING CONDITIONS FOR EQUILIBRIUM AIR

M_s	p_1 max mm Hg	p_1 max psi	p_2 psi	p_4 psi	Limited by
6	114	2.20	94.6	322	Recoil System
7	142	2.75	165	732	↓
8	160	3.10	248	1450	↓
9	173	3.35	338	2670	↓
10	181	3.50	448	4810	↓
11	169	3.27	500	7360	Test Section
12	140	2.71	500	10,000	Driver
13	83.1	1.61	350	10,000	↓
14	50.7	.980	247	10,000	↓
15	30.2	.584	168	10,000	↓
16	17.2	.333	109	10,000	↓
17	9.63	.186	69.4	10,000	↓
18	5.61	.108	45.4	10,000	↓
19	3.04	.0589	27.7	10,000	↓
20	1.63	.0314	16.5	10,000	↓
21	.815	.0158	9.17	10,000	↓
22	.383	.00741	4.76	10,000	↓

TABLE 4

MAXIMUM OPERATING CONDITIONS FOR EQUILIBRIUM ARGON

M_s	p_1 max mm Hg	p_1 max psi	p_2 psi	p_4 psi	Limited by
6	107	2.06	94.6	244	Recoil System
7	136	2.62	165	509	↓
8	154	2.97	248	923	↓
9	165	3.19	338	1540	↓
10	176	3.41	448	2520	↓
11	163	3.15	500	3500	Test Section
12	134	2.60	500	4650	↓
13	112	2.17	500	6280	↓
14	95.1	1.84	500	8590	↓
15	66.8	1.29	412	10,000	Driver
16	40.3	.779	286	10,000	↓
17	23.5	.455	191	10,000	↓
18	13.5	.261	123	10,000	↓

TABLE 5

COMBUSTION DRIVER / DRIVEN AIR
DIMENSIONLESS RATIOS OF THERMODYNAMIC AND DYNAMIC VARIABLES ACROSS MOVING SHOCK WAVE FOR MAXIMUM OPERATING CONDITIONS
EQUILIBRIUM AIR $T_1 = 300\ ^oK$

M_s	p_1 max cm Hg	P_{41}	P_{21}	Γ_{21}	T_{21}	U_{21}	A_{21}
6	11.4	146	43	6.23	6.92	5.05	2.53
7	14.2	266	60	6.77	8.70	6.02	2.82
8	16.0	468	80	7.40	10.5	6.99	3.07
9	17.3	798	101	8.10	12.1	8.00	3.32
10	18.1	1380	128	8.69	13.6	8.98	3.51
11	16.9	2250	153	9.20	15.1	9.94	3.76
12	14.0	3700	185	9.61	16.6	10.8	3.92
13	8.31	6230	218	9.94	18.2	11.8	4.15
14	5.07	1020^1	252	10.4	19.7	12.7	4.34
15	3.02	1710^1	288	10.9	20.8	13.6	4.50
16	1.72	3010^1	329	11.5	21.7	14.6	4.70
17	.963	5370^1	372	12.2	22.5	15.6	4.82
18	.561	9220^1	418	13.0	22.8	16.5	4.94
19	.304	1700^2	471	14.0	22.6	17.4	5.09
20	.163	3180^2	525	14.8	22.7	18.3	5.28
21	.0815	6340^2	582	15.8	22.6	19.2	5.39
22	.0383	1350^3	641	17.0	22.1	20.2	5.52
Fig. No.	75	77	78	78	78	79	79

Note: Superscript indicates power of ten.

TABLE 6

COMBUSTION DRIVER / DRIVEN AIR
THERMODYNAMIC AND DYNAMIC VARIABLES OF QUASI-STEADY REGION
BEHIND MOVING SHOCK WAVE FOR MAXIMUM OPERATING CONDITIONS
EQUILIBRIUM AIR $T_i = 300\ ^oK$

Ms	p_1 max (psi)	p_2 (psi)	p_4 (psi)	ρ_1 (scf)	ρ_2 (scf)	T_2 (^oK)	Z_2	u_2 (fps)	a_2 (fps)	M_2	$(Re/l)_2$ (ft^{-1})	α_N	α_O
6	$.220^{1}$	946^{-1}	322	$.342^{-3}$	$.213^{-2}$	2080	1.000	5760	2890	2.00	9.29^{6}	-	$.392^{-3}$
7	$.275^{1}$	165	732	$.427^{-3}$	$.289^{-2}$	2610	1.003	6870	3220	2.14	1.32^{7}	-	$.346^{-2}$
8	$.310^{1}$	248	1450	$.482^{-3}$	$.356^{-2}$	3140	1.011	7970	3500	2.28	1.70^{7}	$.263^{-4}$	$.132^{-1}$
9	$.335^{1}$	338	2670	$.520^{-3}$	$.421^{-2}$	3620	1.029	9120	3790	2.41	2.16^{7}	$.107^{-3}$	$.364^{-1}$
10	$.350^{1}$	448	4810	$.544^{-3}$	$.472^{-2}$	4070	1.056	1020^{1}	4000	2.56	2.55^{7}	$.425^{-3}$	$.632^{-1}$
11	$.327^{1}$	500	7360	$.508^{-3}$	$.467^{-2}$	4520	1.092	1130^{1}	4290	2.64	2.60^{7}	$.170^{-2}$	$.982^{-1}$
12	$.271^{1}$	500	1000^{1}	$.420^{-3}$	$.404^{-2}$	4980	1.131	1240^{1}	4470	2.76	2.31^{7}	$.304^{-2}$	.134
13	$.161^{1}$	350	1000^{1}	$.250^{-3}$	$.248^{-2}$	5470	1.177	1350^{1}	4730	2.84	1.45^{7}	$.116^{-1}$	.158
14	.980	247	1000^{1}	$.152^{-3}$	$.158^{-2}$	5910	1.219	1450^{1}	4950	2.93	9.36^{6}	$.270^{-1}$	.182
15	.584	168	1000^{1}	$.907^{-4}$	$.989^{-3}$	6240	1.261	1560^{1}	5130	3.03	5.99^{6}	$.618^{-1}$	.191
16	.333	109	1000^{1}	$.517^{-4}$	$.595^{-3}$	6510	1.306	1670^{1}	5360	3.12	3.67^{6}	.106	.197
17	.186	694^{-1}	1000^{1}	$.289^{-4}$	$.352^{-3}$	6740	1.355	1780^{1}	5500	3.24	2.56^{6}	.167	.203
18	.108	454^{-1}	1000^{1}	$.168^{-4}$	$.219^{-3}$	6850	1.415	1880^{1}	5630	3.34	1.43^{6}	.213	.204
19	$.589^{-1}$	277^{-1}	1000^{1}	$.915^{-5}$	$.128^{-3}$	6790	1.482	1980^{1}	5810	3.42	8.68^{5}	.274	.206
20	$.314^{-1}$	165^{-1}	1000^{1}	$.488^{-5}$	$.724^{-4}$	6800	1.524	2090^{1}	6020	3.46	5.09^{5}	.334	.207
21	$.158^{-1}$	917^{-2}	1000^{1}	$.245^{-5}$	$.386^{-4}$	6770	1.621	2190^{1}	6150	3.57	2.79^{5}	.407	.208
22	$.741^{-2}$	476^{-2}	1000^{1}	$.115^{-5}$	$.196^{-4}$	6630	1.706	2300^{1}	6300	3.65	1.49^{5}	.465	.209
Fig. No.	80	80	80	81	81	82	84	83	83	83	85	86	86

Note : Superscript indicates power of ten.

TABLE 7

COMBUSTION DRIVER / DRIVEN AIR
DIMENSIONLESS RATIOS OF THERMODYNAMIC AND DYNAMIC VARIABLES ACROSS MOVING SHOCK WAVE FOR AN INITIAL PRESSURE $p_1 = 1$ cm Hg
EQUILIBRIUM AIR $T_1 = 300\ ^{o}K$

M_s	p_1 cm Hg	P_{41}	P_{21}	Γ_{21}	T_{21}	U_{21}	A_{21}
6	1.0	146	43	6.23	6.92	5.04	2.60
7	↓	266	60	6.85	8.58	5.98	2.80
8		468	80	7.72	9.99	6.93	3.02
9		798	101	8.59	11.2	7.94	3.22
10		1380	128	9.40	12.2	8.94	3.42
11		2250	154	10.0	13.4	9.88	3.60
12		3700	185	10.3	15.0	10.8	3.80
13		6230	218	10.4	17.2	11.8	4.00
14		1020^{1}	252	10.6	19.0	12.7	4.21
15		1710^{1}	289	11.1	20.4	13.6	4.41
16		3010^{1}	329	11.6	21.5	14.6	4.65
17		5370^{1}	372	12.1	22.5	15.6	4.90
18		9220^{1}	418	12.7	23.4	16.6	5.17
19		1700^{2}	468	13.1	24.3	17.6	5.41
20		3180^{2}	520	13.6	25.2	18.6	5.70
Fig. No.		77	87	87	87	88	88

Note: Superscript indicates power of ten.
p_1 max < 1 cm Hg for $M_s \geq 17$.

TABLE 8

COMBUSTION DRIVER / DRIVEN AIR
THERMODYNAMIC AND DYNAMIC VARIABLES OF QUASI-STEADY REGION
BEHIND MOVING SHOCK WAVE FOR AN INITIAL PRESSURE p_1 = 1 cm Hg
EQUILIBRIUM AIR T_1 = 300 °K

M_s	p_1 (psi)	p_2 (psi)	p_4 (psi)	ρ_1 (scf)	ρ_2 (scf)	T_2 (°K)	Z_2	u_2 (fps)	a_2 (fps)	M_2	t_c (μsec)	x_c (ft)
6	.193	83.1^{-1}	283^{-1}	$.300^{-4}$	$.187^{-3}$	2080	1.000	5750	2970	1.94	127^{1}	7.31
7	↓	11.6	515^{-1}	↓	$.206^{-3}$	2570	1.005	[illegible]20	3190	2.14	975	6.65
8	↓	15.5	904^{-1}	↓	$.232^{-3}$	3000	1.023	7900	3440	2.30	773	6.11
9	↓	19.5	154	↓	$.258^{-3}$	3350	1.052	9060	3670	2.47	594	5.38
10	↓	24.8	266	↓	$.282^{-3}$	3660	1.090	1020^{1}	3900	2.61	474	4.84
11	↓	29.8	436	↓	$.301^{-3}$	4030	1.132	1130^{1}	4110	2.74	412	4.65
12	↓	35.8	715	↓	$.309^{-3}$	4510	1.172	1230^{1}	4330	2.84	371	4.57
13	↓	42.2	1200	↓	$.311^{-3}$	5170	1.203	1340^{1}	4560	2.94	319	4.29
14	↓	48.7	1970	↓	$.319^{-3}$	5690	1.233	1450^{1}	4800	3.02	290	4.21
15	↓	55.9	3310	↓	$.333^{-3}$	6110	1.269	1560^{1}	5030	3.09	266	4.14
16	↓	63.6	5810	↓	$.348^{-3}$	6460	1.309	1670^{1}	5300	3.15	232	3.88
17	↓	71.9	1038^{1}	↓	$.365^{-3}$	6750	1.354	1780^{1}	5590	3.19	206	3.68
18	↓	80.8	1780^{1}	↓	$.381^{-3}$	7020	1.405	1890^{1}	5900	3.21	186	3.53
19	↓	90.5	3280^{1}	↓	$.395^{-3}$	7290	1.458	2010^{1}	6170	3.25	168	3.36
20	↓	10.1^{1}	6150^{1}	↓	$.408^{-3}$	7560	1.513	2120^{1}	6500	3.26	155	3.29
Fig. No.		89	89		90	90	92	91	91	91	93	93

Note : Superscript indicates power of ten.
p_1 max < .193 psi for $M_s \geq 17$.

TABLE 9

COMBUSTION DRIVER / DRIVEN ARGON
DIMENSIONLESS RATIOS OF THERMODYNAMIC AND DYNAMIC VARIABLES ACROSS MOVING SHOCK WAVE FOR MAXIMUM OPERATING CONDITIONS
EQUILIBRIUM ARGON $T_1 = 300\ ^{o}K$

M_s	p_1 max cm Hg	P_{41}	P_{21}	Γ_{21}	T_{21}	U_{21}	A_{21}
6	10.7	118	46	3.73	12.6	4.25	3.54
7	13.6	194	63	3.81	16.5	5.03	4.09
8	15.4	311	84	3.86	20.8	5.78	4.60
9	16.5	484	106	3.87	26.3	6.49	5.08
10	17.6	739	131	4.02	31.7	7.33	5.40
11	16.3	1110	159	4.30	36.4	8.20	5.52
12	13.4	1790	193	4.67	40.0	9.22	5.69
13	11.2	2890	230	5.09	42.9	10.2	5.86
14	9.51	4670	272	5.55	45.1	11.3	6.03
15	6.68	7740	319	6.15	46.7	12.4	6.13
16	4.03	1280^{1}	368	6.83	47.3	13.5	6.24
17	2.35	2200^{1}	420	7.62	47.4	14.5	6.28
18	1.35	3830^{1}	472	8.35	47.8	15.5	6.39
Fig. No.	76	94	95	95	95	96	96

Note: Superscript indicates power of ten.

TABLE 10

COMBUSTION DRIVER / DRIVEN ARGON
THERMODYNAMIC AND DYNAMIC VARIABLES OF QUASI-STEADY REGION
BEHIND MOVING SHOCK WAVE FOR MAXIMUM OPERATING CONDITIONS
EQUILIBRIUM ARGON $T_1 = 300\ ^oK$

M_s	p_1 max (psi)	p_2 (psi)	p_4 (psi)	ρ_1 (scf)	ρ_2 (scf)	T_2 (^oK)	u_2 (fps)	a_2 (fps)	M_2	$(Re/l)_2$ (ft^{-1})	X_2
6	2.06	946^{-1}	244	$.442^{-3}$	$.165^{-2}$	3770	4500	3750	1.20	2.90^{6}	$.249^{-8}$
7	2.62	165	509	$.562^{-3}$	$.214^{-2}$	4940	5320	4330	1.23	3.92^{6}	$.195^{-6}$
8	2.97	248	923	$.636^{-3}$	$.245^{-2}$	6250	6120	4870	1.26	4.53^{6}	$.935^{-5}$
9	3.19	338	1540	$.684^{-3}$	$.265^{-2}$	7890	6870	5380	1.28	4.89^{6}	$.243^{-3}$
10	3.41	448	2520	$.731^{-3}$	$.294^{-2}$	9510	7760	5720	1.36	5.57^{6}	$.203^{-2}$
11	3.15	500	3500	$.675^{-3}$	$.290^{-2}$	1090^{1}	8680	5840	1.49	5.73^{6}	$.879^{-2}$
12	2.60	500	4650	$.556^{-3}$	$.260^{-2}$	1200^{1}	9760	6020	1.62	5.48^{6}	$.217^{-1}$
13	2.17	500	6280	$.465^{-3}$	$.237^{-2}$	1290^{1}	1080^{1}	6200	1.75	5.35^{6}	$.403^{-1}$
14	1.84	500	8590	$.394^{-3}$	$.219^{-2}$	1350^{1}	1200^{1}	6380	1.87	5.33^{6}	$.578^{-1}$
15	1.29	413	1000^{1}	$.277^{-3}$	$.170^{-2}$	1400^{1}	1310^{1}	6490	2.02	4.47^{6}	$.864^{-1}$
16	7.79^{-1}	286	1000^{1}	$.167^{-3}$	$.114^{-2}$	1420^{1}	1430^{1}	6610	2.16	3.21^{6}	.112
17	4.55^{-1}	191	1000^{1}	$.974^{-4}$	$.742^{-3}$	1420^{1}	1540^{1}	6650	2.31	2.26^{6}	.145
18	2.61^{-1}	123	1000^{1}	$.559^{-4}$	$.467^{-3}$	1440^{1}	1650^{1}	6770	2.43	1.52^{6}	.189
Fig. No.	97	97	97	98	98	99	100	100	100	101	102

Note : Superscript indicates power of ten.

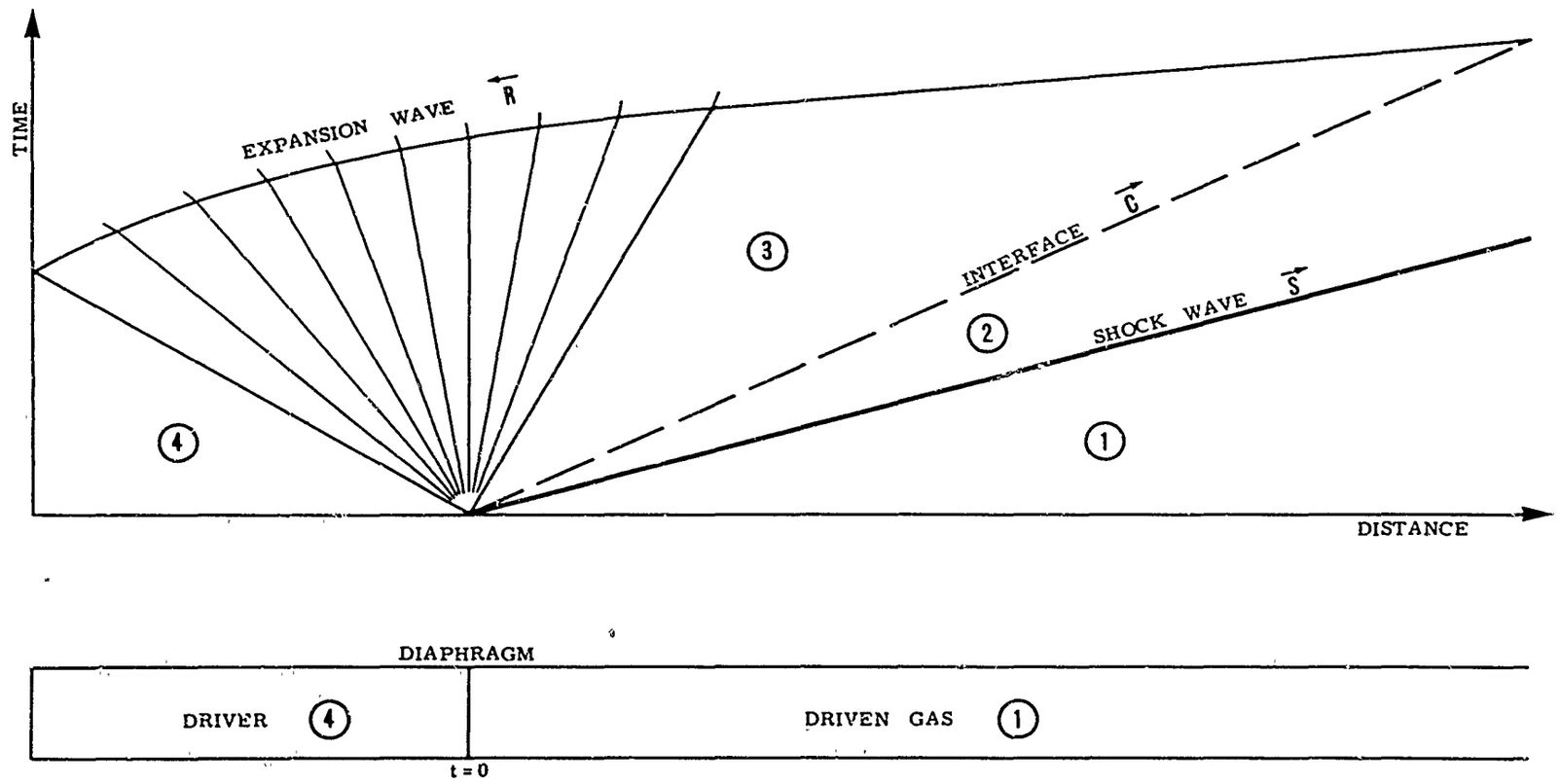

FIG. 1 WAVE DIAGRAM OF BASIC SHOCK TUBE FLOW

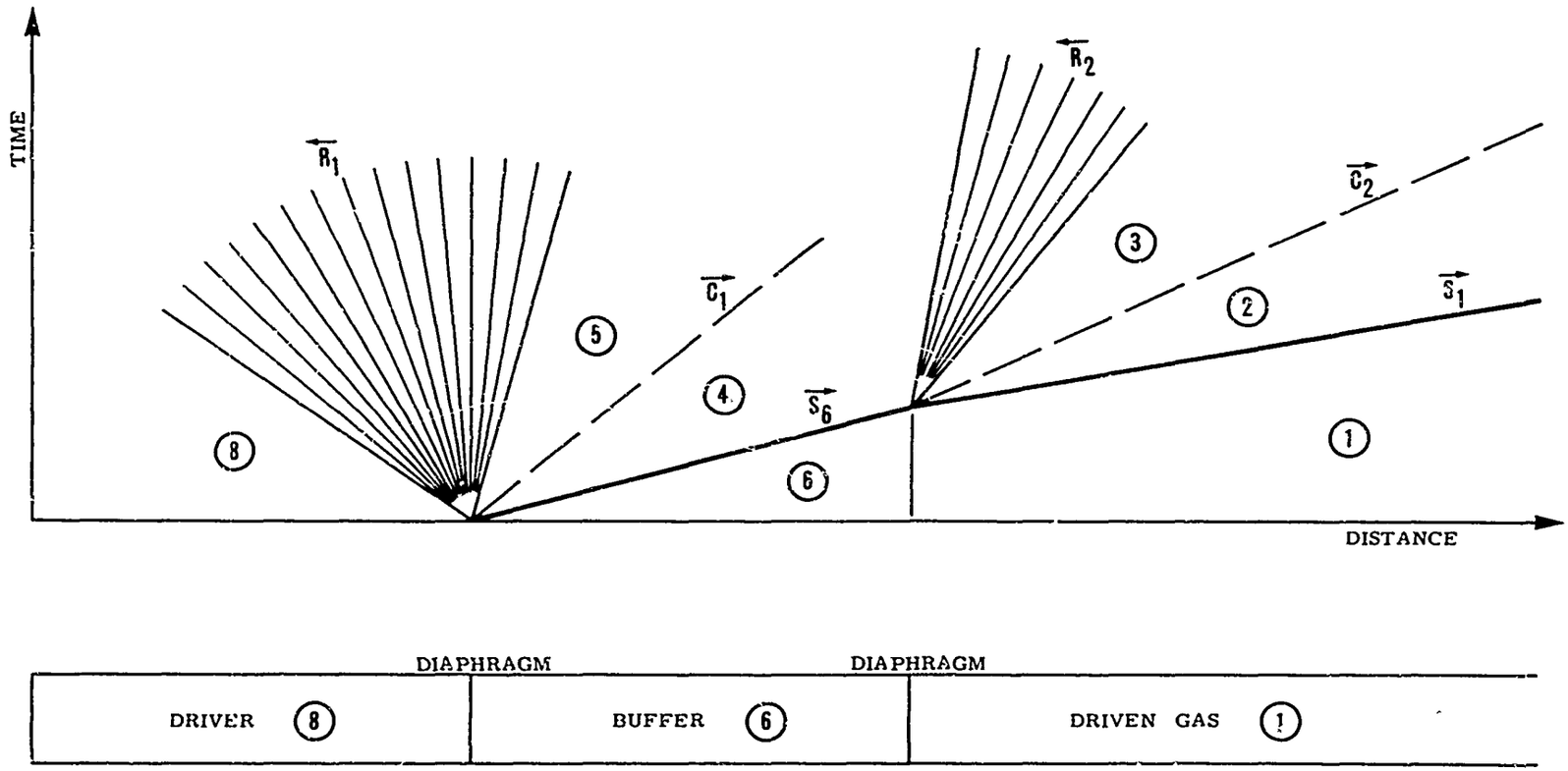

FIG. 2 WAVE DIAGRAM OF INITIAL FLOW IN DOUBLE-DIAPHRAGM ($P_6=P_1$) CONSTANT-AREA TUBE (UNSTEADY EXPANSION METHOD)

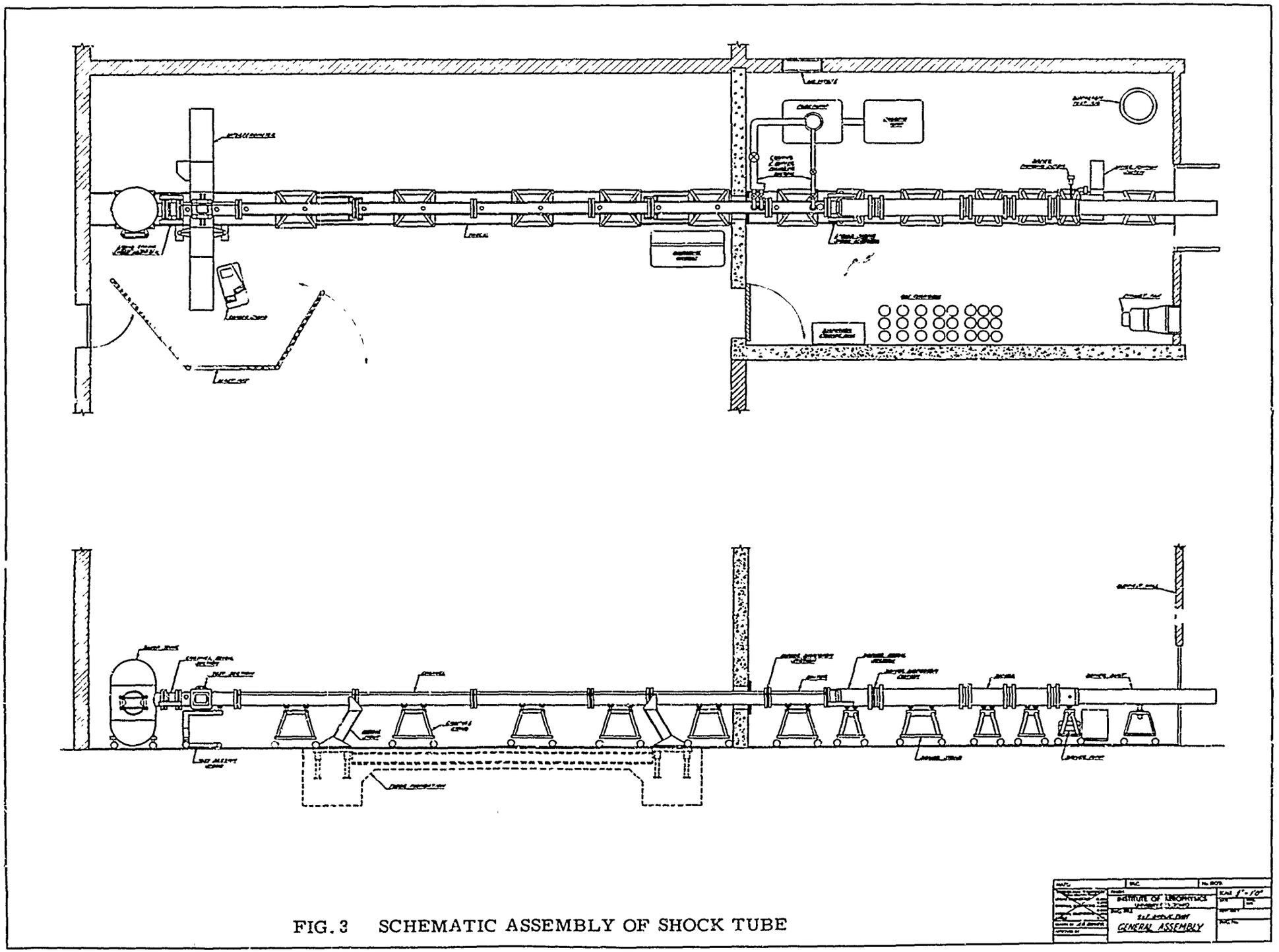

FIG. 3 SCHEMATIC ASSEMBLY OF SHOCK TUBE

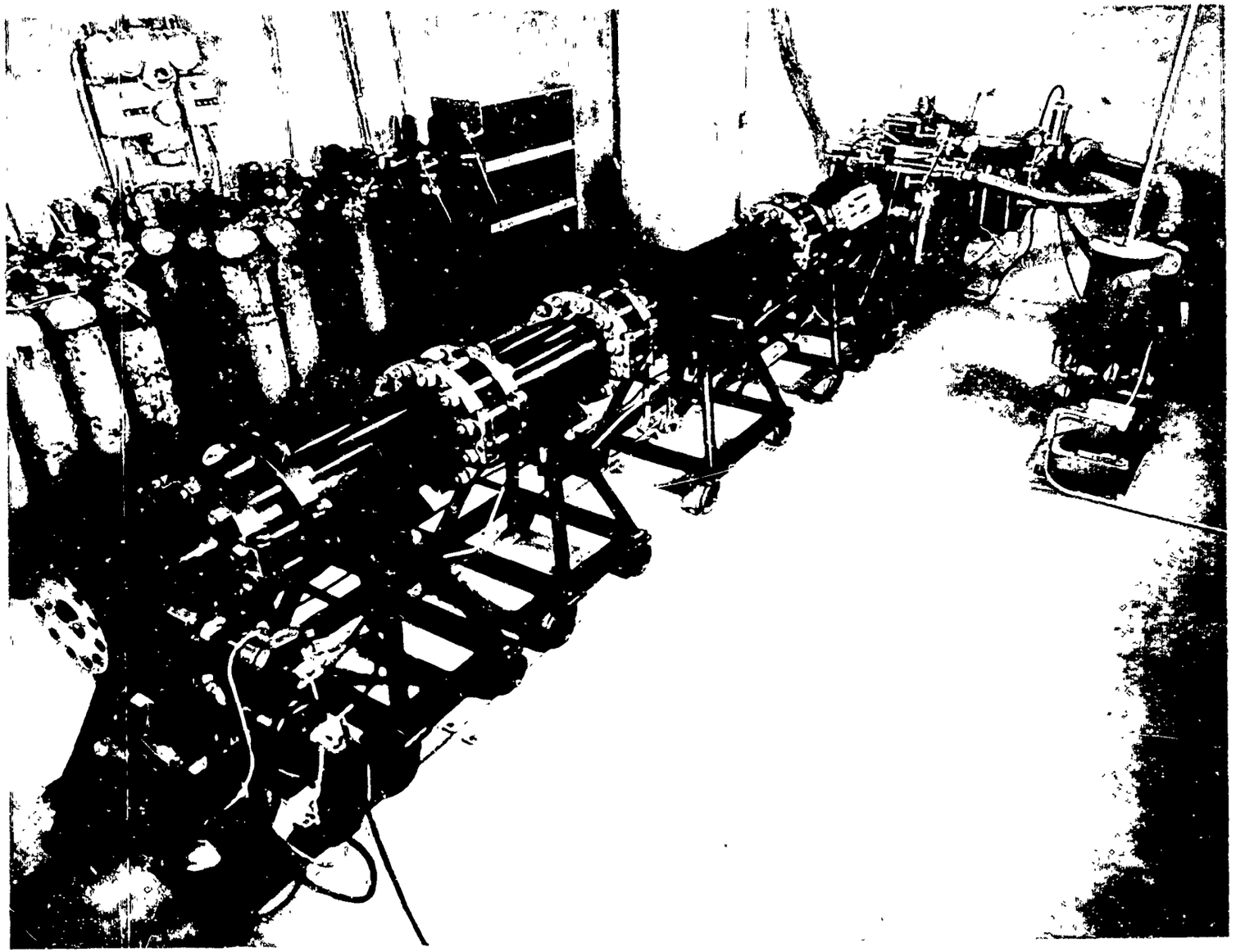

FIG. 4 VIEW OF DRIVER FROM UPSTREAM END

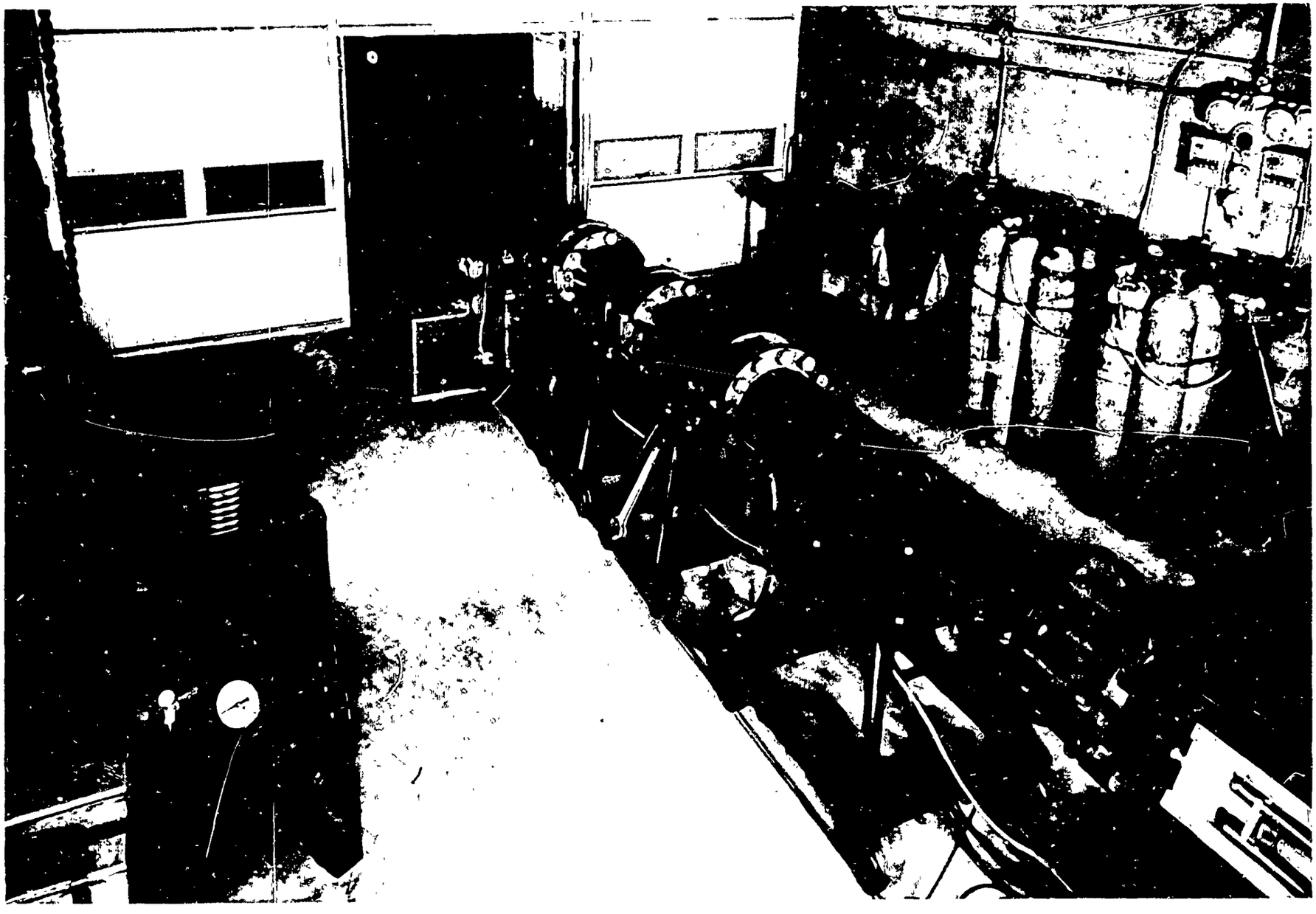

FIG. 5 VIEW OF DRIVER FROM DOWNSTREAM END

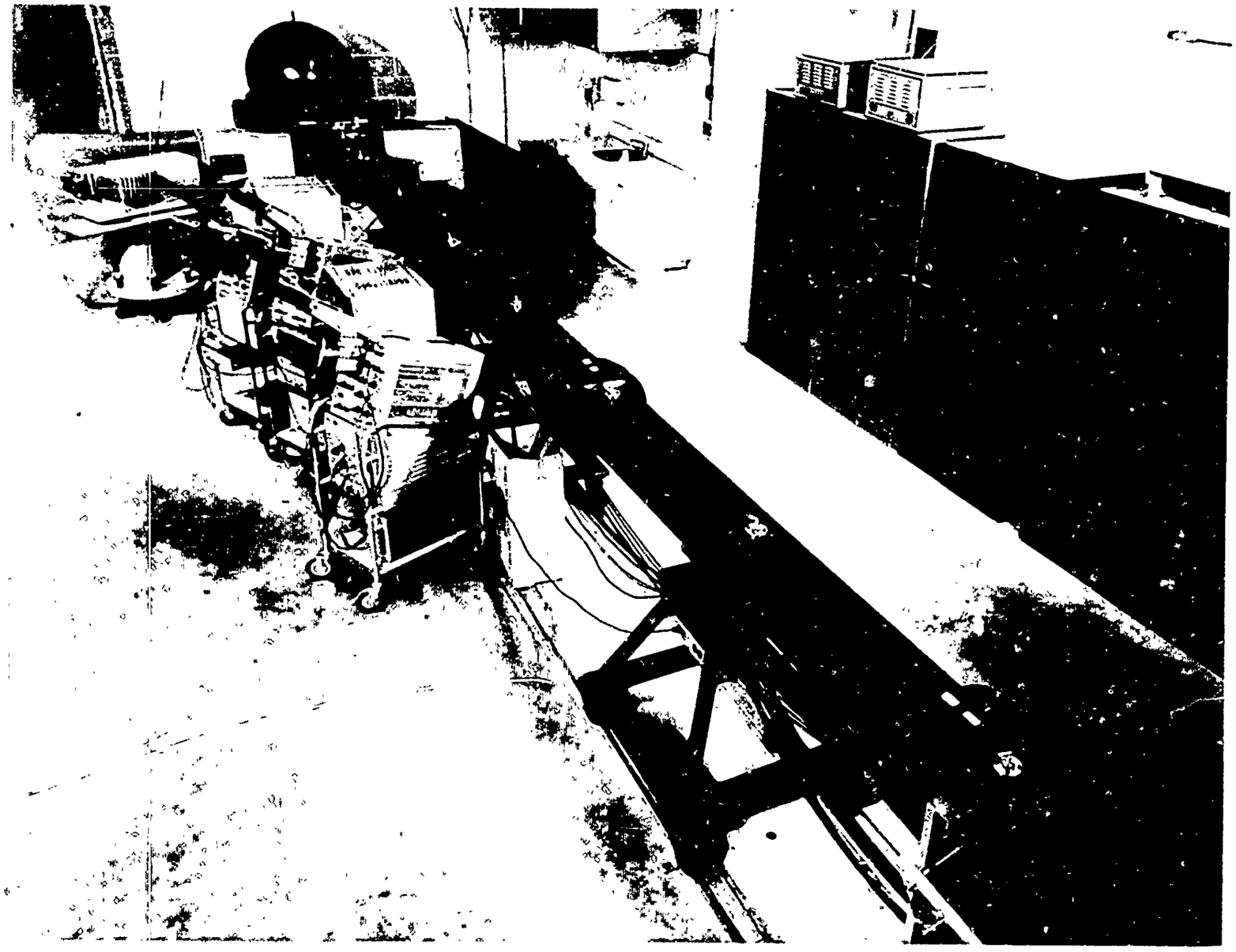

FIG. 6 VIEW OF DRIVEN SECTION SHOWING INTERFEROMETER AND RECORDING INSTRUMENTATION

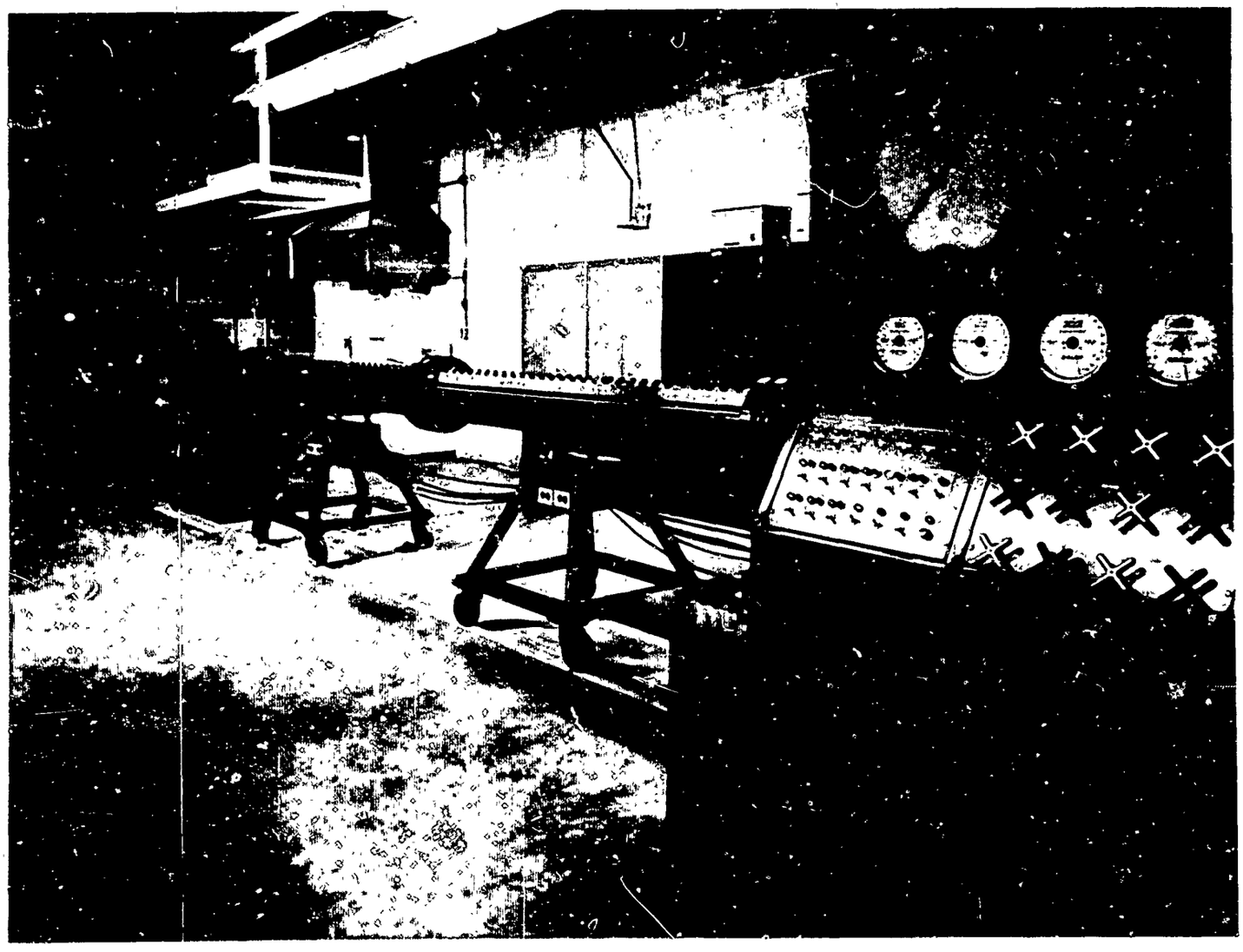

FIG. 7 VIEW OF DRIVEN SECTION FROM CONTROL CONSOLE

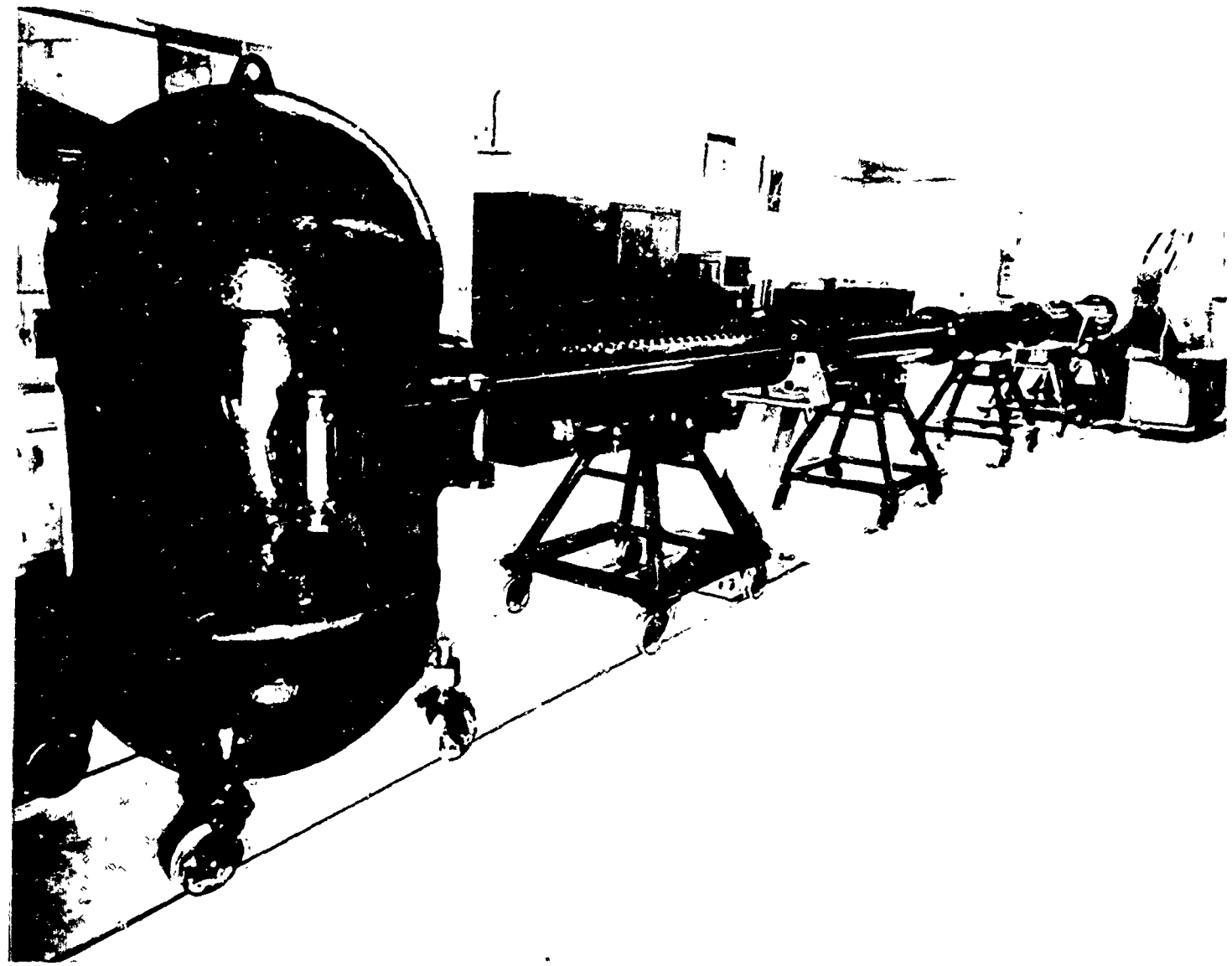

FIG. 8 VIEW OF DRIVEN SECTION AND DUMP TANK

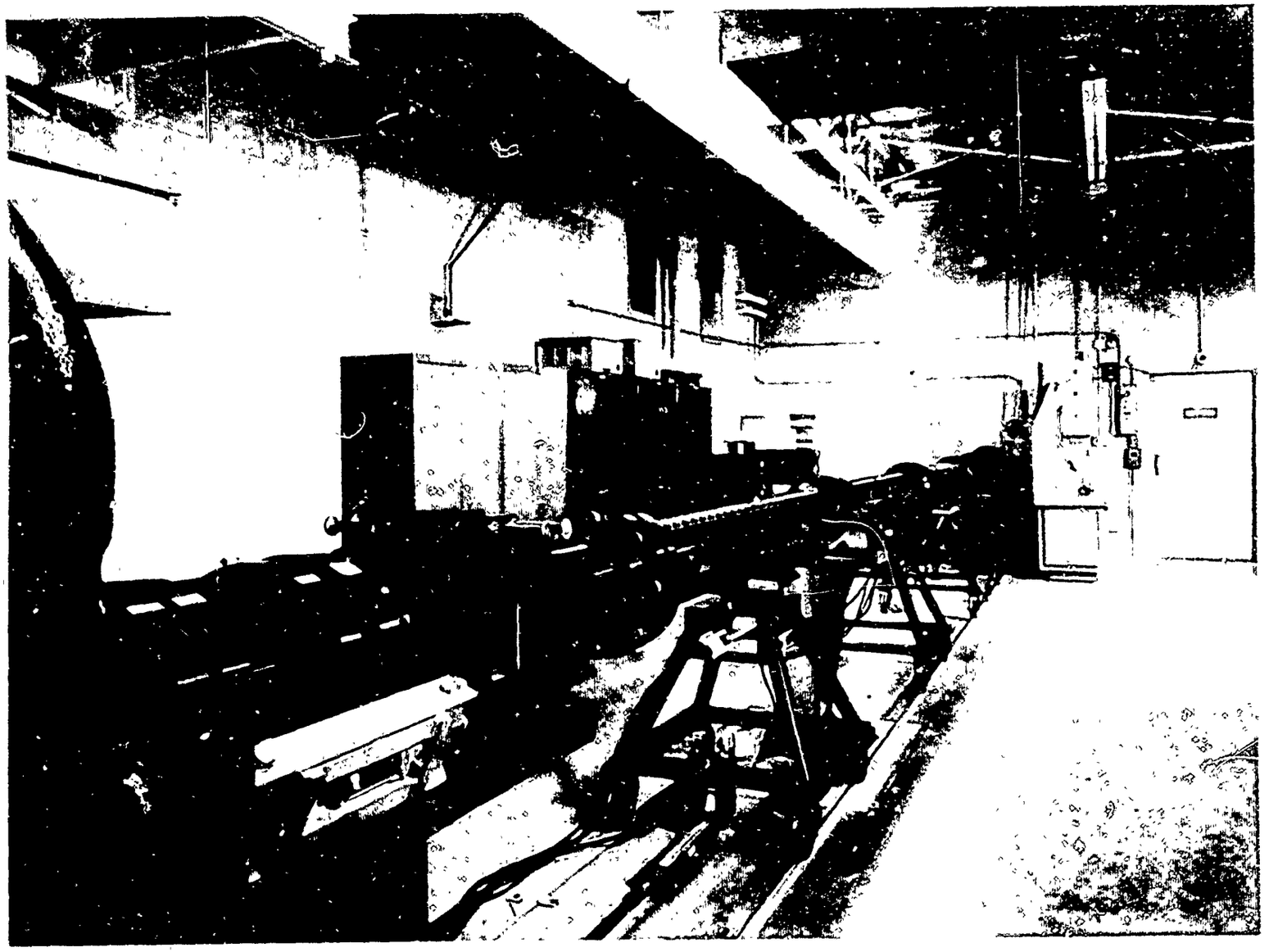

FIG. 9 VIEW OF DRIVEN SECTION FROM DOWNSTREAM END

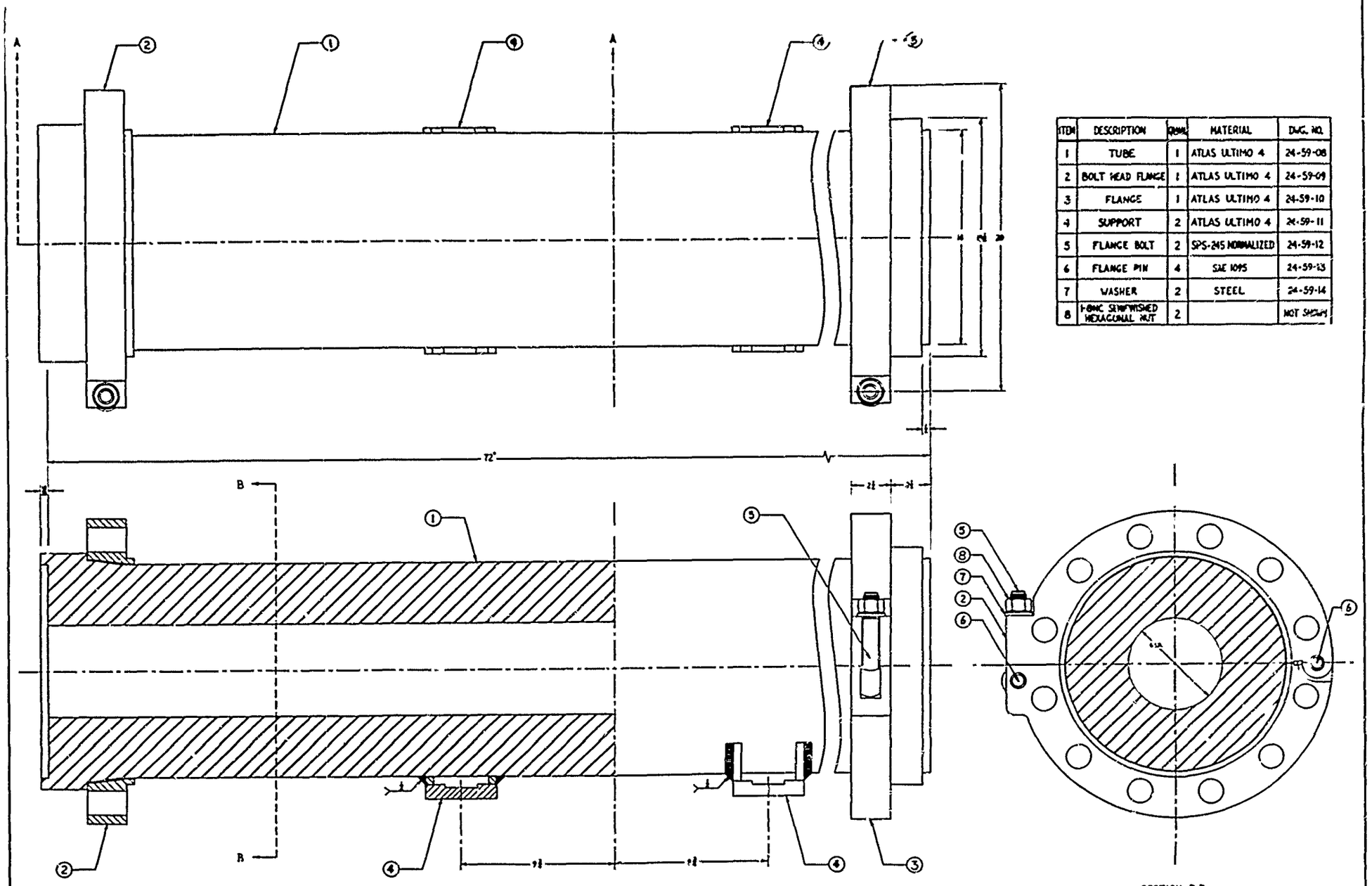

ITEM	DESCRIPTION	QUAN.	MATERIAL	DWG. NO.
1	TUBE	1	ATLAS ULTIMO 4	24-59-08
2	BOLT HEAD FLANGE	1	ATLAS ULTIMO 4	24-59-09
3	FLANGE	1	ATLAS ULTIMO 4	24-59-10
4	SUPPORT	2	ATLAS ULTIMO 4	24-59-11
5	FLANGE BOLT	2	SPS-245 NORMALIZED	24-59-12
6	FLANGE PIN	4	SAE 1095	24-59-13
7	WASHER	2	STEEL	24-59-14
8	1-8NC SEMI-FINISHED HEXAGONAL NUT	2		NOT SHOWN

FIG. 10 DESIGN OF DRIVER SECTION

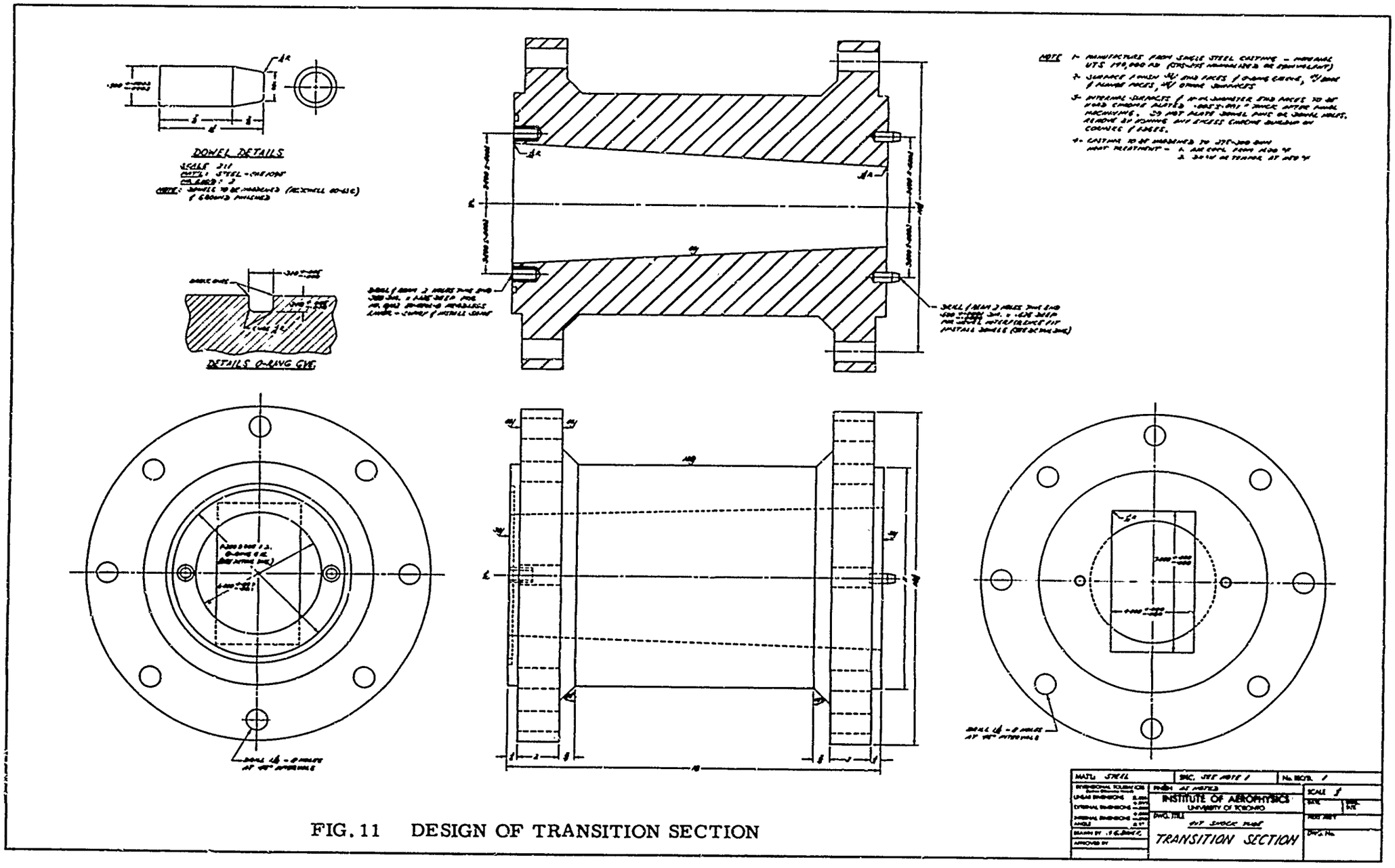

FIG. 11 DESIGN OF TRANSITION SECTION

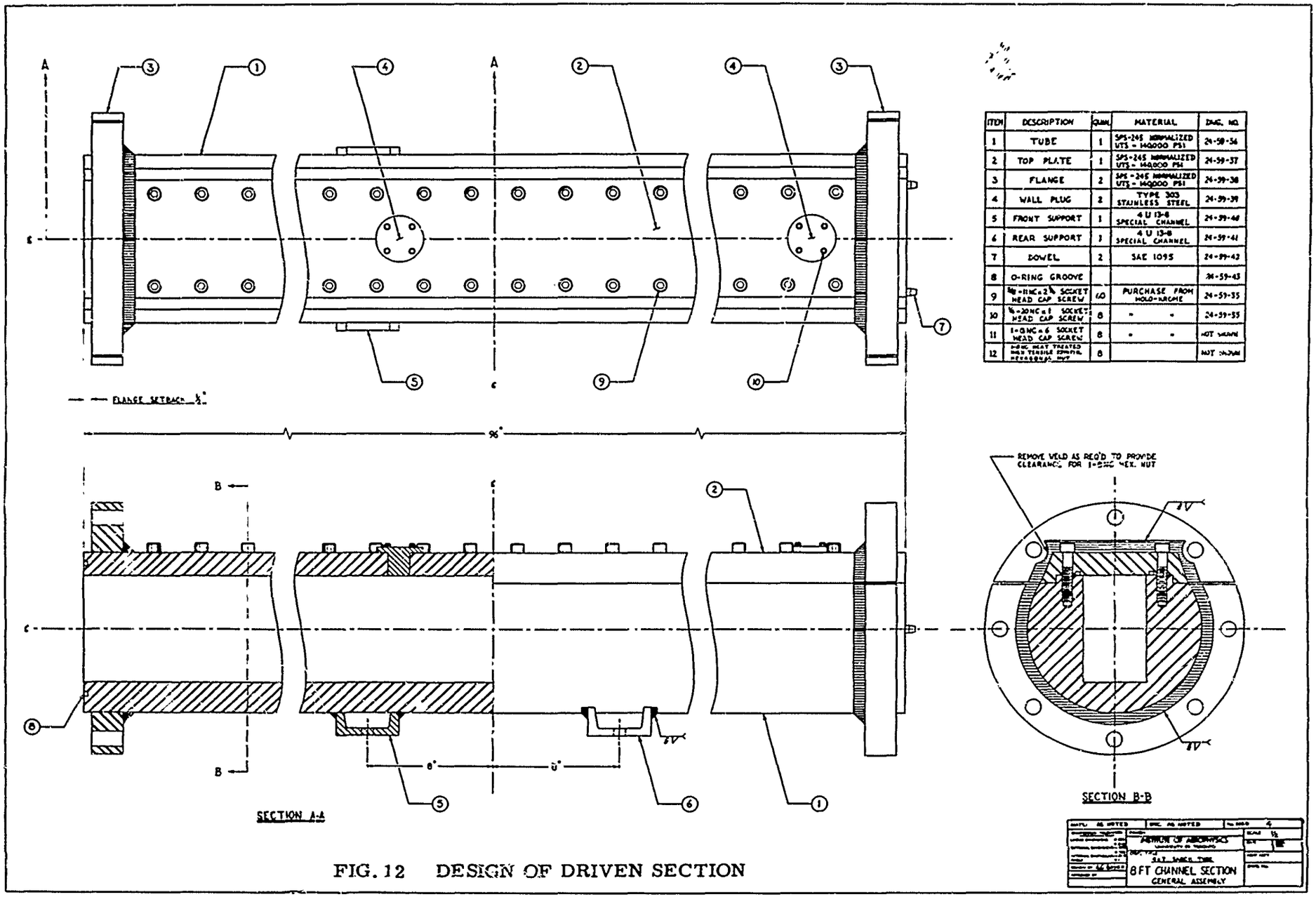

ITEM	DESCRIPTION	QUAN.	MATERIAL	DWG. NO.
1	TUBE	1	SPS-245 NORMALIZED UTS - 140000 PSI	24-59-36
2	TOP PLATE	1	SPS-245 NORMALIZED UTS - 140000 PSI	24-59-37
3	FLANGE	2	SPS-245 NORMALIZED UTS - 140000 PSI	24-59-38
4	WALL PLUG	2	TYPE 303 STAINLESS STEEL	24-59-39
5	FRONT SUPPORT	1	4 U 13-8 SPECIAL CHANNEL	24-59-40
6	REAR SUPPORT	1	4 U 13-8 SPECIAL CHANNEL	24-59-41
7	DOWEL	2	SAE 1095	24-59-42
8	O-RING GROOVE			24-59-43
9	⅝-11NC×2¼ SOCKET HEAD CAP SCREW	60	PURCHASE FROM HOLO-KROME	24-59-35
10	⅝-20NC×1 SOCKET HEAD CAP SCREW	8	" "	24-59-35
11	1-8NC×6 SOCKET HEAD CAP SCREW	8	" "	NOT SHOWN
12	1-8NC HEAT TREATED HIGH TENSILE COMMERCIAL HEXAGONAL NUT	8		NOT SHOWN

FIG. 12 DESIGN OF DRIVEN SECTION

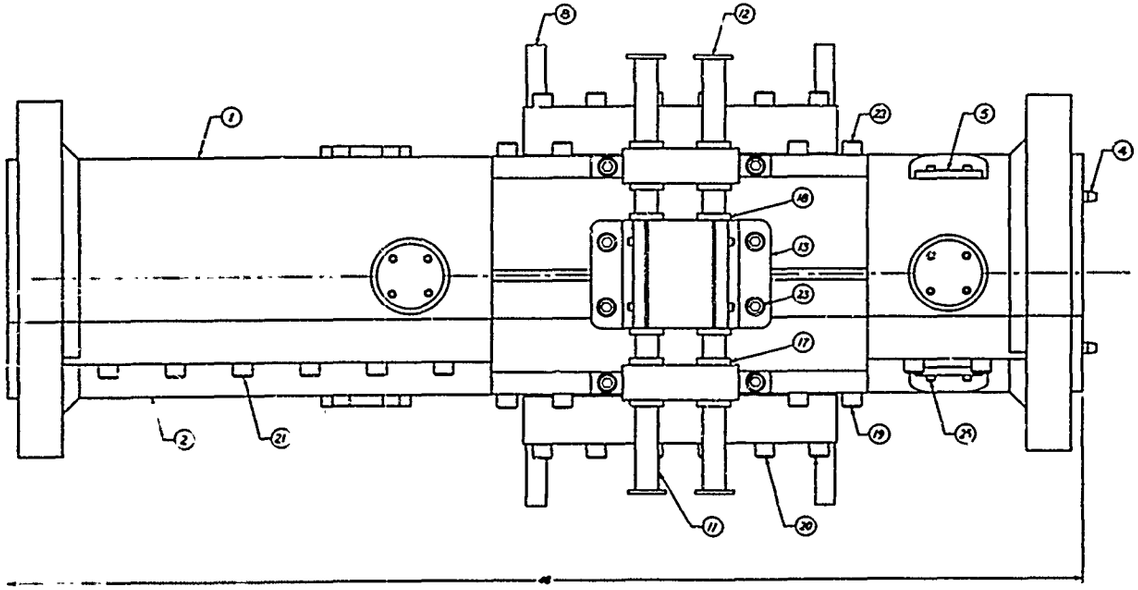

ITEM	DESCRIPTION	QUAN	MATERIAL	DWG. NO
1	TUBE	1	SPS-245 NORMALIZED	24-59-51
2	SIDE PLATE	1	SPS-245 NORMALIZED	24-59-52
3	FRONT SUPPORT	1	SPS-245 NORMALIZED	24-59-54
4	DOWEL	2	SAE 1095	24-59-55
5	WALL PLUG	4	SS TYPE 303	24-59-56
6	INNER FRAME	2	SPS-245 NORMALIZED	24-59-57
7	OUTER FRAME	2	SPS-245 NORMALIZED	24-59-58
8	FRAME HANDLE	4	STEEL	24-59-59
9	WINDOW	2	[illegible]	24-59-60
10	GASKET	4	[illegible]	24-59-61
11	BAR	2	SAE 1095	24-59-62
12	BAR STOP	4	STEEL	24-59-63
13	BAR SUPPORT	1	STEEL	24-59-64
14	FRAME SUPPORT	2	STEEL	24-59-65
15	SHOULDER BOLT	4	[illegible]	24-59-66
16	SPRING	4	[illegible]	NOT SHOWN
17	BALL BUSHING	4	[illegible]	24-59-50
18	ADJ. BALL BUSHING	4	[illegible]	•
19	[illegible]	12	PLANCK NON-FORME	•
20	[illegible]	36	•	•
21	[illegible]	16	•	•
22	[illegible]	20	•	•
23	[illegible]	4	•	
24	[illegible]	8	•	•
25	[illegible]	20	•	•
26	VERTICAL STRUT	1	SS TYPE 440C	24-59-67
27	HORIZONTAL STRUT	1	SS TYPE 440C	24-59-68
28	STRUT PLUG	1	SS TYPE 303	24-59-69
29	STIVE	3	SS TYPE 440C	24-59-70
30	PROBE PLUG	6	SS TYPE 303	24-59-71
31	IONIZATION PLUG	3	SS TYPE 303	24-59-72
32	PRESSURE PLUG	3	SS TYPE 303	24-59-73
33	VALVE PLUG	1	SS TYPE 303	24-59-74
34	SHIM	6	STEEL	24-59-75

NOTE - ITEMS 26-34 NOT SHOWN ON G/A

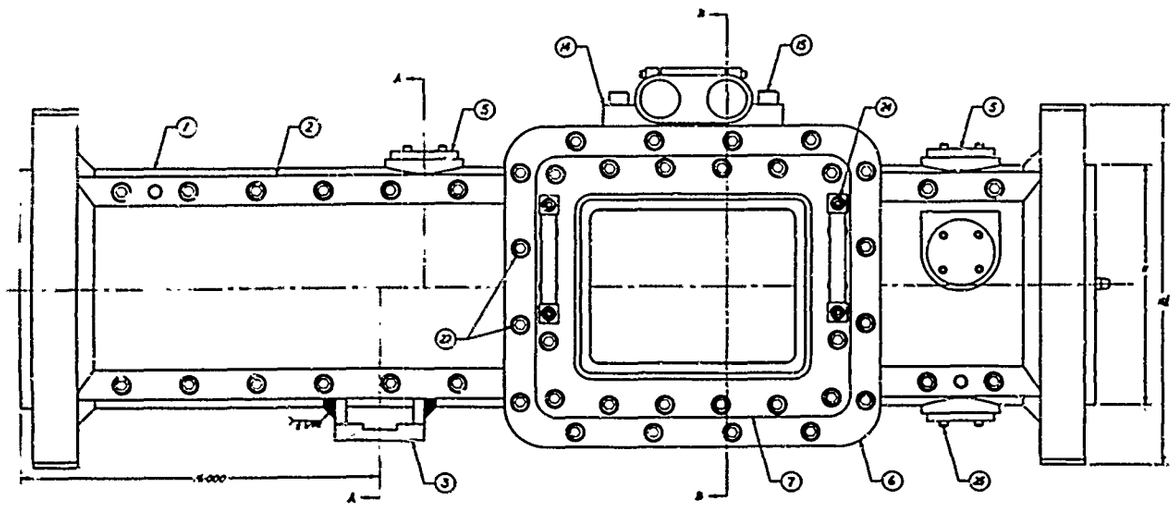

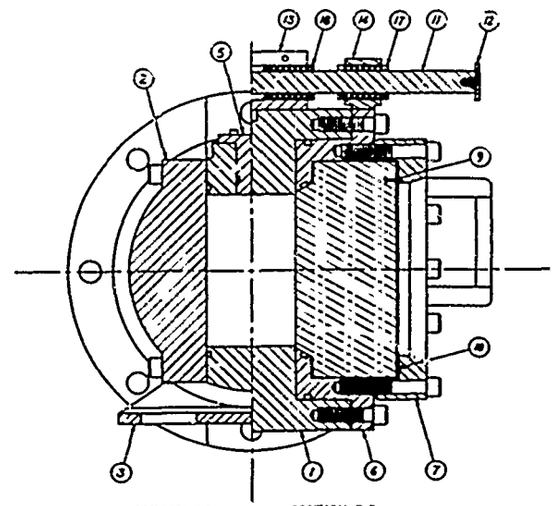

SECTION A-A

SECTION B-B

INSTITUTE OF AERONAUTICS
UNIVERSITY OF SYDNEY

TEST SECTION
GENERAL ASSEMBLY

FIG. 13 DESIGN OF TEST SECTION

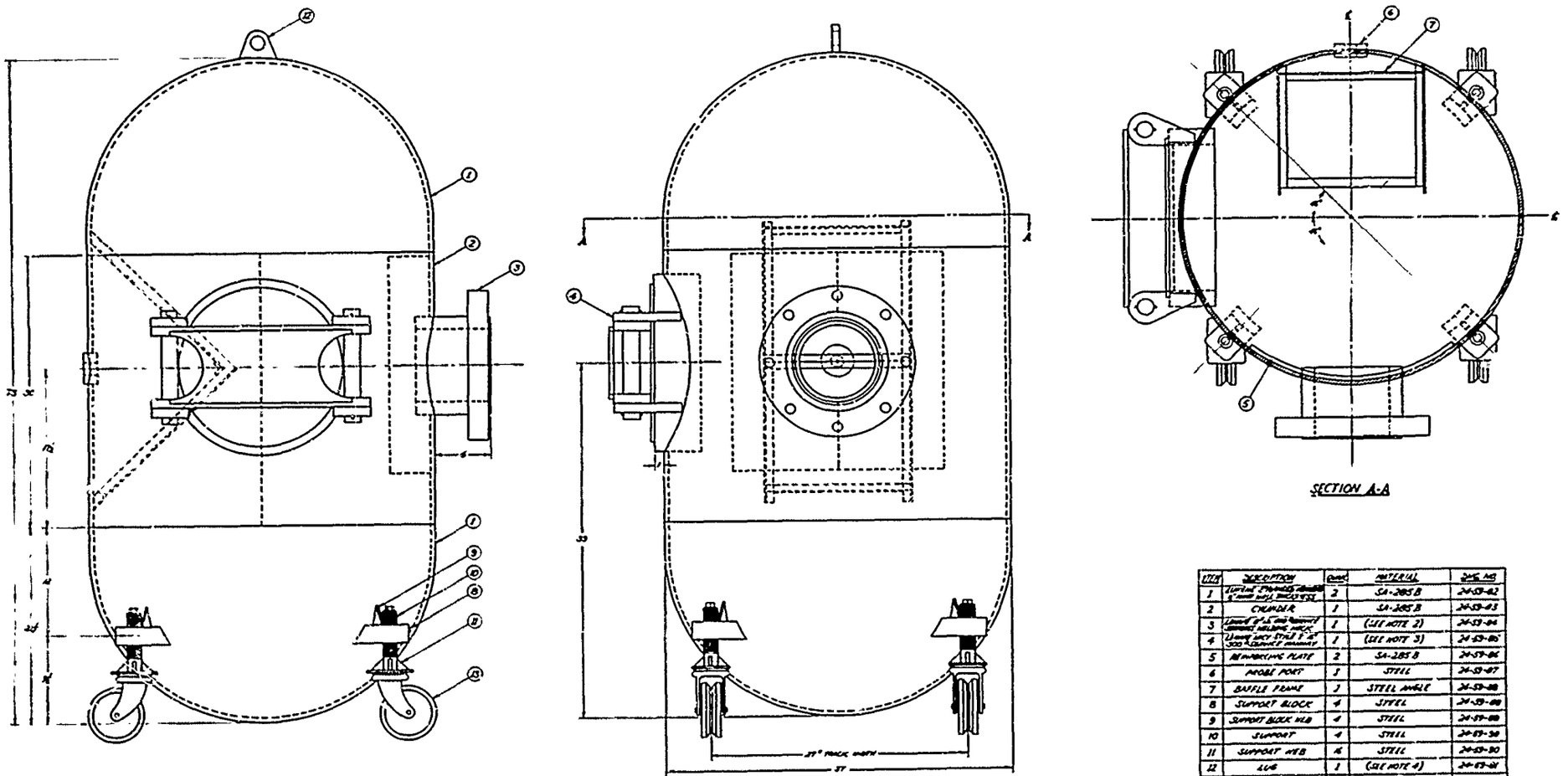

ITEM	DESCRIPTION	QUAN.	MATERIAL	DWG. NO.
1	[illegible]	2	SA-285 B	24-59-82
2	CHAMBER	1	SA-285 B	24-59-83
3	[illegible]	1	(SEE NOTE 2)	24-59-84
4	[illegible]	1	(SEE NOTE 3)	24-59-85
5	REINFORCING PLATE	2	SA-285 B	24-59-86
6	PROBE PORT	1	STEEL	24-59-87
7	BAFFLE FRAME	1	STEEL ANGLE	24-59-88
8	SUPPORT BLOCK	4	STEEL	24-59-89
9	SUPPORT BLOCK WEB	4	STEEL	24-59-89
10	SUPPORT	4	STEEL	24-59-90
11	SUPPORT WEB	4	STEEL	24-59-90
12	LUG	1	(SEE NOTE 4)	24-59-91
13	[illegible]	4		24-59-92
14	[illegible]	6		NOT SHOWN
15	[illegible]	6		NOT SHOWN

NOTES

1 - [illegible]

2 - [illegible]

3 - [illegible]

4 - [illegible]

5 - [illegible]

6 - [illegible]

7 - [illegible]

8 - [illegible]

FIG. 14 DESIGN OF DUMP TANK

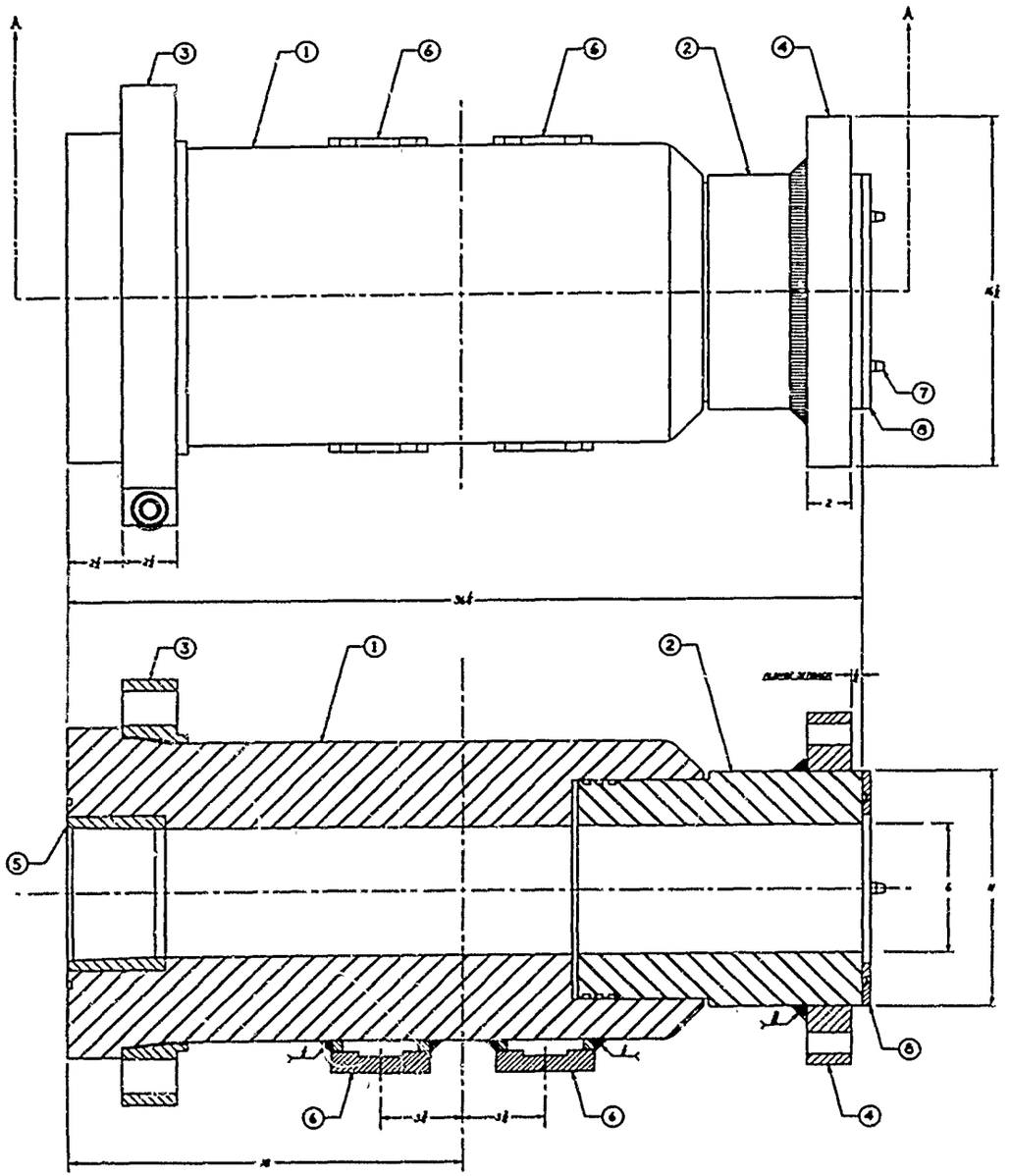

ITEM	DESCRIPTION	QUAN.	MATERIAL	DWG. NO.
1	TUBE	1	ATLAS ULTIMO 4	24-59-28
2	PISTON	1	ATLAS ULTIMO 4	24-59-29
3	BOLT HEAD FLANGE	1	ATLAS ULTIMO 4	24-59-09
4	FLANGE	1	ATLAS ULTIMO 4	24-59-30
5	LINER	1	TYPE 303 STAINLESS STEEL	24-59-31
6	SUPPORT	2	ATLAS ULTIMO 4	24-59-11
7	DOWEL	2	SAE 1095	24-59-32
8	PLATE	1	TYPE 303 STAINLESS STEEL	24-59-33
9	1-8NC×6½ SOCKET HEAD CAP SCREW	8	PURCHASE FROM HOLLRIDGE	NOT SHOWN
10	1-8NC HEAT-TREATED HIGH-TENSILE SERVICE HEX. NUT	8		NOT SHOWN

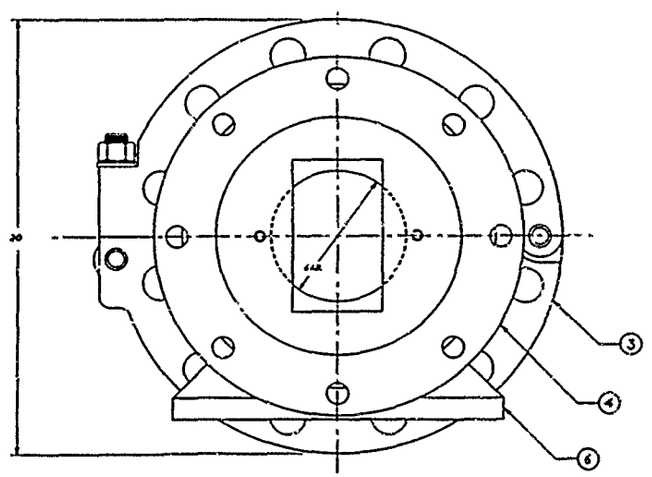

NOTE - ATLAS ULTIMO 4 MATERIAL TO BE HEAT TREATED AS BELOW UPON COMPLETION OF ALL MACHINING & WELDING:
QUENCHED & DRAWN
QUENCH TEMPERATURE 1000°F
BHN = 375,000 MIN

MATL. STEEL	DIST. AS NOTED	FIN. NOTE	
	DRAWN	SCALE	
	INSTITUTE OF AERONAUTICS UNIVERSITY OF MINNESOTA		
	DWG. NO. 4-X-2 SHOCK TUBE		
	DRIVER RECOIL SECTION GENERAL ASSEMBLY		

FIG. 15 DESIGN OF DRIVER RECOIL SECTION

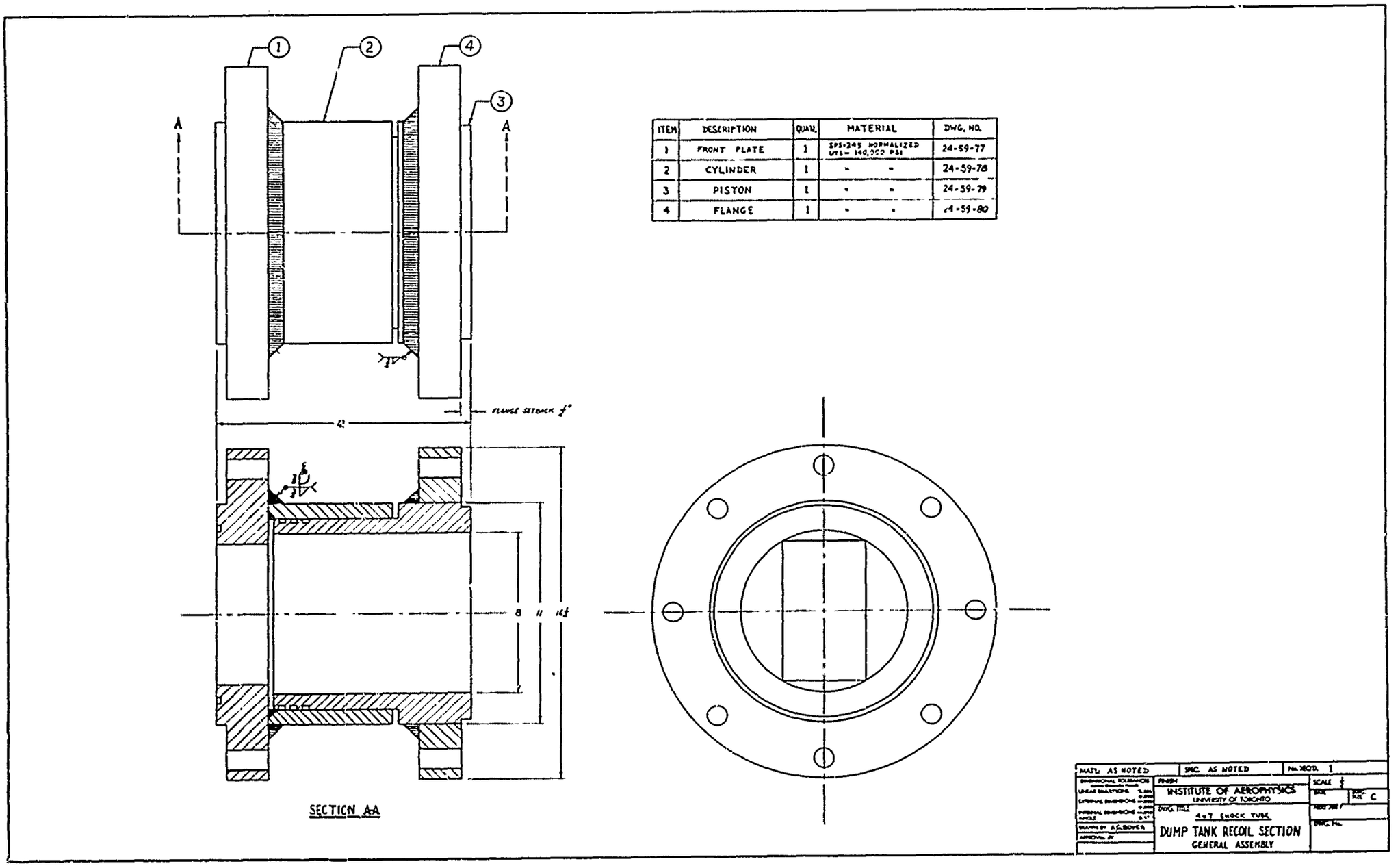

ITEM	DESCRIPTION	QUAN.	MATERIAL	DWG. NO.
1	FRONT PLATE	1	SPS-245 NORMALIZED UTS = 140,000 PSI	24-59-77
2	CYLINDER	1	" "	24-59-78
3	PISTON	1	" "	24-59-79
4	FLANGE	1	" "	24-59-80

FIG. 16 DESIGN OF DUMP TANK RECOIL SECTION

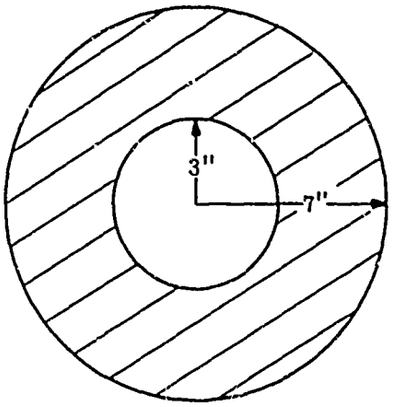

(a) SINGLE CYLINDER
P_{yield} = 61,200 PSI

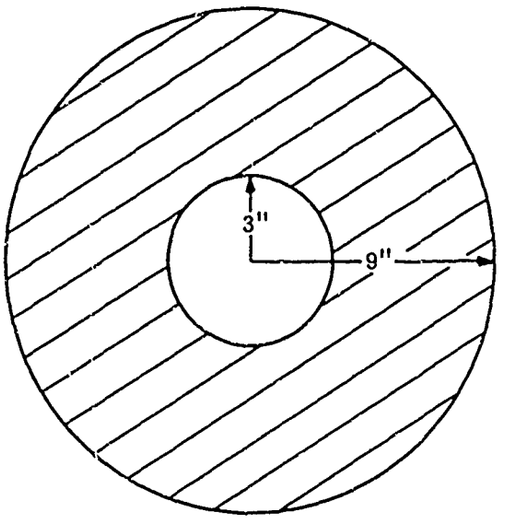

(b) SINGLE CYLINDER
P_{yield} = 66,600 PSI

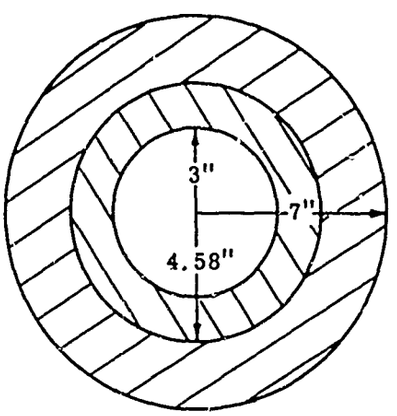

(c) DOUBLE CYLINDER
SHRINKING PRESSURE = 1/5 P_{yield}
P_{yield} = 85,000 PSI

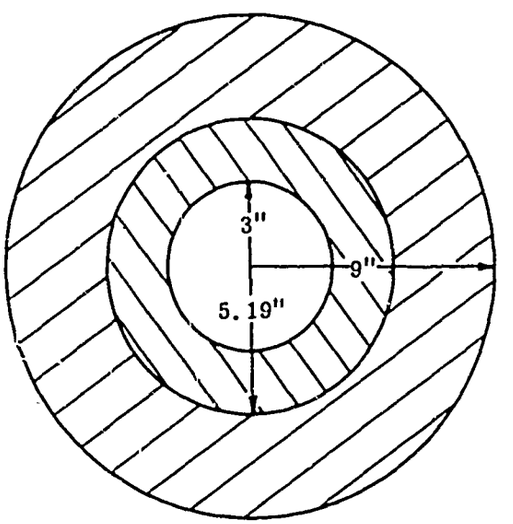

(d) DOUBLE CYLINDER
SHRINKING PRESSURE = 1/4 P_{yield}
P_{yield} = 100,000 PSI

FIG. 17 CONSTRUCTION METHODS FOR DRIVER SECTION
(Yield pressures indicated for Atlas Ultimo-4 material)

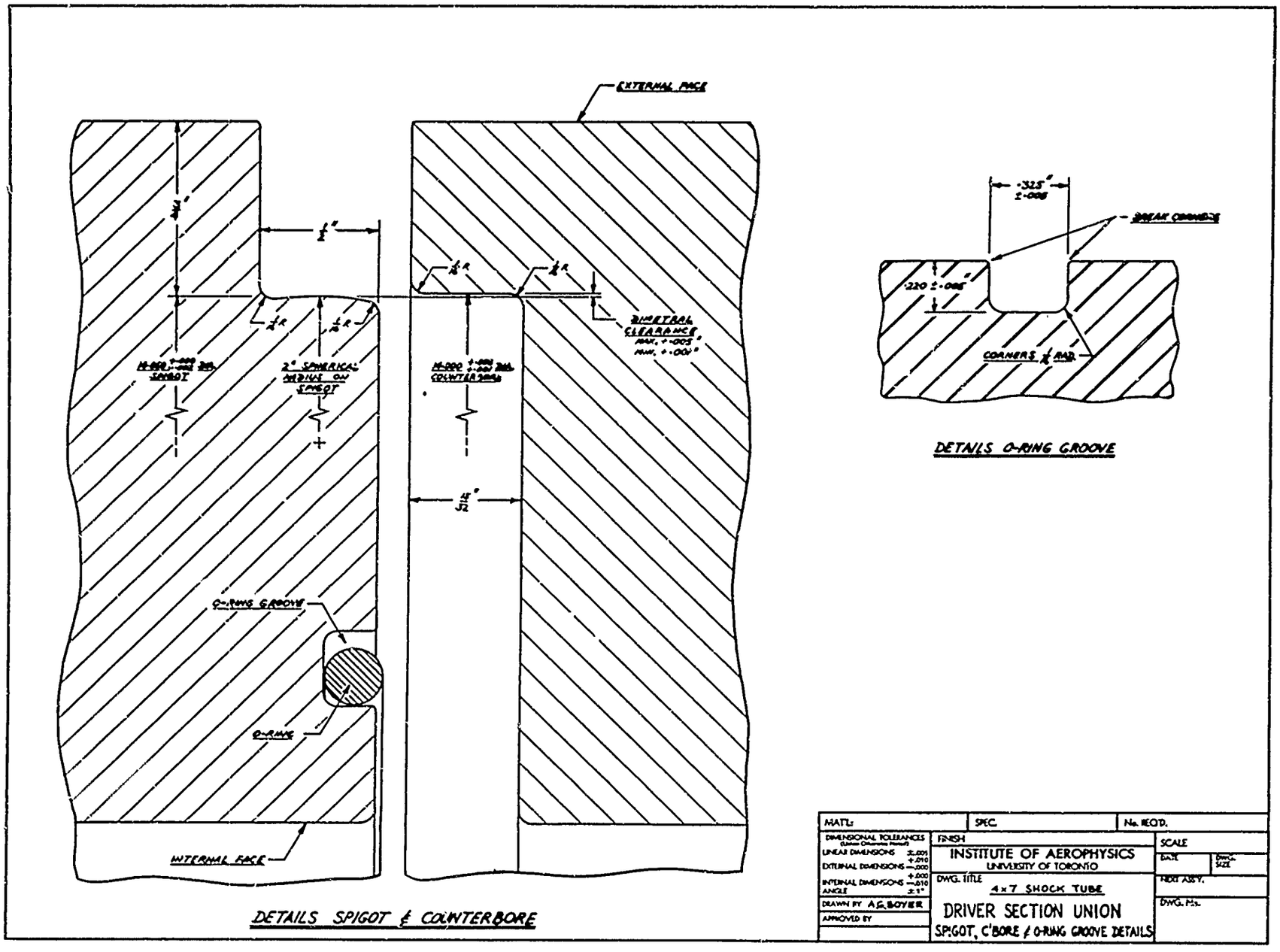

FIG. 18 DESIGN DETAILS OF DRIVER COUPLING

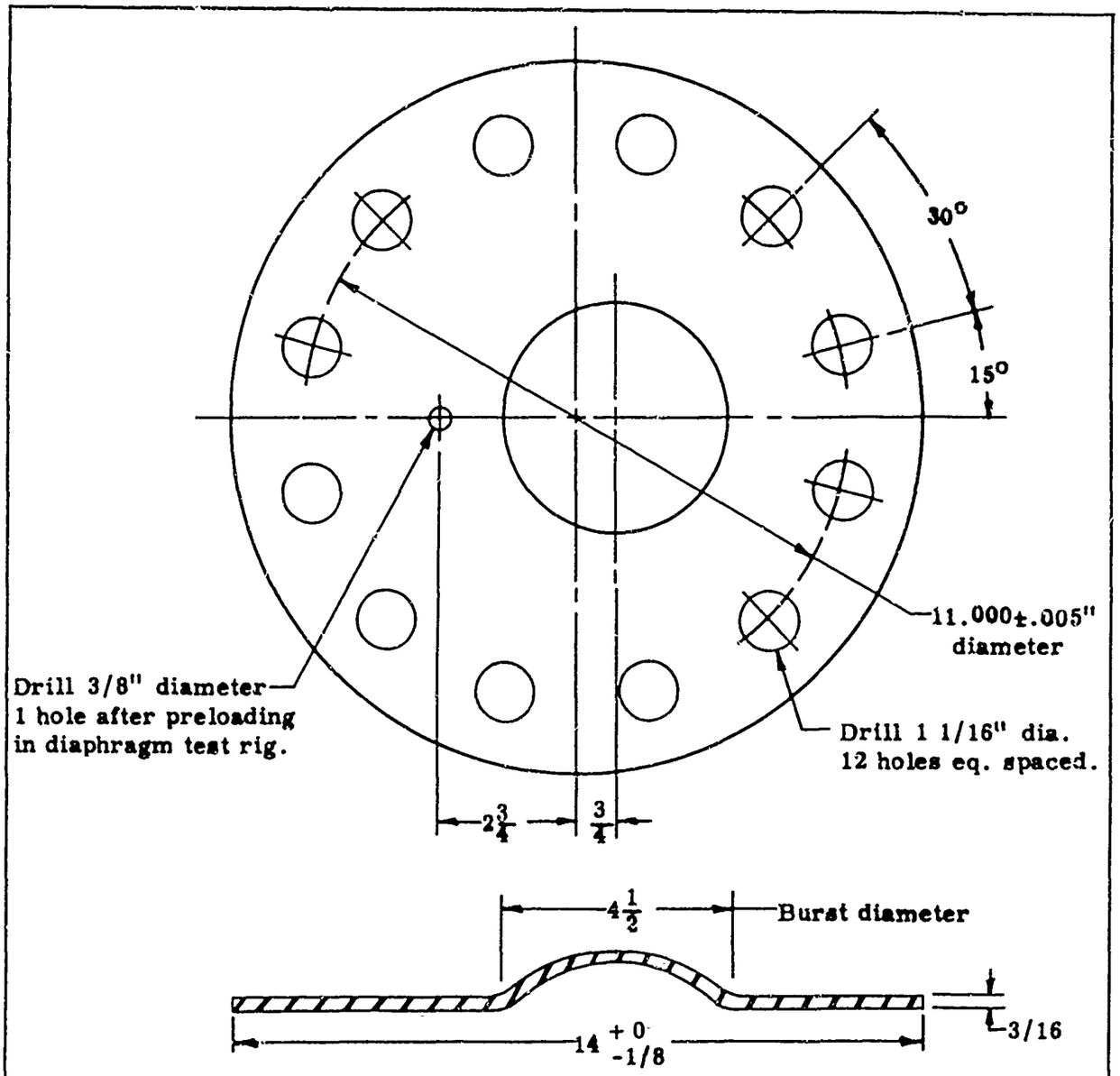

Note : Rupture disc burst pressure to be 14,000 psi minimum to 15,500 psi maximum at 72 °F.

MAT'L: Stainless Steel	SPEC. Type 302	No. REQ'D.
DIMENSIONAL TOLERANCES (Unless Otherwise Noted) LINEAR DIMENSIONS ±.080	FINISH	SCALE 1/3
	INSTITUTE OF AEROPHYSICS UNIVERSITY OF TORONTO	DATE / DWG. SIZE
ANGLE ±1°	DWG. TITLE 4 x 7 Shock Tube	NEXT ASS'Y.
DRAWN BY A.G. Boyer	DRIVER RUPTURE DISC	DWG. No.
APPROVED BY		

FIG. 19 DESIGN OF DRIVER RUPTURE DISC

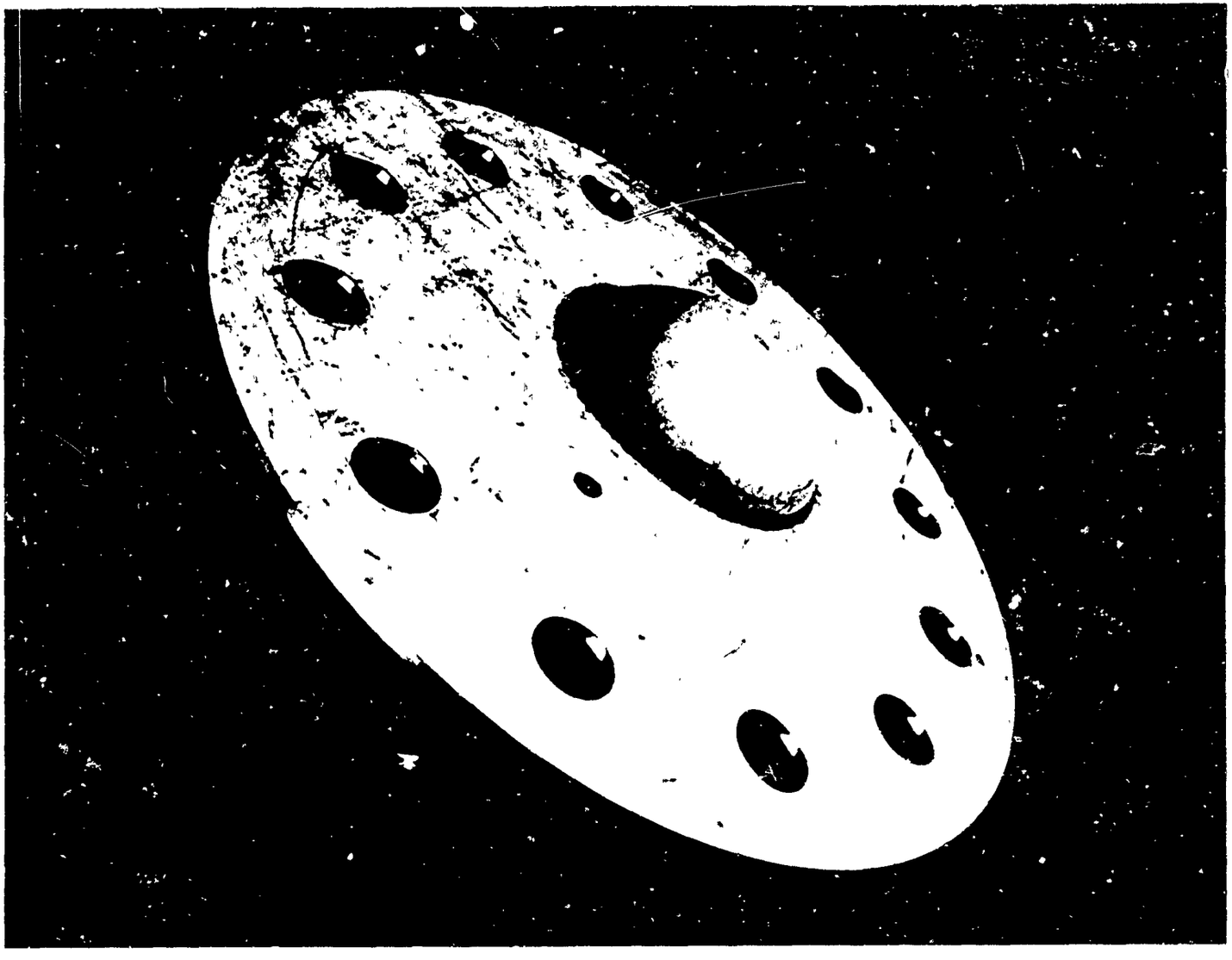

FIG. 20 DRIVER RUPTURE DISC

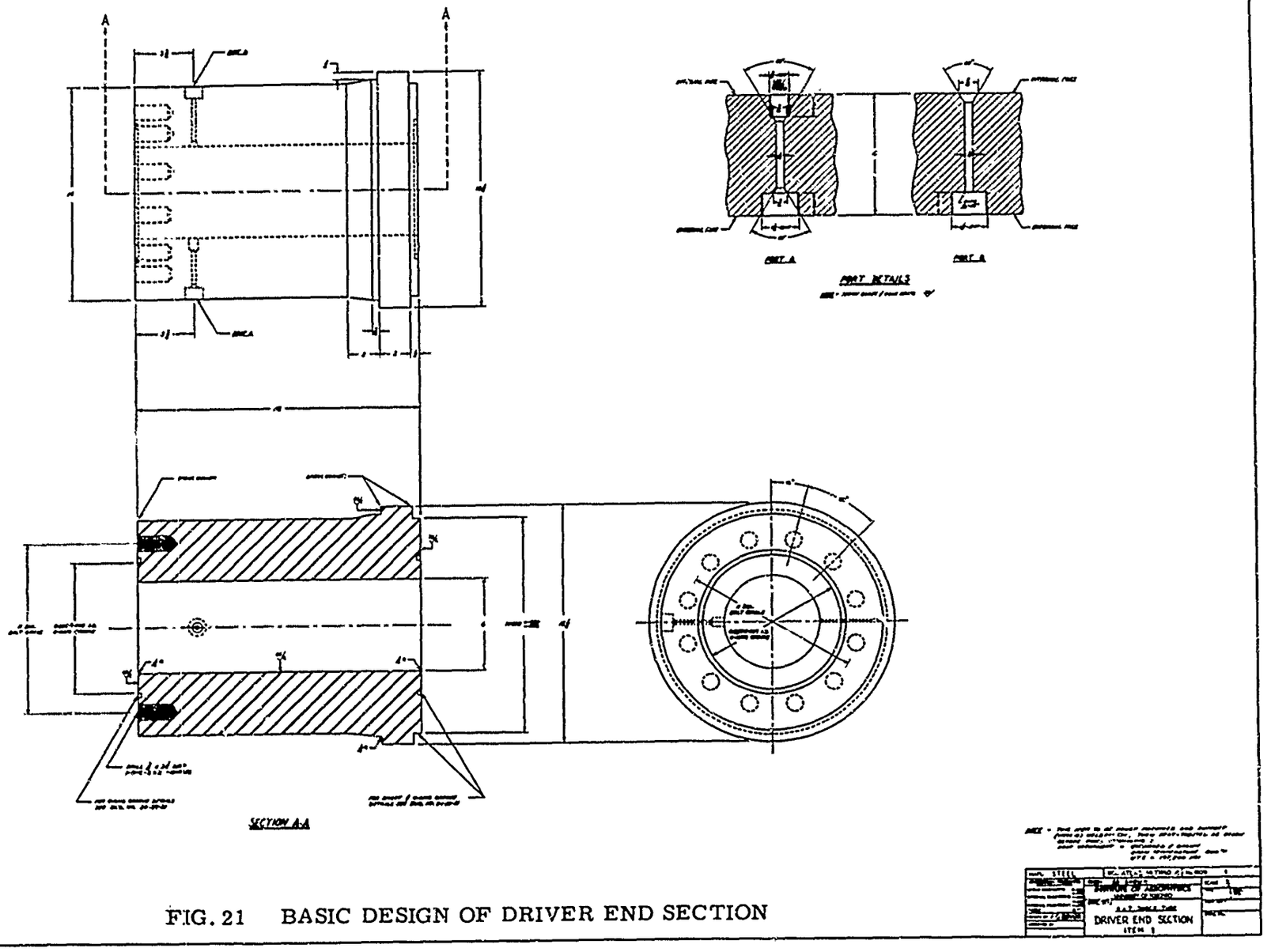

FIG. 21 BASIC DESIGN OF DRIVER END SECTION

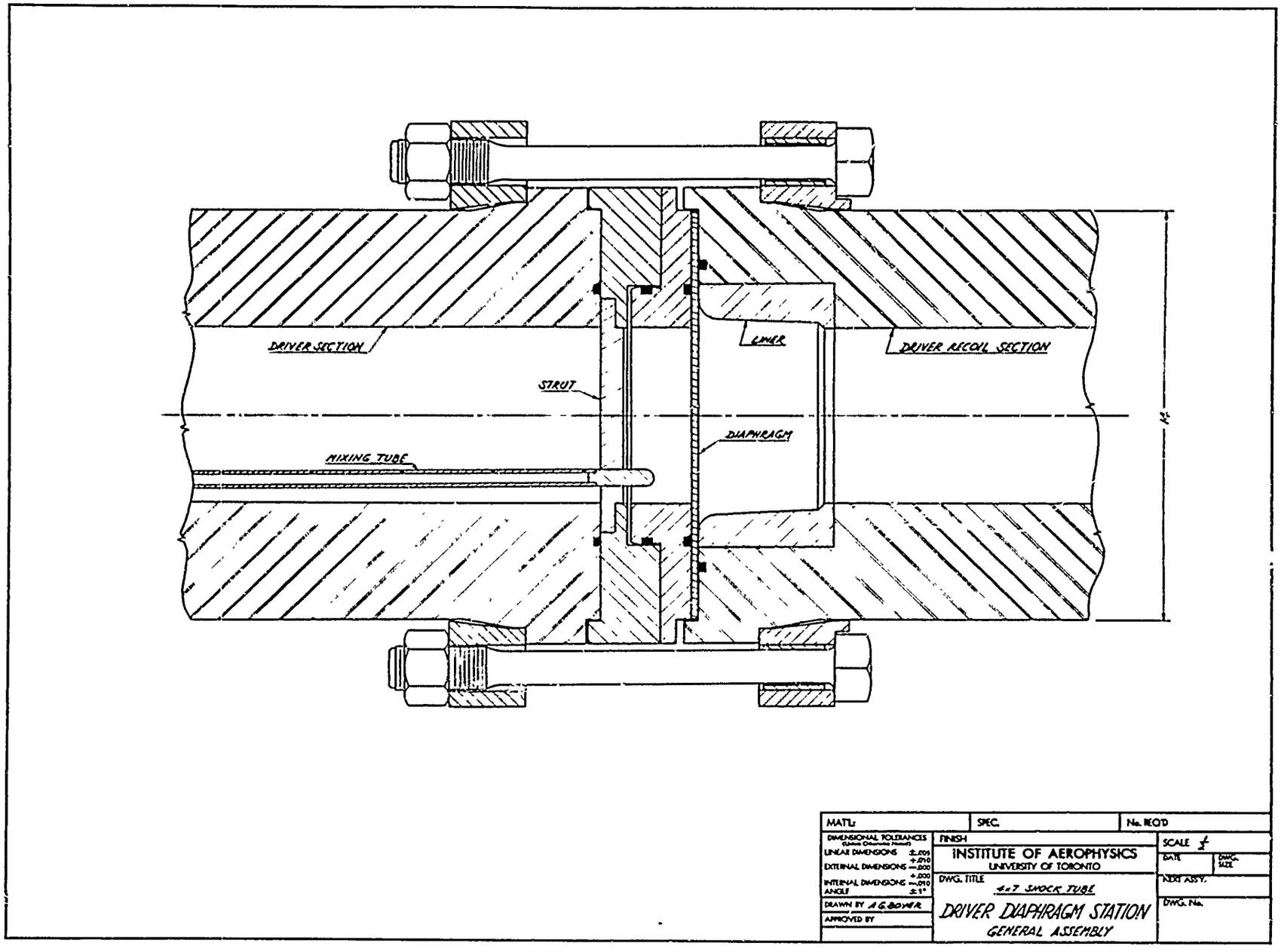

FIG. 22 DRIVER DIAPHRAGM STATION

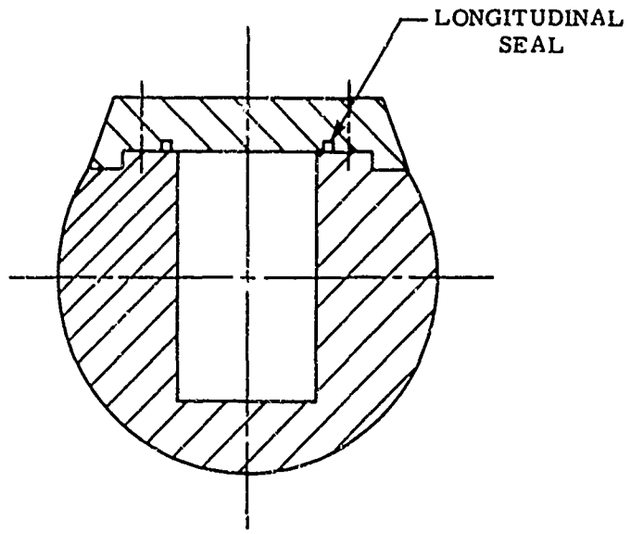

(a) SLOT MACHINED FROM SOLID STOCK

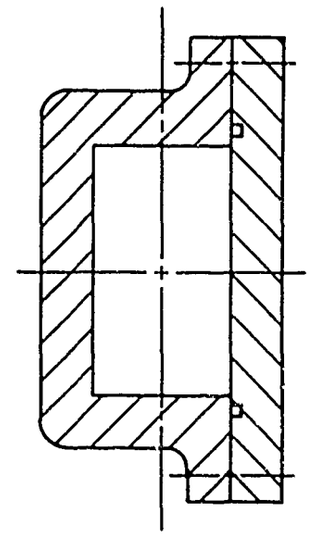

(b) CAST CONSTRUCTION

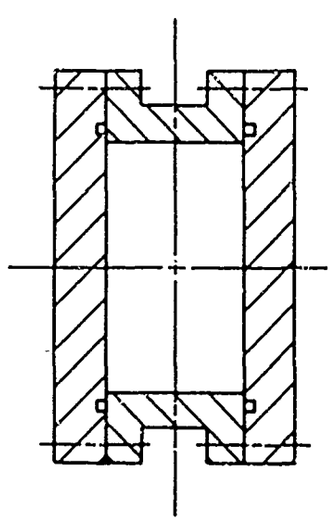

(c) FOUR PLATE CONSTRUCTION

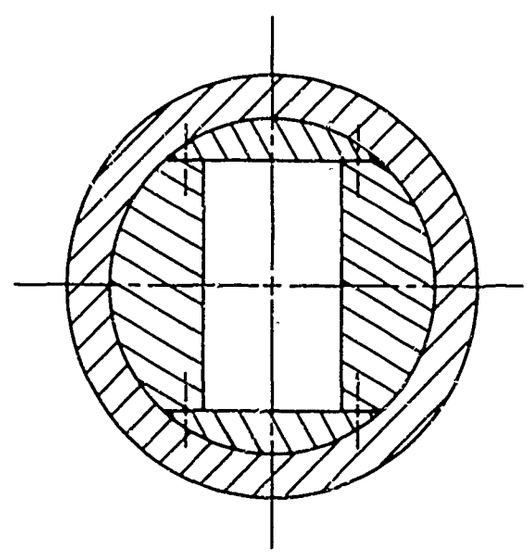

(d) INSERT METHOD OF CONSTRUCTION

FIG. 23 CONSTRUCTION METHODS FOR DRIVEN SECTION

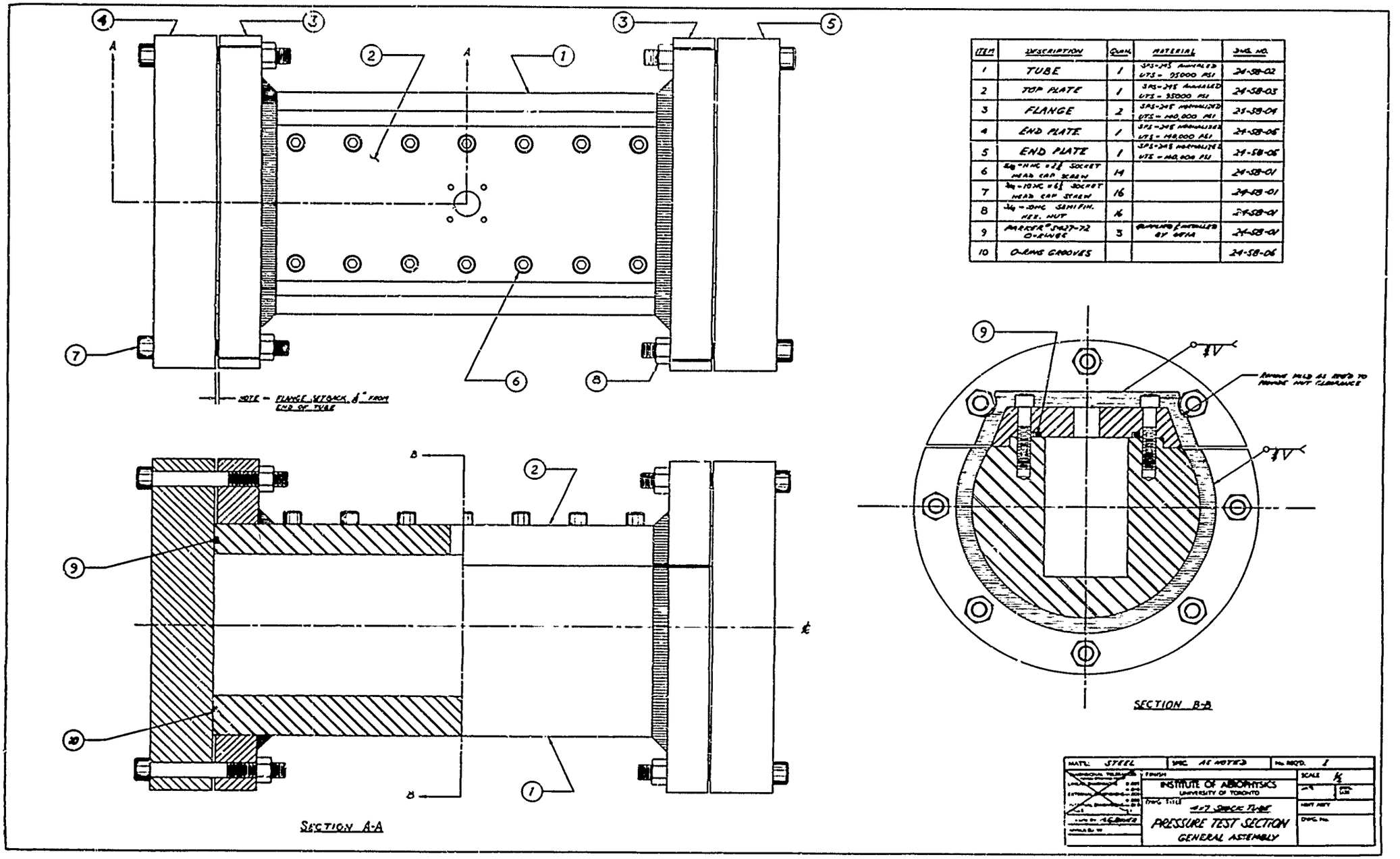

ITEM	DESCRIPTION	QUAN.	MATERIAL	DWG. NO.
1	TUBE	1	SAE-245 ANNEALED UTS - 95000 PSI	24-58-02
2	TOP PLATE	1	SAE-245 ANNEALED UTS - 95000 PSI	24-58-03
3	FLANGE	2	SAE-245 NORMALIZED UTS - 140,000 PSI	24-58-04
4	END PLATE	1	SAE-245 NORMALIZED UTS - 140,000 PSI	24-58-05
5	END PLATE	1	SAE-245 NORMALIZED UTS - 140,000 PSI	24-58-05
6	5/8-11NC x 2 1/2 SOCKET HEAD CAP SCREW	14		24-58-01
7	3/4-10NC x 6 1/2 SOCKET HEAD CAP SCREW	16		24-58-01
8	3/4-10NC SEMI FIN. HEX. NUT	16		24-58-01
9	PARKER 2-237-72 O-RINGS	3	[illegible] BY GMA	24-58-01
10	O-RING GROOVES			24-58-06

FIG. 24 DESIGN OF DRIVEN PRESSURE TEST SECTION

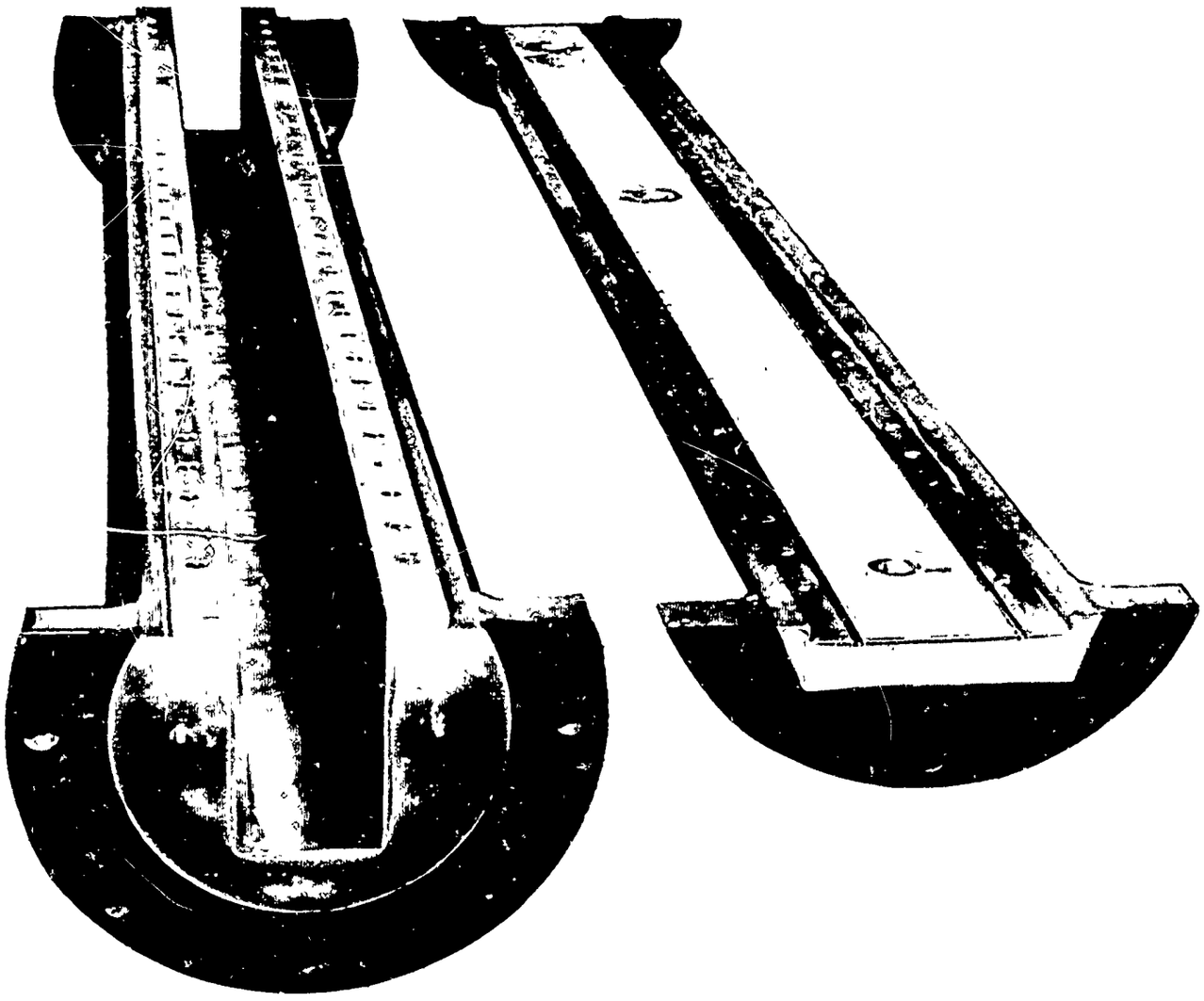

FIG. 25 CONSTRUCTION DETAILS OF DRIVEN SECTION

FIG. 26 CONSTRUCTION DETAILS OF DRIVEN SECTION SHOWING SEALING GROOVES

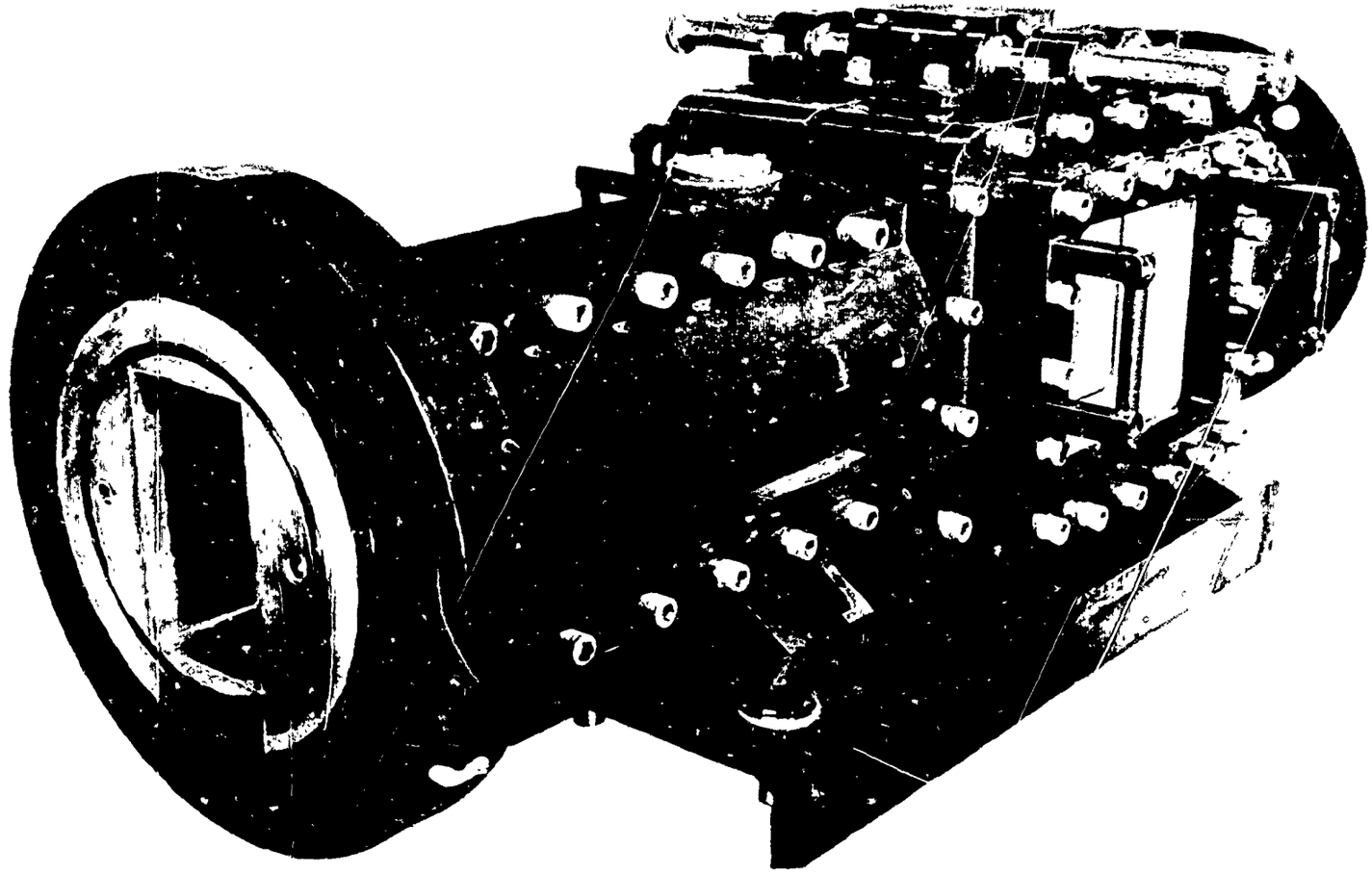

FIG. 27 VIEW OF TEST SECTION

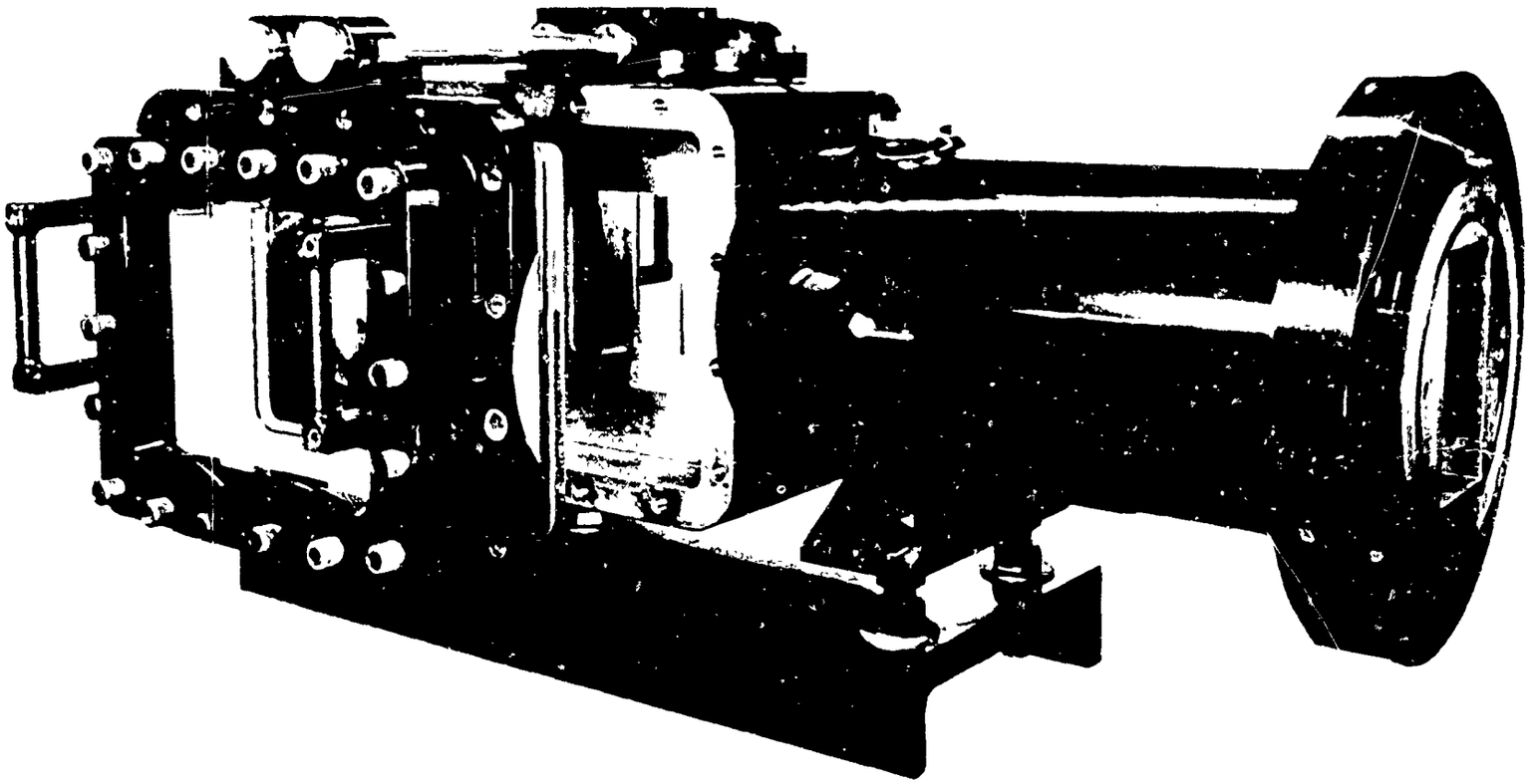

FIG. 28 VIEW OF TEST SECTION WITH WINDOW FRAME EXTENDED

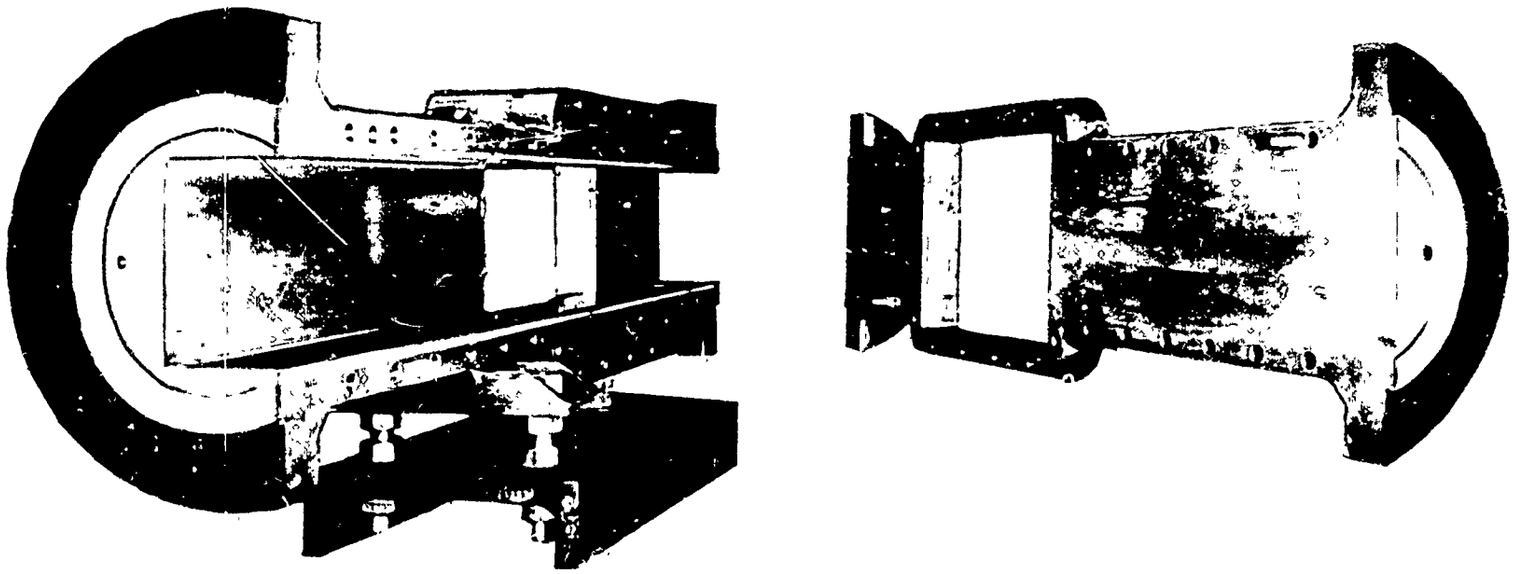

FIG. 29 CONSTRUCTION DETAILS OF TEST SECTION

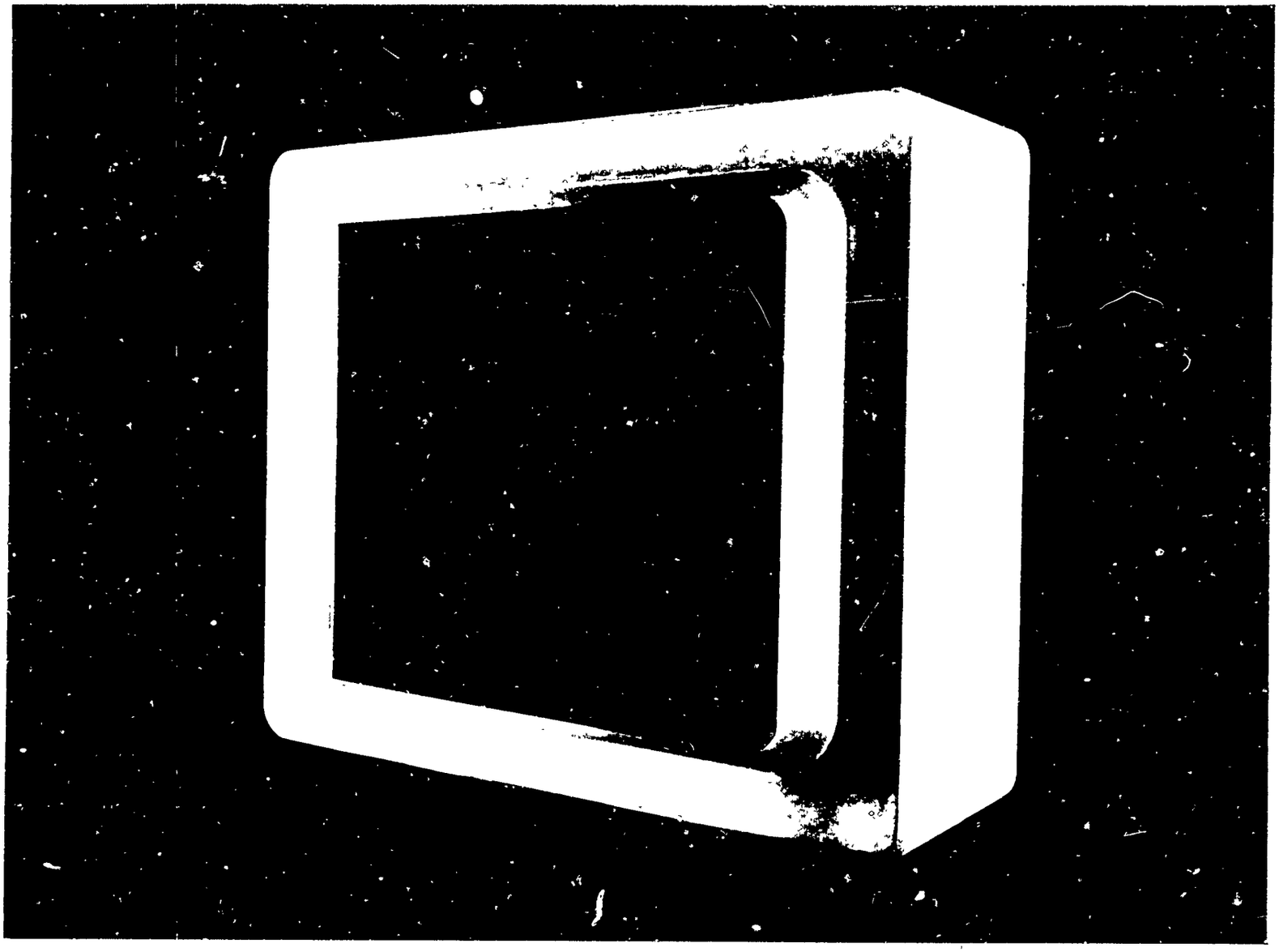

FIG. 30 TEST SECTION WINDOW

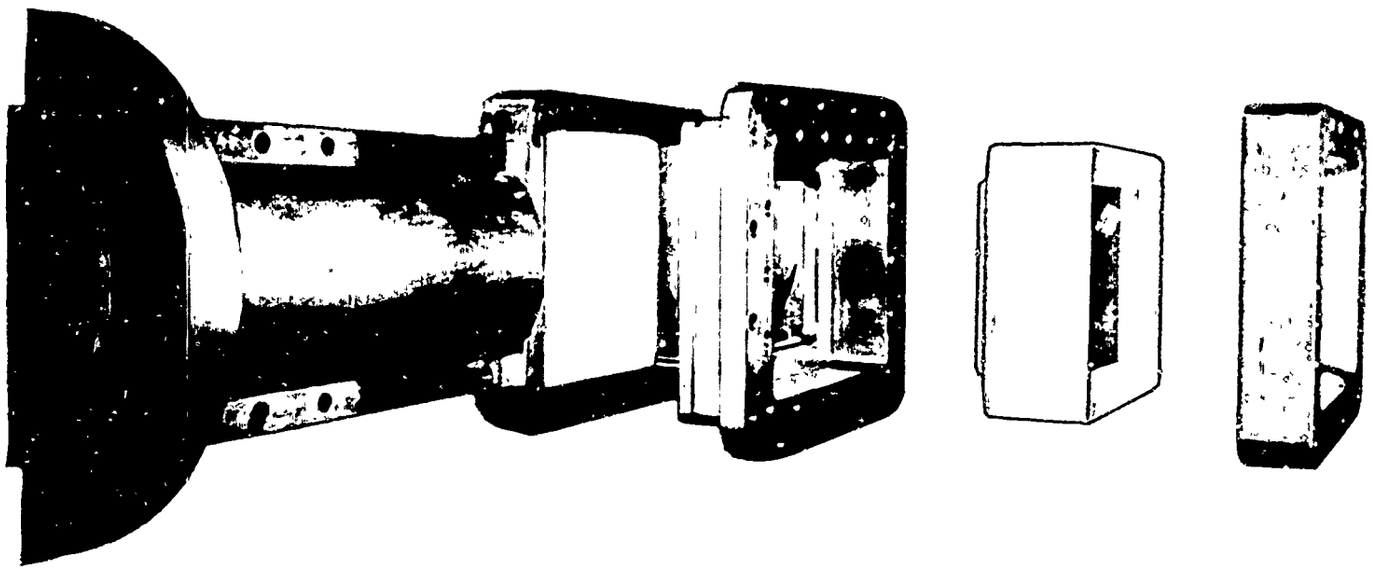

FIG. 31 EXPLODED VIEW OF TEST SECTION SIDE PLATE WINDOW FRAME ASSEMBLY

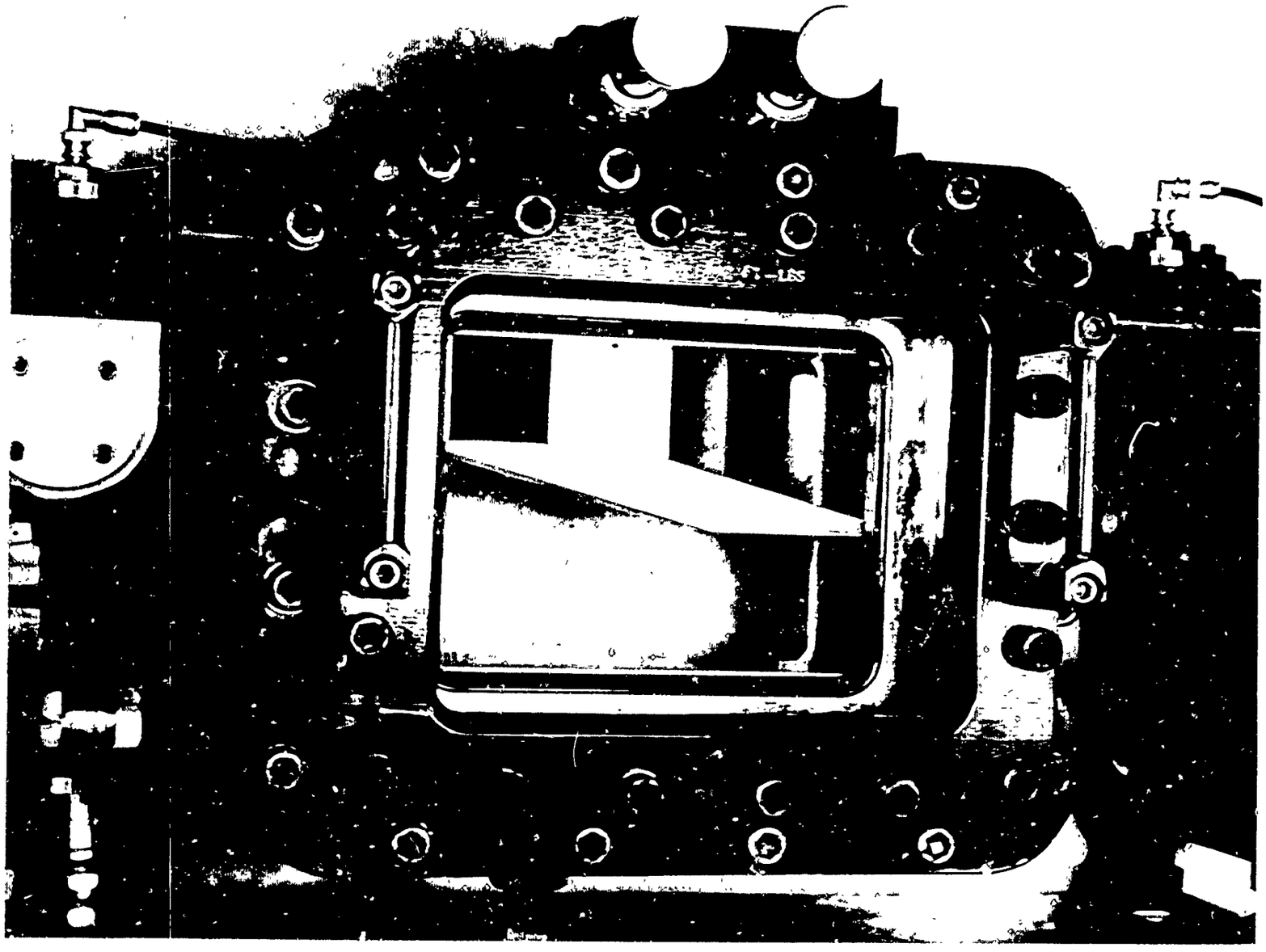

FIG. 32 DOUBLE-WEDGE TYPE EXPANSION MODEL MOUNTED IN TEST SECTION

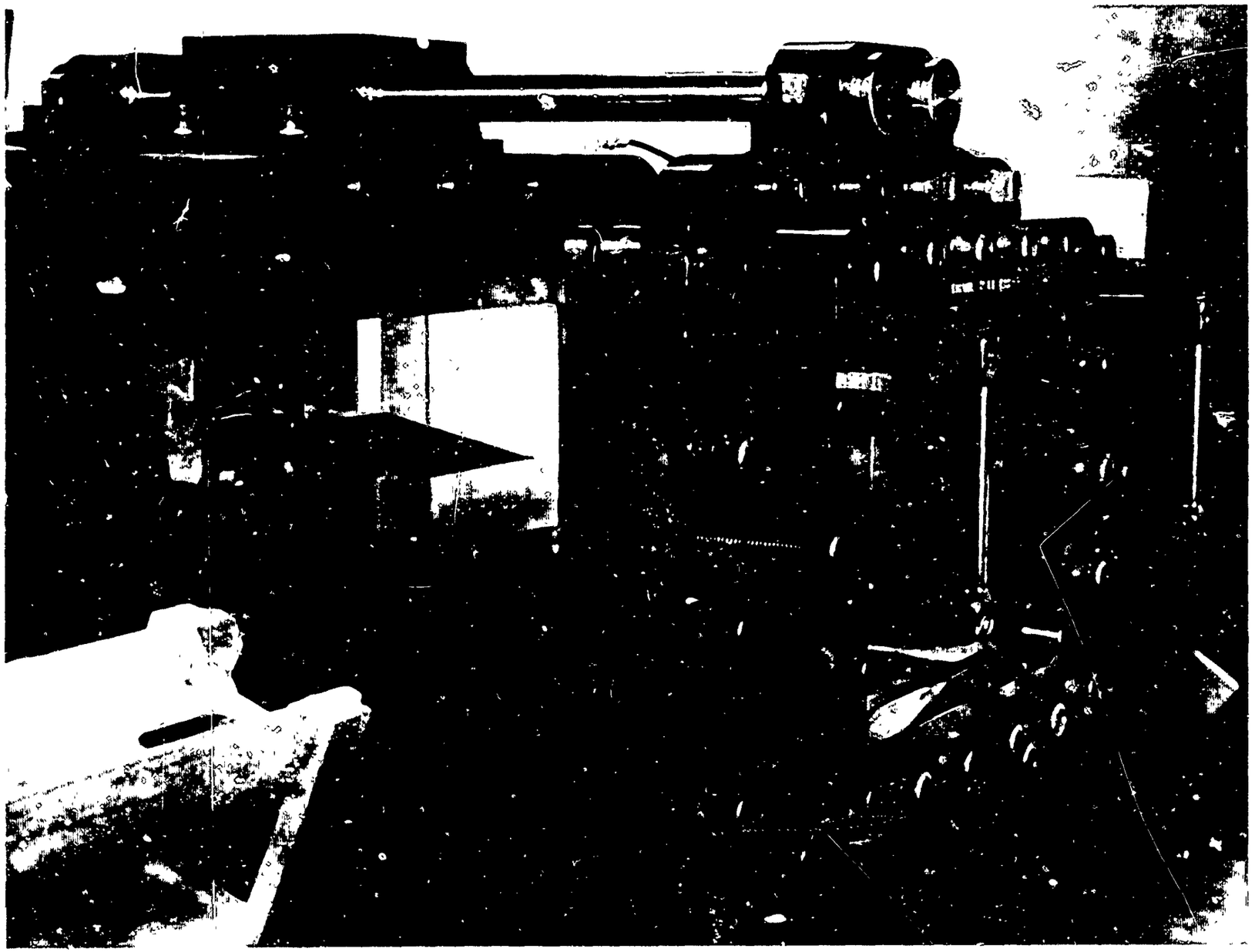

FIG. 33 TEST SECTION WINDOW FRAME EXTENDED TO PROVIDE ACCESS TO EXPANSION MODEL

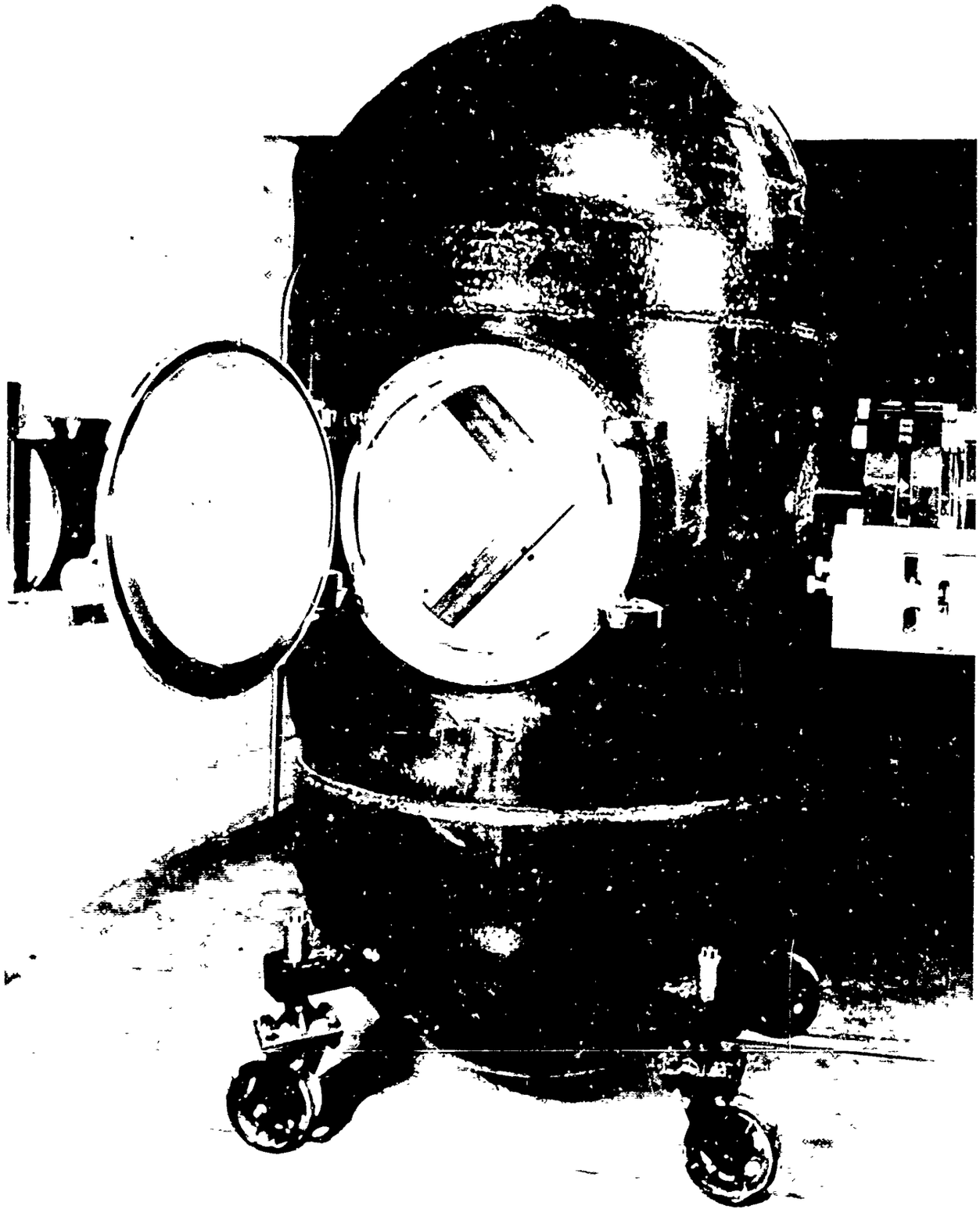

FIG. 34 VIEW OF DUMP TANK

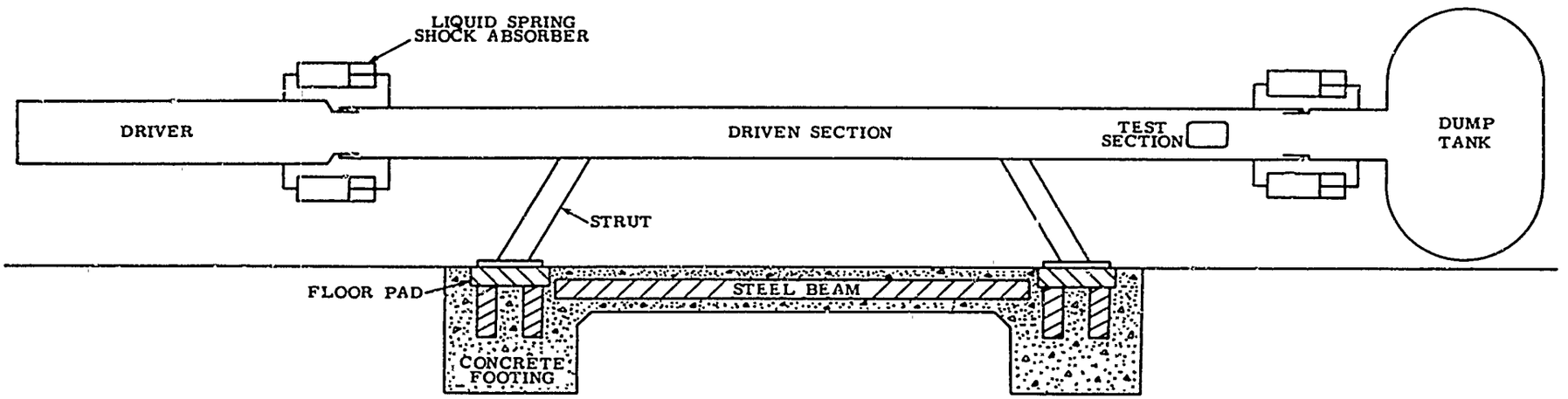

FIG. 35 SCHEMATIC OF RECOIL SYSTEM

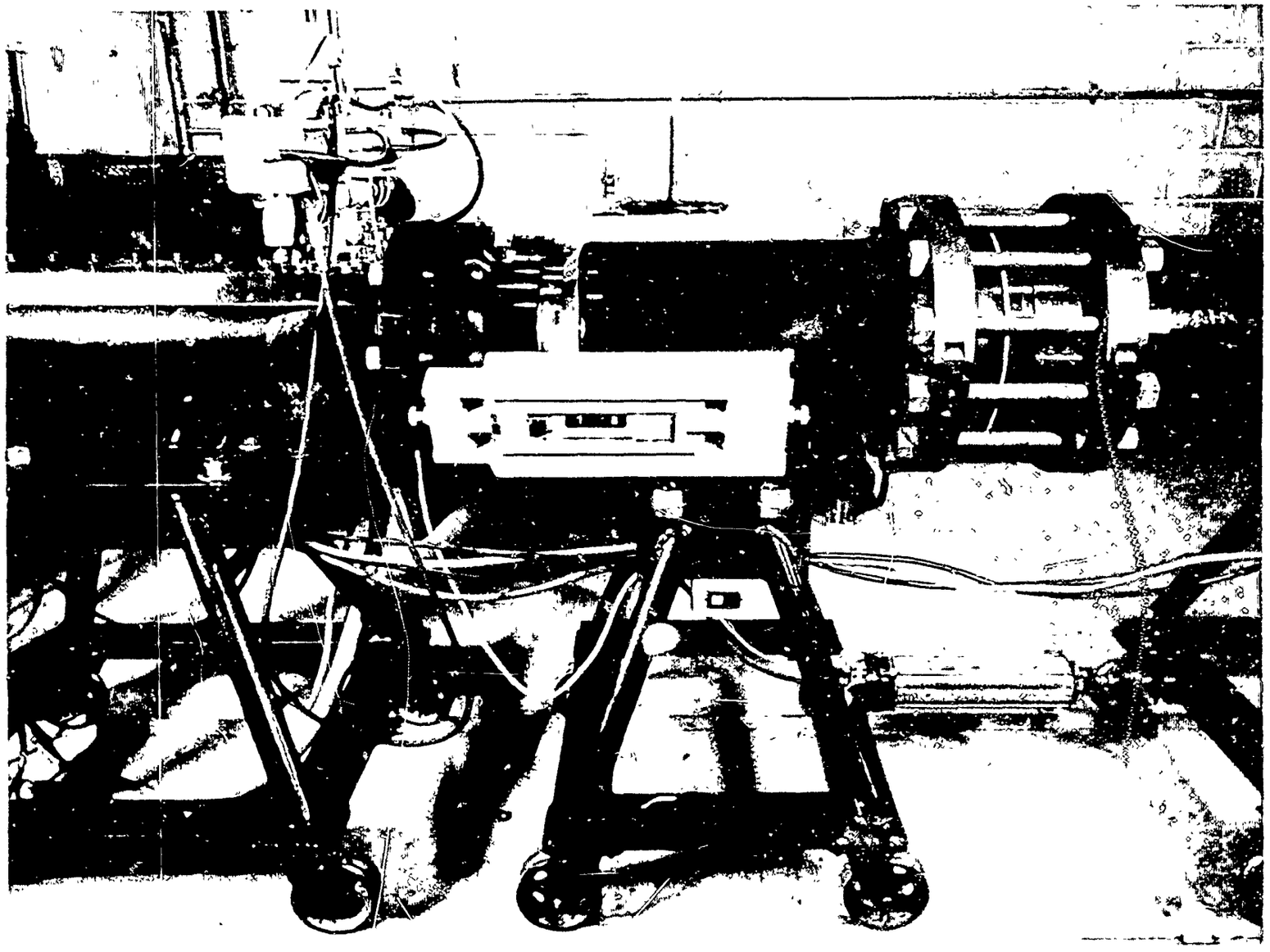

FIG. 36 VIEW OF DRIVER RECOIL SECTION

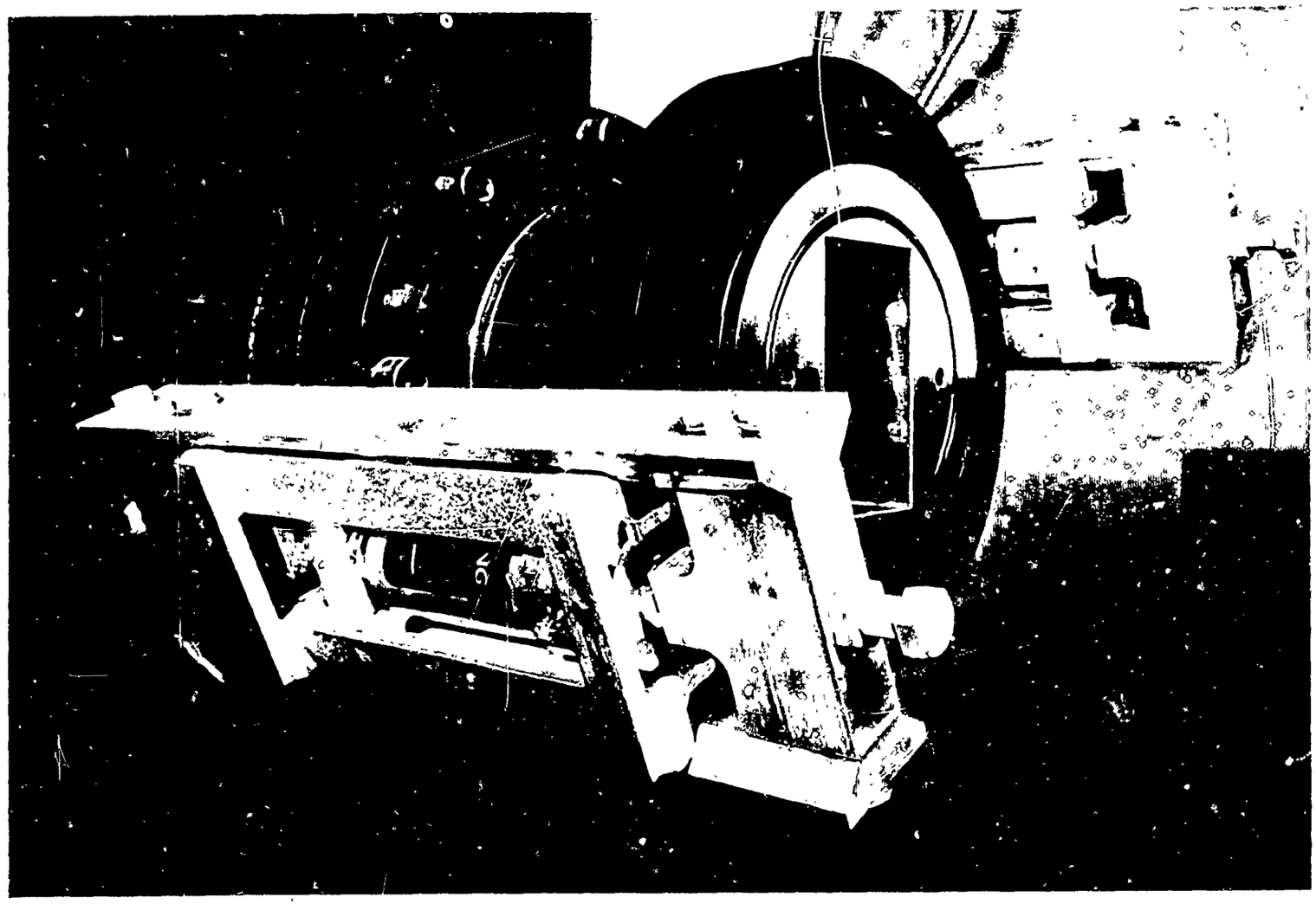

FIG. 37 VIEW OF DUMP TANK RECOIL SECTION

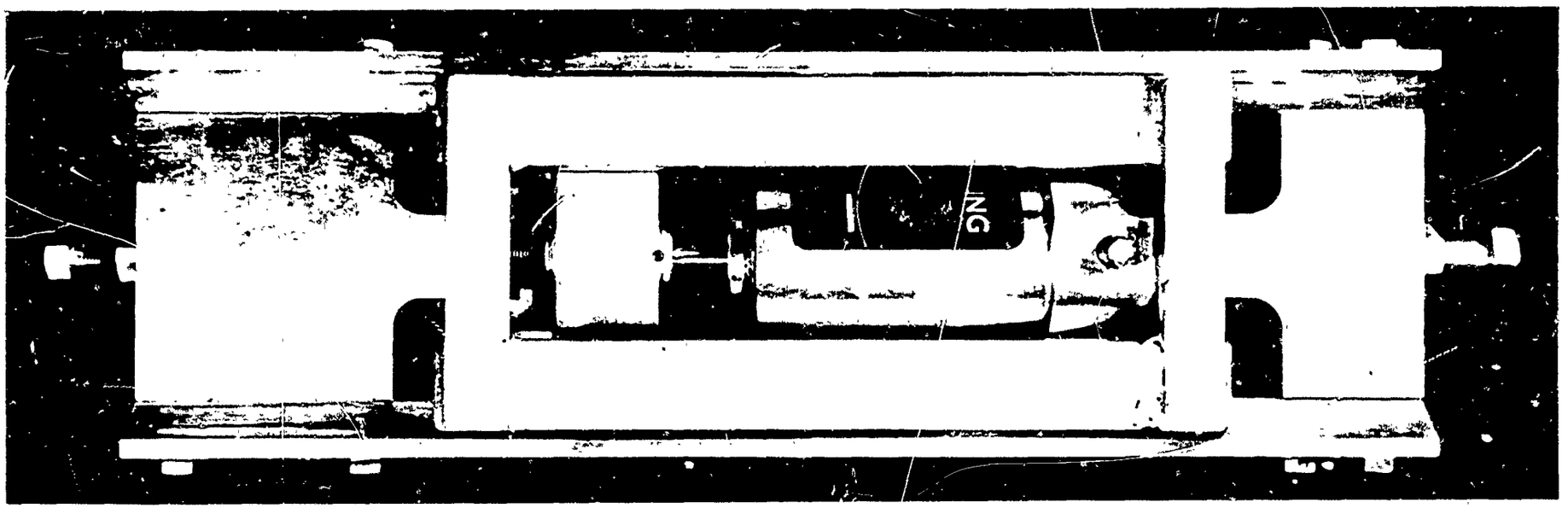

FIG. 38 LIQUID SPRING SHOCK ABSORBER AND CRADLE

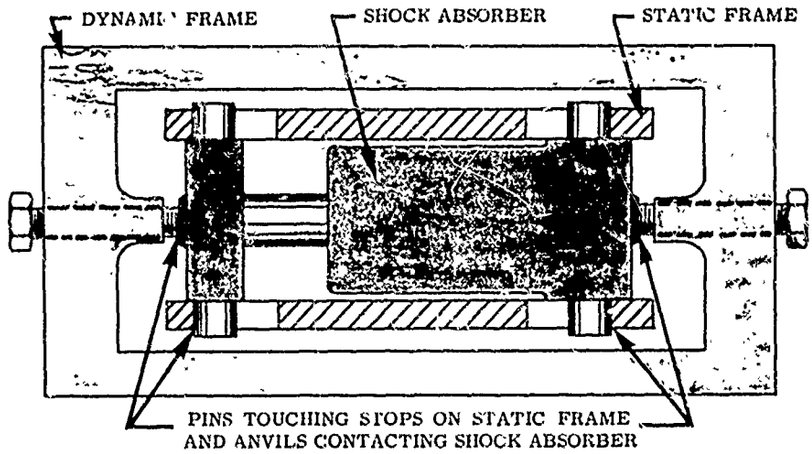

(a) SHOCK ABSORBER AND CRADLE IN SET POSITION

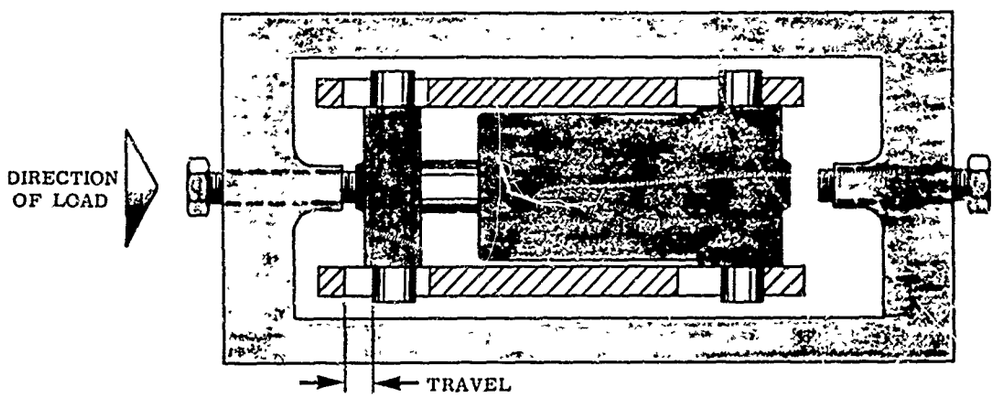

(b) SHOCK ABSORBER & CRADLE UNDER NORMAL LOAD (DIAPHRAGM BURST)

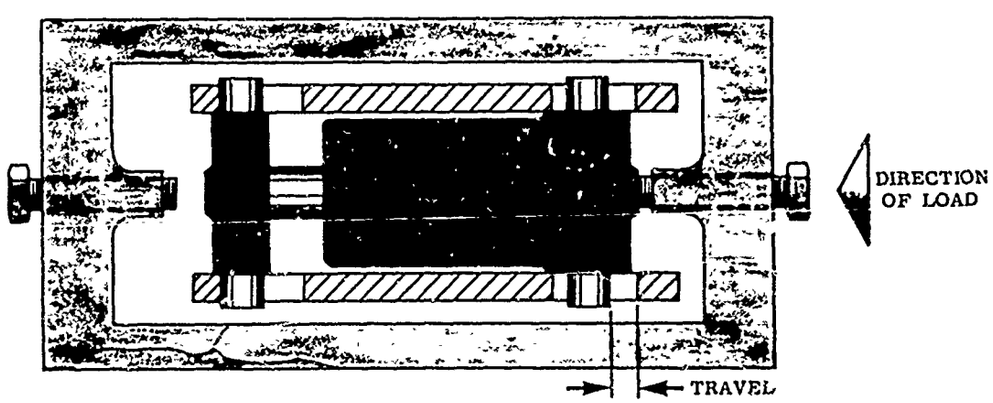

(c) SHOCK ABSORBER & CRADLE UNDER REVERSE LOAD (RUPTURE DISC BURST)

FIG. 39 SHOCK ABSORBER AND CRADLE UNDER LOAD

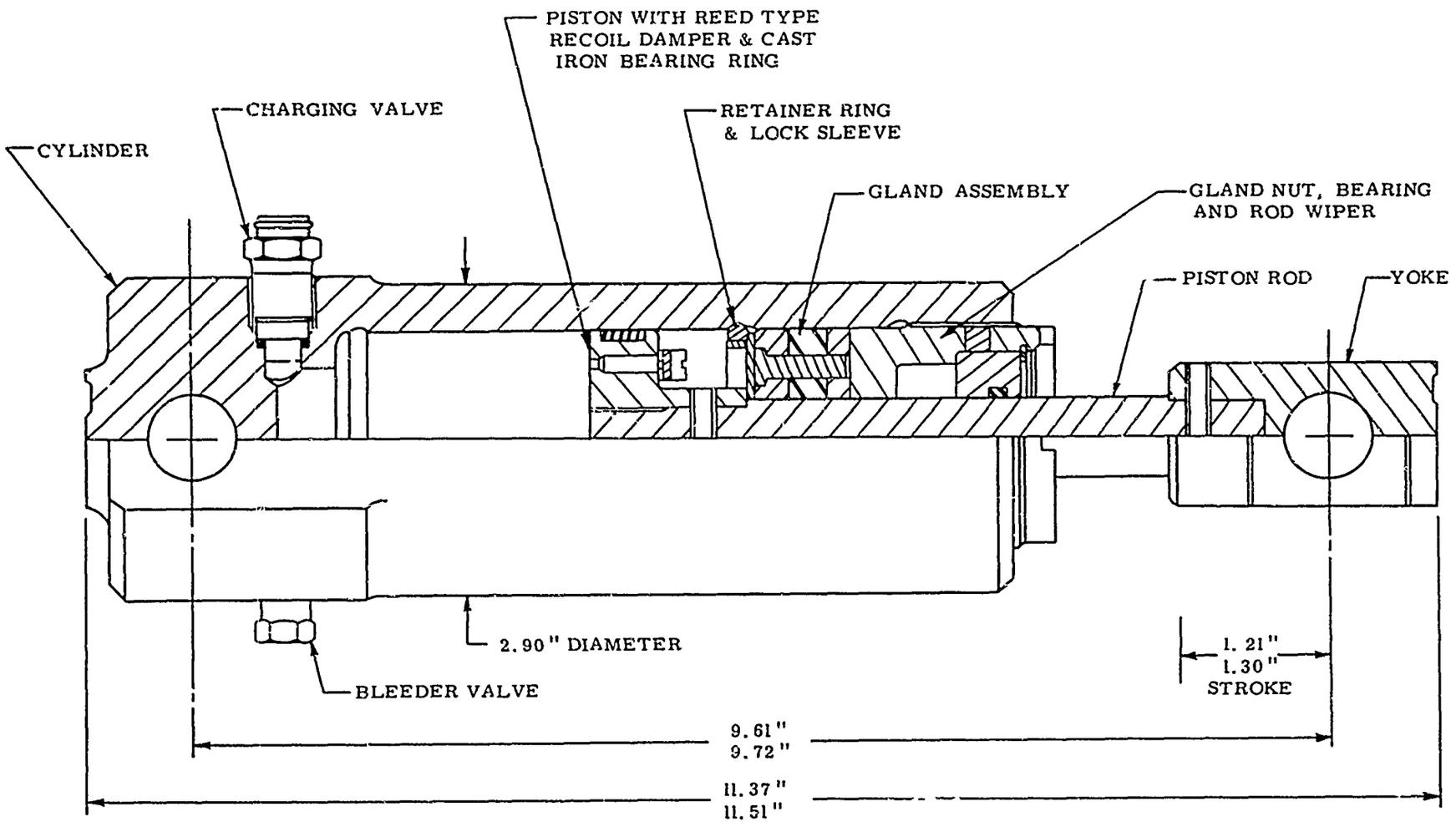

FIG. 40 SCHEMATIC OF LIQUID SPRING SHOCK ABSORBER DESIGNED AND MANUFACTURED BY DOWTY EQUIPMENT OF CANADA

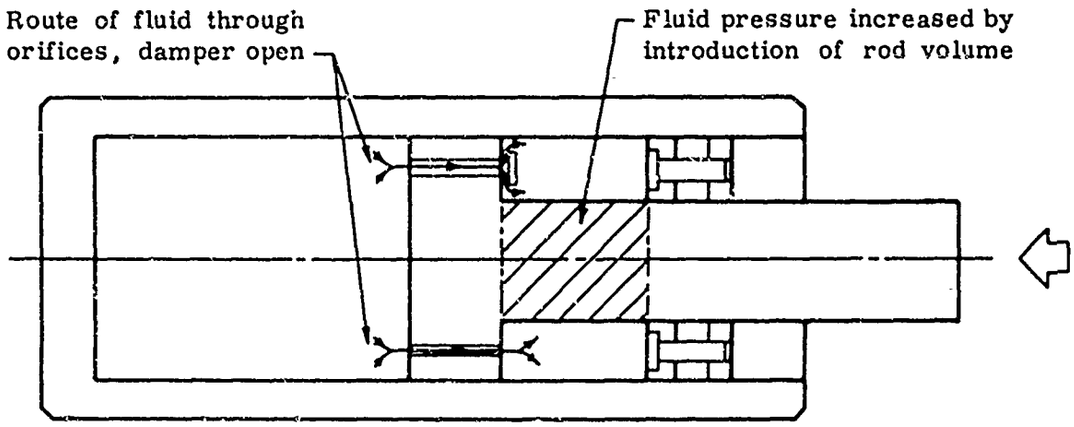

(a) ROD ENTERING CYLINDER

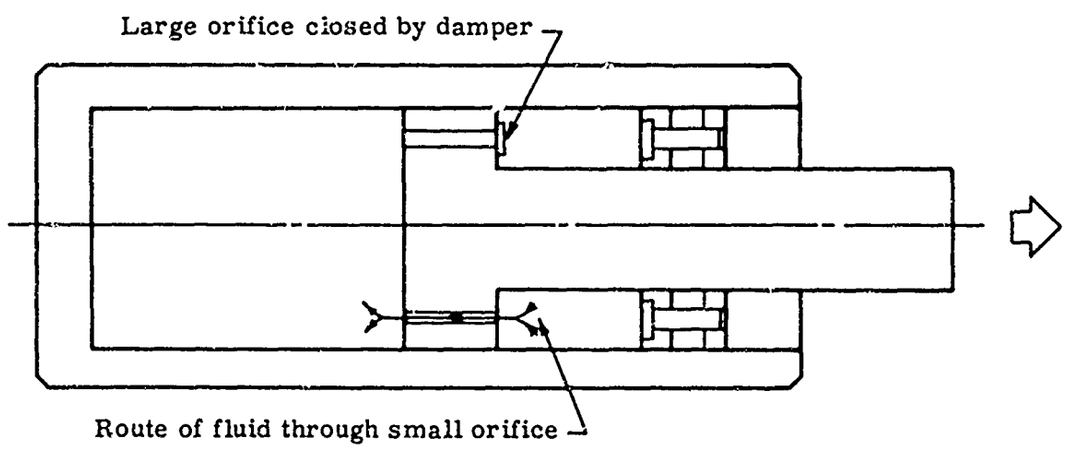

(b) ROD LEAVING CYLINDER

FIG. 41 FUNCTIONAL DIAGRAM OF SHOCK ABSORBER

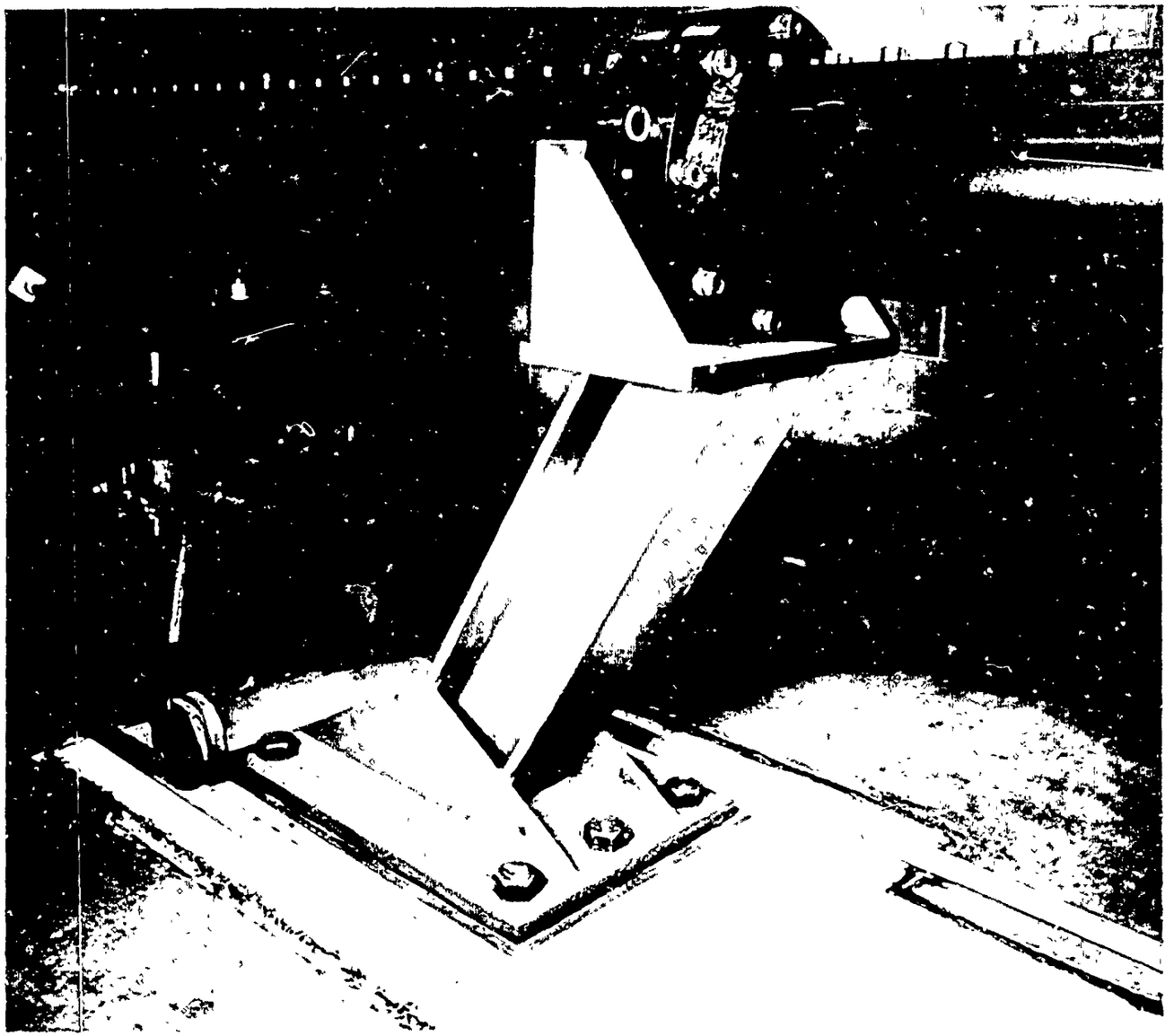

FIG. 42 RECOIL STRUT

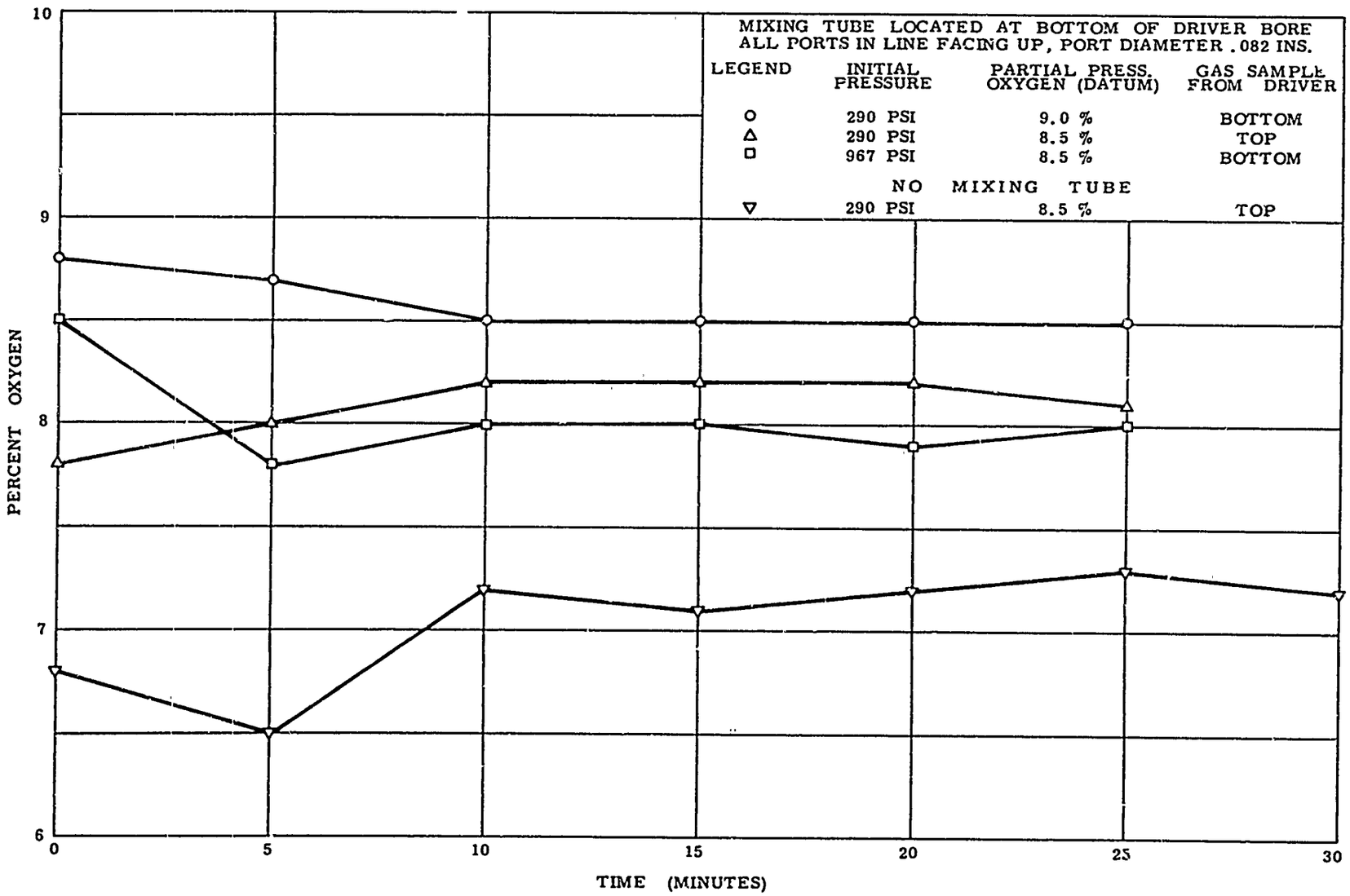

FIG. 43 DRIVER GAS MIXING RESULTS

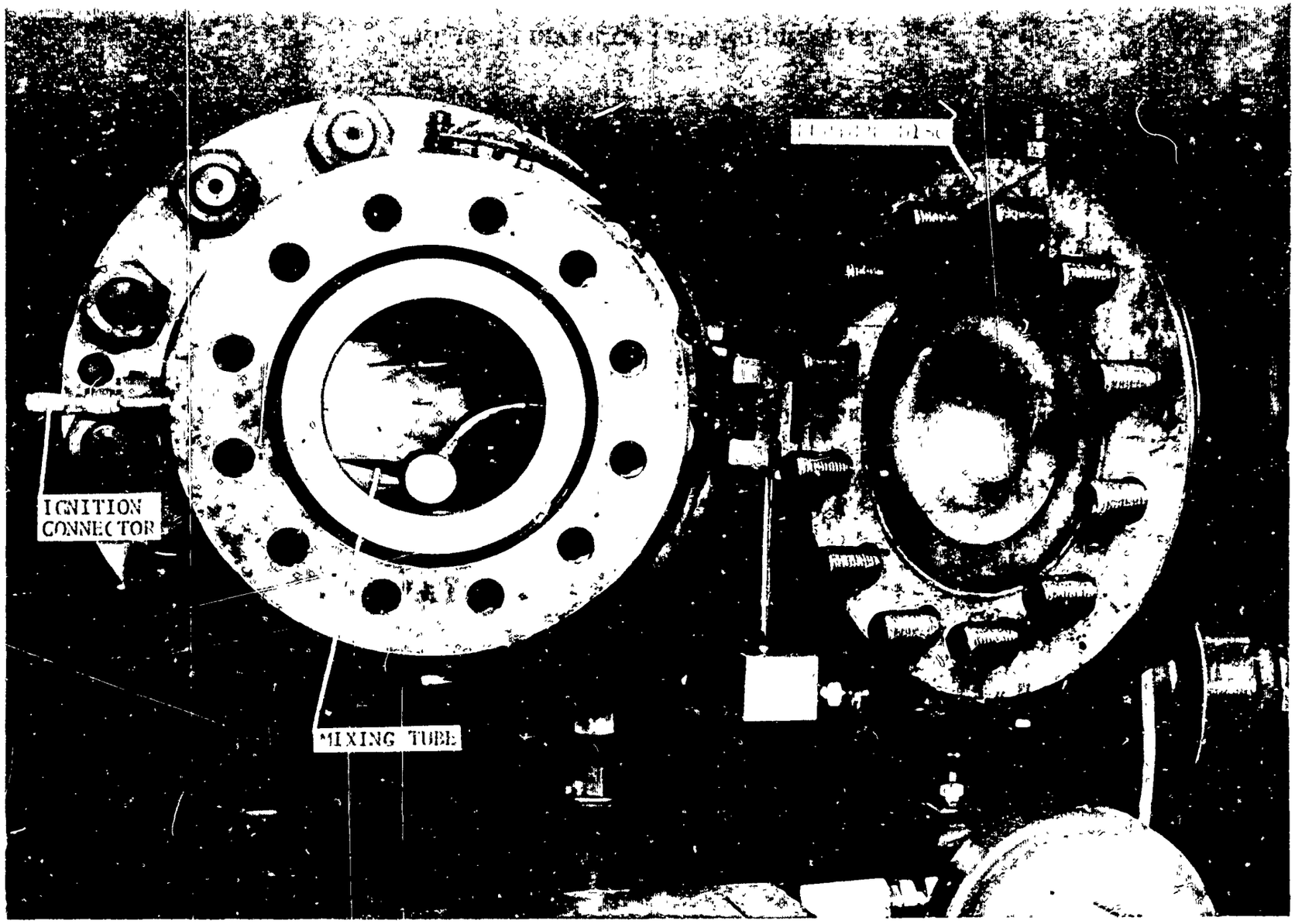

FIG. 44 DRIVER END SECTION SHOWING MIXING TUBE, IGNITION CONNECTOR, AND RUPTURE DISC

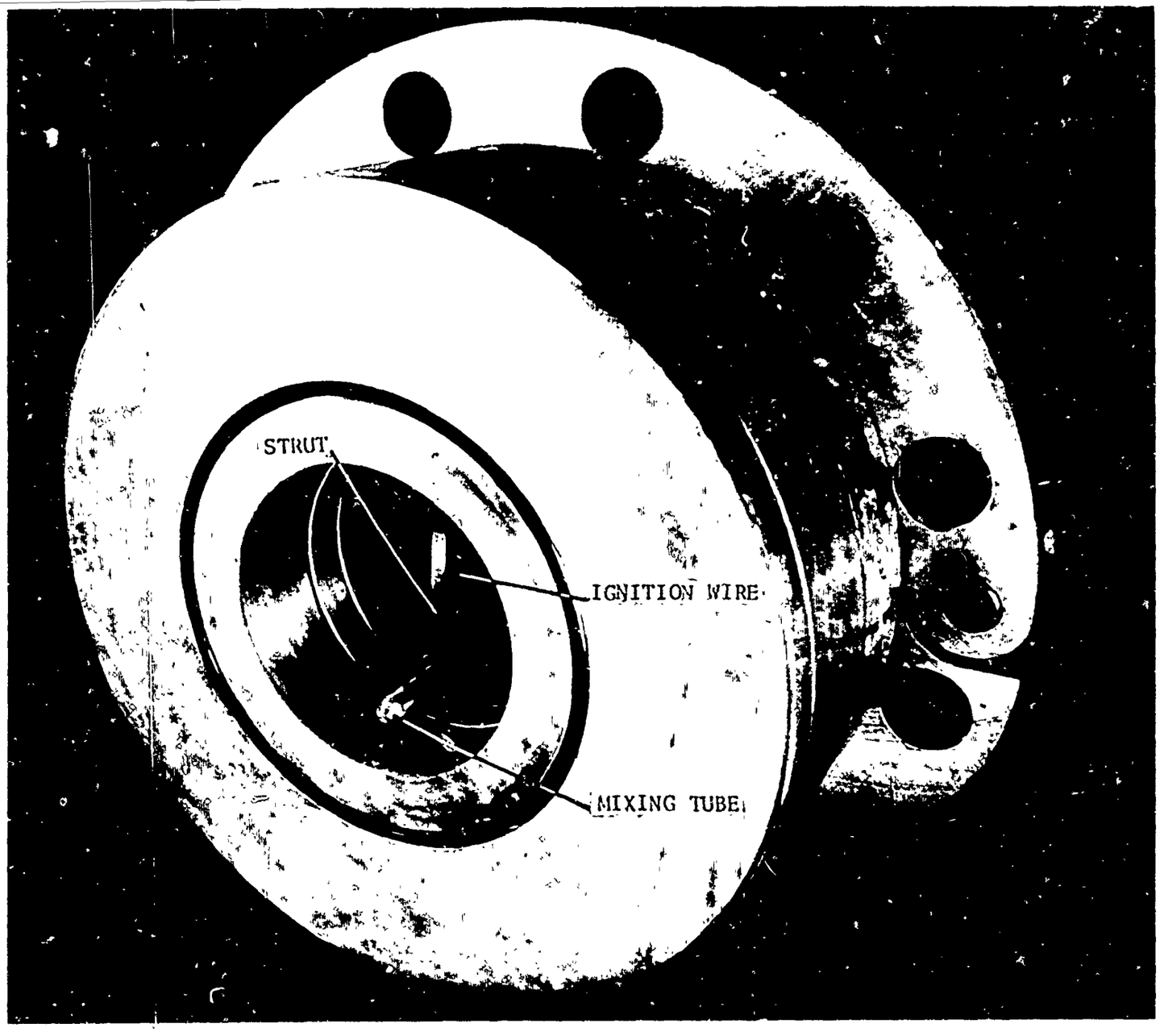

FIG. 45 DRIVER DIAPHRAGM STATION SHOWING MIXING TUBE, STRUT, AND IGNITION WIRE

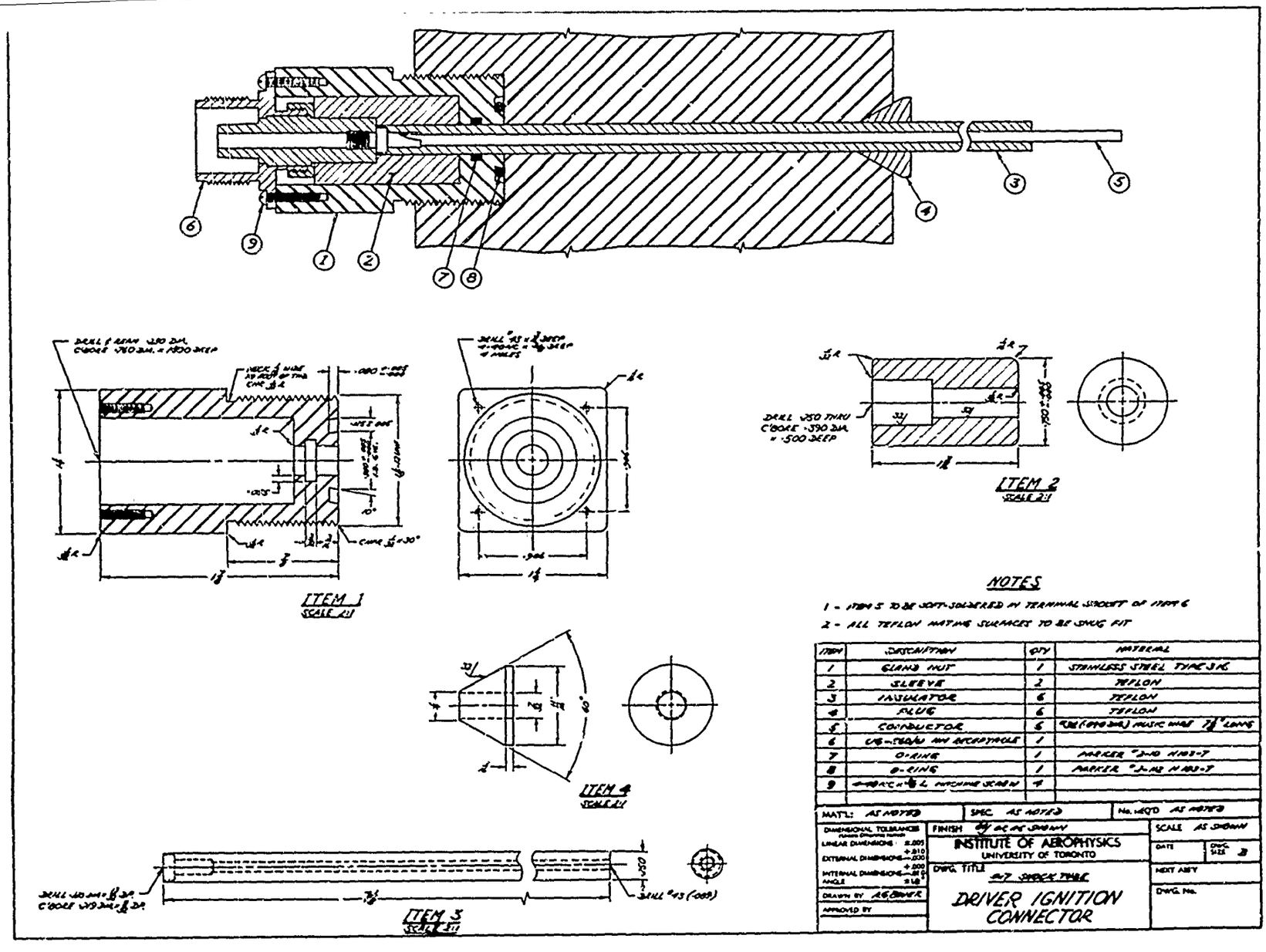

FIG. 46 DESIGN OF DRIVER IGNITION CONNECTOR

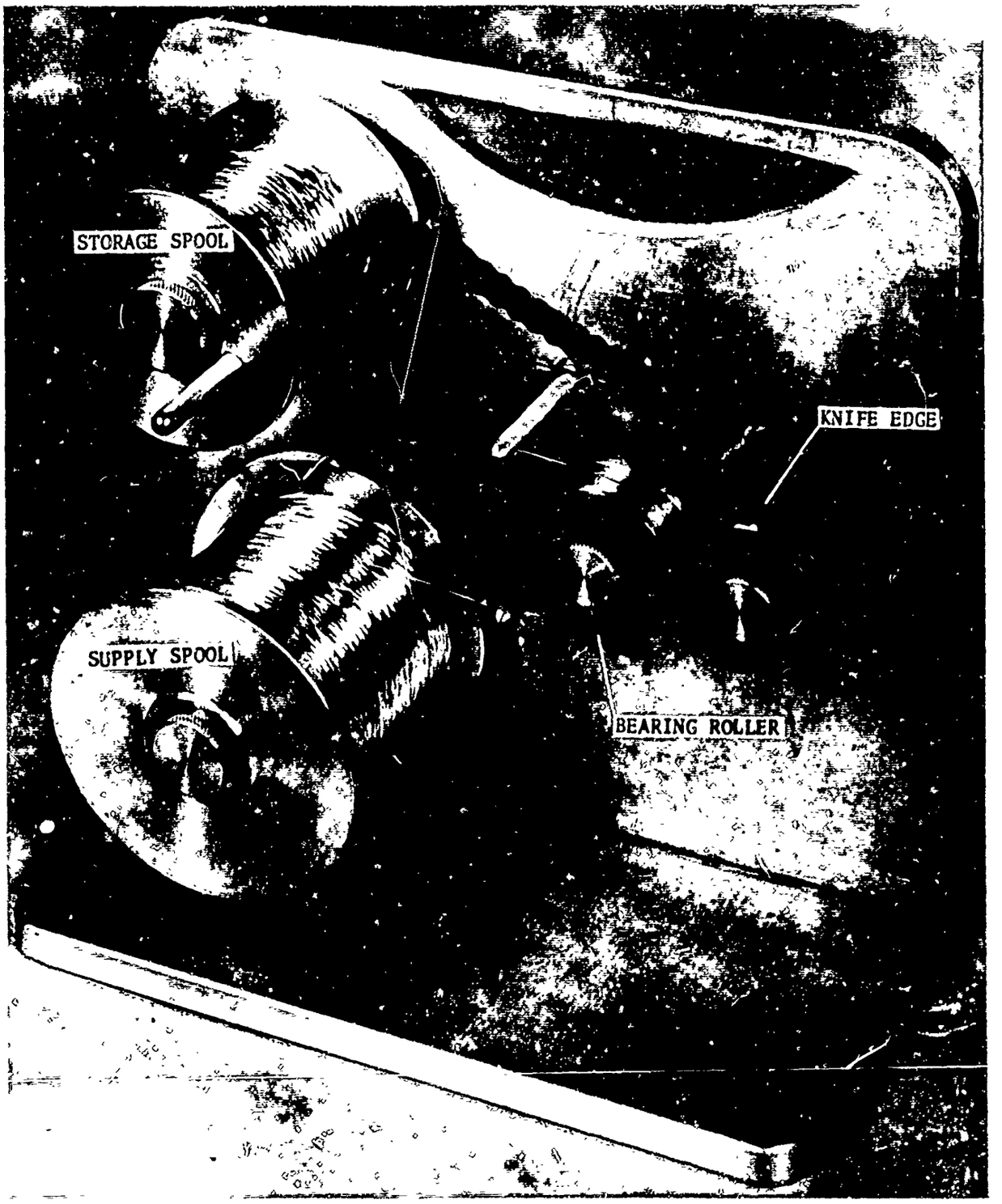

FIG. 47 ALUMINIUM IGNITION WIRE CRIMPING RIG

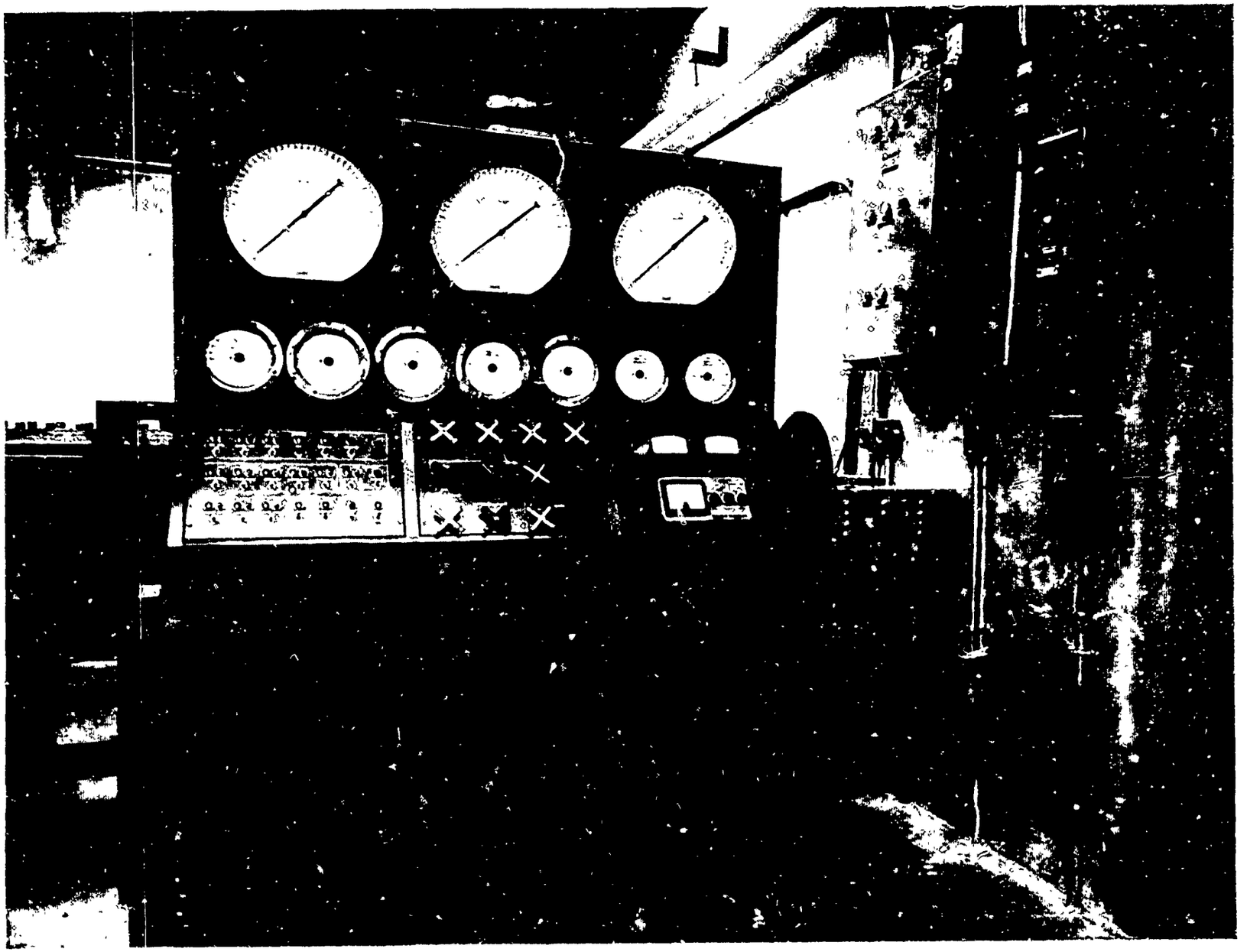

FIG. 48 VIEW OF OPERATING CONSOLE AND AUXILIARY CONTROLS

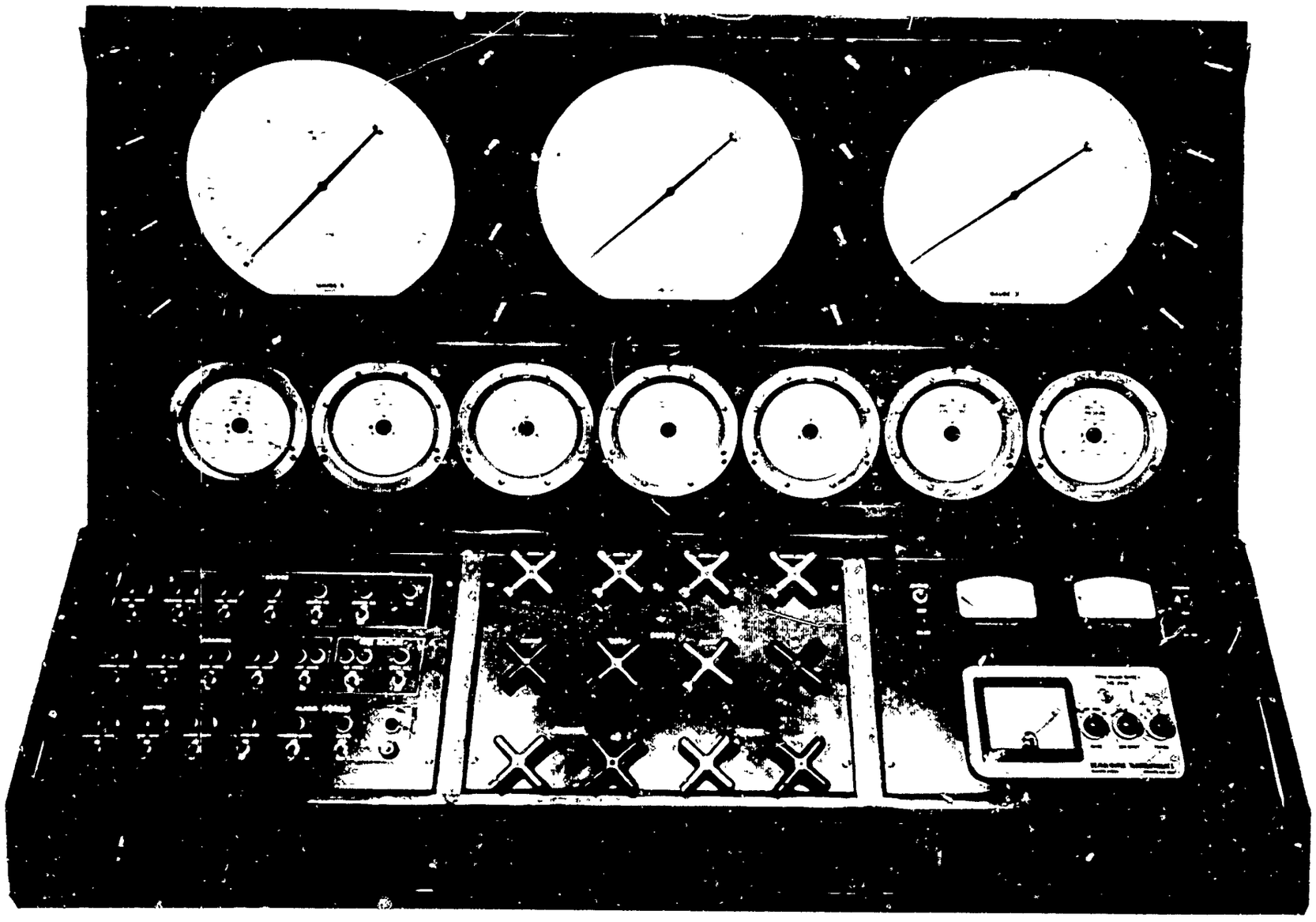

FIG. 49 CLOSE-UP OF OPERATING CONSOLE PANELS

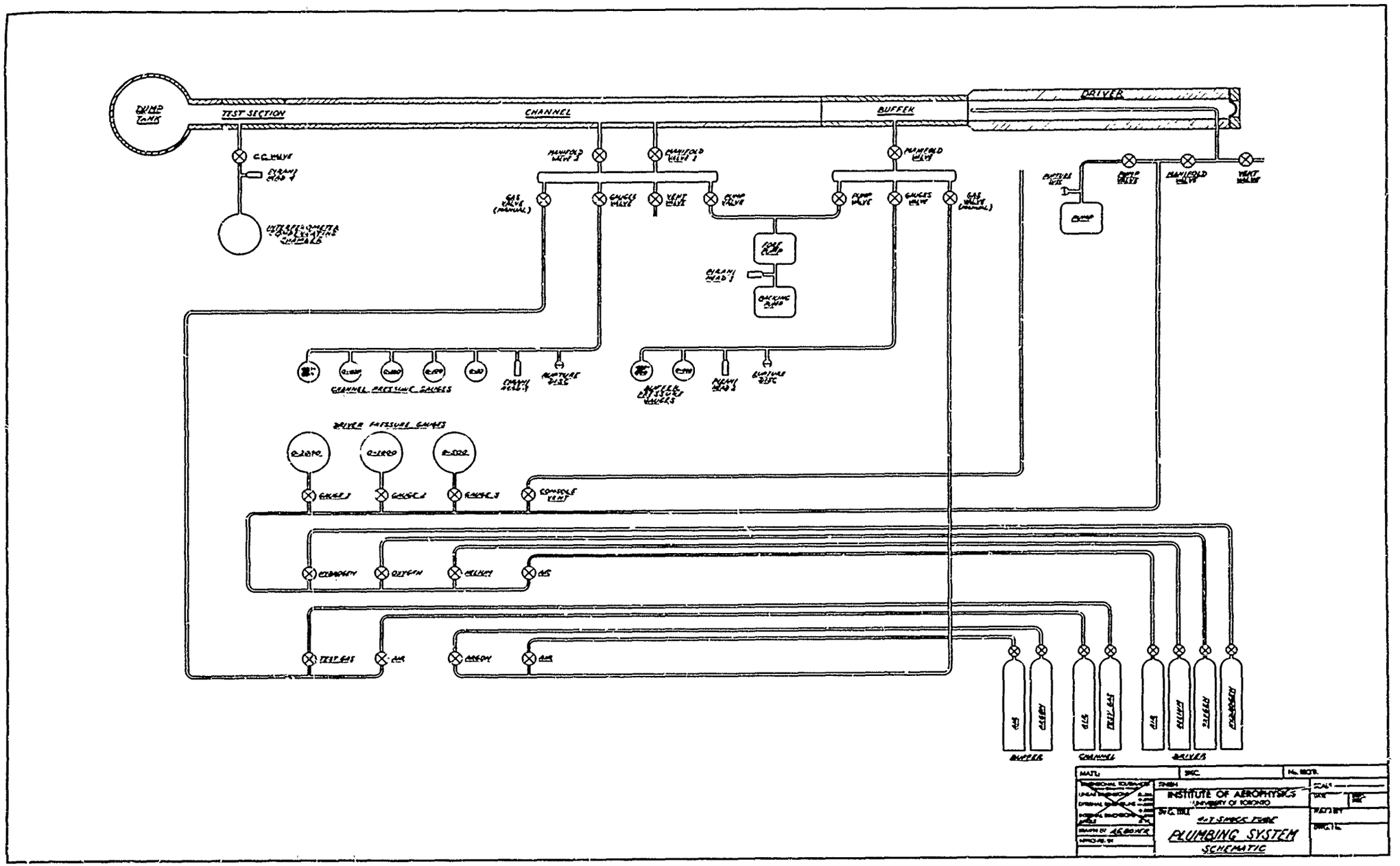

FIG. 50 SCHEMATIC OF PLUMBING SYSTEM

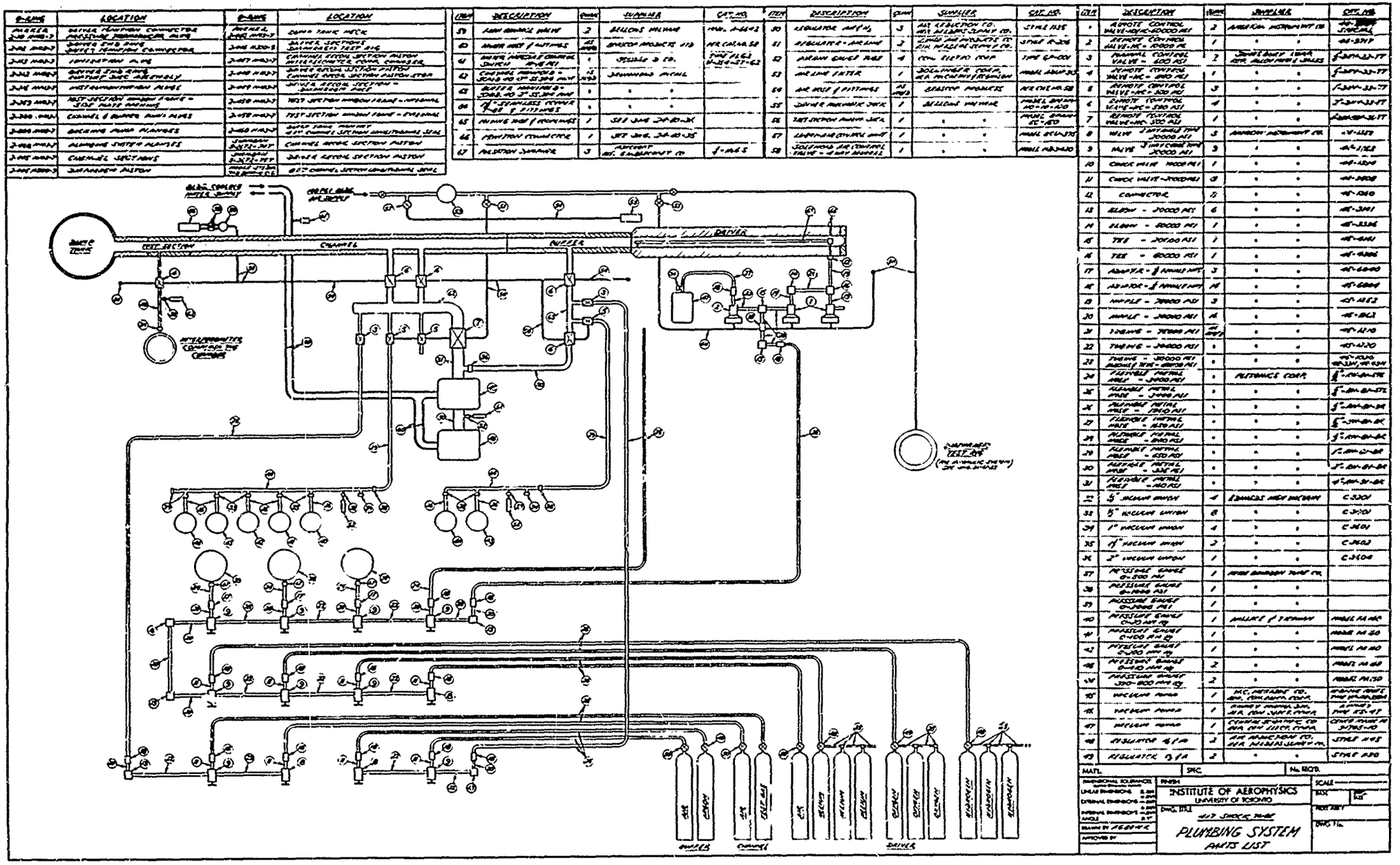

FIG. 51 PLUMBING SYSTEM PARTS LIST

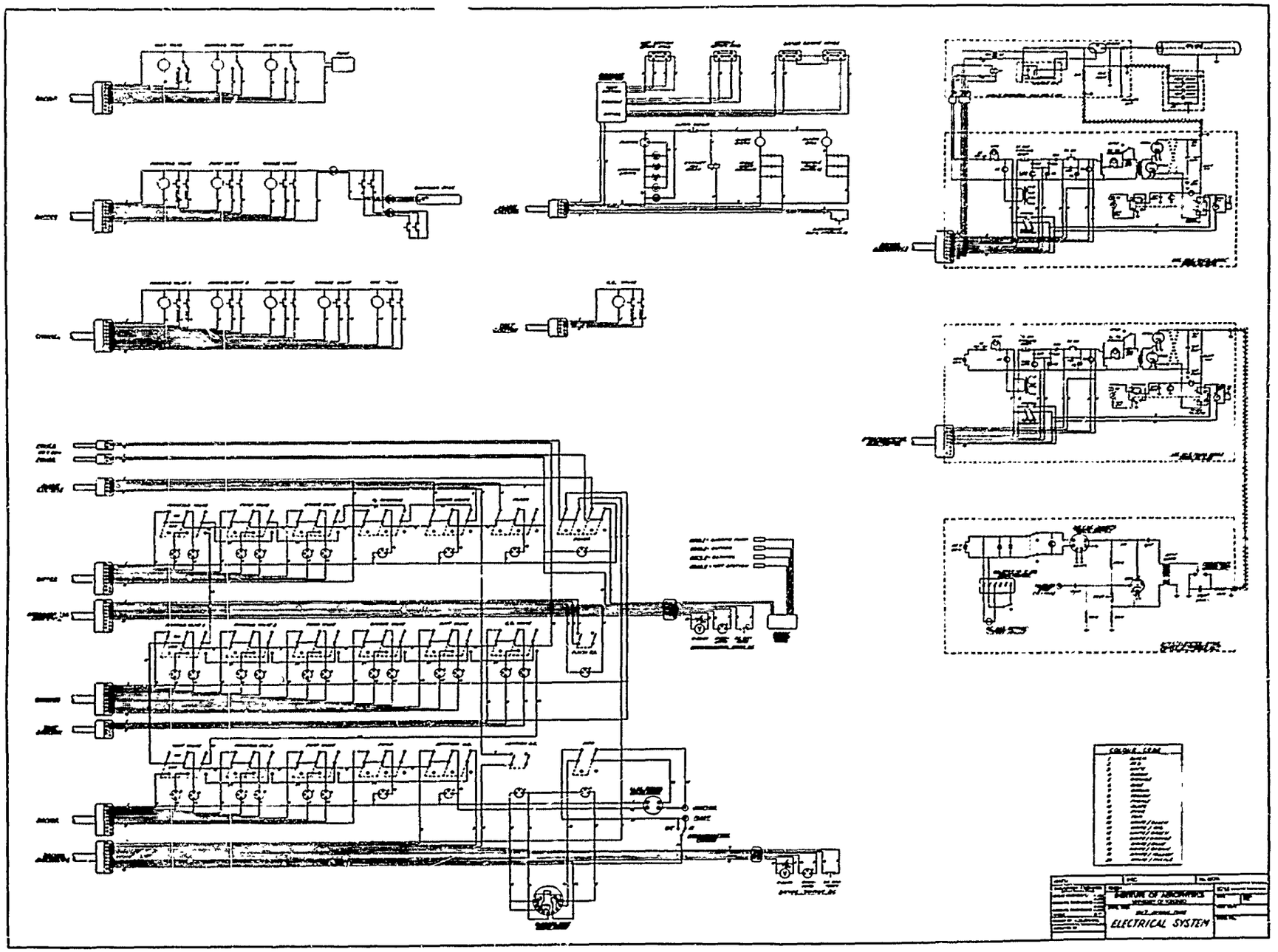

FIG. 52 ELECTRICAL SYSTEM WIRING DIAGRAM

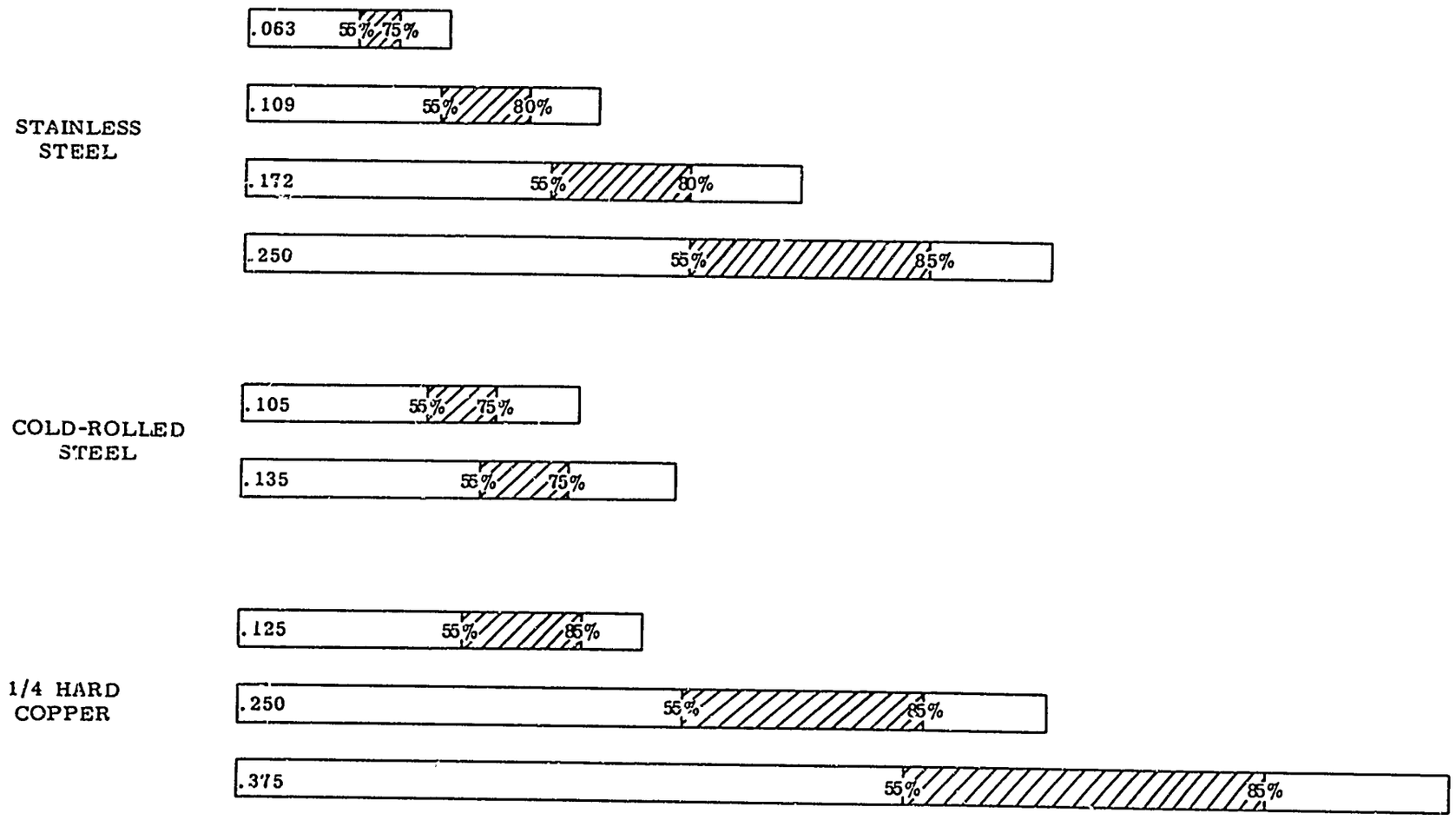

FIG. 53 RANGE OF DIAPHRAGM MATERIALS

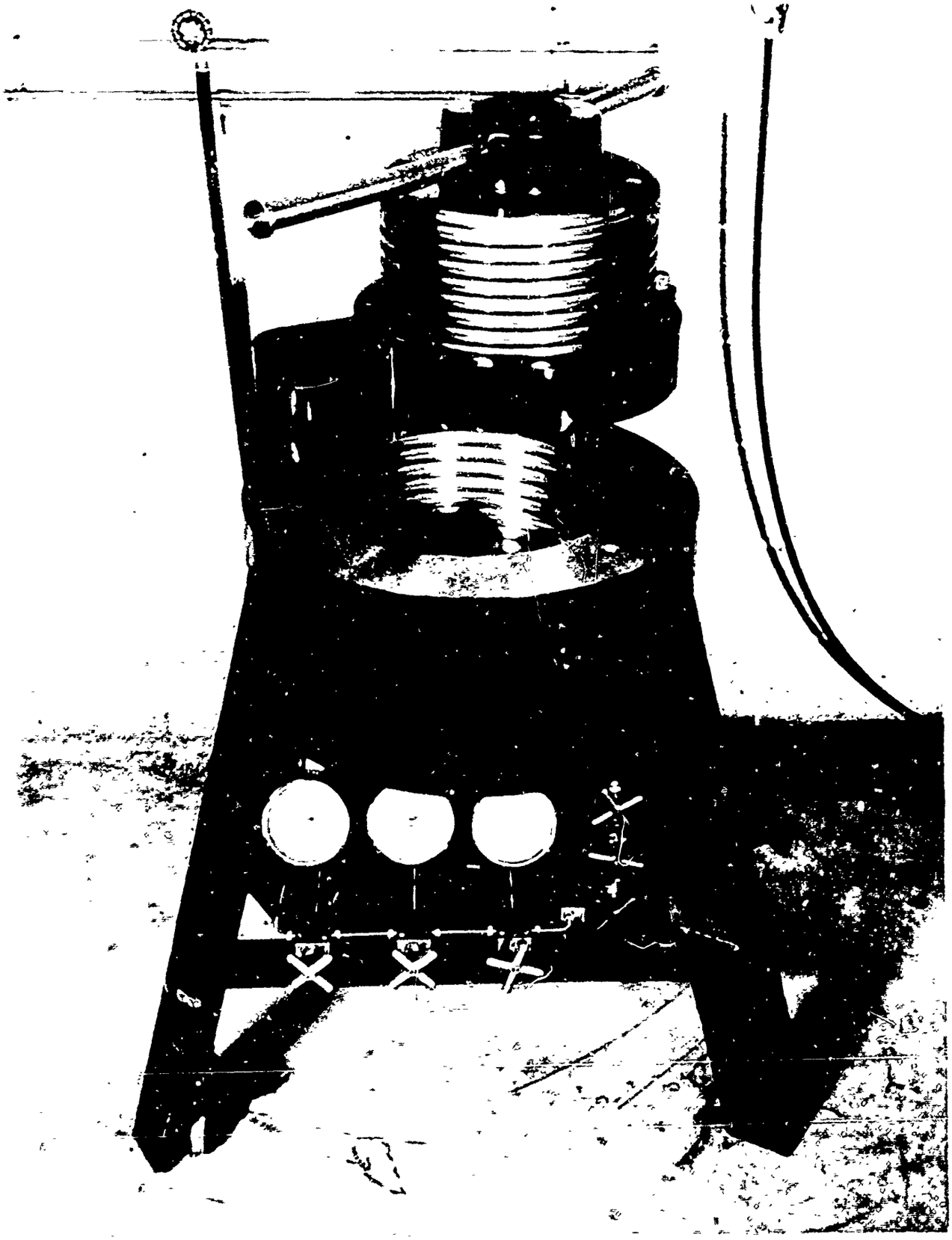

FIG. 54 DIAPHRAGM HYDRAULIC TEST RIG

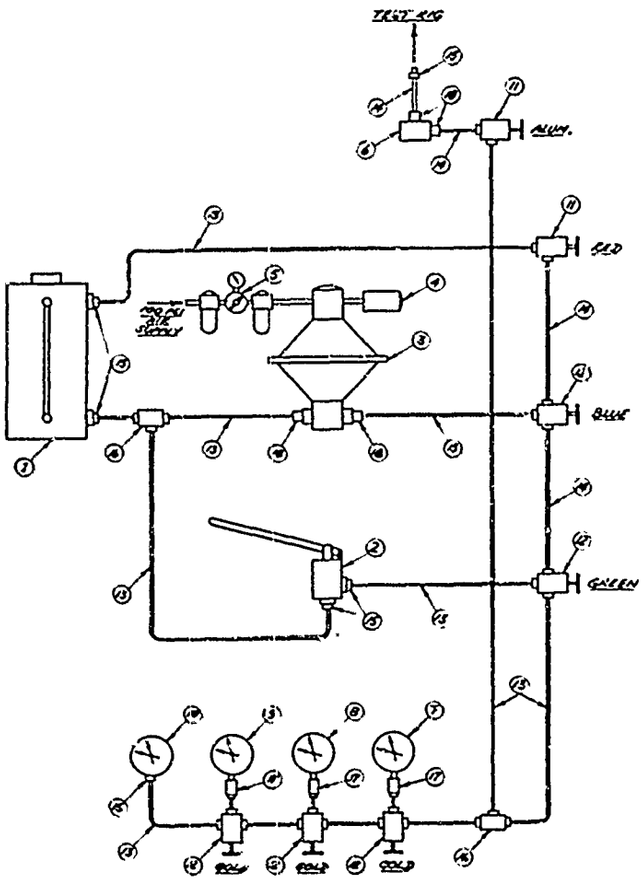

ITEM	DESCRIPTION	QUAN.	SUPPLIER	CAT. NO.
1	RESERVOIR - DWG. 24-U-31	1		
2	HIGH PRESSURE HAND PUMP 24 000 PSI	1	N.C. 'T HART CO. REP. HIGH PRES. PUMP CO. DALE PA	
3	HIGH PRESSURE AIR DRIVEN PUMP - 22750 PSI	1	SARGENT ENG. CORP. REP. ROUSSEAU CONTROLS LTD.	S-246-C-200
4	EXHAUST MUFFLER	1	" "	MODEL 0-5
5	LUBRO CONTROL UNIT	1	" "	P/N 5960
6	RESTRICTOR VALVE	1	" "	NL 001-036
7	0-30000 PSI PRESSURE GAUGE 4½" DIA WITH MAST POINTER & SNUBBER CARTRIDGE	1	AMERICAN GAGE DIV. REP. WATSON BROADBENT & JAMES	MODEL 4200 SNUBBER, MODEL 304
8	0-7000 PSI PRESSURE GAUGE 4½" DIA. WITH MAST POINTER & SNUBBER CARTRIDGE	1	" "	"
9	0-10000 PSI PRESSURE GAUGE 4½" DIA. WITH MAST POINTER & SNUBBER CARTRIDGE	1	" "	"
10	0-30000 PSI PRESSURE GAUGE 6" DIA. WITH MAST POINTER	1	MARSH REP. SYCON LTD	MODEL 100 30000 PSI
11	VALVE 2-WAY (ANGLE) TYPE 30000 PSI	2	AMERICAN INSTRUMENT Co.	44-3125
12	VALVE 3-WAY (ANGLE) TYPE 30000 PSI	5	" "	44-3145
13	TUBING 1/4 OD x 1/8 ID 30000 PSI	AS REQD.	" "	45-1020
14	NIPPLE 1/4 OD x 1/8 ID x 2 1/2 L 30000 PSI	5	" "	45-1062
15	CONNECTOR	6	" "	45-1310
16	TEE 60000 PSI	2	" "	45-6211
17	ADAPTOR 1/4 OD TUBING TO 1/8 MAT NIPPLE	3	" "	45-6196
18	ADAPTOR 1/4 OD TUBING TO 1/4 MAT NIPPLE	2	" "	45-6370

MATL: | SPEC. | NO. REQ'D

DIMENSIONAL TOLERANCES (Unless Otherwise Noted)
LINEAR DIMENSION ± .005
EXTERNAL DIMENSIONS + .015 − .000
INTERNAL DIMENSIONS + .000 − .015
ANGLE ±1°

FINISH

INSTITUTE OF AEROPHYSICS
UNIVERSITY OF TORONTO

DWG. TITLE 4x7 SHOCK TUBE
DIAPHRAGM TEST RIG
HYDRAULIC SYSTEM

SCALE
DATE | DWG. SIZE
NEXT ASSY
DWG. NO

DRAWN BY A.G. DOYER
APPROVED BY

FIG. 55 DIAPHRAGM TEST RIG HYDRAULIC SYSTEM

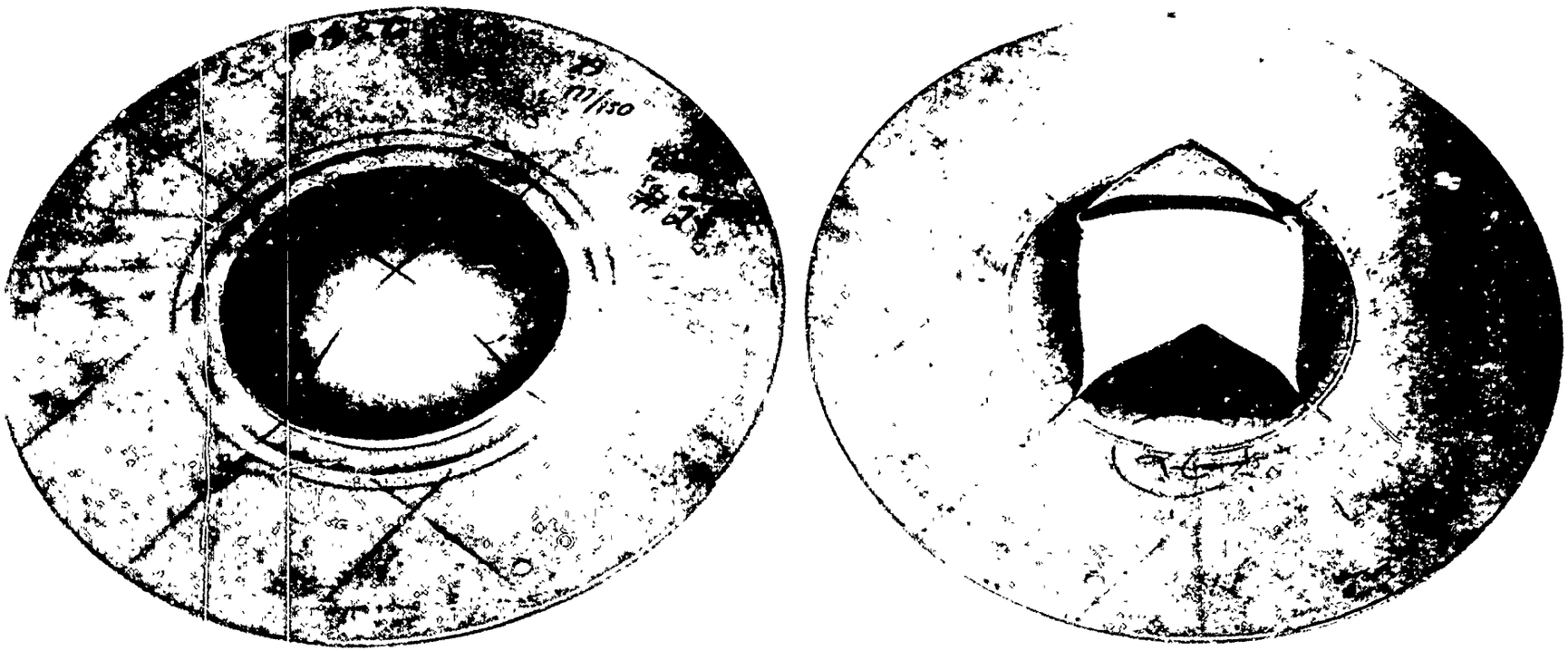

FIG. 56 PRELOADED AND BURST DIAPHRAGMS (STAINLESS STEEL TYPE 302)
(Preloaded: .177-in. thick, .027-in. scribe depth, 6200 psi burst pressure)
(Burst: .177-in. thick, .088-in. scribe depth, 1500 psi burst pressure)

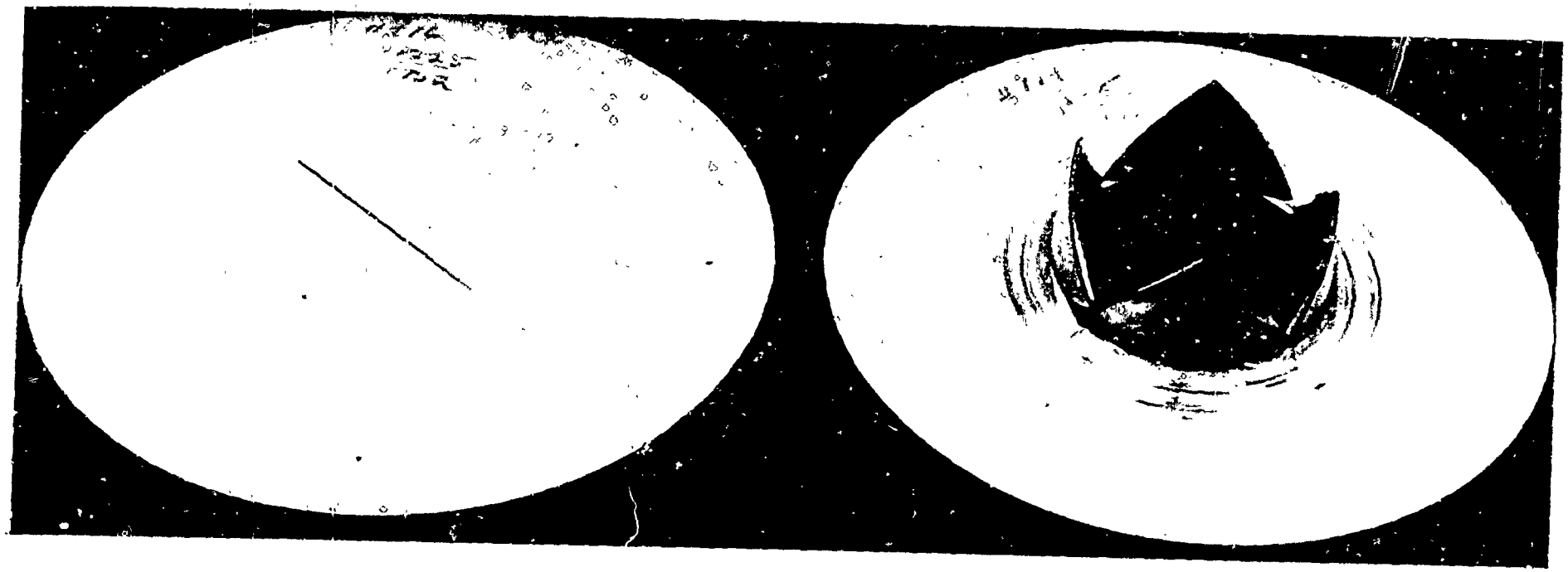

FIG. 57 FLAT-SCORED AND BURST DIAPHRAGMS (STAINLESS STEEL TYPE 302)
(Flat-scored: .175-in. thick, .053-in. scribe depth, 4100 psi burst pressure)
(Burst: .173-in. thick, .051-in. scribe depth, 4370 psi burst pressure)

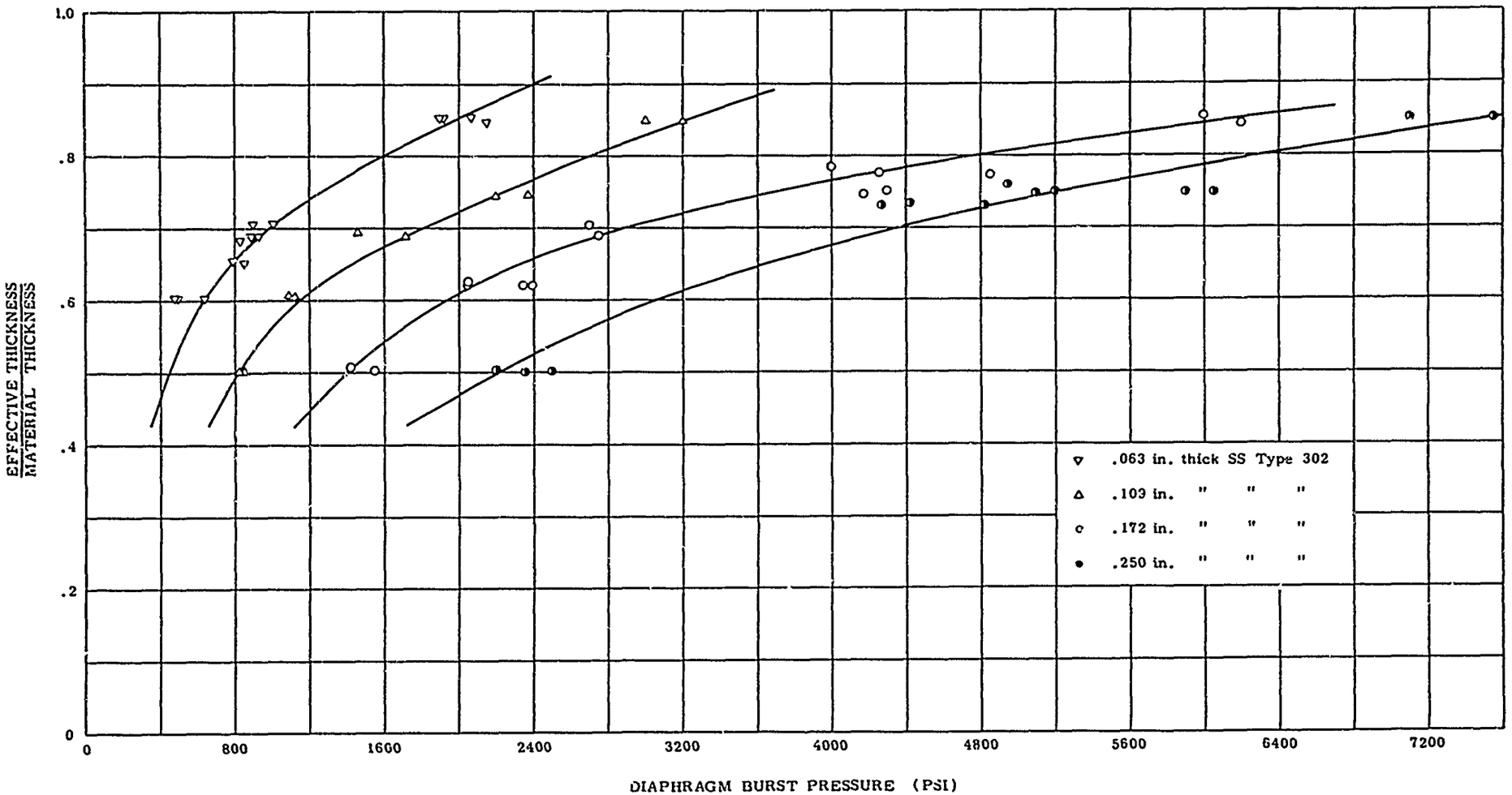

FIG. 58 STAINLESS STEEL DIAPHRAGM BURST-PRESSURE CALIBRATION CURVES

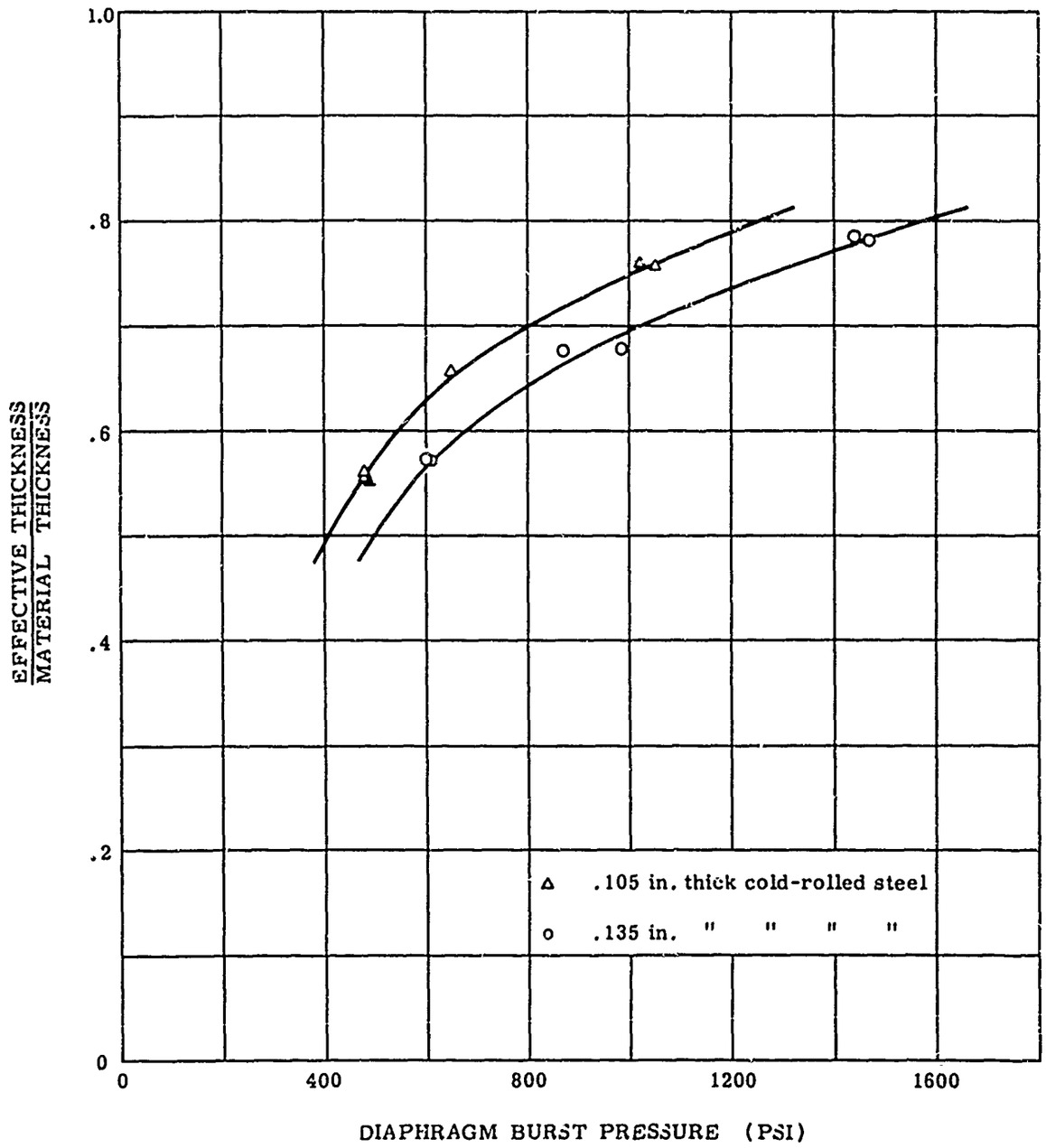

FIG. 59 COLD-ROLLED STEEL DIAPHRAGM BURST-PRESSURE CALIBRATION CURVES

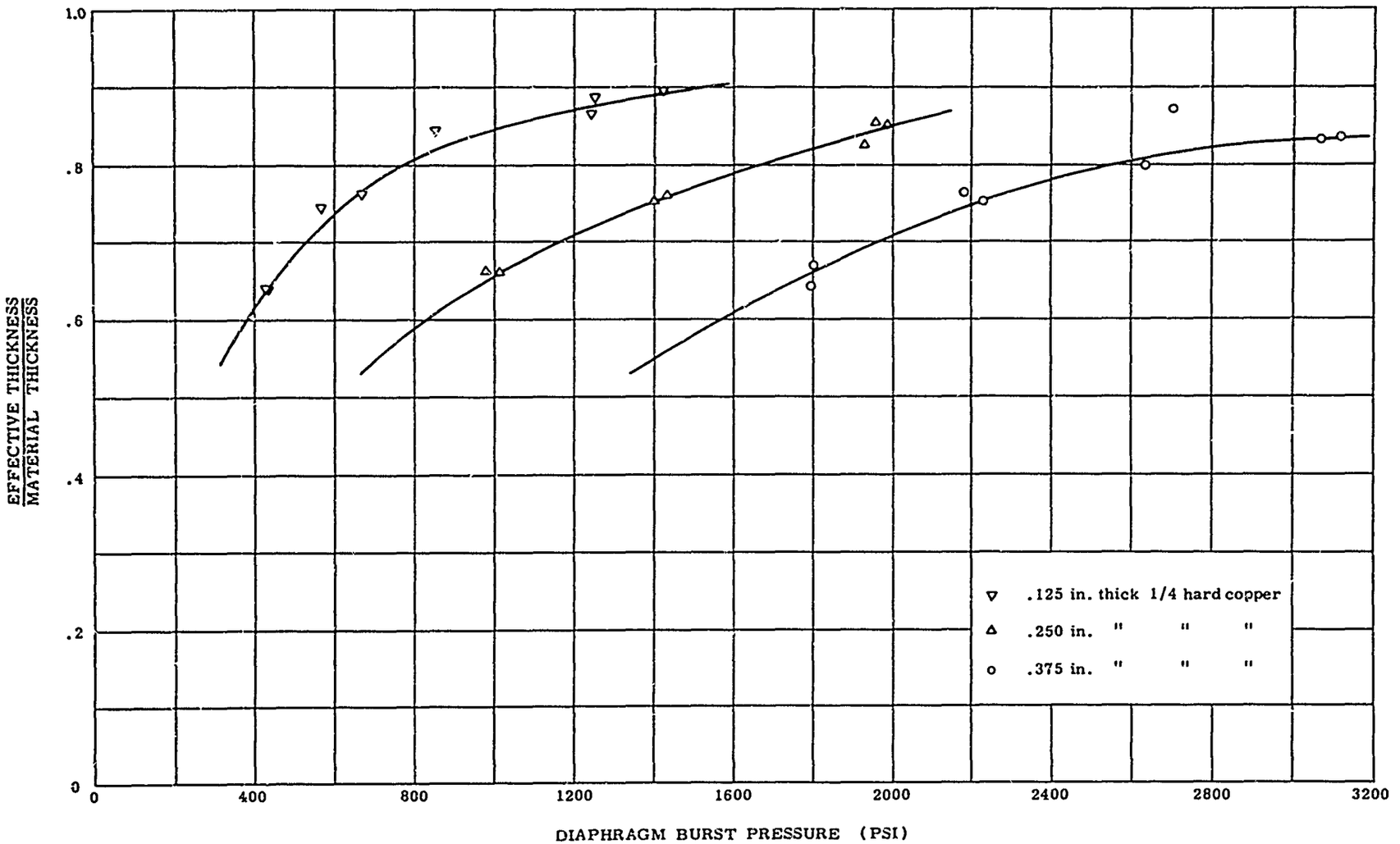

FIG. 60 COPPER DIAPHRAGM BURST-PRESSURE CALIBRATION CURVES

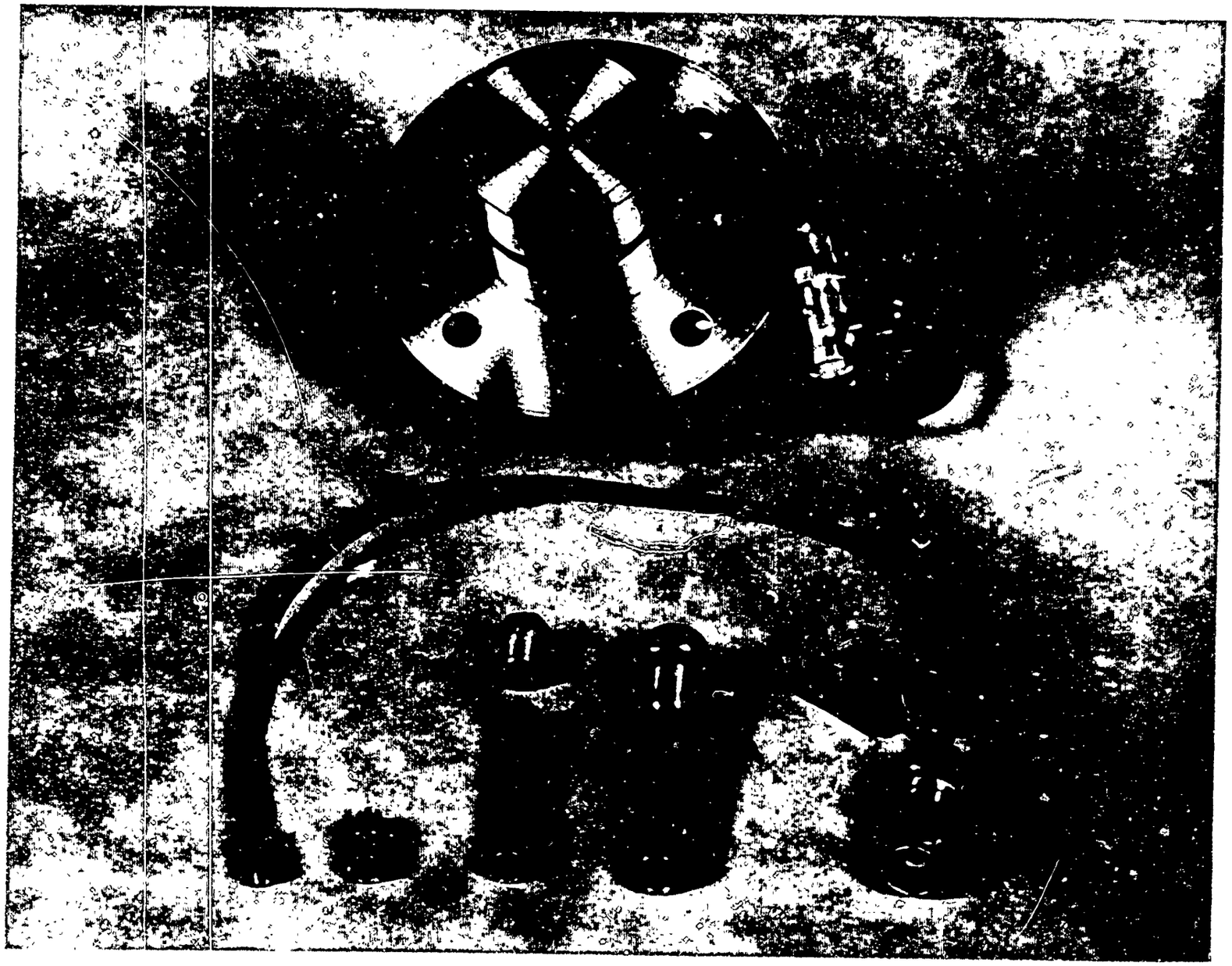

FIG. 61 ASSEMBLED AND EXPLODED VIEWS OF KISTLER #601 PRESSURE TRANSDUCER

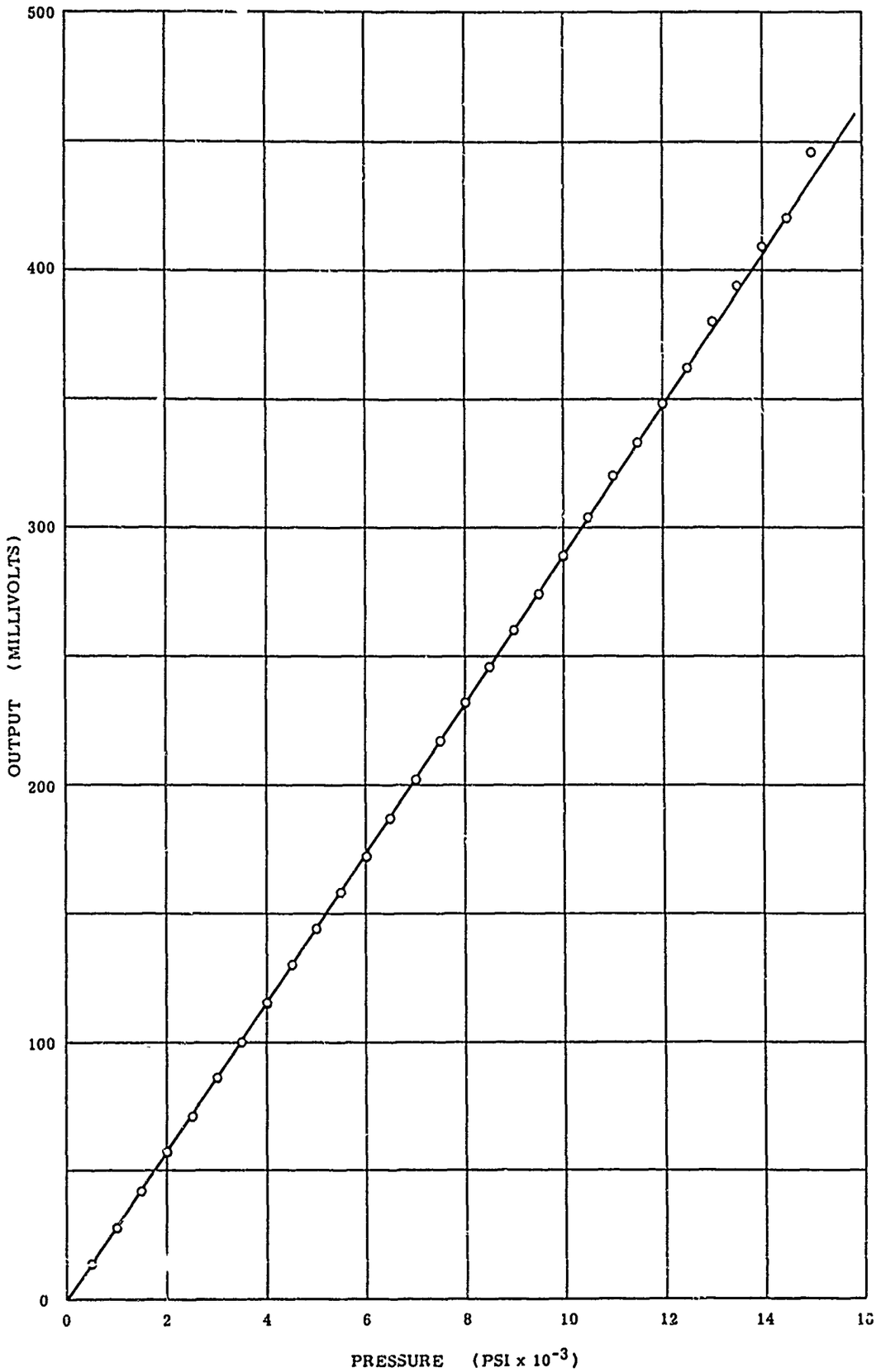

FIG. 62 CALIBRATION CURVE OF KISTLER #605 PRESSURE TRANSDUCER

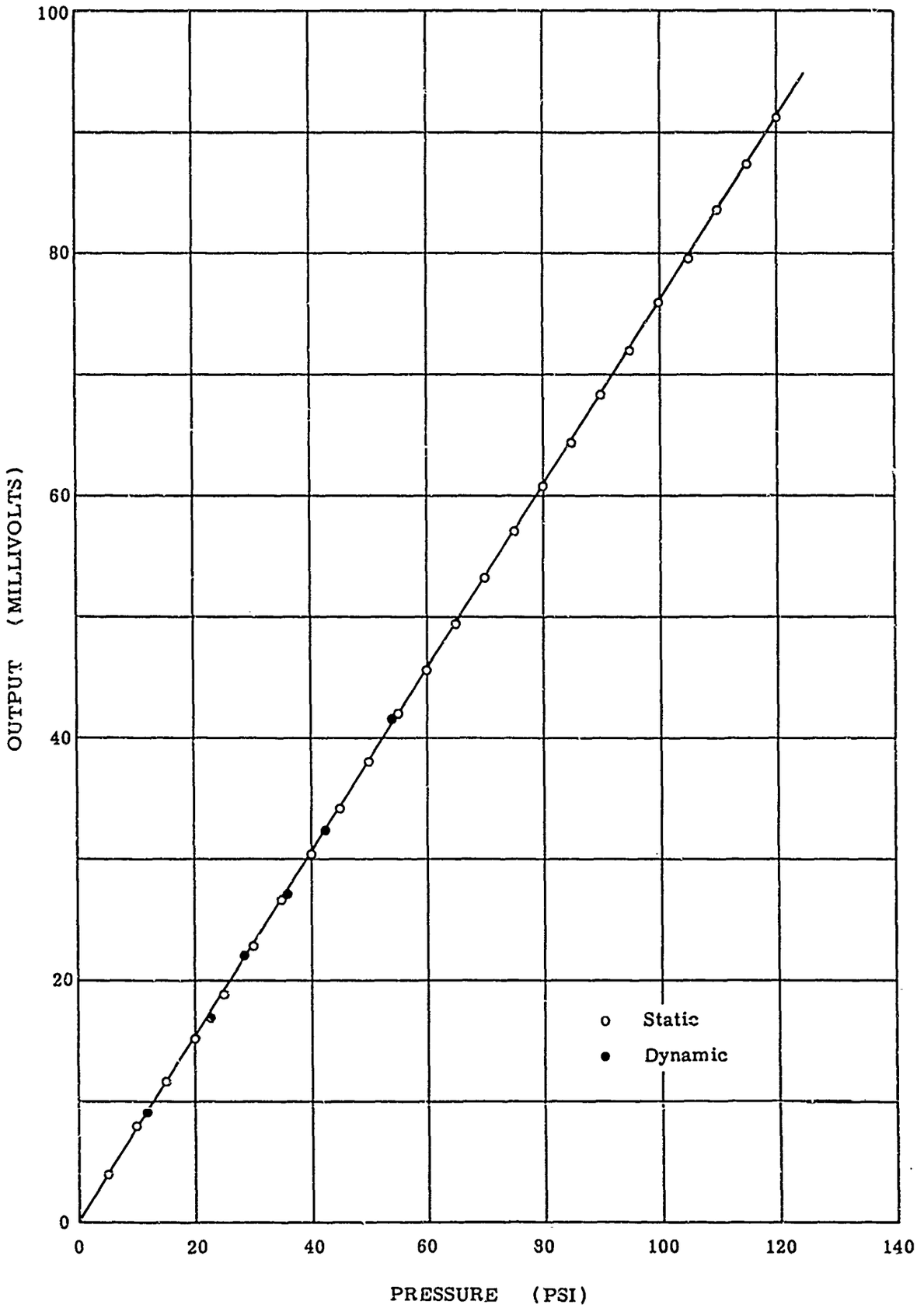

FIG. 63 CALIBRATION CURVE OF KISTLER #601 PRESSURE TRANSDUCER

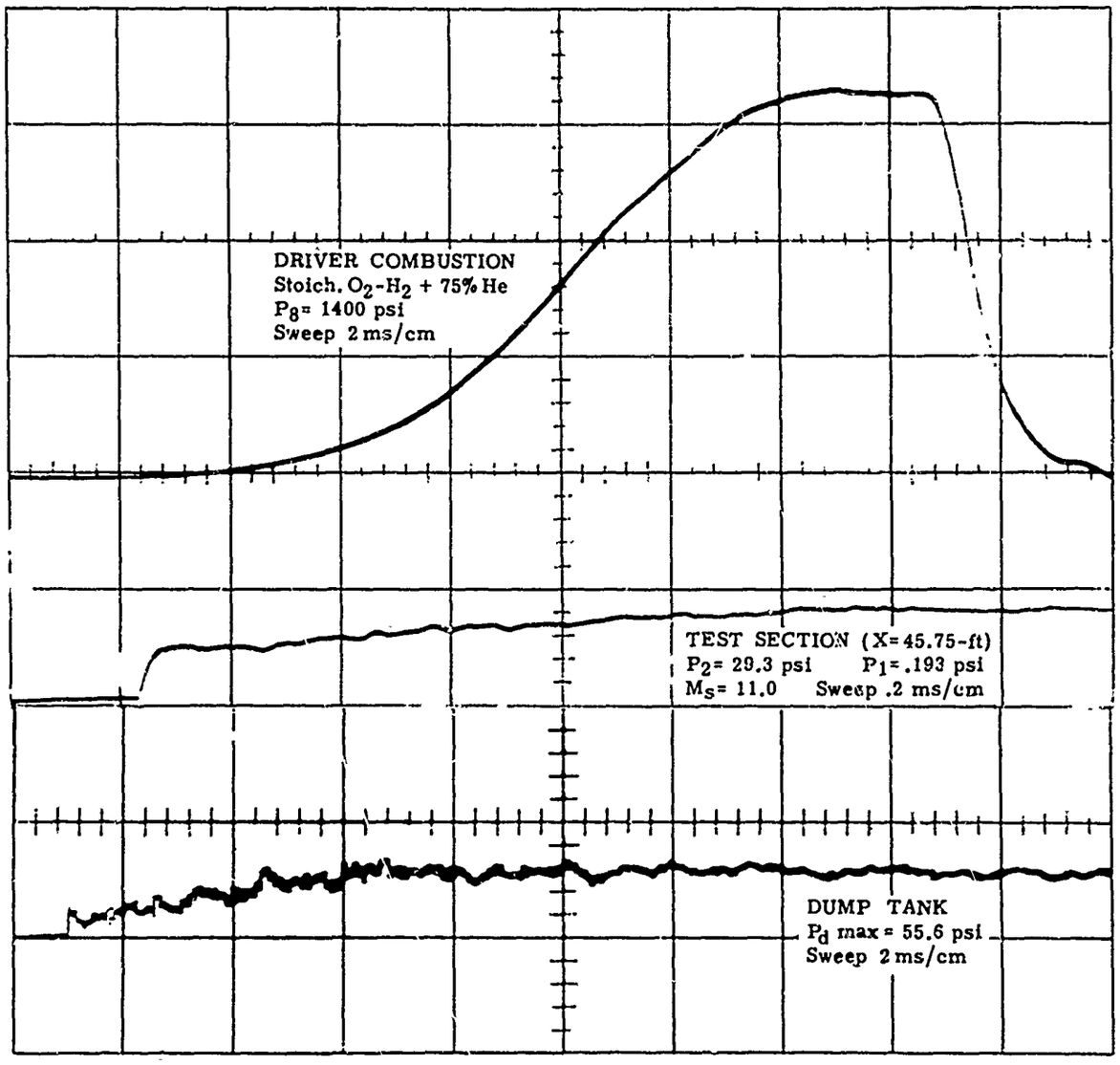

FIG. 64 PRESSURE-TIME HISTORY IN DRIVER, TEST SECTION, AND DUMP TANK

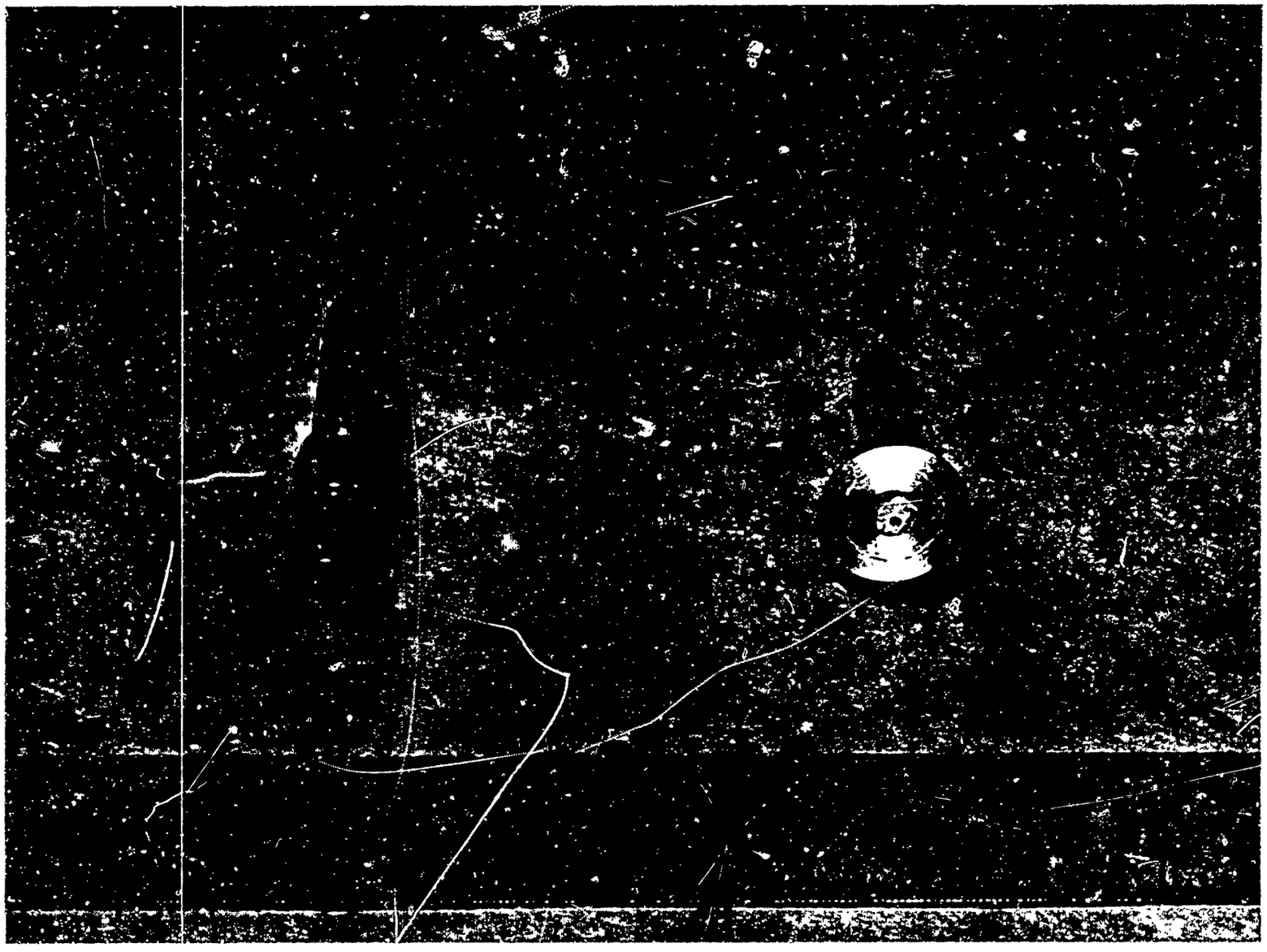

FIG. 65 KISTLER #601 (LEFT) AND PZT (RIGHT) PRESSURE TRANSDUCERS

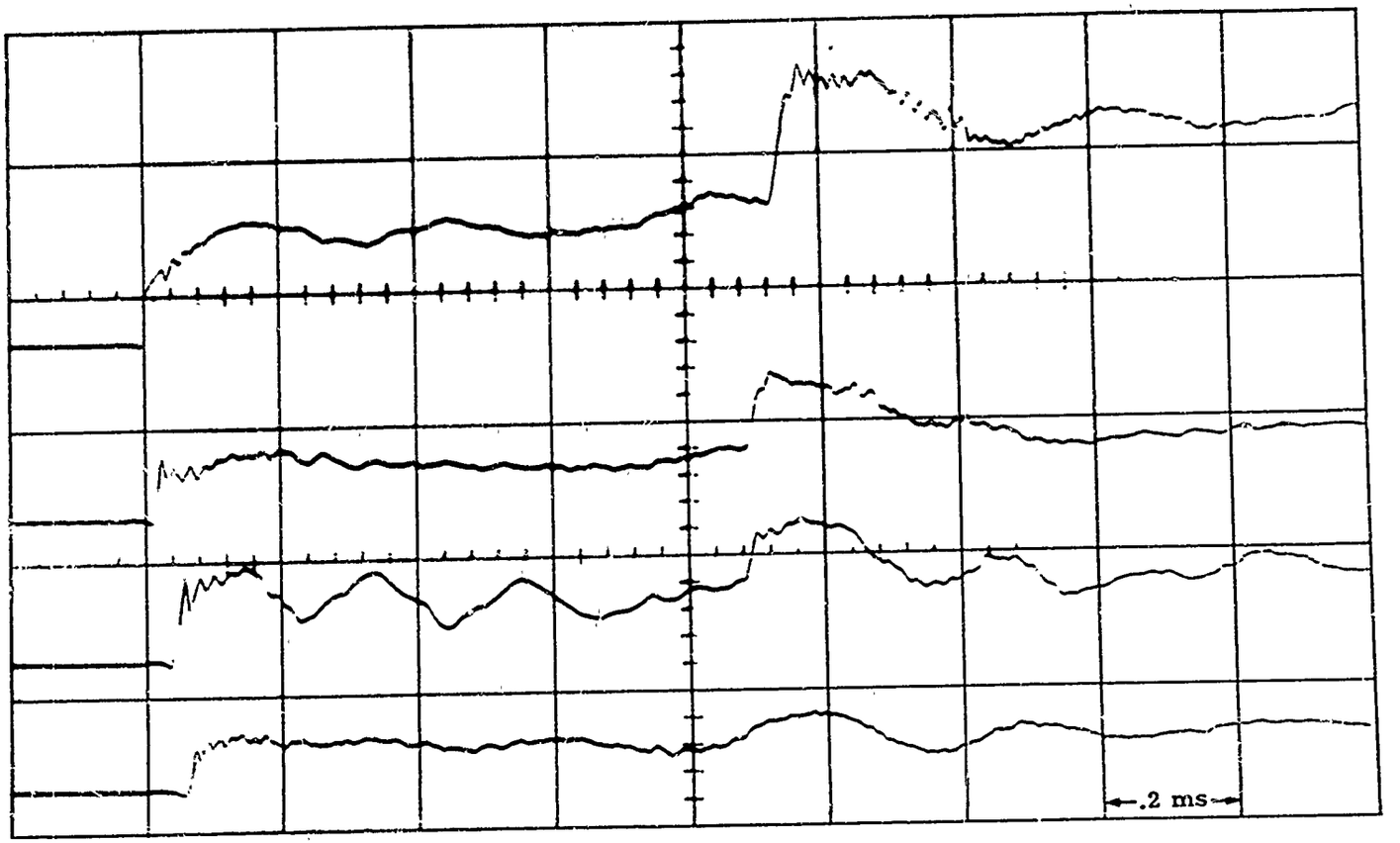

FIG. 66 PRESSURE-TIME HISTORY FOR CORNER EXPANSION MODEL
PZT PRESSURE TRANSDUCERS ($M_S = 3.61$)

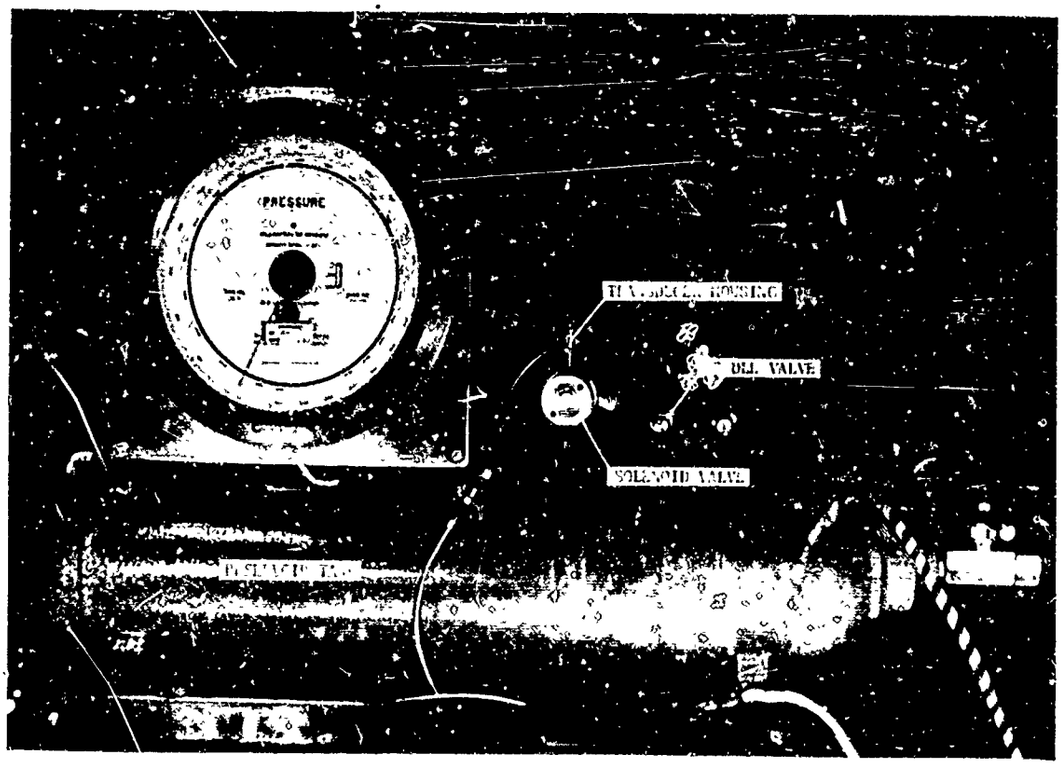

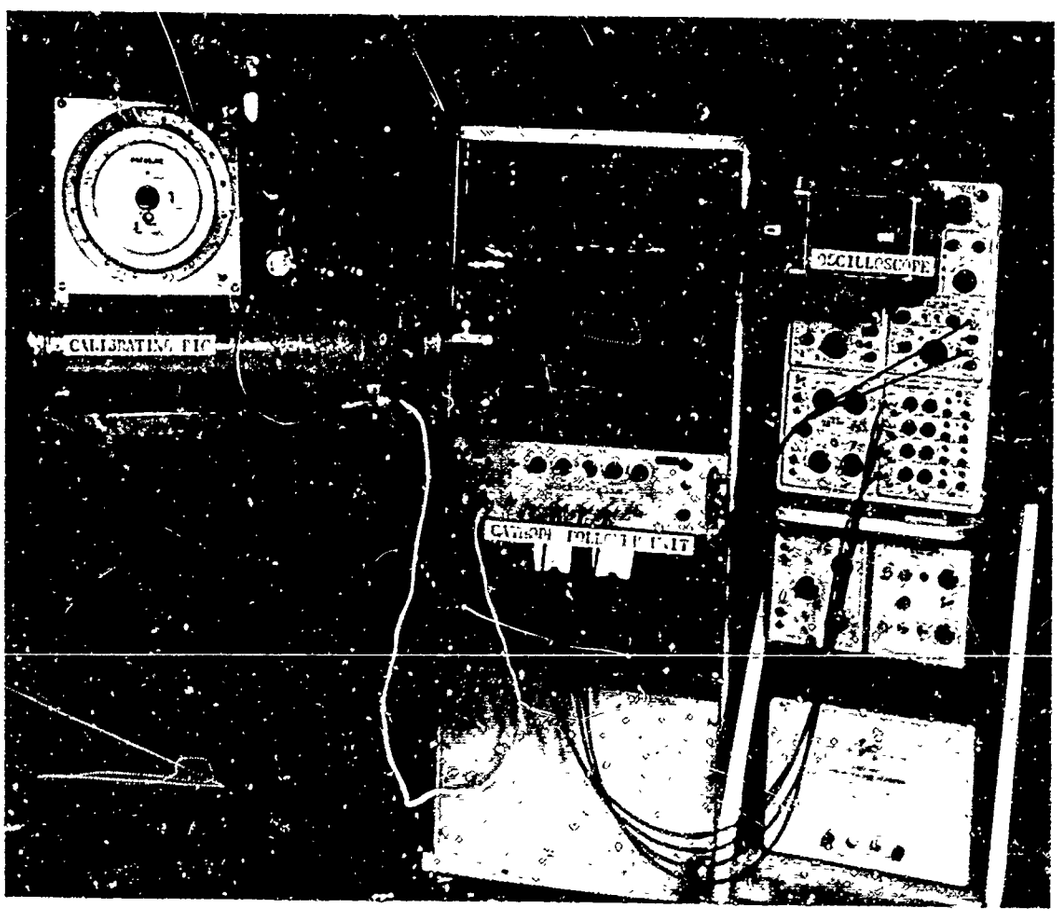

FIG. 67 CALIBRATING RIG FOR PZT PRESSURE TRANSDUCER

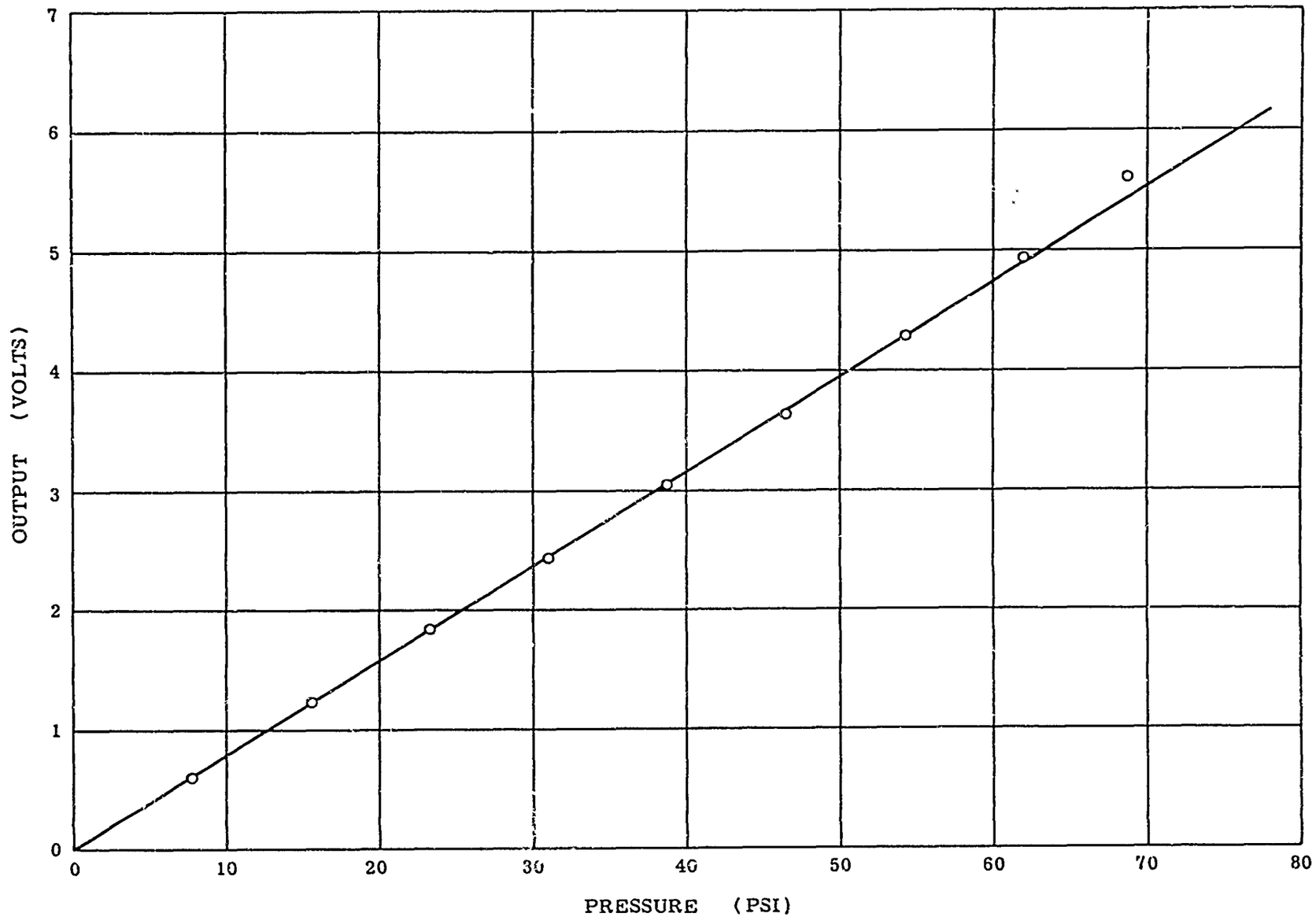

FIG. 68 CALIBRATION CURVE OF PZT PRESSURE TRANSDUCER

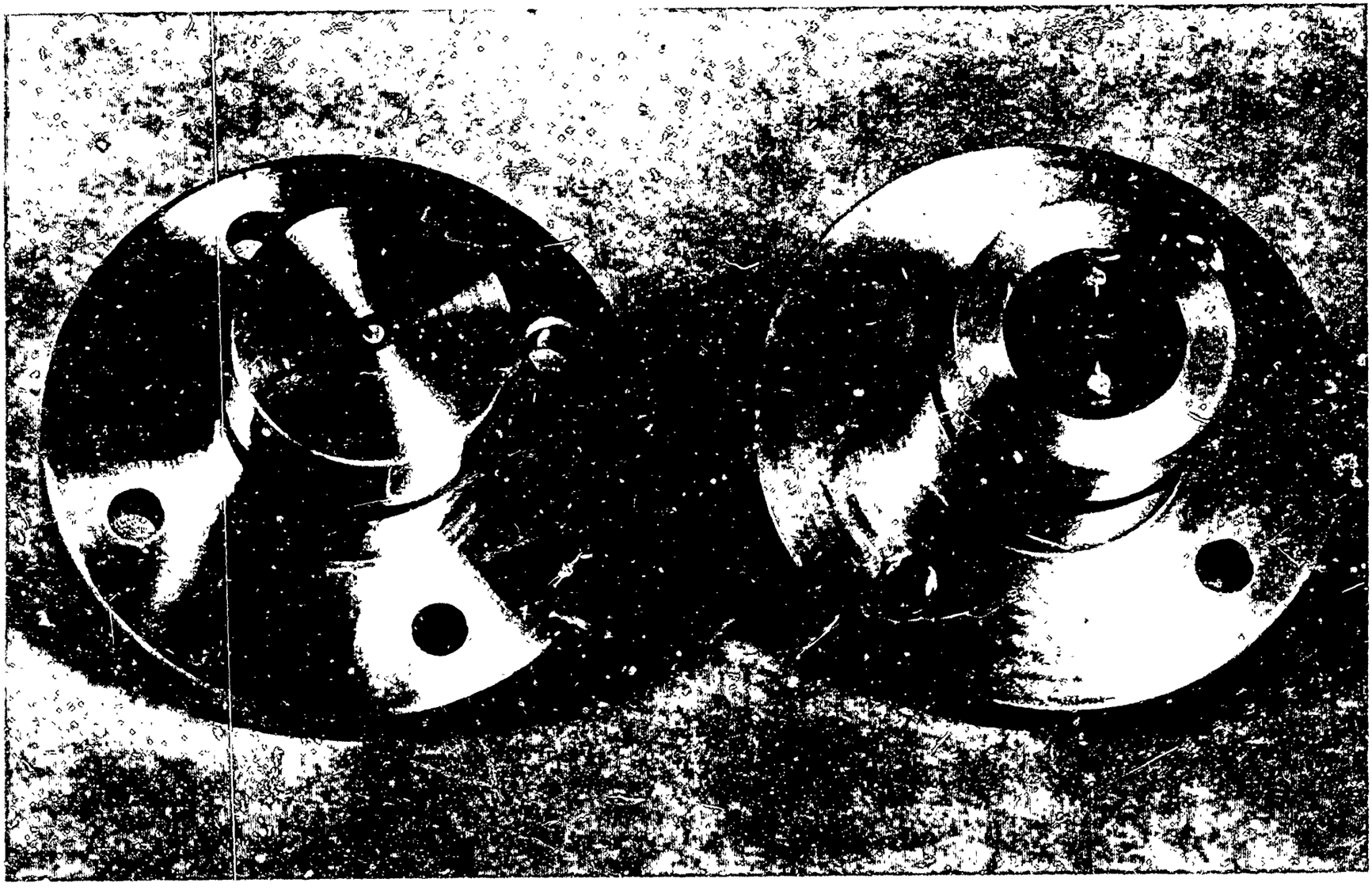

FIG. 69 IONIZATION (LEFT) AND HEAT FLUX (RIGHT) GAUGES

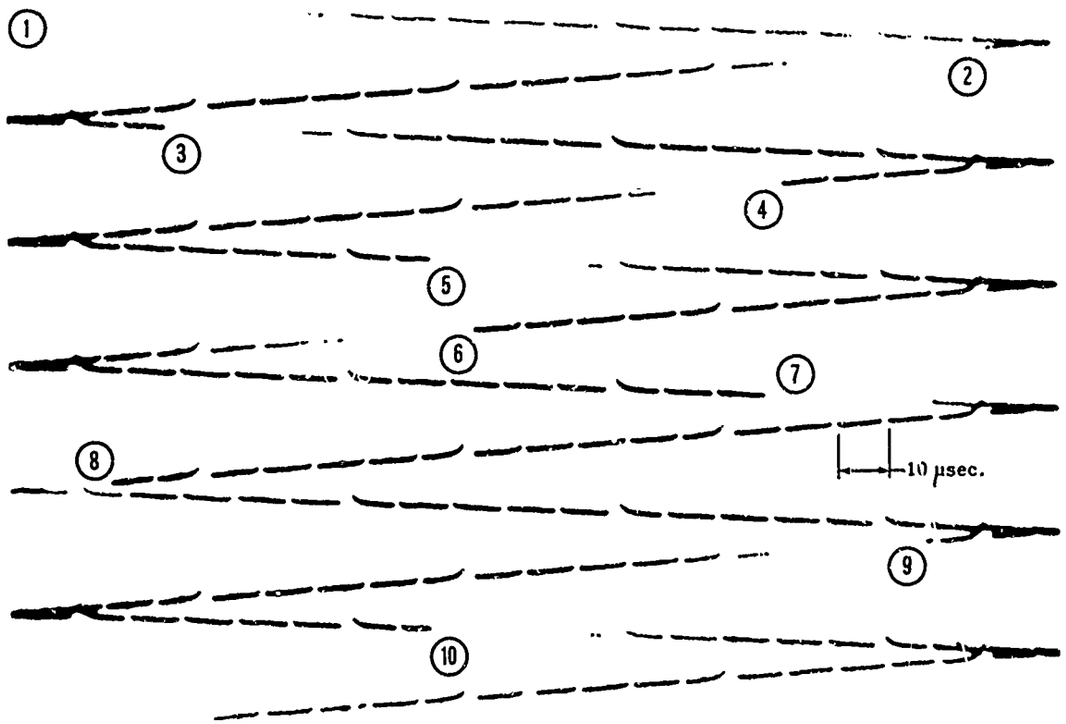

FIG. 70(a) TYPICAL RASTER DISPLAY FOR WAVE SPEED MEASUREMENT

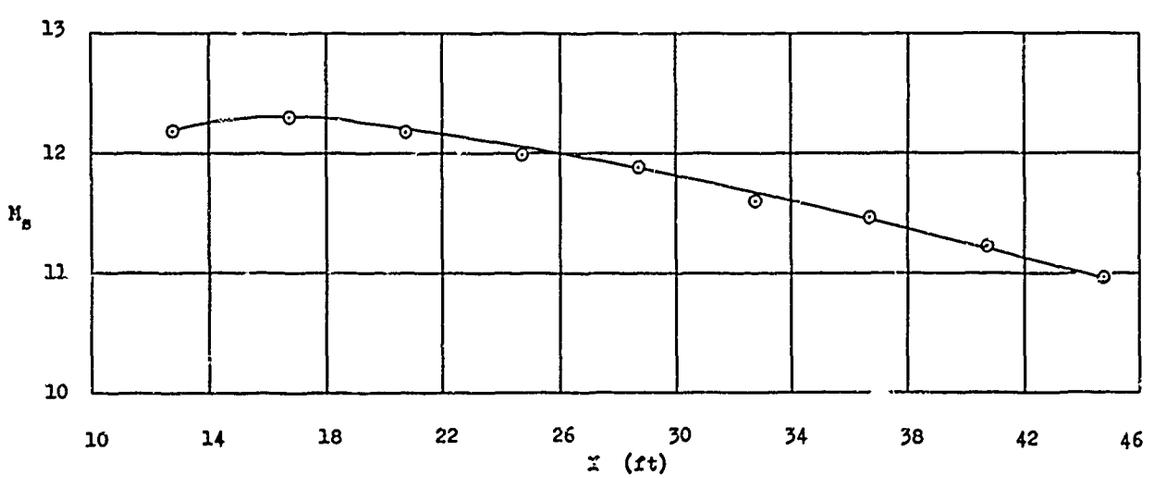

FIG. 70(b) SHOCK MACH NUMBER (M_S) vs DISTANCE (X) ALONG DRIVEN SECTION

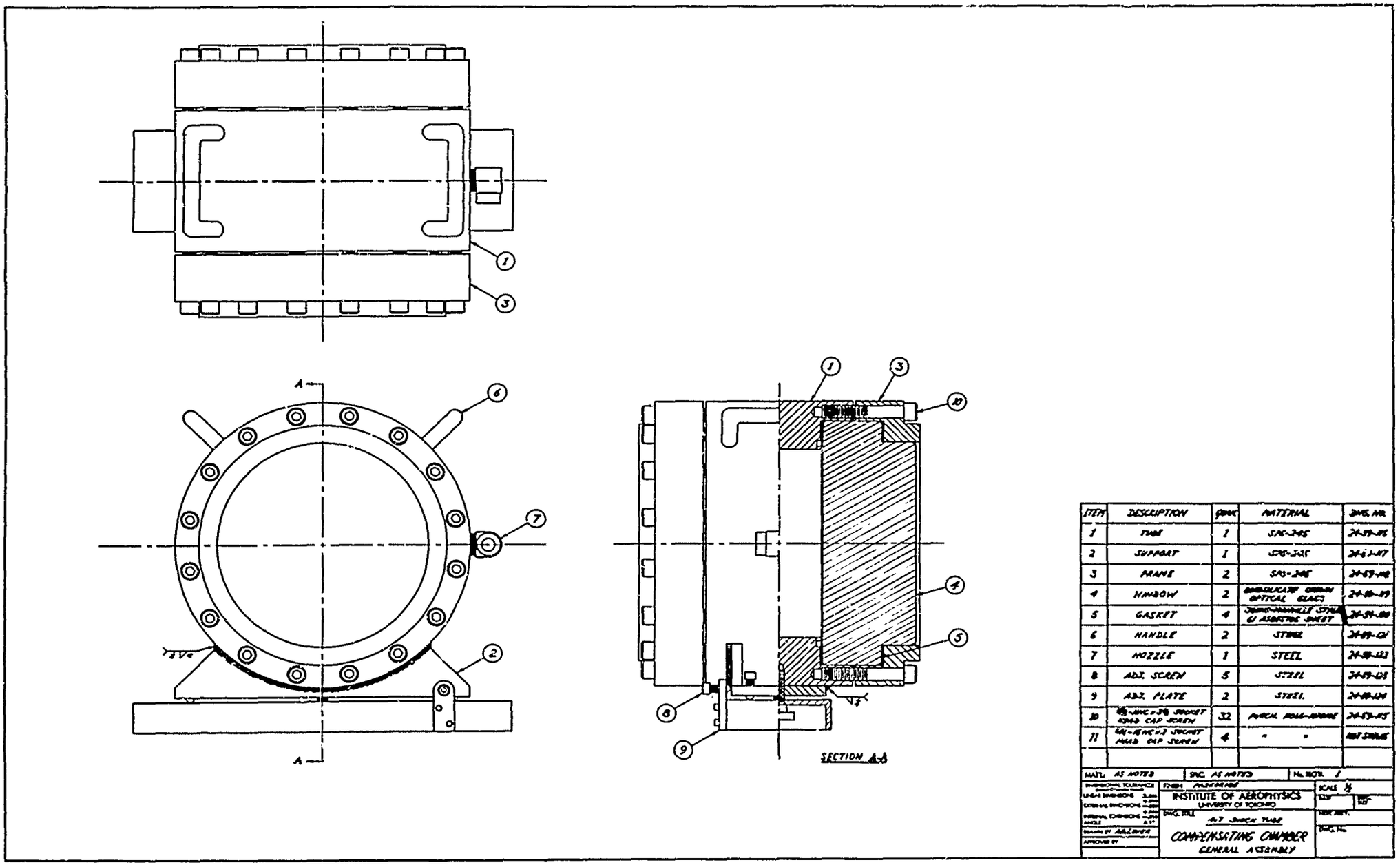

FIG. 71 DESIGN OF INTERFEROMETER COMPENSATING CHAMBER

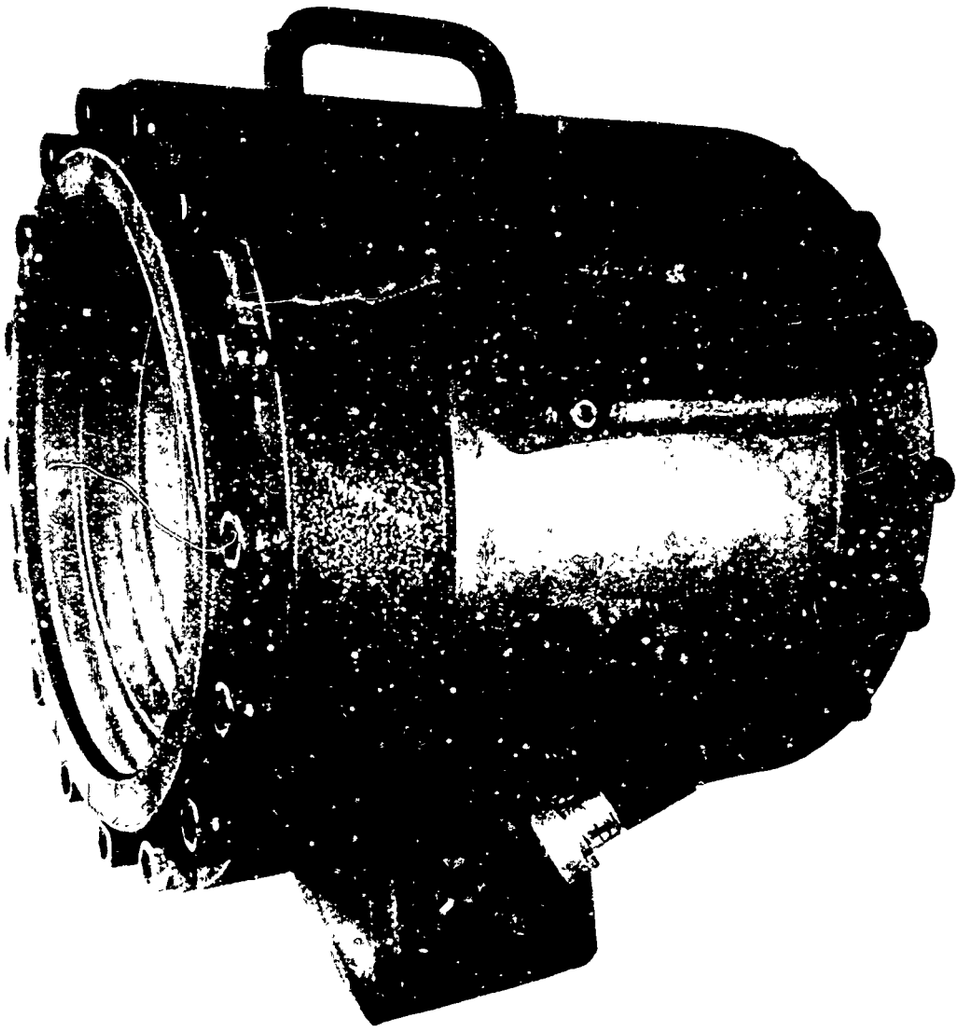

FIG. 72 VIEW OF INTERFEROMETER COMPENSATING CHAMBER

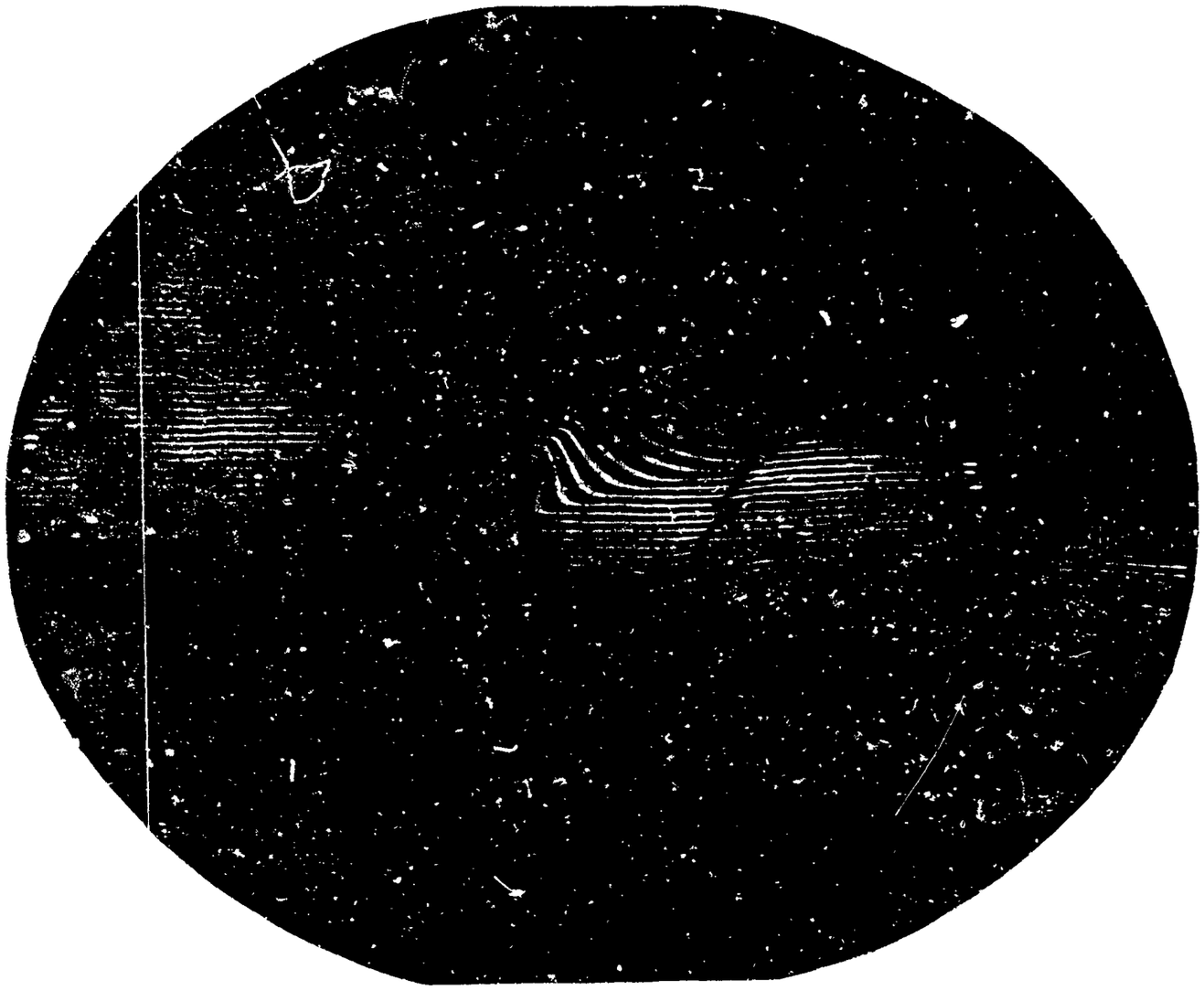

FIG. 73 INTERFEROGRAM OF FLOW OVER EXPANSION MODEL ($M_S = 3.67$)

before

after

FIG. 74 DAMAGE INFLICTED BY DIAPHRAGM PARTICLES

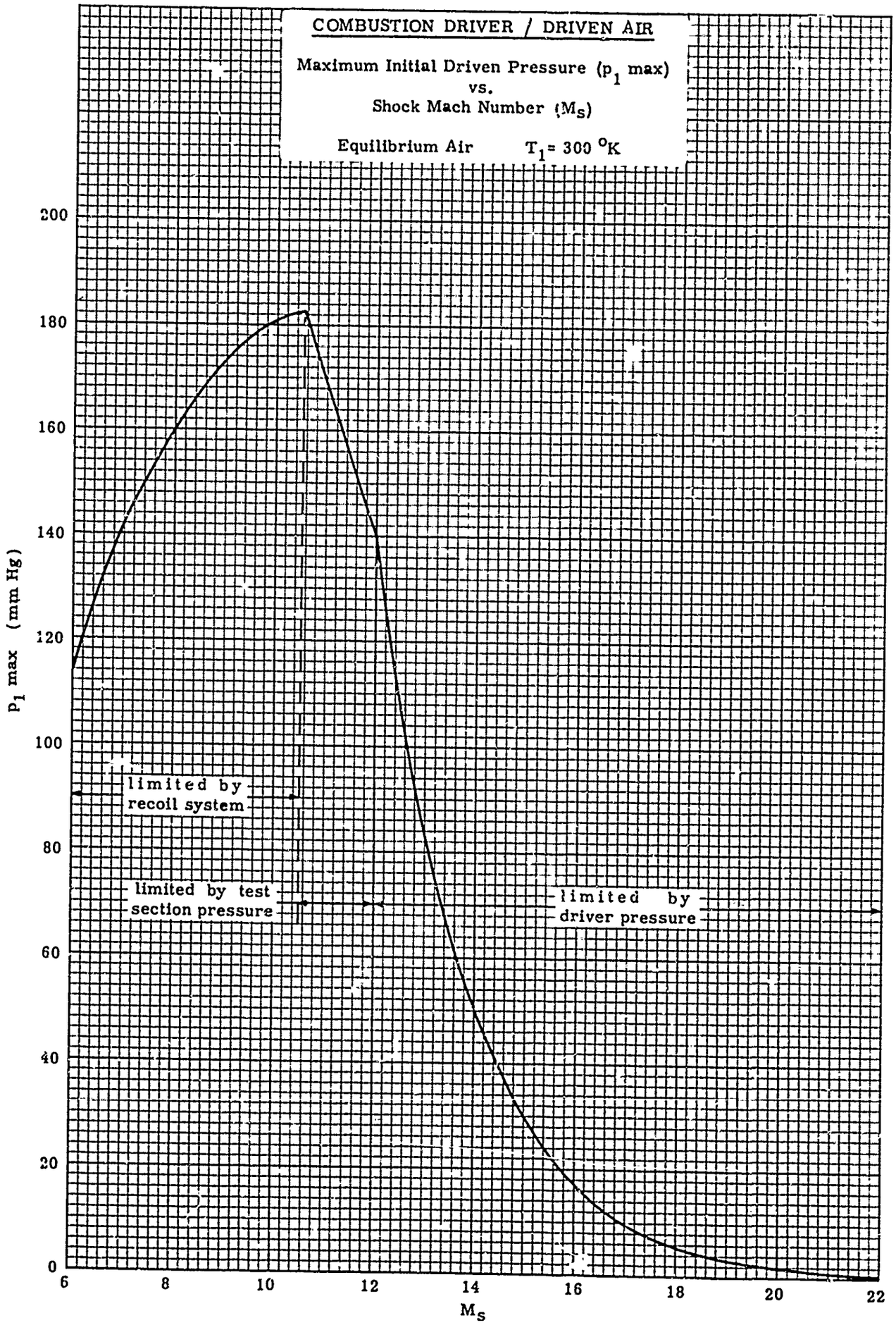
COMBUSTION DRIVER / DRIVEN AIR
Maximum Initial Driven Pressure (p_1 max)
vs.
Shock Mach Number (M_s)
Equilibrium Air
T_1 = 300 °K
p_1 max (mm Hg)
0
20
40
60
80
100
120
140
160
180
200
limited by recoil system
limited by test section pressure
limited by driver pressure
6
8
10
12
14
16
18
20
22
M_s

FIGURE 75

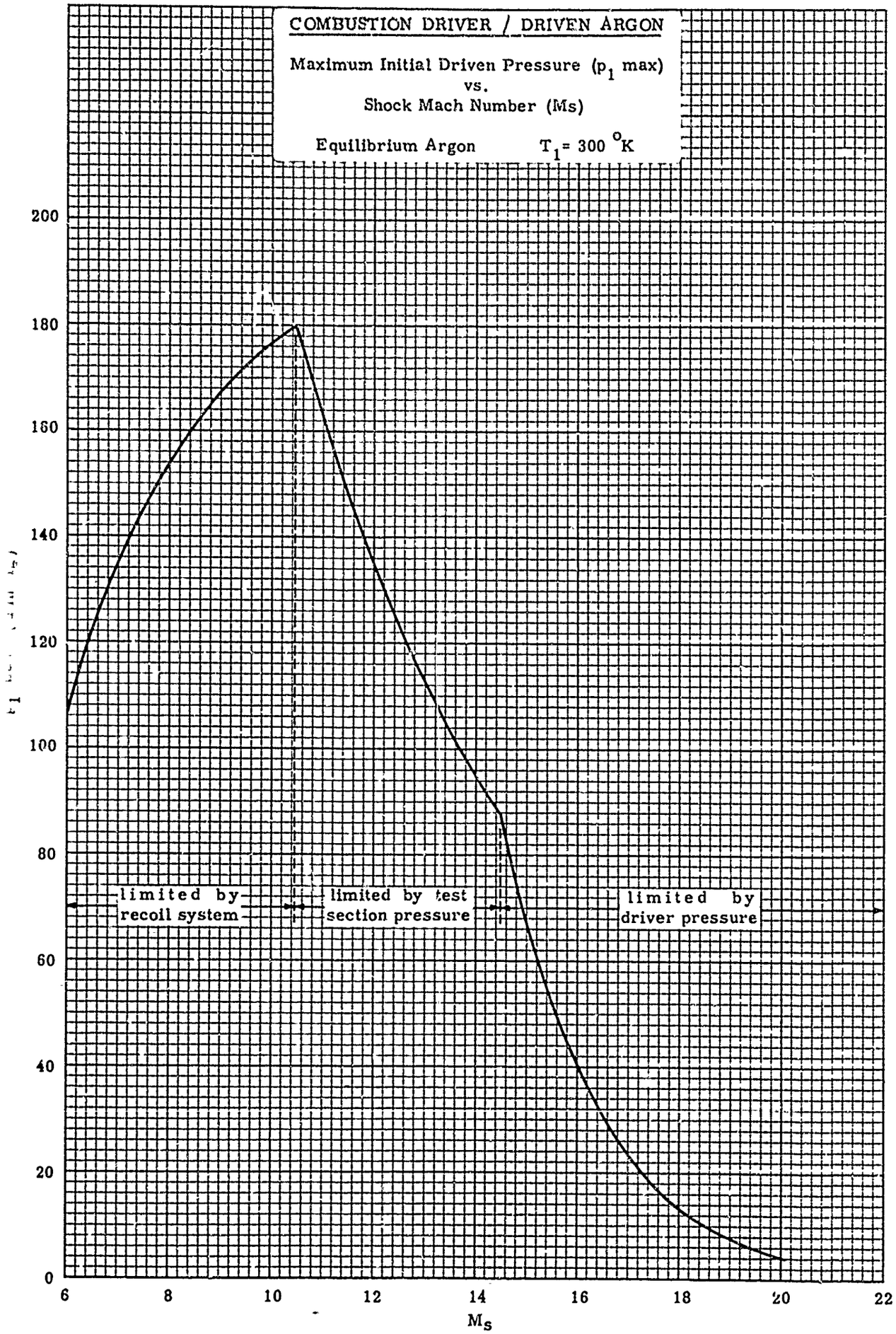
COMBUSTION DRIVER / DRIVEN ARGON
Maximum Initial Driven Pressure (p_1 max)
vs.
Shock Mach Number (Ms)
Equilibrium Argon
T_1 = 300 °K
200
180
160
140
120
100
80
60
40
20
0
6
8
10
12
14
16
18
20
22
M_s
limited by recoil system
limited by test section pressure
limited by driver pressure

FIGURE 76

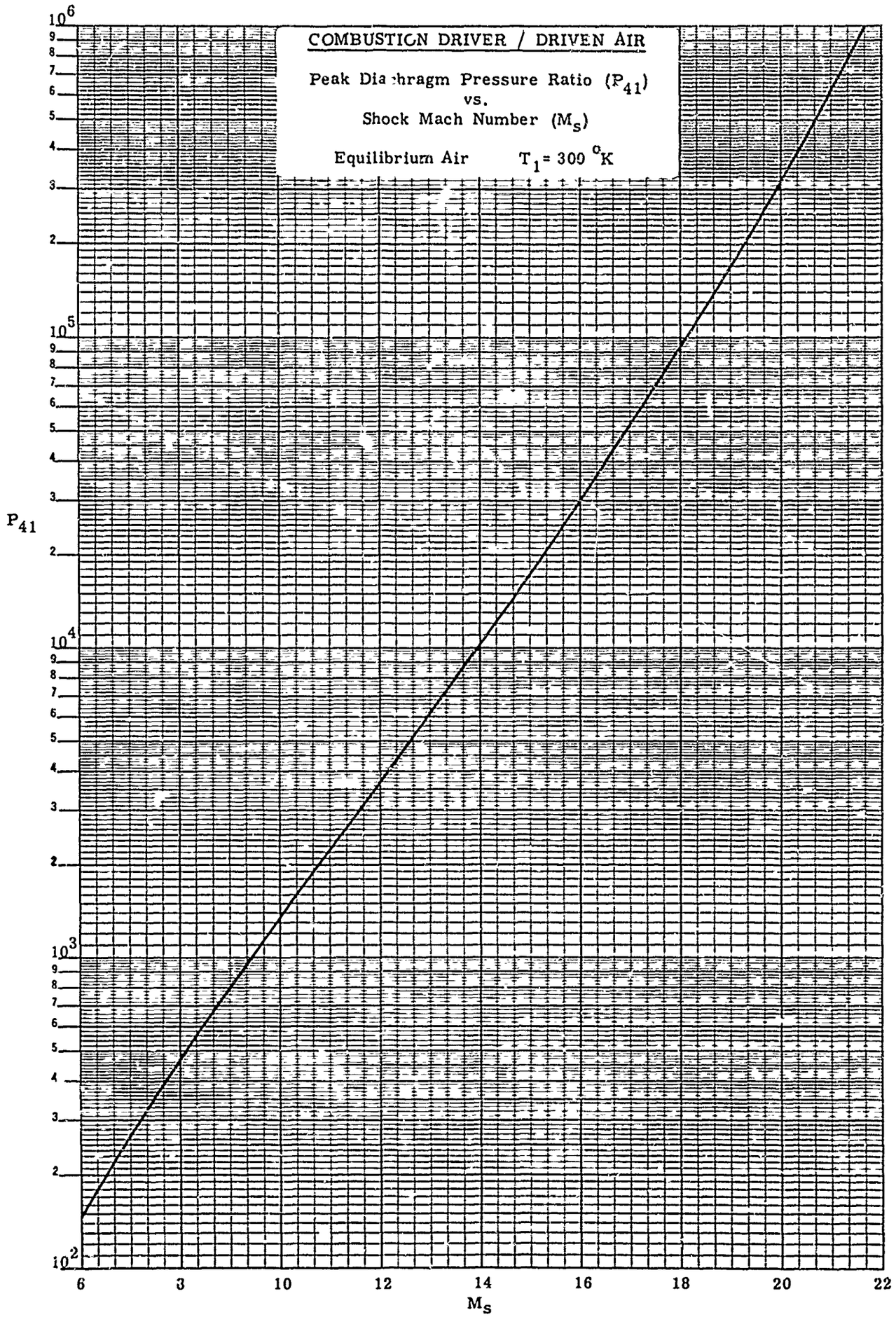

FIGURE 77
(See Fig. 75 for limitations on p_1)

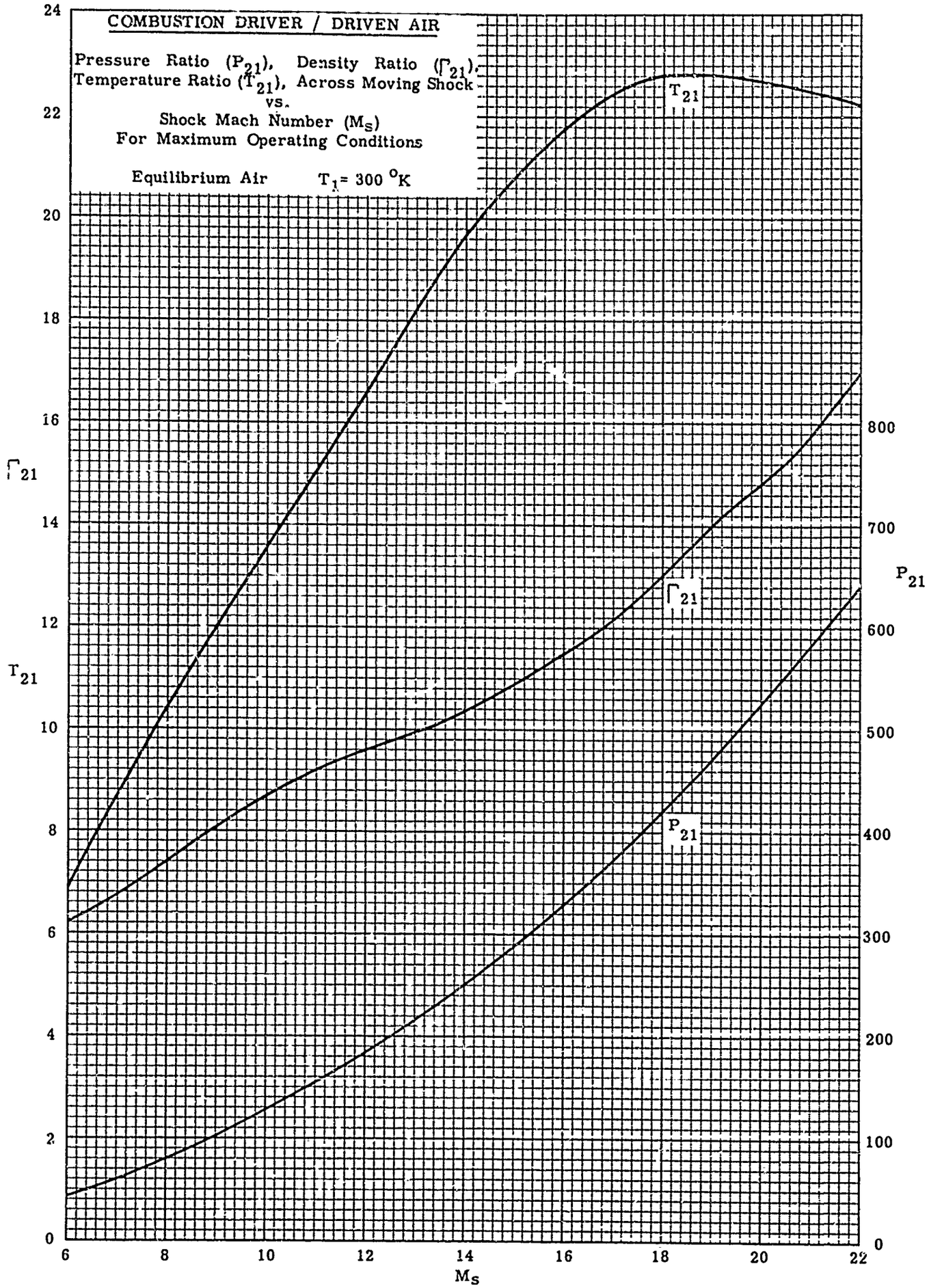
COMBUSTION DRIVER / DRIVEN AIR
Pressure Ratio (P_{21}), Density Ratio (Γ_{21}), Temperature Ratio (T_{21}), Across Moving Shock
vs.
Shock Mach Number (M_s)
For Maximum Operating Conditions
Equilibrium Air T_1 = 300 °K
T_{21}
Γ_{21}
P_{21}
M_s
0
2
4
6
8
10
12
14
16
18
20
22
24
100
200
300
400
500
600
700
800

FIGURE 78

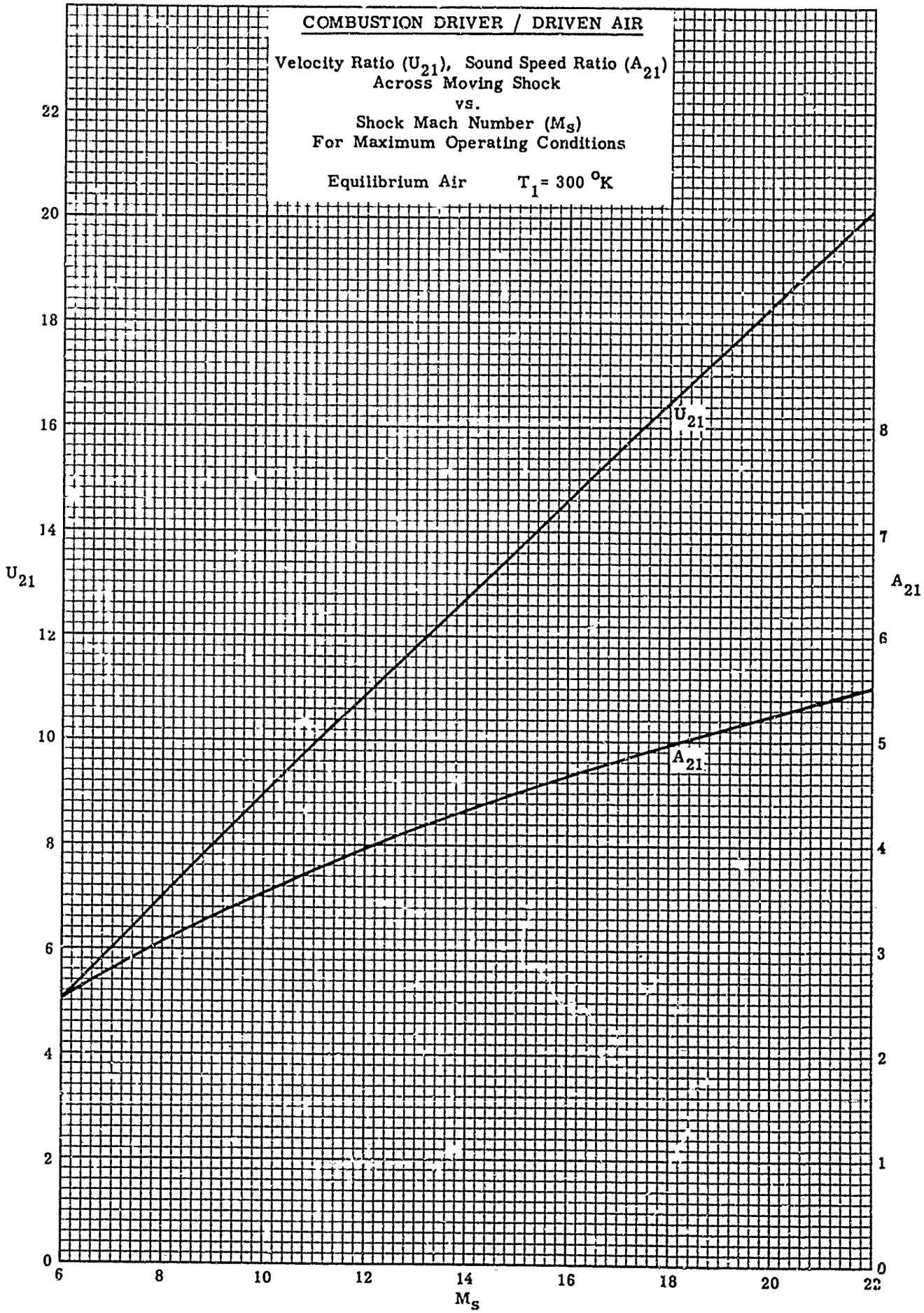
COMBUSTION DRIVER / DRIVEN AIR
Velocity Ratio (U_{21}), Sound Speed Ratio (A_{21})
Across Moving Shock
vs.
Shock Mach Number (M_s)
For Maximum Operating Conditions
Equilibrium Air T_1 = 300 °K
U_{21}
A_{21}
M_s
0
2
4
6
8
10
12
14
16
18
20
22
1
3
5
7
6
8
10
12
14
16
18
20
22

FIGURE 79

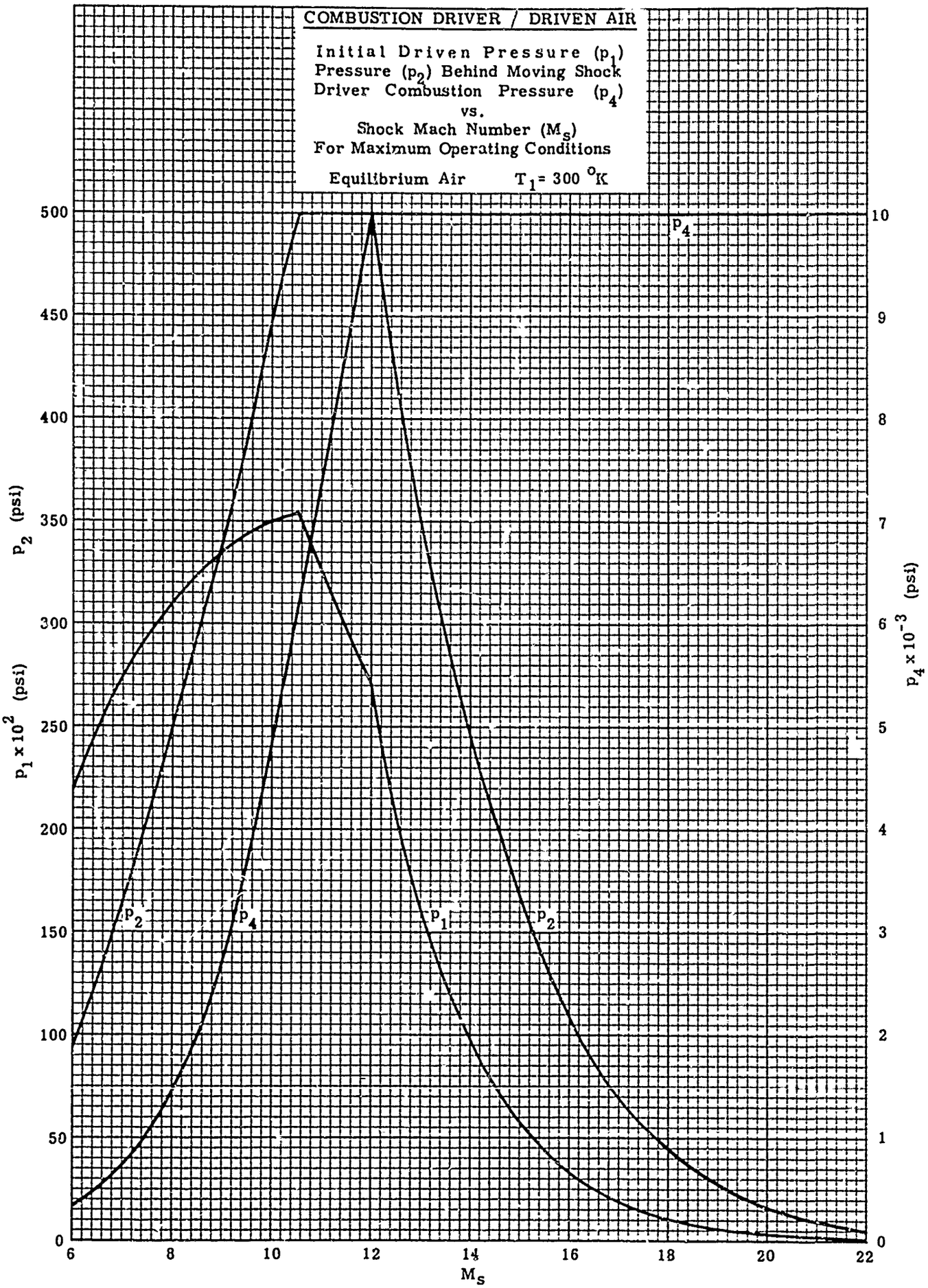
COMBUSTION DRIVER / DRIVEN AIR
Initial Driven Pressure (p_1)
Pressure (p_2) Behind Moving Shock
Driver Combustion Pressure (p_4)
vs.
Shock Mach Number (M_s)
For Maximum Operating Conditions
Equilibrium Air T_1 = 300 °K
p_2 (psi)
$p_1 \times 10^2$ (psi)
$p_4 \times 10^{-3}$ (psi)
M_s
p_2
p_4
p_1
p_2
p_4
0
50
100
150
200
250
300
350
400
450
500
0
1
2
3
4
5
6
7
8
9
10
6
8
10
12
14
16
18
20
22

FIGURE 80

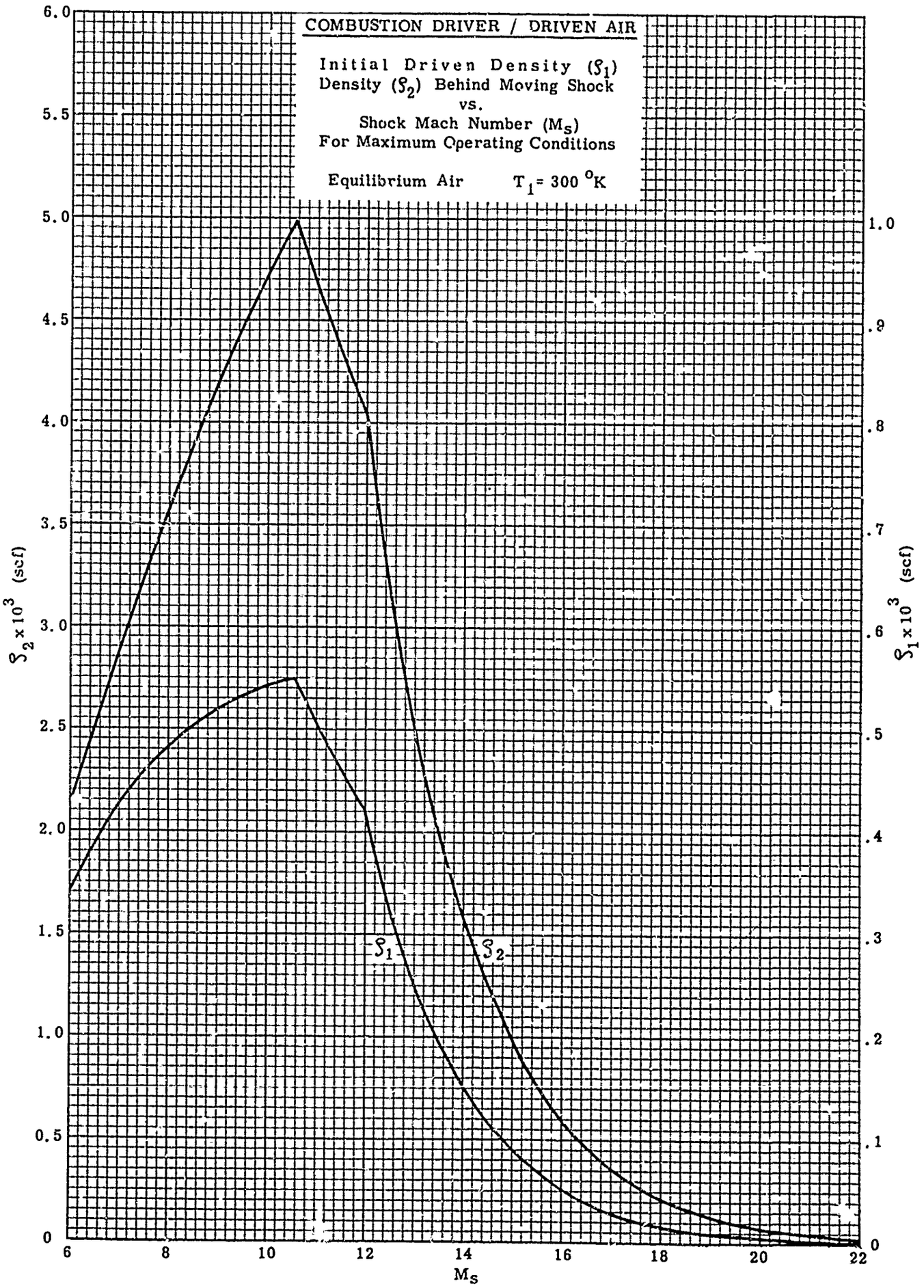
COMBUSTION DRIVER / DRIVEN AIR
Initial Driven Density (ρ_1)
Density (ρ_2) Behind Moving Shock
vs.
Shock Mach Number (M_s)
For Maximum Operating Conditions
Equilibrium Air
T_1 = 300 °K
$\rho_2 \times 10^3$ (scf)
$\rho_1 \times 10^3$ (scf)
M_s
ρ_1
ρ_2
6.0
5.5
5.0
4.5
4.0
3.5
3.0
2.5
2.0
1.5
1.0
0.5
0
1.0
.9
.8
.7
.6
.5
.4
.3
.2
.1
0
6
8
10
12
14
16
18
20
22

FIGURE 81

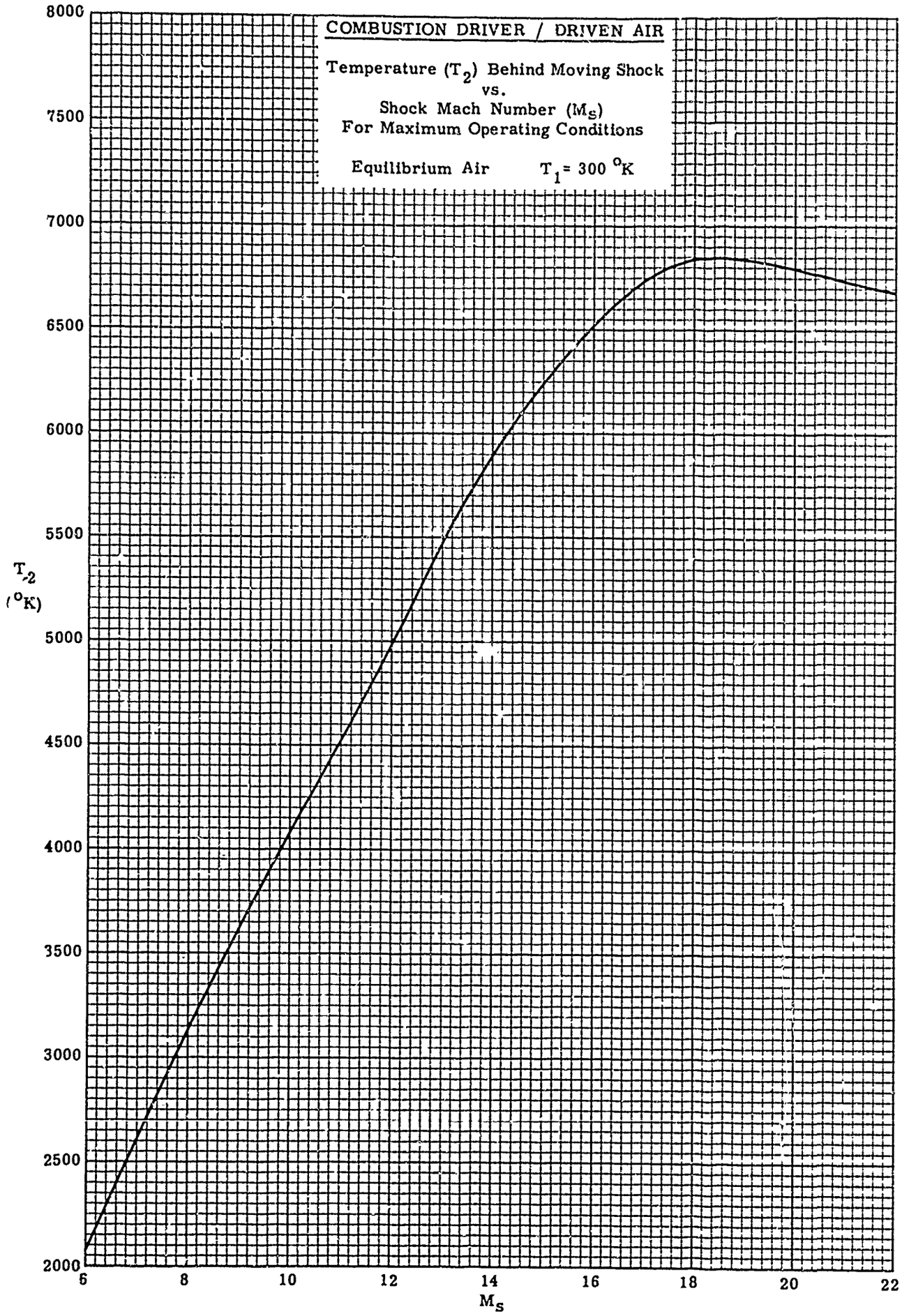
COMBUSTION DRIVER / DRIVEN AIR
Temperature (T_2) Behind Moving Shock
vs.
Shock Mach Number (M_s)
For Maximum Operating Conditions
Equilibrium Air
T_1 = 300 °K
8000
7500
7000
6500
6000
5500
5000
4500
4000
3500
3000
2500
2000
T_2
(°K)
6
8
10
12
14
16
18
20
22
M_s

FIGURE 82

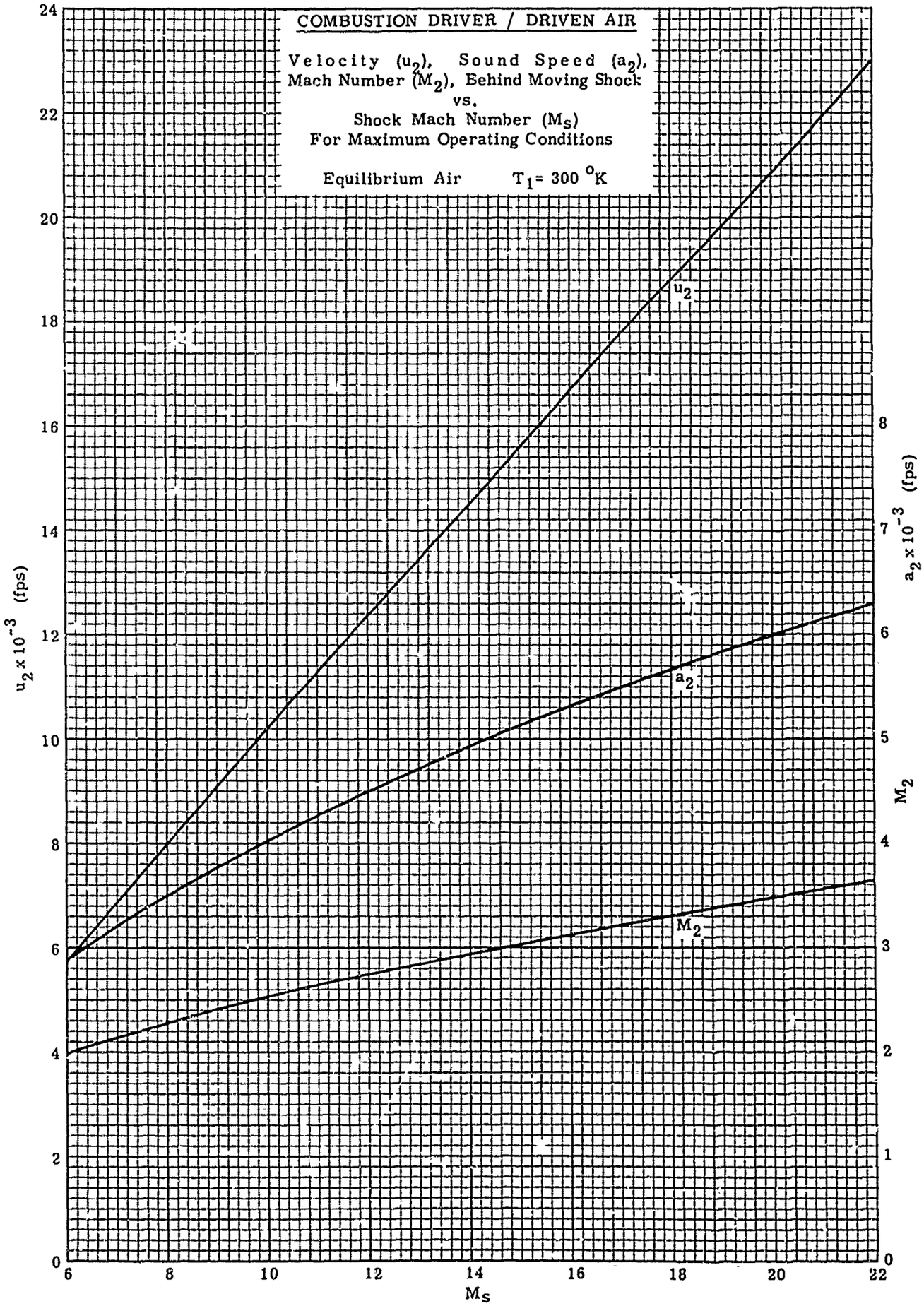
COMBUSTION DRIVER / DRIVEN AIR
Velocity (u_2), Sound Speed (a_2), Mach Number (M_2), Behind Moving Shock
vs.
Shock Mach Number (M_s)
For Maximum Operating Conditions
Equilibrium Air T_1 = 300 °K
u_2
a_2
M_2
$u_2 \times 10^{-3}$ (fps)
$a_2 \times 10^{-3}$ (fps)
M_2
M_s
0
2
4
6
8
10
12
14
16
18
20
22
24
1
3
5
7
6
8
10
12
14
16
18
20
22

FIGURE 83

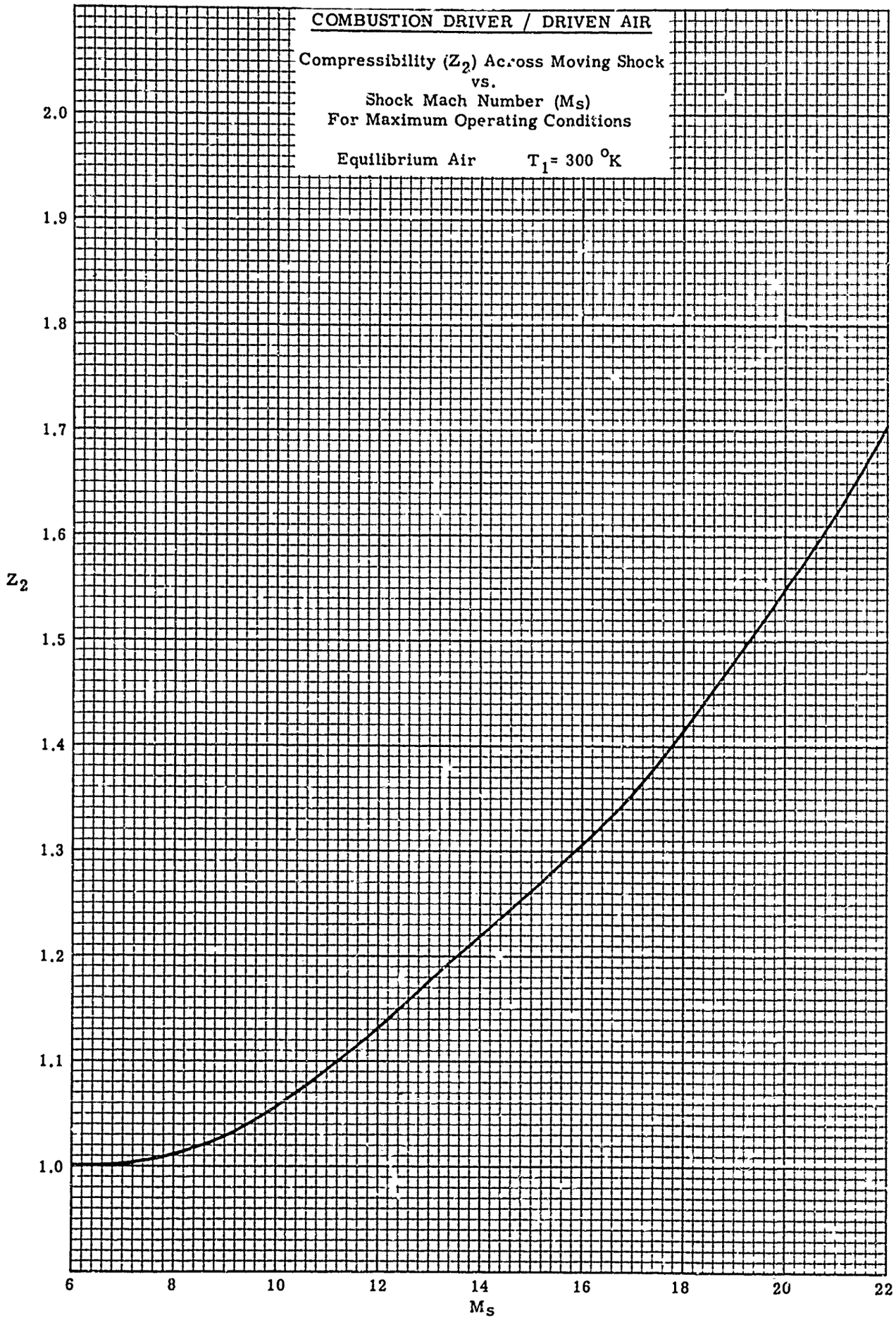
COMBUSTION DRIVER / DRIVEN AIR
Compressibility (Z_2) Across Moving Shock
vs.
Shock Mach Number (M_S)
For Maximum Operating Conditions
Equilibrium Air T_1 = 300 °K
2.0
1.9
1.8
1.7
1.6
Z_2
1.5
1.4
1.3
1.2
1.1
1.0
6
8
10
12
14
16
18
20
22
M_S

FIGURE 84

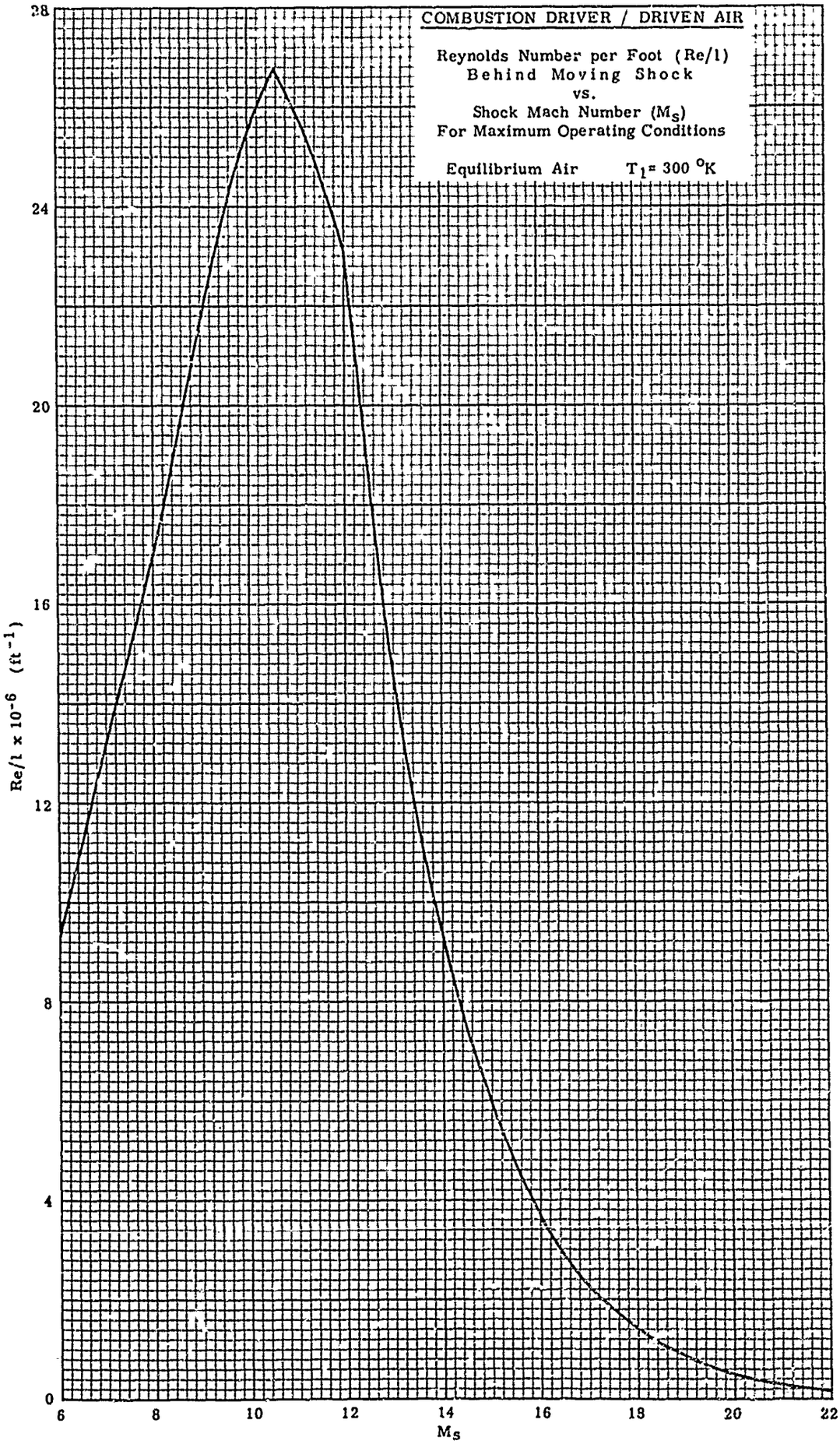
COMBUSTION DRIVER / DRIVEN AIR
Reynolds Number per Foot (Re/l)
Behind Moving Shock
vs.
Shock Mach Number (M_S)
For Maximum Operating Conditions
Equilibrium Air T_1 = 300 °K
Re/l x 10^{-6} (ft^{-1})
0
4
8
12
16
20
24
28
6
8
10
12
14
16
18
20
22
M_S

FIGURE 85

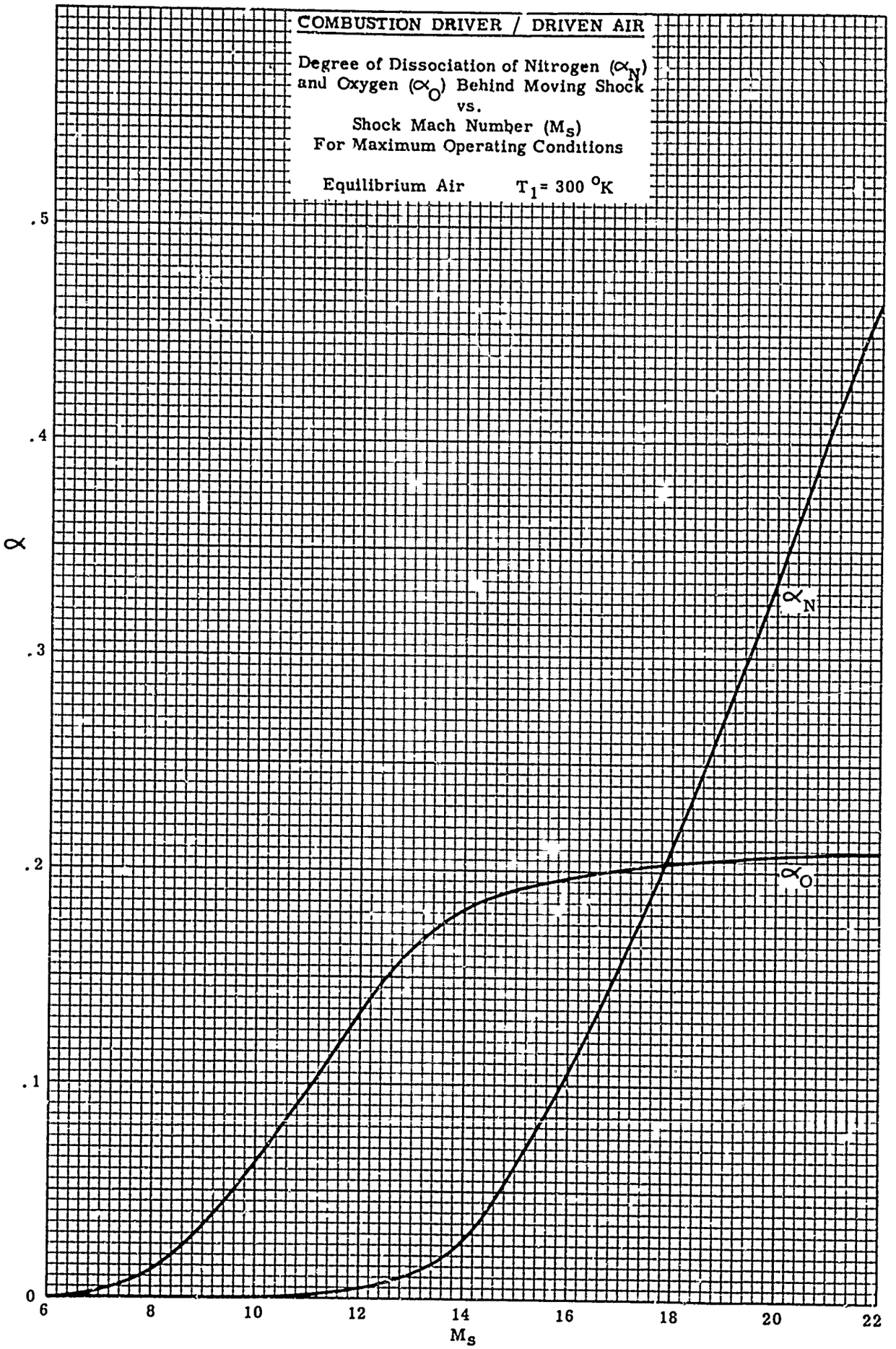
COMBUSTION DRIVER / DRIVEN AIR
Degree of Dissociation of Nitrogen (α_N) and Oxygen (α_O) Behind Moving Shock
vs.
Shock Mach Number (M_s)
For Maximum Operating Conditions
Equilibrium Air $T_1 = 300\ ^oK$
α
.5
.4
.3
.2
.1
0
6
8
10
12
14
16
18
20
22
M_s
α_N
α_O

FIGURE 86

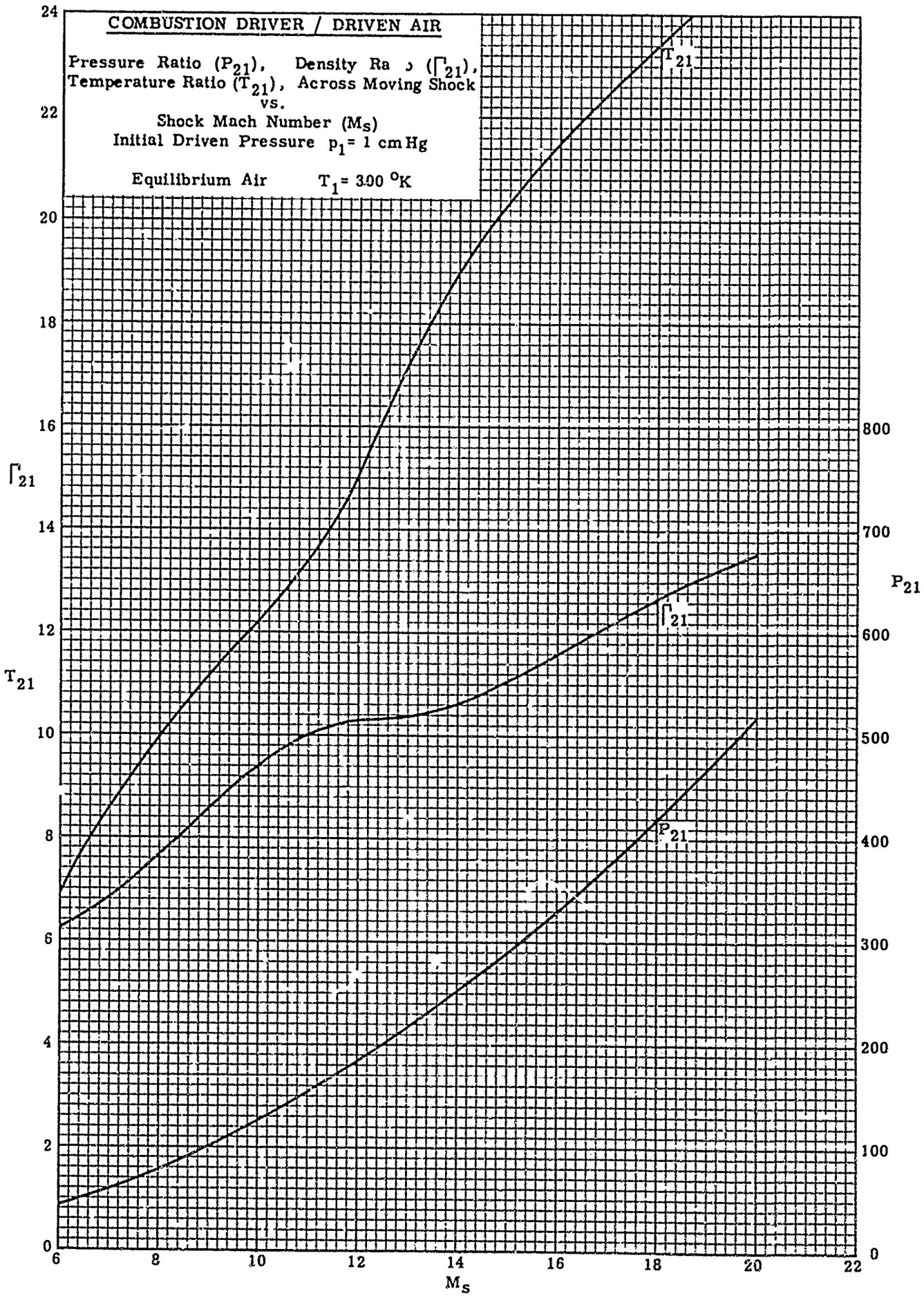
COMBUSTION DRIVER / DRIVEN AIR
Pressure Ratio (P_{21}), Density Ra ɔ (Γ_{21}),
Temperature Ratio (T_{21}), Across Moving Shock
vs.
Shock Mach Number (M_s)
Initial Driven Pressure p_1 = 1 cm Hg
Equilibrium Air T_1 = 300 °K
T_{21}
Γ_{21}
P_{21}
M_s
0
2
4
6
8
10
12
14
16
18
20
22
24
100
200
300
400
500
600
700
800

FIGURE 87

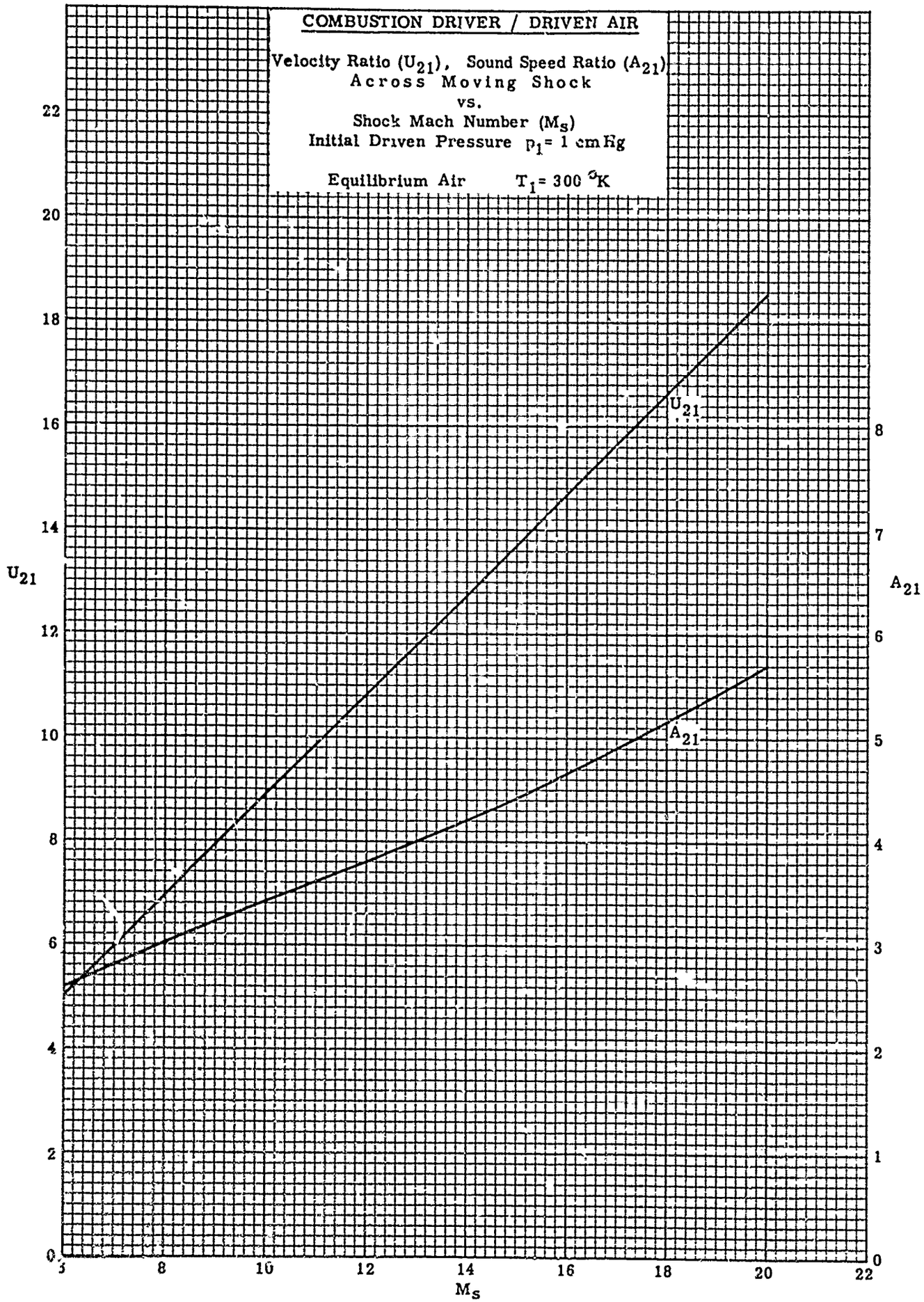
COMBUSTION DRIVER / DRIVEN AIR
Velocity Ratio (U_{21}), Sound Speed Ratio (A_{21})
Across Moving Shock
vs.
Shock Mach Number (M_s)
Initial Driven Pressure p_1 = 1 cmHg
Equilibrium Air T_1 = 300 °K
U_{21}
A_{21}
M_s
0
2
4
6
8
10
12
14
16
18
20
22
1
3
5
7

FIGURE 88

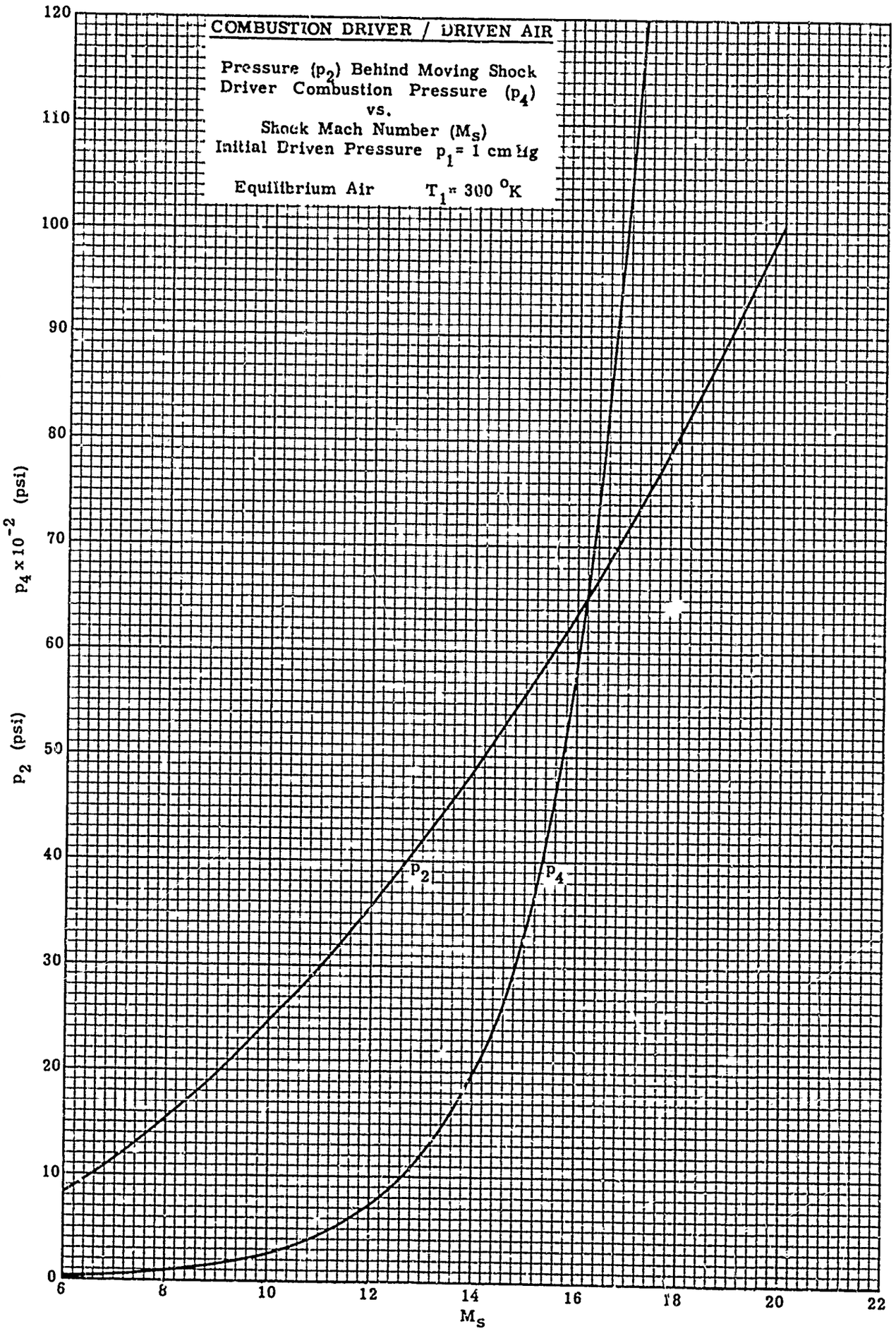
COMBUSTION DRIVER / DRIVEN AIR
Pressure (p_2) Behind Moving Shock
Driver Combustion Pressure (p_4)
vs.
Shock Mach Number (M_s)
Initial Driven Pressure p_1 = 1 cm Hg
Equilibrium Air T_1 = 300 °K
p_2
p_4
$p_4 \times 10^{-2}$ (psi)
p_2 (psi)
M_s
0
10
20
30
40
50
60
70
80
90
100
110
120
6
8
10
12
14
16
18
20
22

FIGURE 89

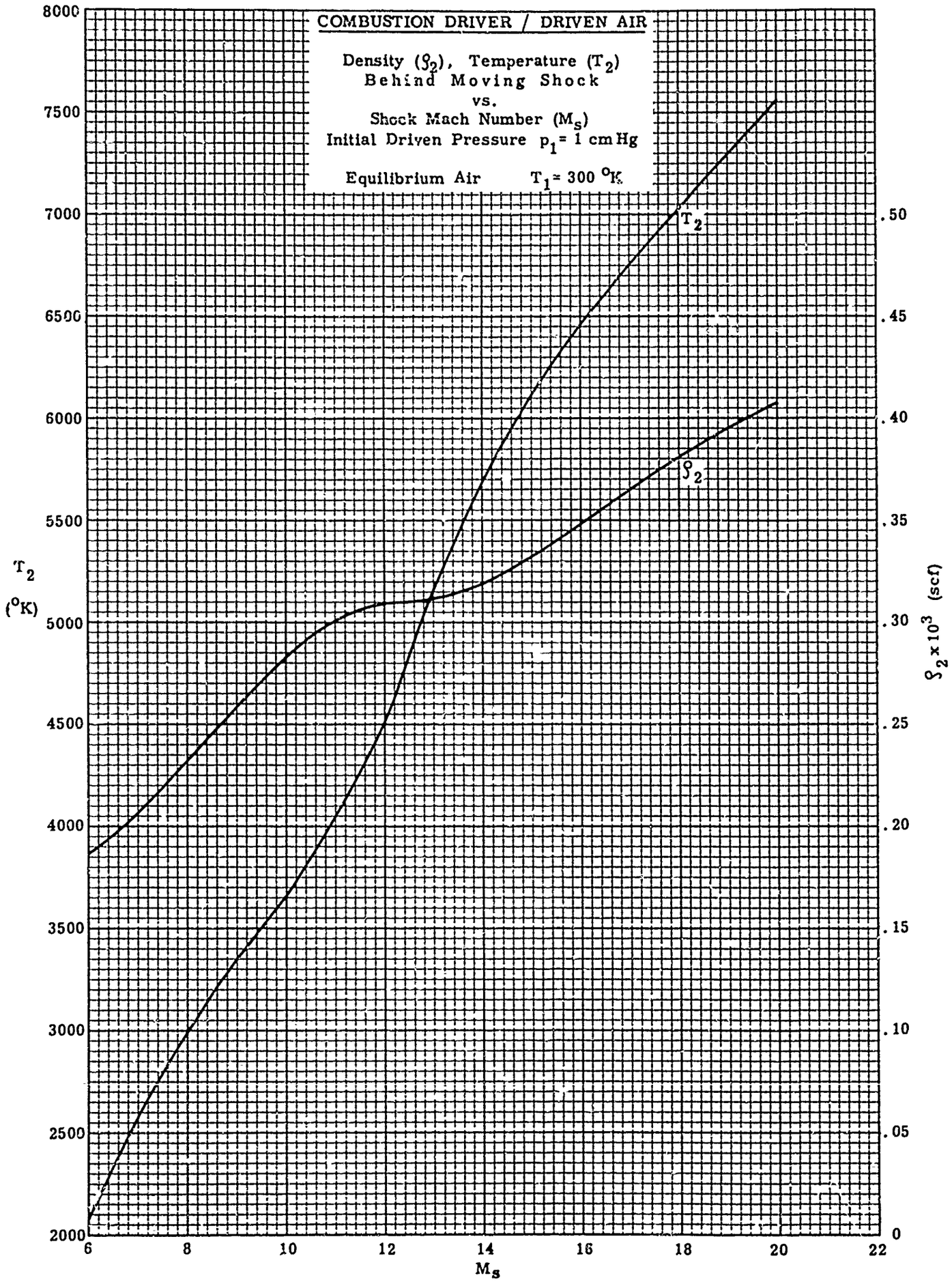
COMBUSTION DRIVER / DRIVEN AIR
Density (ρ_2), Temperature (T_2)
Behind Moving Shock
vs.
Shock Mach Number (M_s)
Initial Driven Pressure p_1 = 1 cm Hg
Equilibrium Air T_1 = 300 °K
T_2
ρ_2
T_2 (°K)
$\rho_2 \times 10^3$ (scf)
M_s
8000
7500
7000
6500
6000
5500
5000
4500
4000
3500
3000
2500
2000
.50
.45
.40
.35
.30
.25
.20
.15
.10
.05
0
6
8
10
12
14
16
18
20
22

FIGURE 90

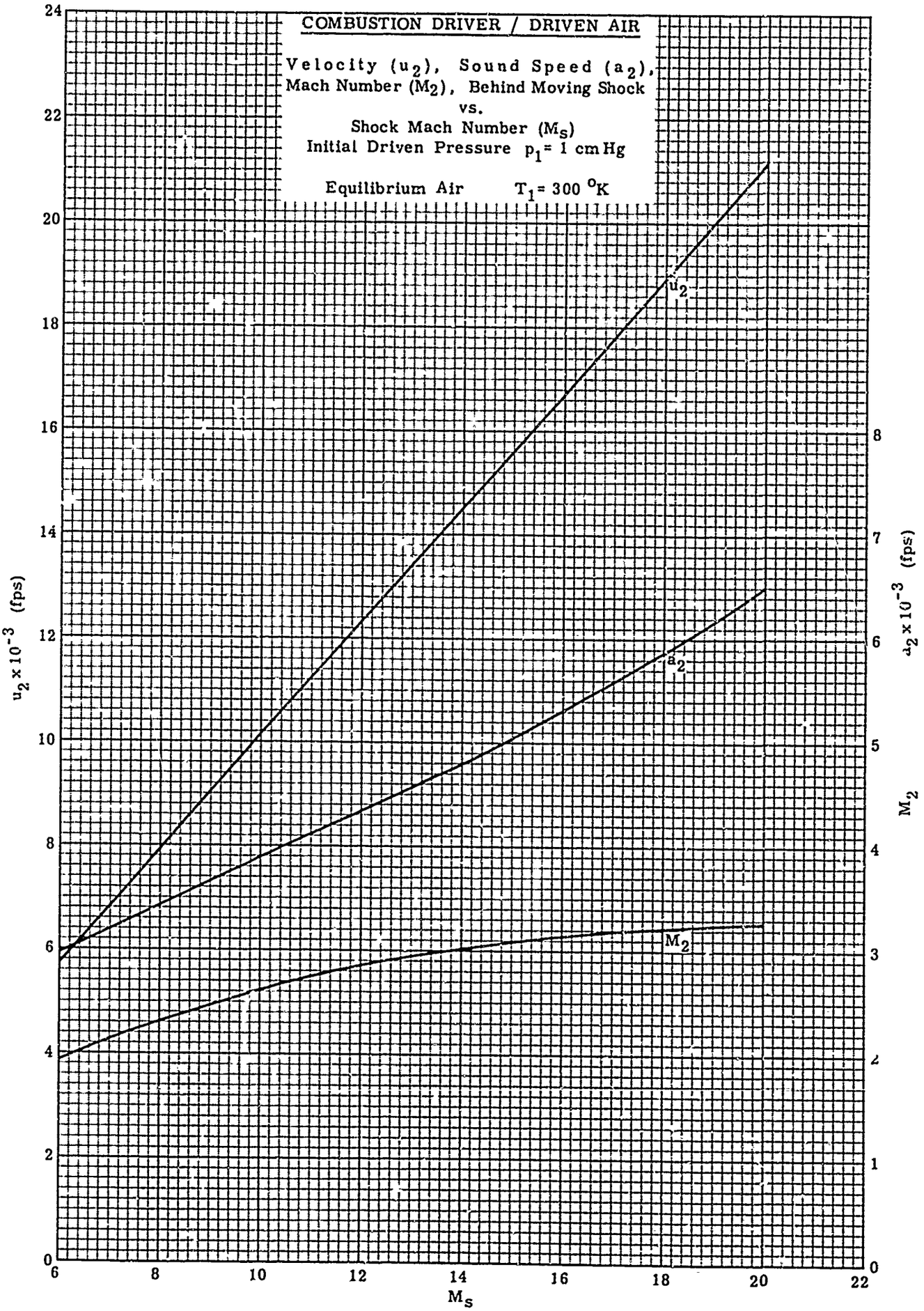
COMBUSTION DRIVER / DRIVEN AIR
Velocity (u_2), Sound Speed (a_2), Mach Number (M_2), Behind Moving Shock
vs.
Shock Mach Number (M_s)
Initial Driven Pressure p_1 = 1 cm Hg
Equilibrium Air T_1 = 300 °K
u_2
a_2
M_2
$u_2 \times 10^{-3}$ (fps)
$a_2 \times 10^{-3}$ (fps)
M_2
M_s
0
2
4
6
8
10
12
14
16
18
20
22
24
1
3
5
7
6
8
10
12
14
16
18
20
22

FIGURE 91

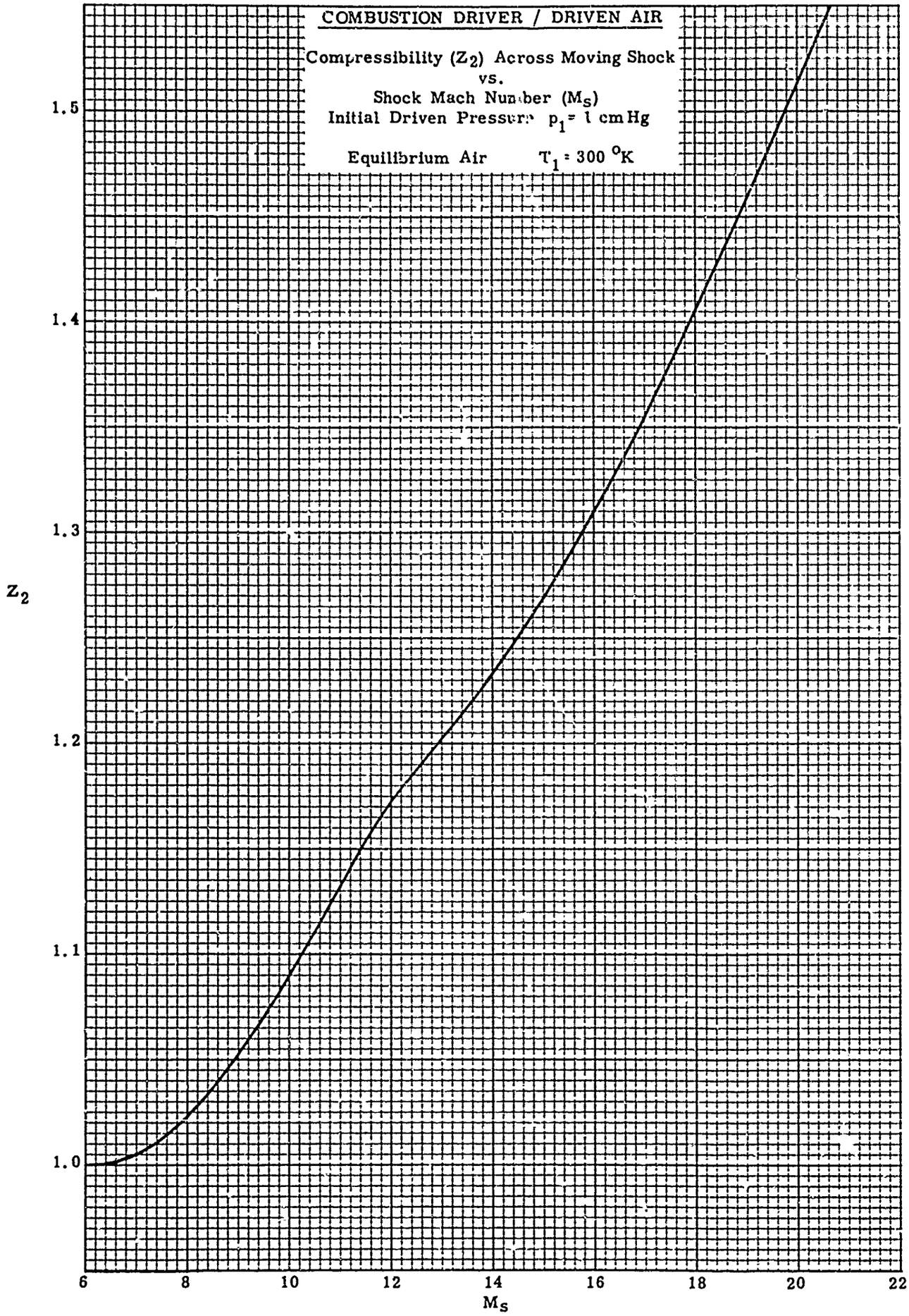
COMBUSTION DRIVER / DRIVEN AIR
Compressibility (Z_2) Across Moving Shock
vs.
Shock Mach Number (M_S)
Initial Driven Pressure p_1 = 1 cm Hg
Equilibrium Air T_1 = 300 °K
1.5
1.4
1.3
1.2
1.1
1.0
Z_2
6
8
10
12
14
16
18
20
22
M_S

FIGURE 92

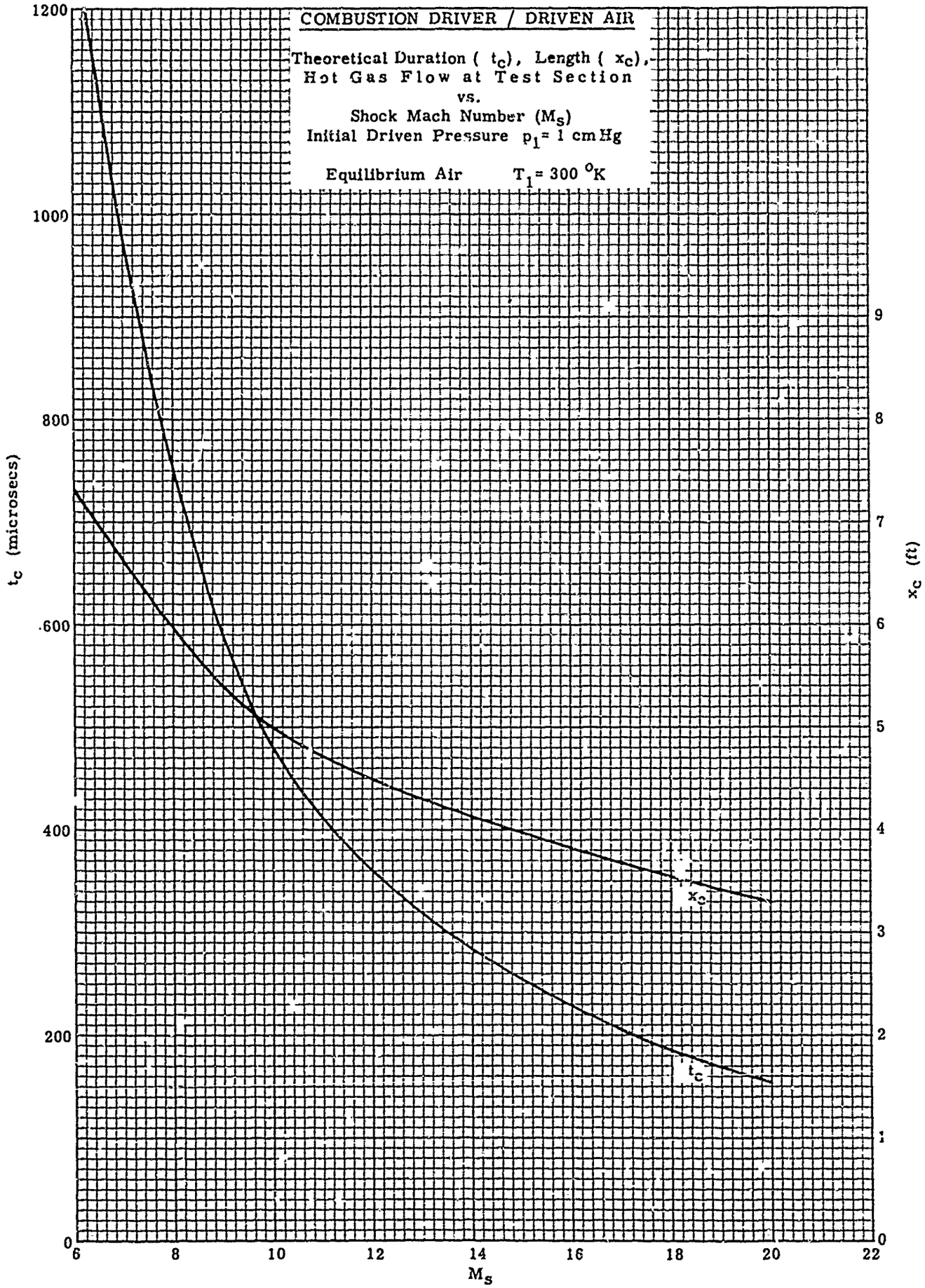
COMBUSTION DRIVER / DRIVEN AIR
Theoretical Duration (t_c), Length (x_c),
Hot Gas Flow at Test Section
vs.
Shock Mach Number (M_s)
Initial Driven Pressure p_1 = 1 cm Hg
Equilibrium Air T_1 = 300 °K
t_c (microsecs)
x_c (ft)
M_s
x_c
t_c
1200
1000
800
600
400
200
0
9
8
7
6
5
4
3
2
1
0
6
8
10
12
14
16
18
20
22

FIGURE 93

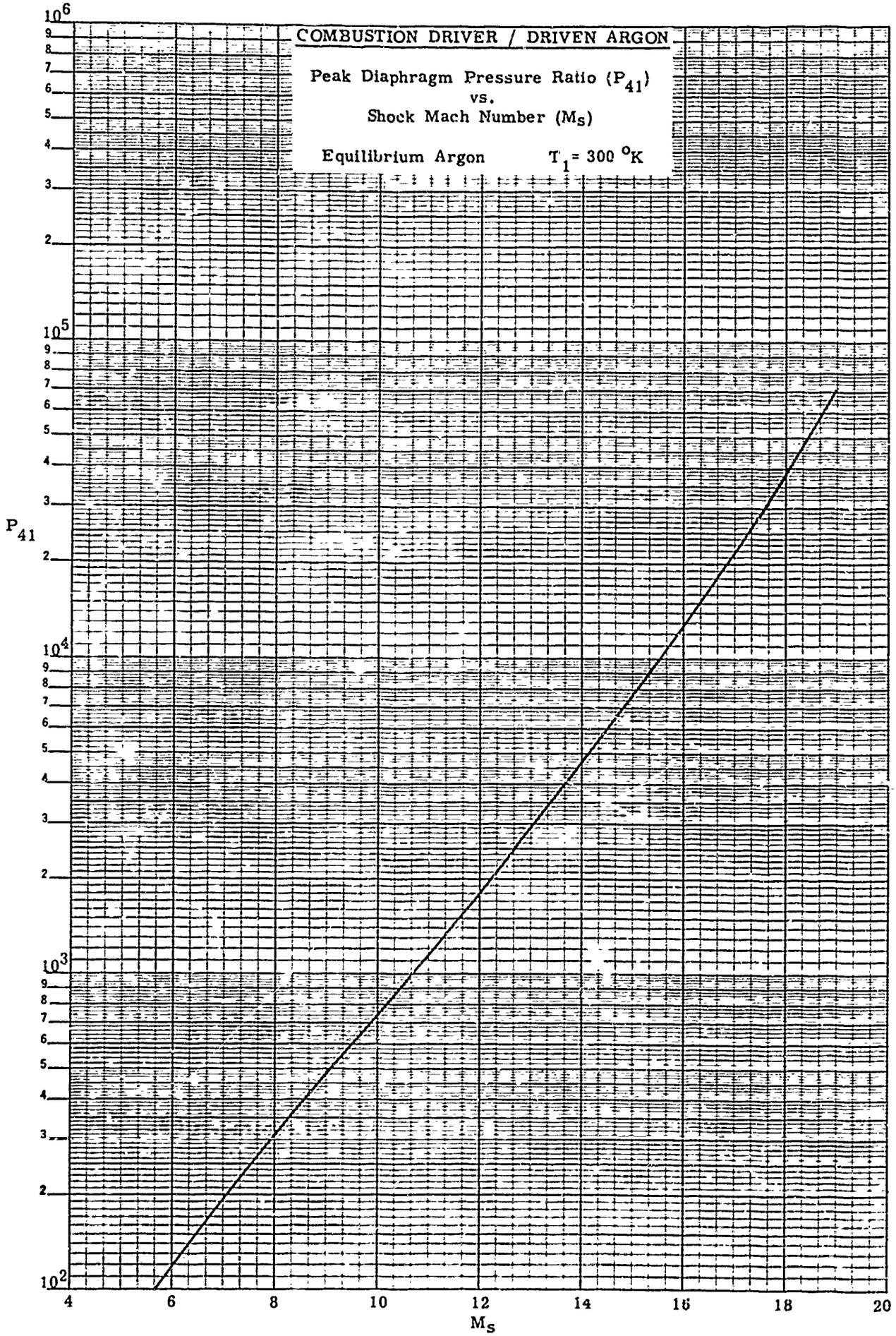

FIGURE 94
(See Fig. 76 for limitations on p_1)

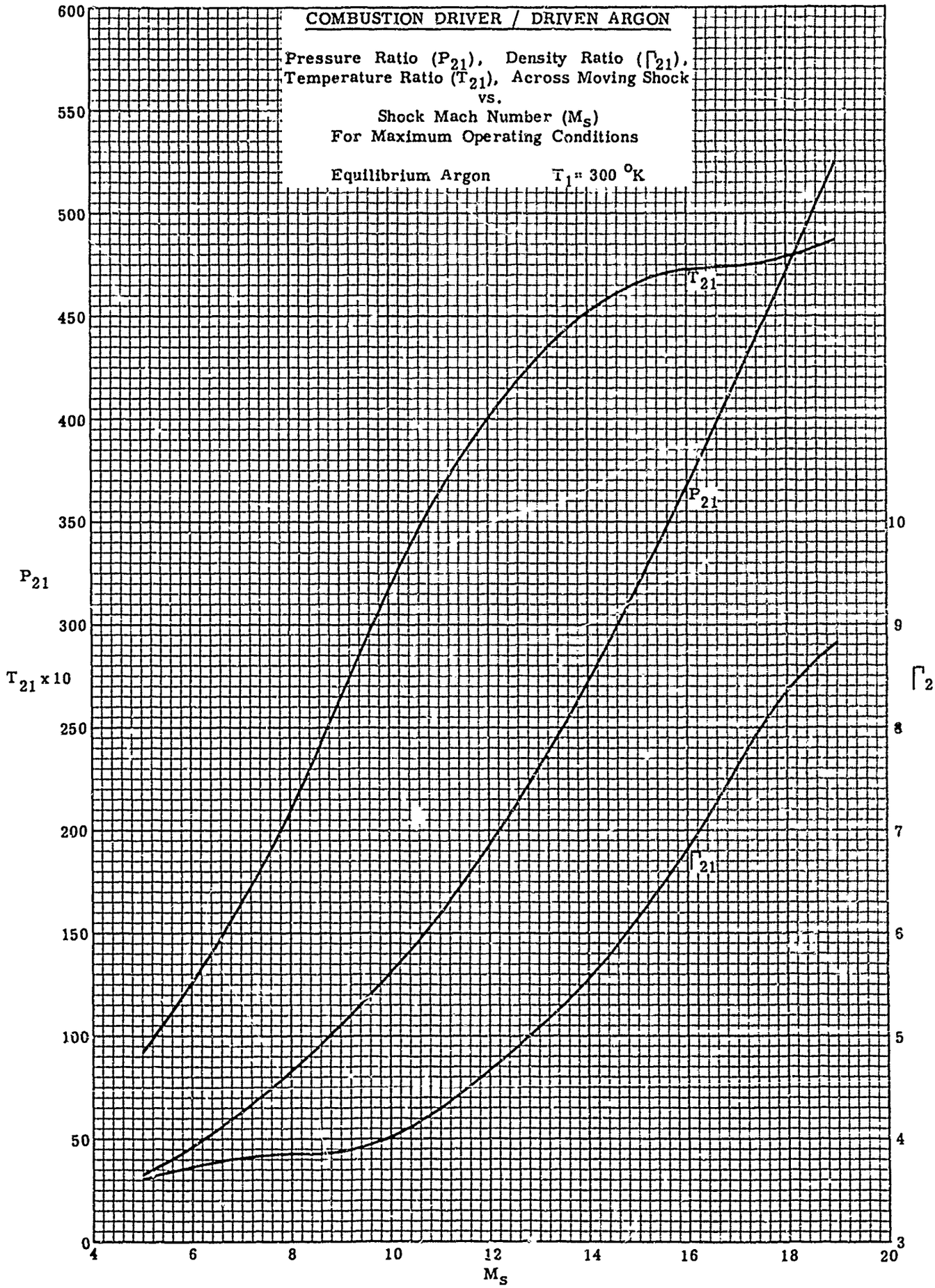
COMBUSTION DRIVER / DRIVEN ARGON
Pressure Ratio (P_{21}), Density Ratio (Γ_{21}), Temperature Ratio (T_{21}), Across Moving Shock
vs.
Shock Mach Number (M_s)
For Maximum Operating Conditions
Equilibrium Argon
T_1 = 300 °K
T_{21}
P_{21}
Γ_{21}
P_{21}
$T_{21} \times 10$
Γ_{21}
M_s
600
550
500
450
400
350
300
250
200
150
100
50
0
4
6
8
10
12
14
16
18
20
10
9
8
7
6
5
4
3

FIGURE 95

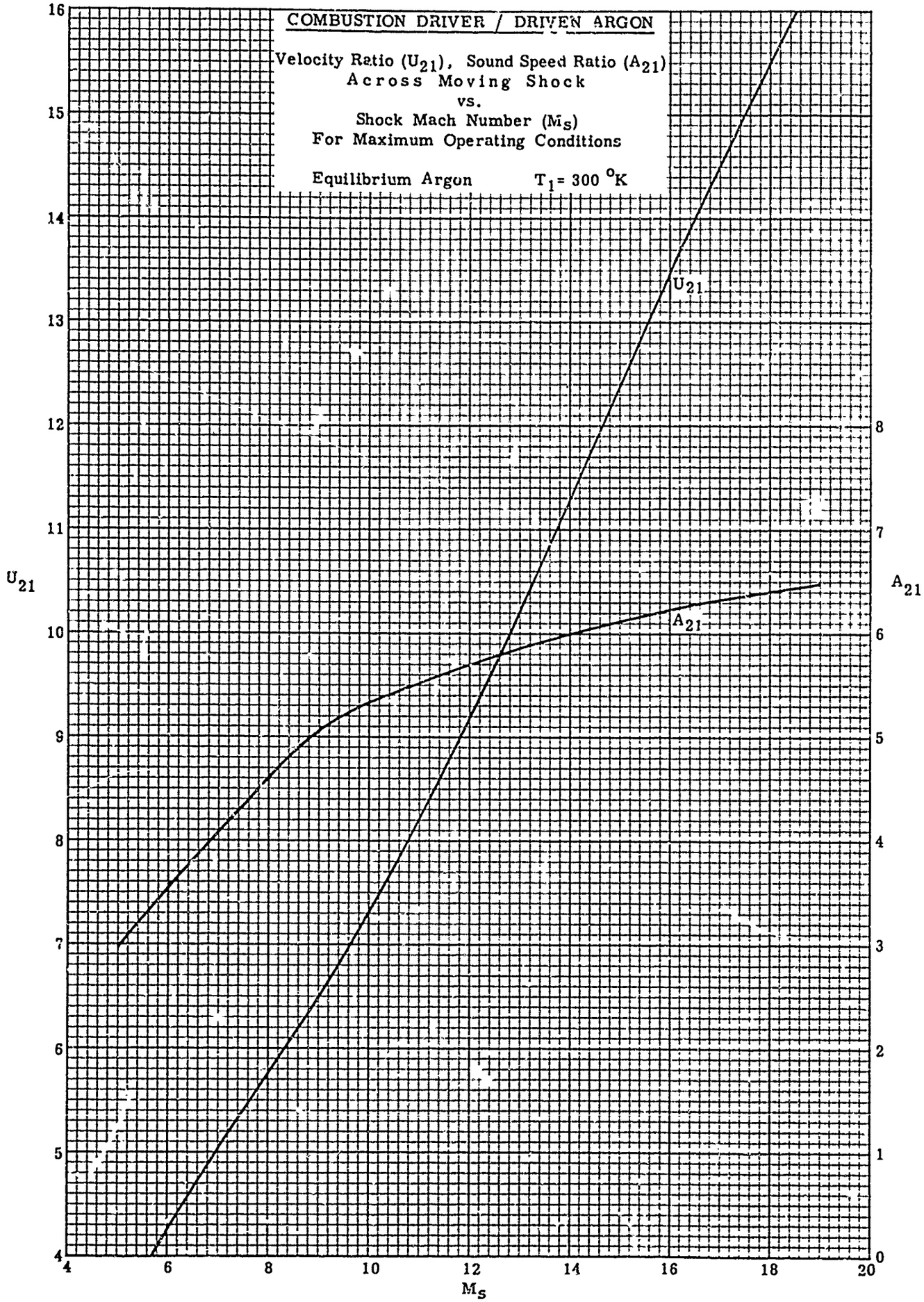
COMBUSTION DRIVER / DRIVEN ARGON
Velocity Ratio (U_{21}), Sound Speed Ratio (A_{21})
Across Moving Shock
vs.
Shock Mach Number (M_S)
For Maximum Operating Conditions
Equilibrium Argon
T_1 = 300 °K
U_{21}
A_{21}
M_S
16
15
14
13
12
11
10
9
8
7
6
5
4
8
7
6
5
4
3
2
1
0
4
6
8
10
12
14
16
18
20

FIGURE 96

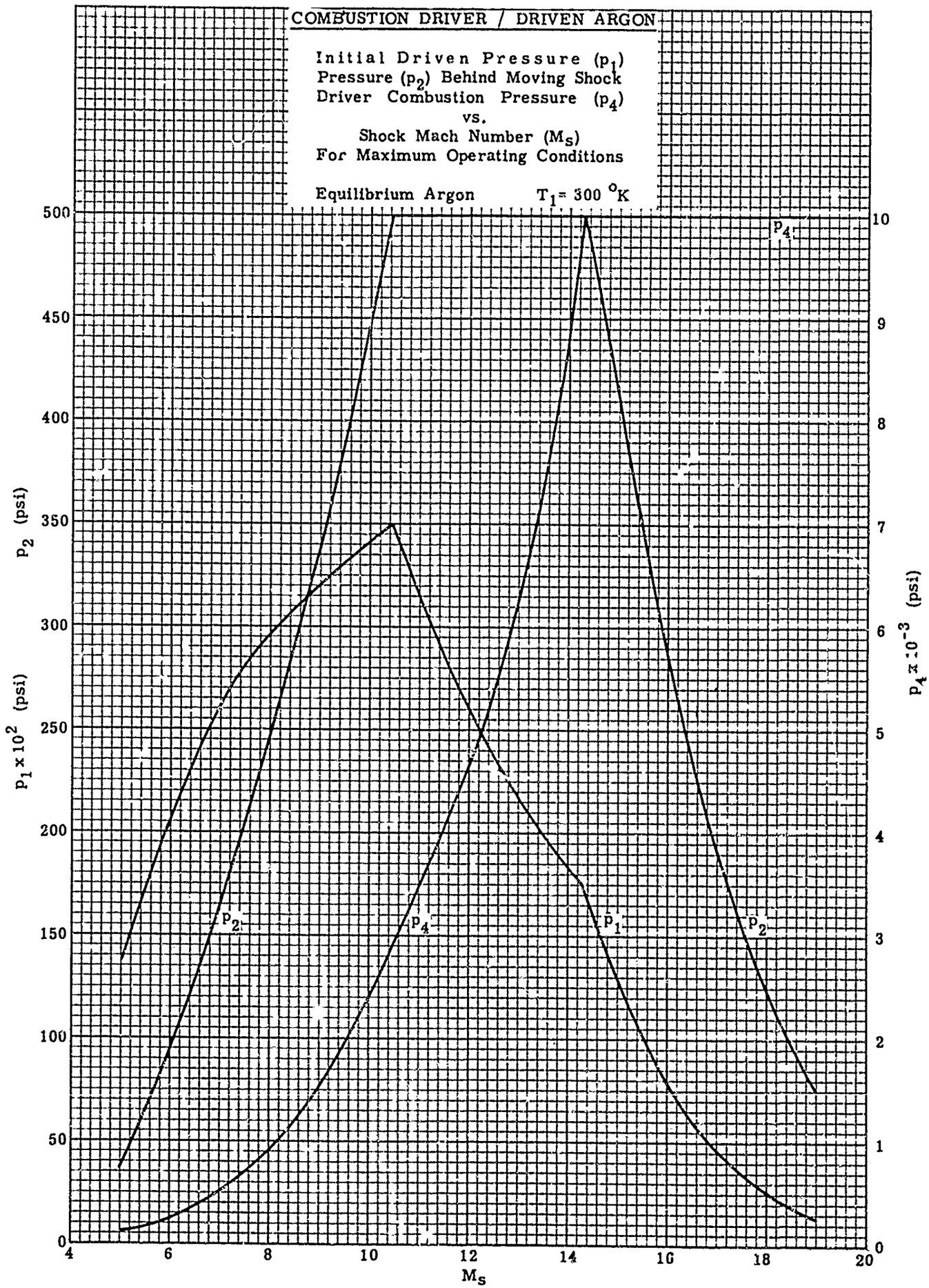
COMBUSTION DRIVER / DRIVEN ARGON
Initial Driven Pressure (p_1)
Pressure (p_2) Behind Moving Shock
Driver Combustion Pressure (p_4)
vs.
Shock Mach Number (M_s)
For Maximum Operating Conditions
Equilibrium Argon
T_1 = 300 °K
p_2 (psi)
$p_1 \times 10^2$ (psi)
$p_4 \times 10^{-3}$ (psi)
M_s
p_4
p_2
p_4
p_1
p_2
0
50
100
150
200
250
300
350
400
450
500
0
1
2
3
4
5
6
7
8
9
10
4
6
8
10
12
14
16
18
20

FIGURE 97

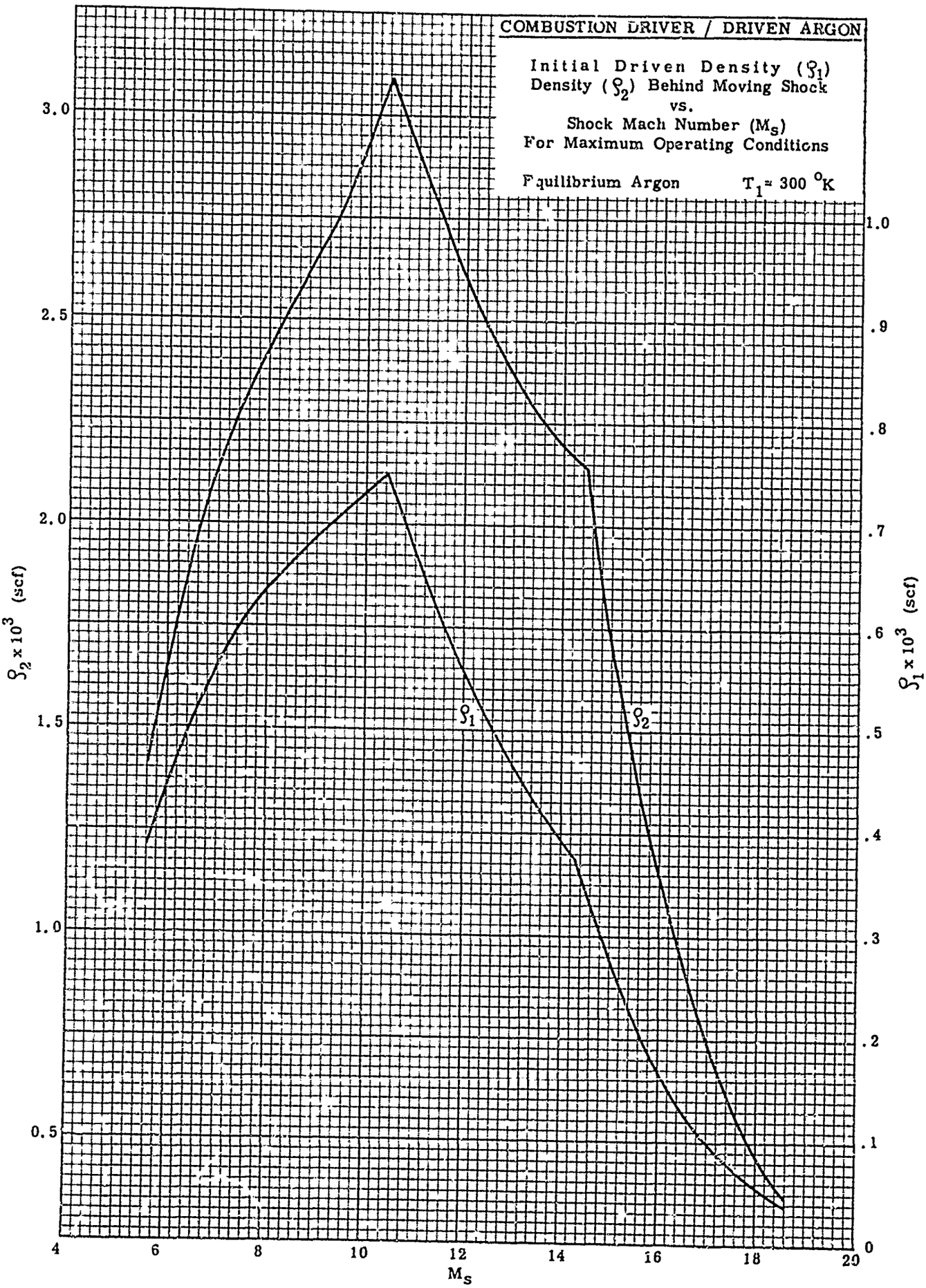
COMBUSTION DRIVER / DRIVEN ARGON
Initial Driven Density (ρ_1)
Density (ρ_2) Behind Moving Shock
vs.
Shock Mach Number (M_s)
For Maximum Operating Conditions
Equilibrium Argon
$T_1 = 300\ ^oK$
$\rho_2 \times 10^3$ (scf)
$\rho_1 \times 10^3$ (scf)
ρ_1
ρ_2
M_s
3.0
2.5
2.0
1.5
1.0
0.5
1.0
.9
.8
.7
.6
.5
.4
.3
.2
.1
0
4
6
8
10
12
14
16
18
20

FIGURE 98

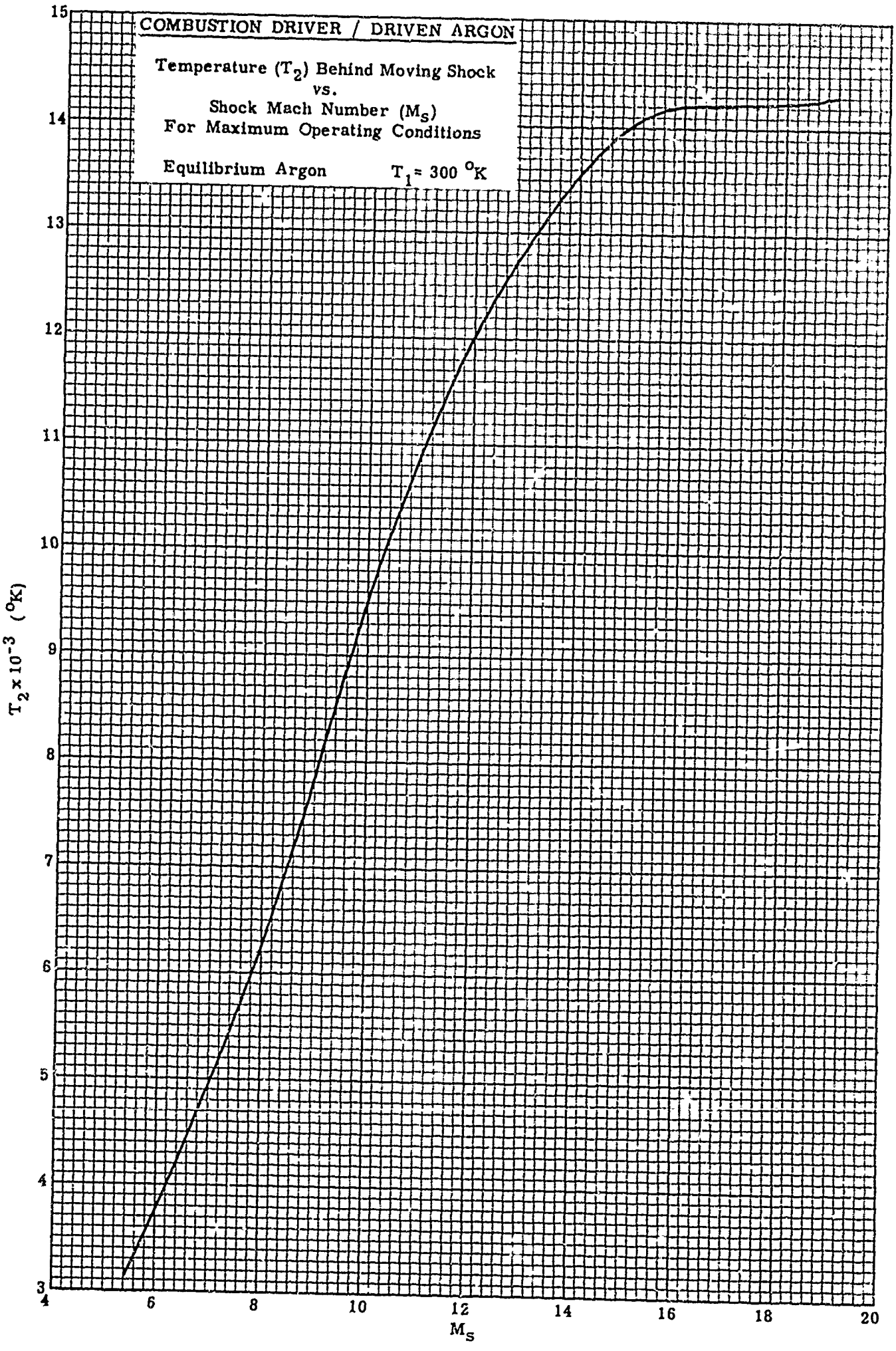
COMBUSTION DRIVER / DRIVEN ARGON
Temperature (T_2) Behind Moving Shock
vs.
Shock Mach Number (M_s)
For Maximum Operating Conditions
Equilibrium Argon
$T_1 = 300\ ^oK$
$T_2 \times 10^{-3}$ (^oK)
15
14
13
12
11
10
9
8
7
6
5
4
3
4
6
8
10
12
14
16
18
20
M_s

FIGURE 99

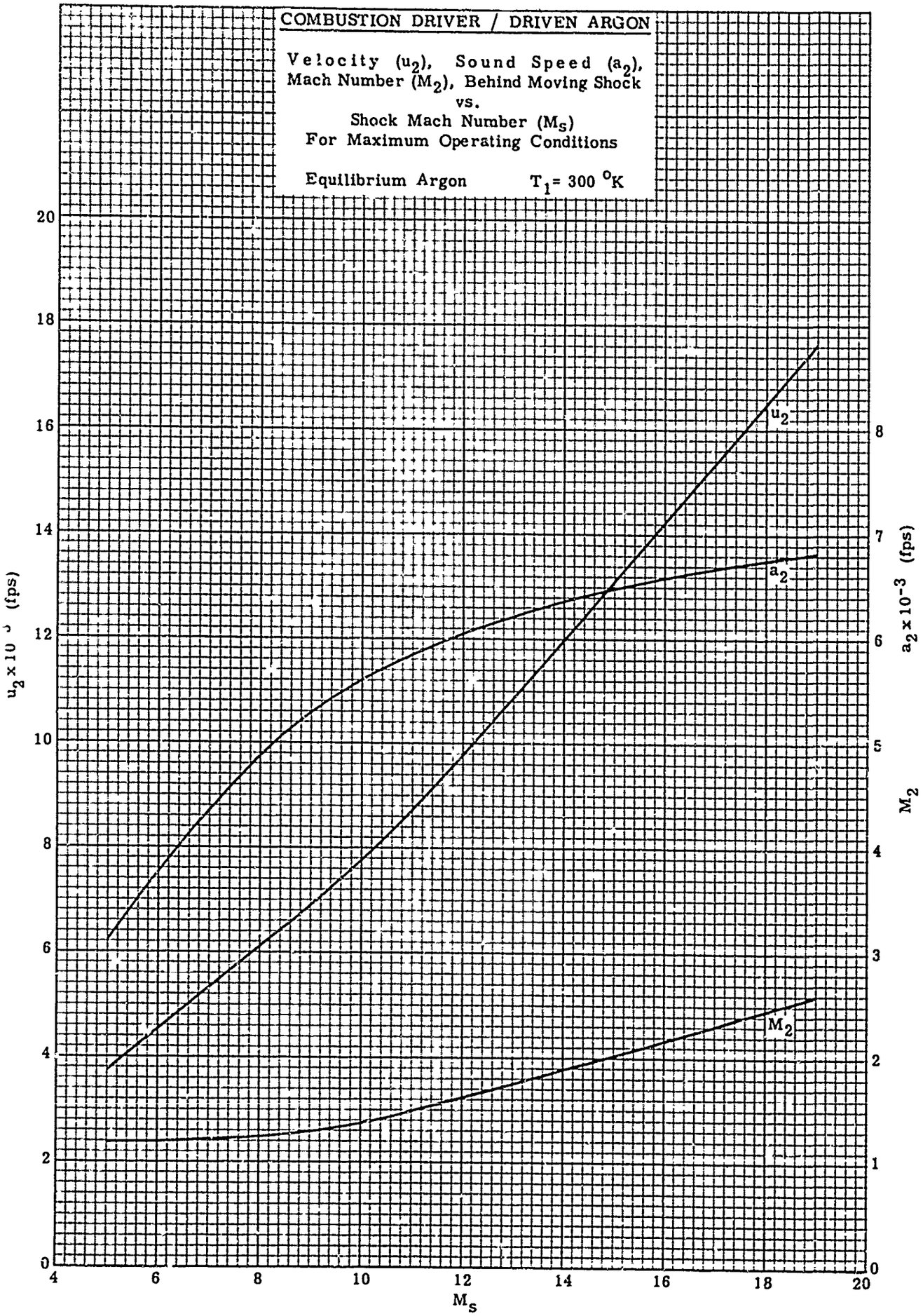
COMBUSTION DRIVER / DRIVEN ARGON
Velocity (u_2), Sound Speed (a_2), Mach Number (M_2), Behind Moving Shock
vs.
Shock Mach Number (M_s)
For Maximum Operating Conditions
Equilibrium Argon
T_1 = 300 °K
u_2
a_2
M_2
$u_2 \times 10^{-3}$ (fps)
$a_2 \times 10^{-3}$ (fps)
M_2
M_s
0
2
4
6
8
10
12
14
16
18
20
1
3
5
7

FIGURE 100

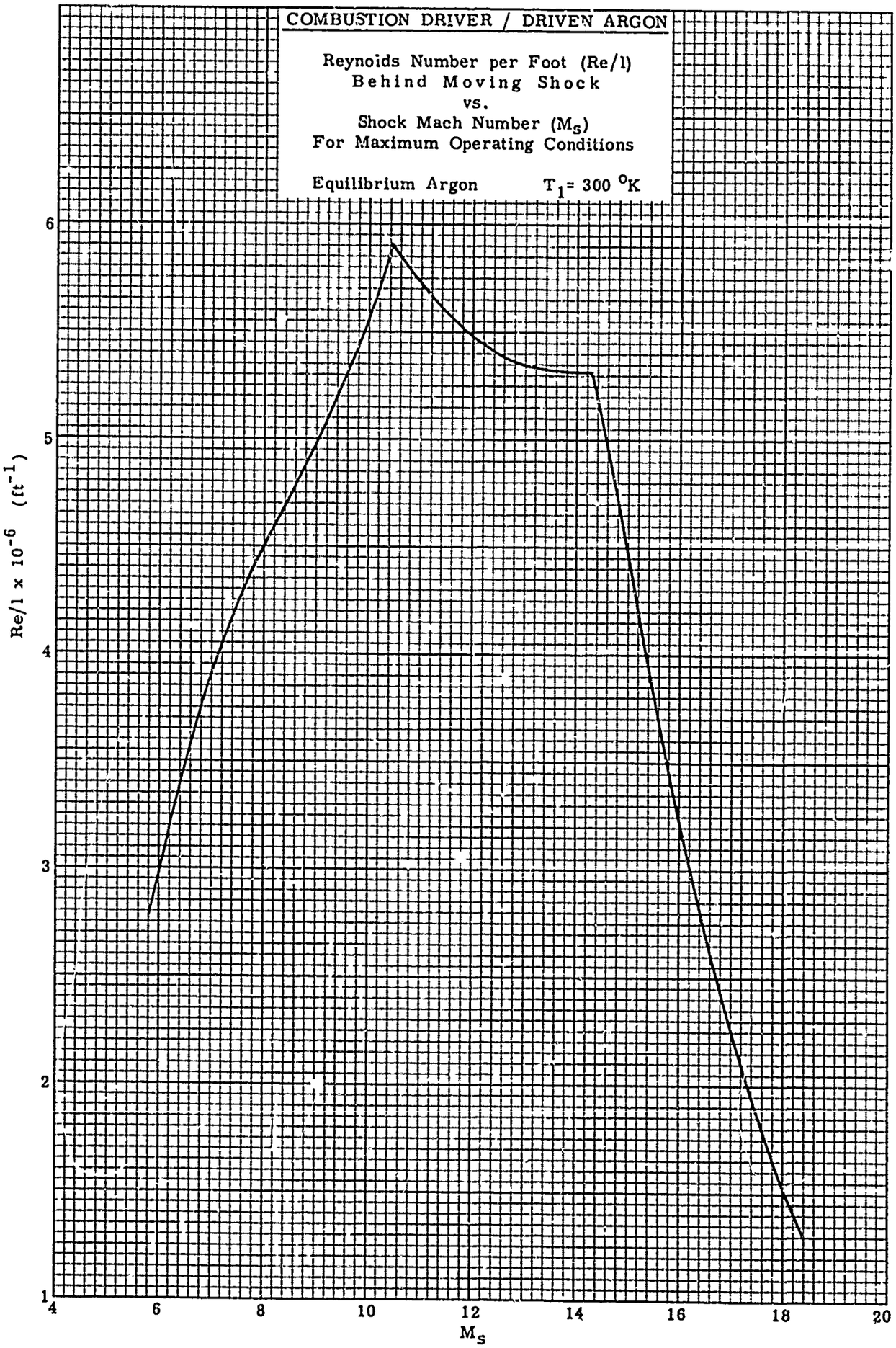
COMBUSTION DRIVER / DRIVEN ARGON
Reynoids Number per Foot (Re/l)
Behind Moving Shock
vs.
Shock Mach Number (M_s)
For Maximum Operating Conditions
Equilibrium Argon
T_1 = 300 °K
Re/l x 10^{-6} (ft^{-1})
1
2
3
4
5
6
4
6
8
10
12
14
16
18
20
M_s

FIGURE 101

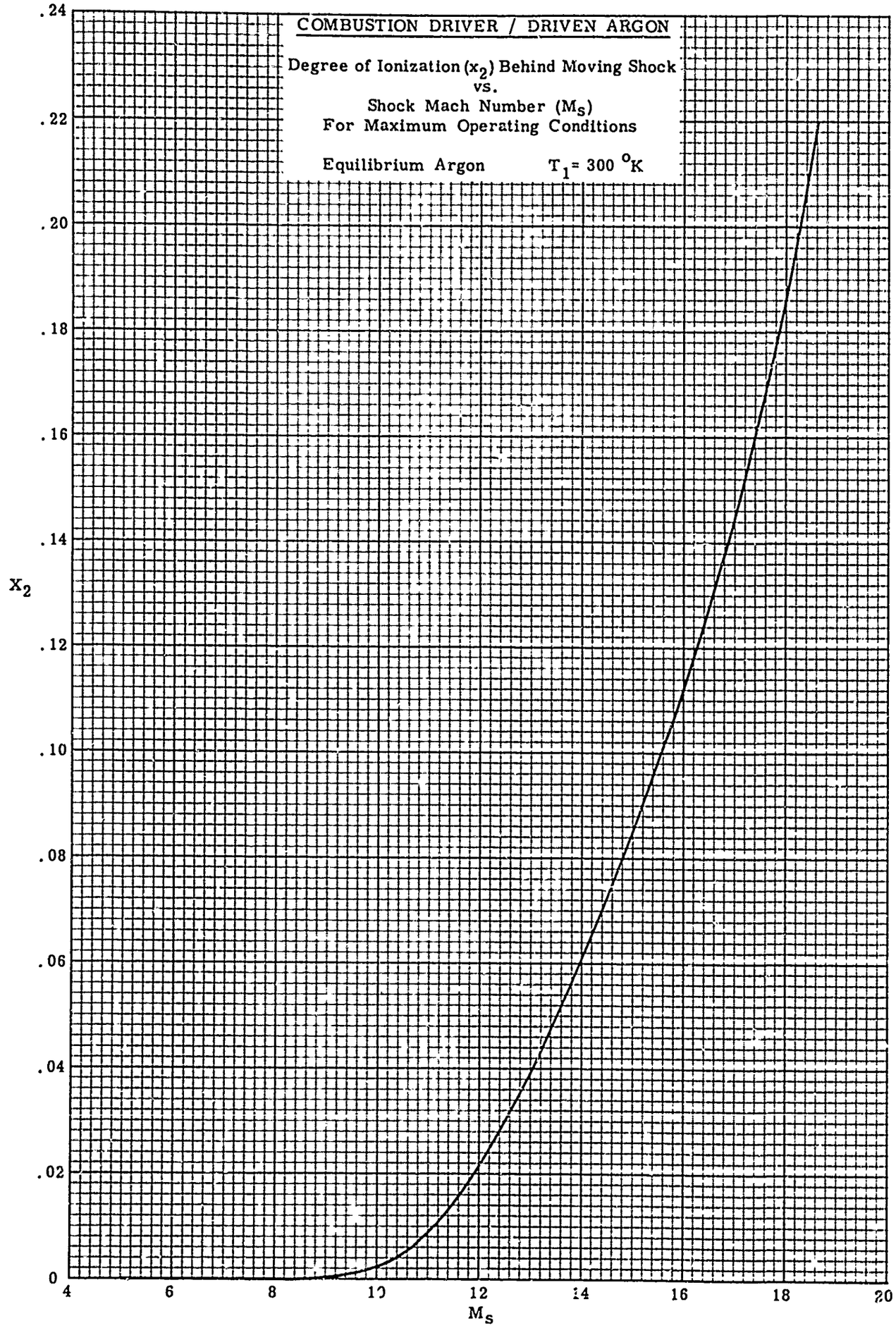
COMBUSTION DRIVER / DRIVEN ARGON
Degree of Ionization (x_2) Behind Moving Shock
vs.
Shock Mach Number (M_s)
For Maximum Operating Conditions
Equilibrium Argon
T_1 = 300 °K
X_2
.24
.22
.20
.18
.16
.14
.12
.10
.08
.06
.04
.02
0
4
6
8
10
12
14
16
18
20
M_s

FIGURE 102

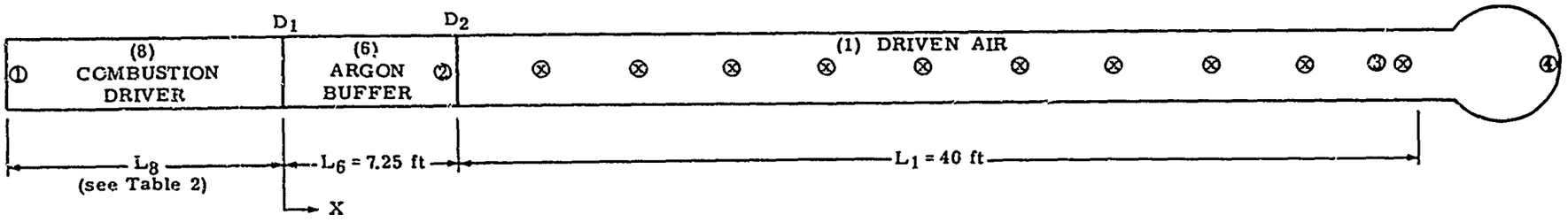

PRESSURE TRANSDUCERS (KISTLER)

① 605 - DRIVER END PLATE

② 601 - BUFFER X = 6.67 ft.

③ 601 - TEST SECTION X = 45.75 ft.

④ 601 - DUMP TANK X = 51.85 ft.

SHOCK DETECTORS

⊗ IONIZATION GAUGES

4-FOOT INTERVALS FROM

X = 10.75 ft. TO X = 46.75 ft.

FIG. 103 CONFIGURATION FOR SHOCK TUBE CALIBRATION

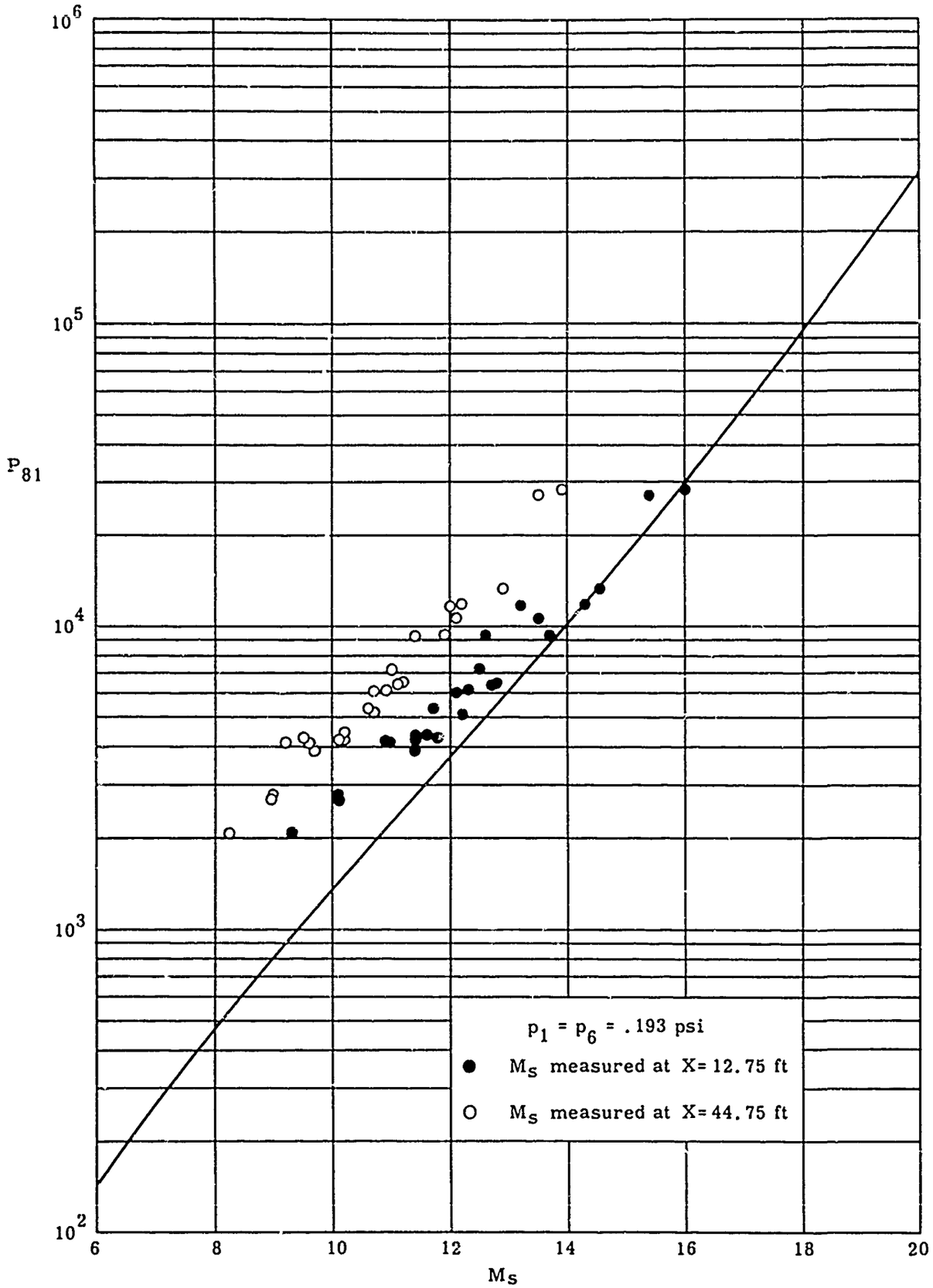

FIG. 104 PEAK OVERALL PRESSURE RATIO (P_{81}) vs SHOCK MACH NUMBER (M_s) IN DRIVEN AIR

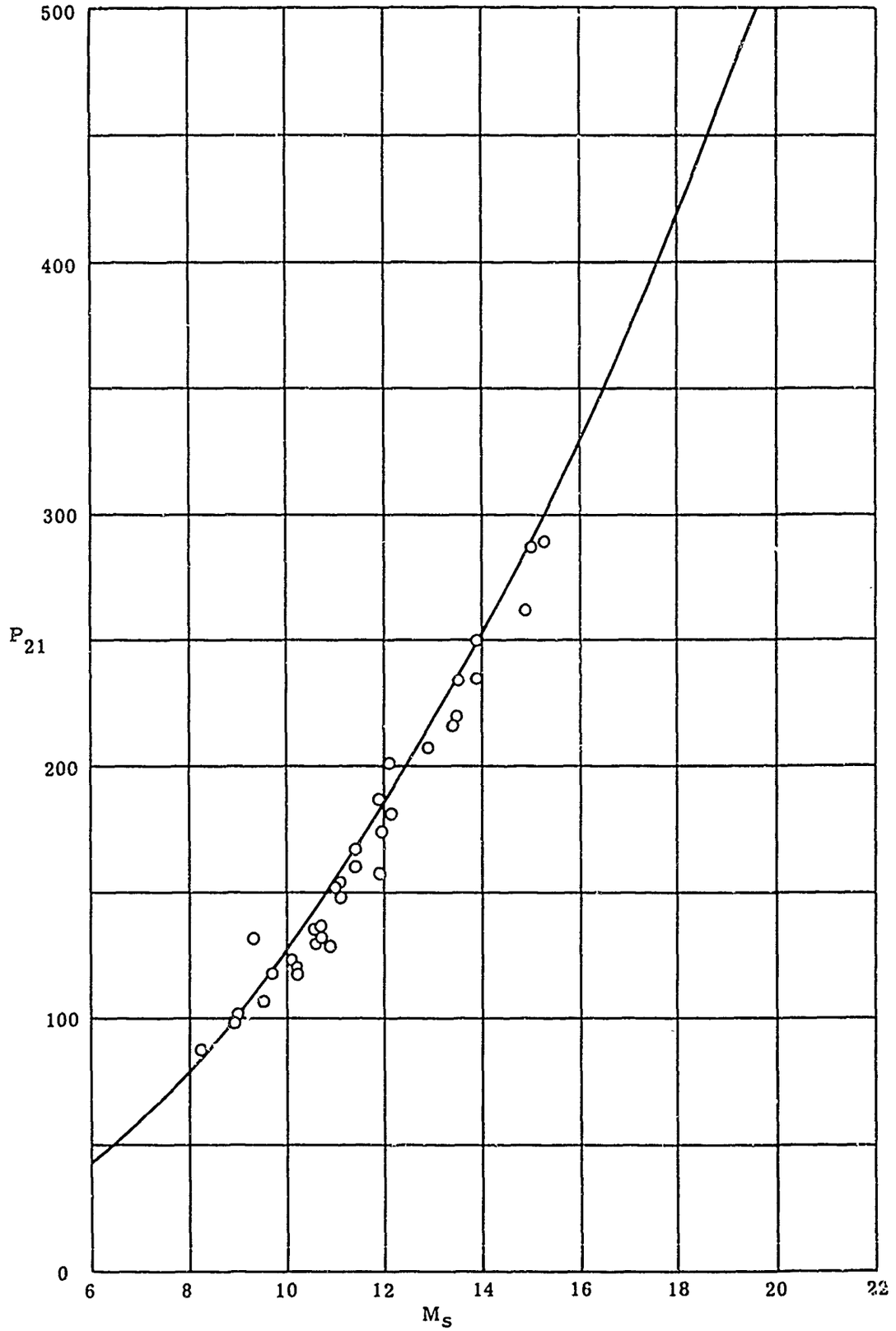

FIG. 105 SHOCK PRESSURE RATIO (P_{21}) vs SHOCK MACH NUMBER (M_s) IN DRIVEN AIR

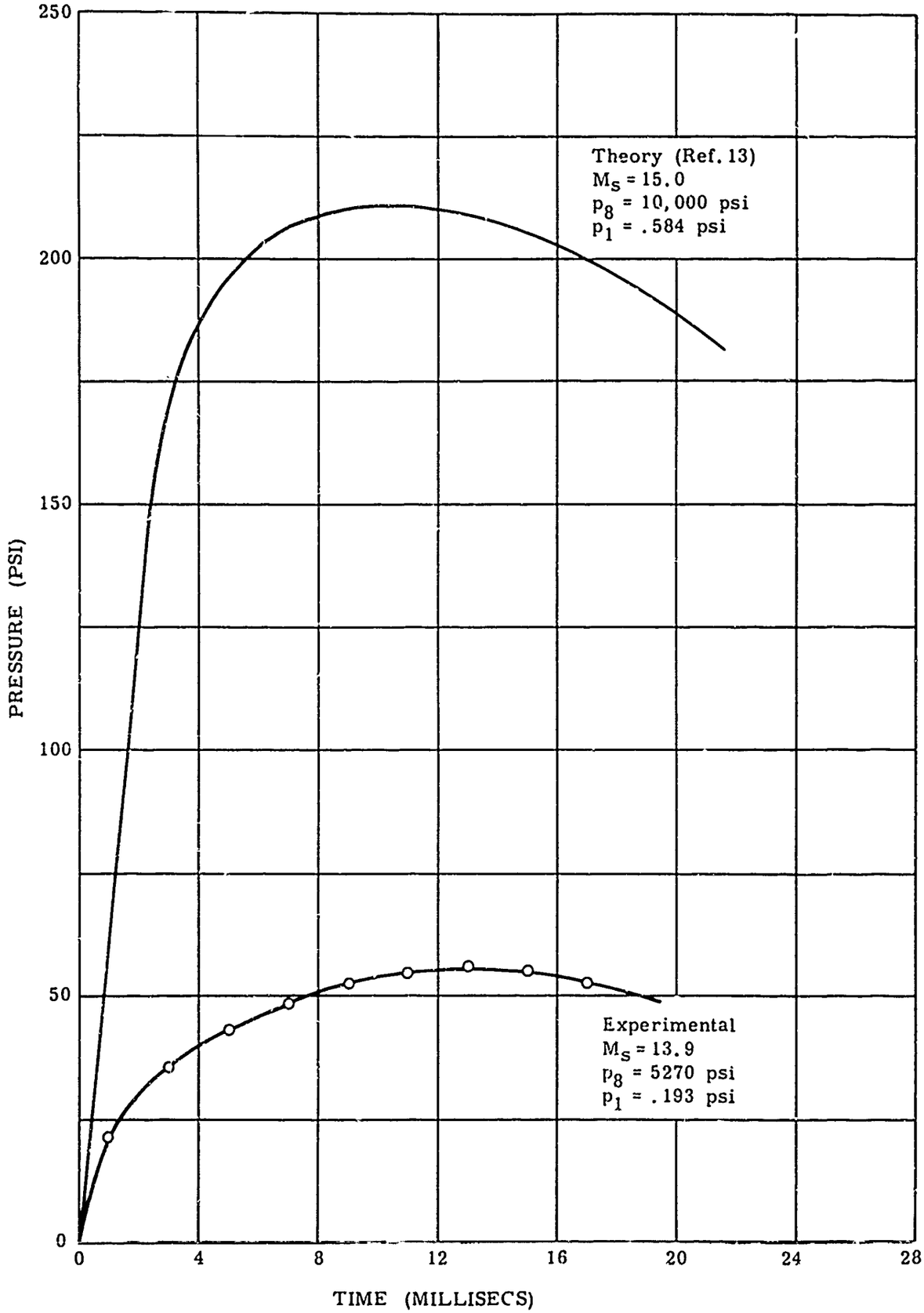

FIG. 106 PRESSURE-TIME HISTORY IN DUMP TANK

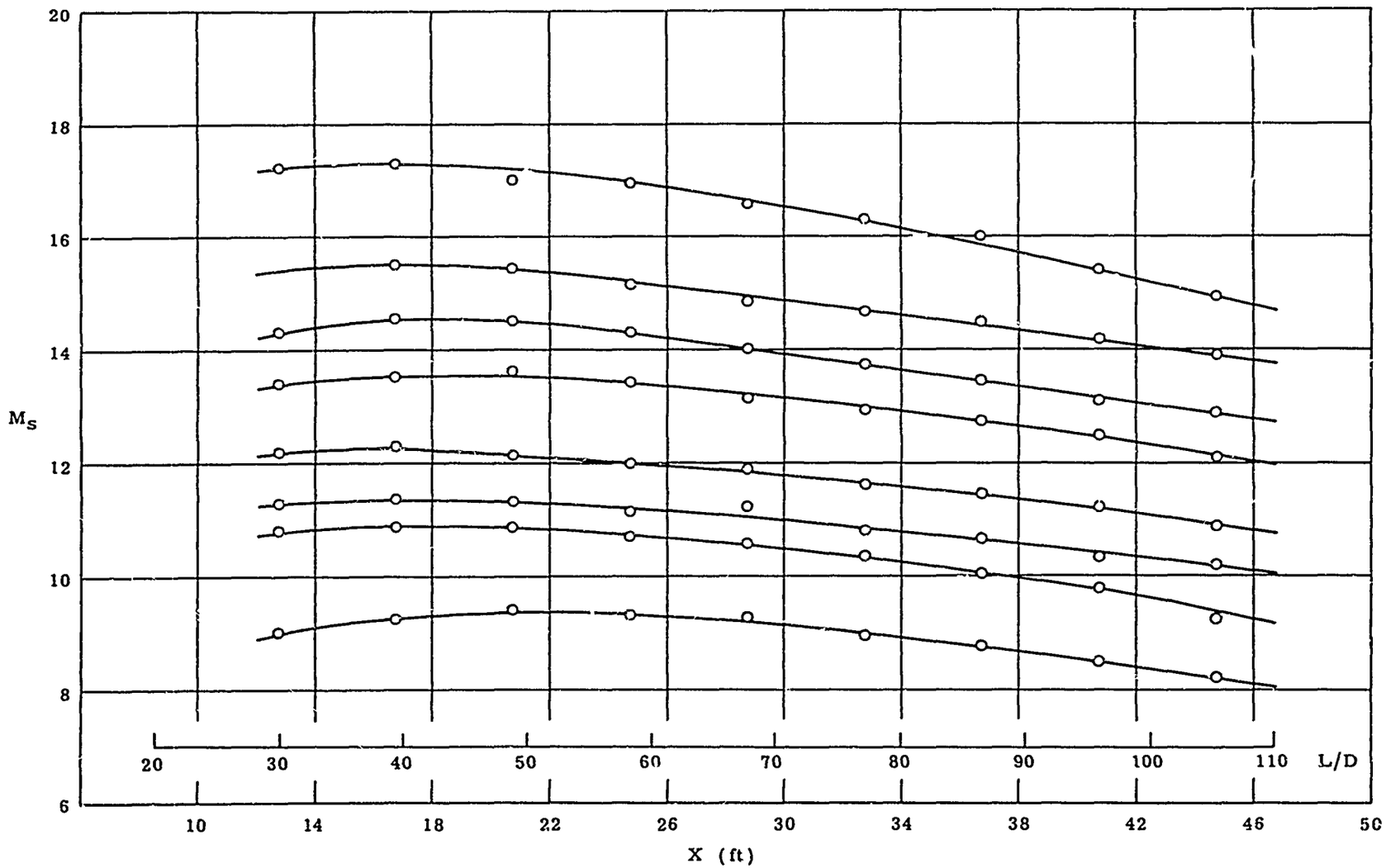

FIG. 107 SHOCK MACH NUMBER (M_S) vs DISTANCE (X) ALONG DRIVEN SECTION

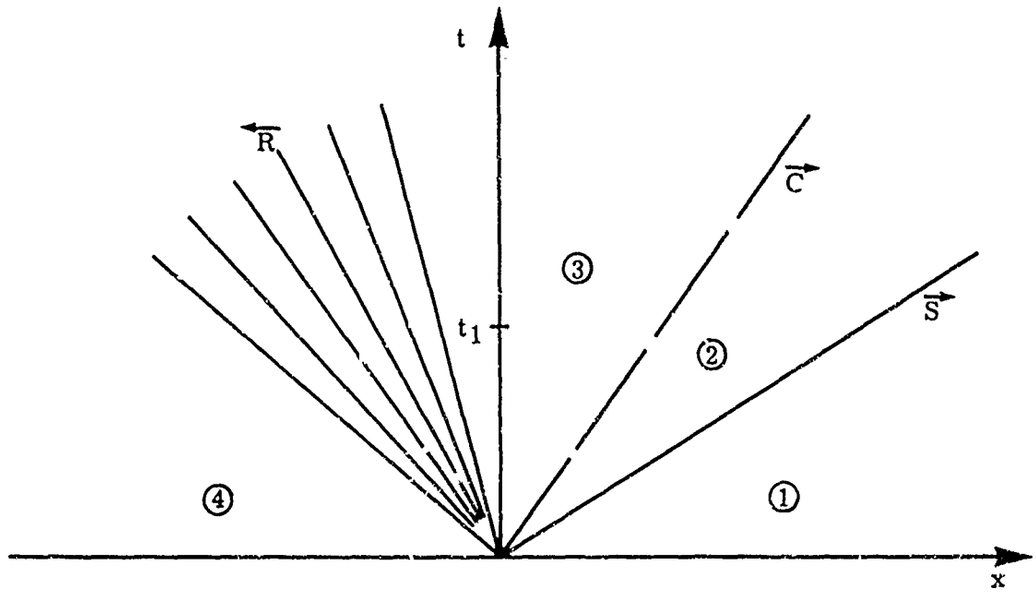

(a) TYPICAL WAVE DIAGRAM

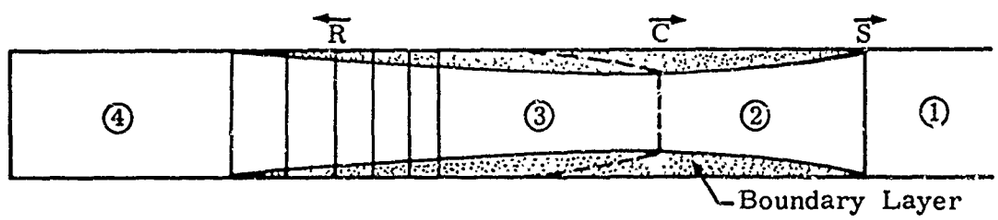

(b) FLOW AT TIME t_1

FIG. 108 BOUNDARY LAYER ON SHOCK TUBE WALL